Flows and mixing in liquid metal batteries

Sabrina Bénard

Sabrina Bénard. Flows and mixing in liquid metal batteries. Fluid mechanics [physics.class-ph]. Université Paris-Saclay, 2023. English. NNT : 2023UPAST139 . tel-04409555v2

HAL Id: tel-04409555
https://theses.hal.science/tel-04409555v2

Flows and mixing in liquid metal batteries

Écoulements et mélange dans les batteries à métaux liquides

Thèse de doctorat de l'université Paris-Saclay

École doctorale n° 579, sciences mécaniques et énergétiques, matériaux et géosciences (SMEMaG)
Spécialité de doctorat : Mécanique des fluides
Graduate School : Sciences de l'ingénierie et des systèmes. Référent : Faculté des sciences d'Orsay

Thèse préparée dans l'unité de recherche **LISN** (Université Paris-Saclay, CNRS), sous la direction de **Caroline NORE**, professeure, et le co-encadrement de **Wietze HERREMAN**, maître de conférences.

Thèse soutenue à Paris-Saclay, le 02 novembre 2023, par

Sabrina BÉNARD

Composition du jury

Membres du jury avec voix délibérative

Bérengère PODVIN Directrice de recherche, CNRS, Université Paris-Saclay	Présidente
Thierry ALBOUSSIÈRE Directeur de recherche, CNRS, Université Claude Bernard Lyon 1	Rapporteur & Examinateur
Alban POTHERAT Professeur, Coventry University	Rapporteur & Examinateur
Marie-Charlotte RENOULT Maîtresse de conférences, Normandie Université	Examinatrice

THESE DE DOCTORAT

NNT : 2023UPAST139

université
PARIS-SACLAY

ÉCOLE DOCTORALE
Sciences mécaniques et
énergétiques, matériaux
et géosciences (SMEMAG)

Titre : Écoulements et mélange dans les batteries à métaux liquides

Mots clés : Batterie à métaux liquides, analyse numérique, mécanique des fluides, magnétohydrodynamique, calcul haute performance

Résumé : Les batteries à métaux liquides (BMLs) sont une solution prometteuse pour le stockage à grande échelle des énergies renouvelables qui sont produites de manière intermittente. Ces BMLs sont moins chères et peuvent fonctionner plus longtemps que les batteries habituelles. Elles sont composées de trois couches : une électrode négative en métal liquide, un électrolyte en sel fondu et une électrode positive, alliage formé avec le métal liquide supérieur. Les BMLs sont des systèmes multiphysiques dans lesquels des instabilités magnétohydrodynamiques se produisent et des écoulements apparaissent pendant le fonctionnement. Les écoulements peuvent être néfastes, car ils peuvent déformer les interfaces jusqu'à induire un court-circuit. Ils peuvent cependant aussi être utiles pour mélanger l'alliage, ce qui limite la chute du potentiel de la cellule. Dans cette thèse, nous nous concentrons sur le problème du mélange de l'alliage.

Nous présentons d'abord des contributions pré-doctorales. Dans une première partie, nous étudions l'effet de la flottabilité solutale sur l'écoulement electrovortex. Nous montrons que, pendant la décharge, cet écoulement n'est pas assez intense pour s'opposer à la flottabilité et donc ne peut pas mélanger l'alliage. Cependant, l'écoulement electrovortex tournant, qui se produit sous l'action d'un champ magnétique externe, mélange efficacement l'alliage. Pendant la charge, se met en place de la convection solutale qui est vraiment efficace pour mélanger l'alliage. La flottabilité solutale a alors une influence significative sur l'écoulement. Dans une seconde partie, nous étudions le transfert de gouttes de l'électrode négative vers l'électrode positive. Nous montrons que, selon les prototypes, le détachement et le transfert de gouttes peuvent se produire au cours du fonctionnement. Dans certains cas, cela peut conduire à des courts-circuits.

Ensuite, nous caractérisons l'écoulement electrovortex tournant. Nous menons une étude numérique paramétrique tridimensionnelle et axisymétrique afin de mieux comprendre les différents régimes d'écoulement. Nous choisissons comme prototype un cylindre rempli d'un métal liquide et connecté symétriquement à deux fils, ce qui crée un écoulement similaire à l'écoulement de von Kármán. Nous analysons l'impact des différents paramètres sur l'intensité de l'écoulement et fournissons des lois d'échelle.

Nous nous intéressons par la suite à l'amélioration de notre modèle pour les BMLs. Pour cela, le potentiel électrique doit être considéré comme une variable locale dans les équations, et non pas calculé en post-traitement comme fait dans nos études précédentes. La distribution du potentiel électrique est influencée par un saut de potentiel qui apparaît à l'interface alliage-électrolyte. Ce saut affecte les distributions de courant et de concentration. Cependant, notre solveur est basé sur une formulation en champ magnétique et ne calcule pas le potentiel électrique. Nous déterminons une nouvelle condition d'interface, en utilisant la variable de champ magnétique, qui modélise les distributions de potentiel discontinues à une interface. Nous validons numériquement cette nouvelle formulation. Ensuite, nous implémentons la concentration dans ce modèle et étudions l'impact du saut de potentiel sur la composition de l'alliage. Nous montrons que ce saut affecte modérément la distribution de la concentration, mais influence le potentiel de la cellule. Il est alors plus exact de considérer le saut dans le modèle. Dans la dernière partie, nous étudions les écoulements électrocapillaires qui apparaissent en raison du saut de potentiel électrique, qui modifie localement la tension de surface. Nous montrons que la flottabilité solutale a un impact significatif sur l'écoulement, localisé dans une petite zone proche de l'interface alliage-électrolyte. L'écoulement est capable de mélanger cette zone et de limiter la chute du potentiel de la cellule.

université
PARIS-SACLAY

ÉCOLE DOCTORALE
Sciences mécaniques et
énergétiques, matériaux
et géosciences (SMEMAG)

Title : Flows and mixing in liquid metal batteries

Keywords : Liquid metal battery, numerical analysis, fluid mechanics, magnetohydrodynamics, high performance computing

Abstract : Liquid metal batteries (LMBs) are a promising solution for large-scale energy storage of renewable energies, which are produced in an intermittent way. These LMBs are cheaper and have a longer lifetime than usual batteries. They are composed of three layers : a negative electrode in liquid metal, an electrolyte in molten salt, and a positive electrode which alloys with the top liquid metal. LMBs are multi-physical systems where magnetohydrodynamics instabilities occur and flows appear during operation. Flows can be detrimental, as they can deform the interfaces until a short circuit appears. They can however also be useful for mixing the alloy, which limits the drop of the cell potential. In this thesis, we focus on the mixing problem of the alloy phase.

We first present pre-thesis contributions. In the first part, we study the effect of solutal buoyancy on the electrovortex flow. We show that, during discharge, this flow is not intense enough to counteract the buoyancy, and then not able to mix the alloy. However, swirling electrovortex flow, which is driven when an external magnetic field is applied, mixes efficiently the alloy. During charge, solutal convection occurs, which is really efficient to mix the alloy. Solutal buoyancy has then a really significant influence on the flow. In the second part, we study the droplets transfer from the negative electrode to the positive electrode. We show that, depending on the prototypes, droplet detachment and transfer can occur during operation. In certain cases, it can lead to short circuits.

Later, we characterize the swirling electrovortex flow. We conduct a three-dimensional and axisymmetric numerical parametric study in order to better understand the different flow regimes. We choose for the prototype a cylinder filled with a liquid metal and symmetrically connected to two wires, which drives a flow similar to the von Kármán flow. We analyze the impacts of different parameters on the flow intensity and provide scaling laws.

Then, we are interested in improving our model for LMBs. For this purpose, the electrical potential should be considered as a local variable in the equations, and not computed in post-processing as done before in our previous studies. The electrical potential distribution is impacted by a jump in potential which appears at the interface alloy-electrolyte. This jump affects the current and concentration distributions. However, our solver is based on a magnetic field-based formulation and does not compute the electrical potential. We determine a new interface condition using the magnetic field variable modeling discontinuous potential distributions at an interface. We validate numerically this new formulation. Then, we implement the concentration in this model and investigate the impact of the jump in potential on the alloy composition. We show that this jump affects moderately the concentration distribution, but influences the cell potential. It is then more accurate to consider the jump in the model. In the last part, we study electrocapillary flows that appear due to the jump in electrical potential, which modifies locally the surface tension. We show that the solutal buoyancy impacts significantly the flow, which is localized in a small zone close to the alloy-electrolyte interface. The flow is able to mix this zone and to limit the drop of the cell potential.

Remerciements

Je remercie tout d'abord ma directrice de thèse Caroline Nore et mon co-encadrant Wietze Herreman, qui forment un duo très complémentaire, pour leur assistance, leur disponibilité, leur soutien et leurs conseils, qui m'ont permis de mener à bien cette thèse. Je remercie Caroline pour son aide pour la partie numérique, sa réactivité et son efficacité, et Wietze pour son aide pour la partie théorique, l'écriture des articles et son exigence qui m'a permis de nettement m'améliorer sur certains points. Leur encadrement était exceptionnel, et je leur en suis très reconnaissante.
Je voudrais maintenant remercier les membres du jury, Alban Pothérat et Thierry Alboussière en tant que rapporteurs pour avoir accepté d'examiner mon manuscrit, ainsi que Bérengère Podvin et Marie-Charlotte Renoult pour avoir accepté d'assister à ma soutenance. Les discussions lors des questions durant la soutenance ont été très intéressantes. Je remercie également Bérengère Podvin et Laurent Davoust, membres du comité de suivi de thèse, pour les échanges constructifs sur mon travail.
J'ai pu, lors de ce travail, échanger avec d'autres collaborateurs. Tout d'abord, je remercie Norbert Weber, Tom Weier, Gerrit Horstmann et Paolo Personnettaz pour le travail réalisé ensemble et pour la collaboration lors de mon séjour à HZDR, qui fut une expérience très enrichissante. Je remercie également Jean-Luc Guermond et Loïc Cappanera pour leur aide précieuse lors des développements apportés à SFEMaNS, et en particulier Loïc pour le temps passé à m'aider à résoudre les problèmes techniques.
Le bon déroulement d'une thèse nécessite également une aide admnistrative et technique. Merci aux équipes administratives du LISN, de l'université Paris-Saclay et de l'école doctorale SMEMaG pour leur réactivité et leur assistance, ainsi qu'aux équipes informatiques du LISN et de l'IDRIS, pour leur support et leur aide.
Je voudrais ensuite remercier l'équipe de doctorants et stagiaires du LISN, du département mécanique et des autres départements, qui ont fortement participé à la très bonne ambiance régnant dans le laboratoire, et sans qui les pauses cafés et les repas au CESFO n'auraient pas été aussi agréables: Amine, Antoine, Artur, Daniele, Gen, Hugues, Manon, Marion, Melvin, Michele, Nathan, Paul, Pierre-Adams, Rémi, Rémy, Stéphane, Thibault, Yanis. Merci également pour les bons moments et les aventures en dehors du laboratoire.
Je remercie également mes amis, anciens et plus récents, et en particulier Claire, Elodie et Marouchka, pour les très bons moments, pour le soutien moral et pour toutes les aventures vécues ensemble lors de ces longues années d'amitié. Je remercie aussi ma famille, et plus particulièrement mes grands-parents et mes parents. Merci à tous ceux qui ont fait le déplacement pour assister à ma soutenance.
Enfin, je remercie chaudement Frederik pour tout son soutien, ses encouragements et sa présence tout au long de ces trois années de doctorat, et un peu avant aussi. Merci pour toujours trouver les bons mots pour me réconforter, et pour tout simplement être là à mes côtés.

Publications et travaux en cours relatifs à cette thèse

- *Solutal buoyancy and electrovortex flow in liquid metal batteries*, Physical Review Fluids, doi:10.1103/PhysRevFluids.5.074501 (Herreman et al., 2020).
  Section §2.2 of chapter 2.

- *Anode-metal drop formation and detachment mechanisms in liquid metal batteries*, Journal of Power Sources, doi:10.1016/j.jpowsour.2021.230339 (Bénard et al., 2021).
  Section §2.3 of chapter 2.

- *Numerical simulations of swirling electrovortex flows in cylinders*, Journal of Fluid Mechanics, doi:10.1017/jfm.2022.779 (Bénard et al., 2022).
  Chapter 3.

- *Magnetic field based finite element method for magneto-static problems with discontinuous electric potential distributions*, Comptes Rendus. Mécanique, doi:10.5802/crmeca.184 (Bénard et al., 2023).
  Chapter 4.

- *Connecting alloy composition to electrical potential in liquid metal batteries*, submitted to Journal of Power Sources.
  Chapter 5.

Contents

Chapter 1

Introduction

1.1 Need of energy storage

In the actual context of climate change, the way electricity is generated needs to be changed. The Paris Agreement aims to limit the global warming at 2°C, which means reducing drastically the greenhouse gases. Thus, the production of fossil energy has to be massively reduced. However, the energy demand keeps growing. In 2050, global worldwide electricity demand is predicted to be 75% higher than today, for a scenario where current policies are applied. A more ambitious scenario, with an objective of net zero emissions by 2050, predicts a global electricity demand 150% higher than today (IEA, 2022). Hence, new ways of generating electricity have to be used to answer both the energy demand and the Paris Agreement objectives. A solution is to increase the use of renewable energies, such as solar or wind energies, which are much more environmentally friendly. The European Commission (EC, 2023) predicts that the share of renewable energy in EU will reach 80% of the total energy production in 2050, compared to 37% in 2021. Their electricity production is however intermittent, since it highly depends on environmental conditions. They are then not able to follow instantaneously the energy demand - production peaks do not concord with demand peaks. Thus, flexibility of these electrical systems - i.e. the capacity of increasing or reducing the provided energy - is required. By 2050, the flexibility is predicted to reach 30% of the EU energy demand, compared to 11% in 2021 (EC, 2023). An efficient massive energy storage is then required to provide higher flexibility. More particularly, long-duration energy storage systems should be used, so that the energy production is ensured to be cost-effective and decarbonized (EC, 2023). In the US, the US Advanced Research Projects Agency- Energy has fixed a goal for the cost of energy and power of storage systems: the energy cost should remain lower than $\$100\text{kWh}^{-1}$ and the power cost lower than $\$1000\text{kW}^{-1}$ (Spatocco and Sadoway, 2015).

Different kinds of storage systems exist, such as thermal, mechanical and electrochemical storage. LDES Council (LC, 2021) has shown that chemical storage technologies, such as batteries, can answer the requirement of a long-duration energy storage. In the EU, batteries are considered as strategic in order to be independent from non-EU countries (EC, 2022).
Among different kinds of batteries, liquid metal batteries (LMBs) are promising candidates for large-scale and long-duration stationary storage.

1.2 Liquid metal batteries

1.2.1 Description of a liquid metal battery

An LMB is an electrochemical cell composed of three liquid layers: a negative electrode of light liquid metal A at the top, an intermediate layer of molten salt electrolyte, and a positive electrode made of an alloy between A and a heavy liquid metal B at the bottom. Because of the difference of densities of each fluid, the fluids are stacked stably on top of each other.
The battery operates as follows: during discharge, the liquid metal A gives n_e electrons e^- to the electrical circuit, where n_e is the charge number. An electrochemical reaction at the negative electrode-electrolyte interface (oxidation reaction) occurs:

$$\mathrm{A} \;\longrightarrow\; \mathrm{A}^{n_e+} + n_e\mathrm{e}^- . \tag{1.2.1}$$

Then, the ions $\mathrm{A}^{\mathrm{n_e}+}$ diffuse in the electrolyte to the alloy, where the following electrochemical reaction occurs at the positive electrode-electrolyte interface (reduction reaction)

$$\mathrm{A}^{n_e+} + n_e\mathrm{e}^- \;\longrightarrow\; \mathrm{A}\,(\mathrm{in\,B}). \tag{1.2.2}$$

A atoms diffuse then in the alloy. The thickness of the layer of liquid metal A decreases and the thickness of the alloy layer increases. The battery is in this case a generator; the negative electrode corresponds to the anode and the positive electrode corresponds to the cathode. During charge, the process is reversed. The alloy gives n_e electrons to the external circuit. An ion A^{n_e+} formed in the alloy diffuses in the electrolyte to be combined with n_e electrons of the circuit coming from the alloy. The upper layer of metal is restored. The battery is in this case a receptor; the negative electrode corresponds to the cathode and the positive electrode corresponds to the anode. See figure 1.1 for a scheme of operation during discharge and charge. During the process, electrical energy is converted into electrochemical energy (or vice versa), which is the Gibbs free energy of the cell $\Delta\bar{G}_{\mathrm{cell}}$, such as:

$$\Delta\bar{G}_{\mathrm{cell}} = \bar{G}_{\mathrm{A(inB)}} - \bar{G}_{\mathrm{A}} \tag{1.2.3}$$

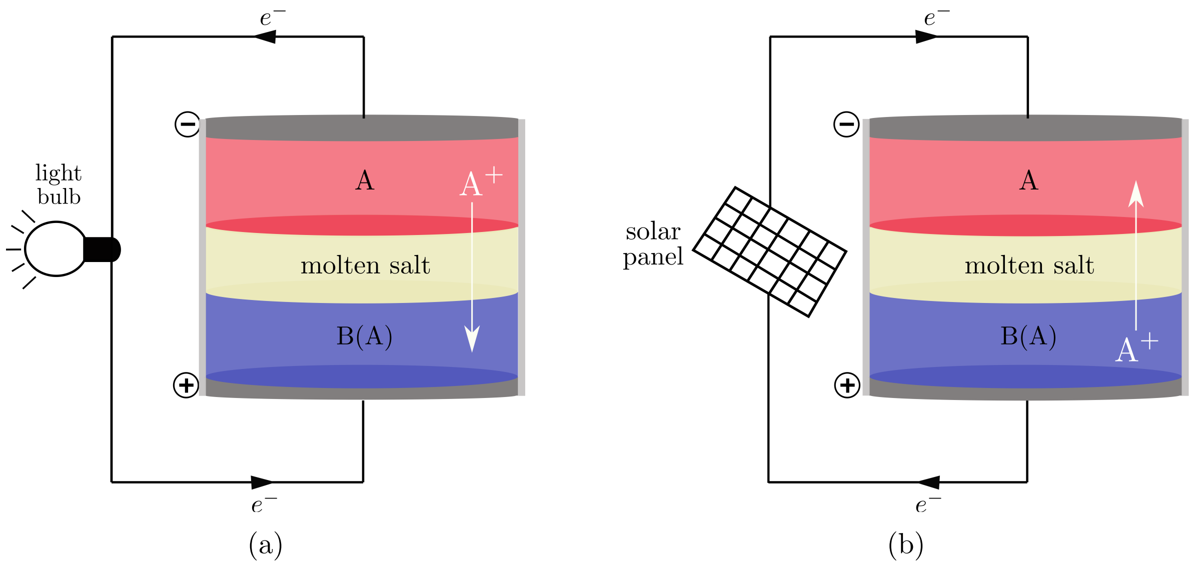

(a) (b)

Figure 1.1 – Scheme of an LMB during (a) discharge (b) charge.

The typical size of current LMBs is $O(10^{-2} - 10^{-1})$ m (Ning et al. (2015); Weber et al. (2020); Zhang et al. (2022)). An example of an experimental setup of a Li||Bi LMB is shown in figure

1.2. The electrical conductivity of the electrolyte is typically $\mathcal{O}(10^2)\,\mathrm{S\,m^{-1}}$ and the electrical conductivity of the liquid metals is $\mathcal{O}(10^5 - 10^6)\,\mathrm{S\,m^{-1}}$. In order to remain liquid, the cell is heated at high temperature. Even though it is possible to use metals which have a quite low melting temperature ($T < 200°$ C), the usual molten salts have a melting temperature above 350° C (Weier et al., 2017). It is however not necessary to provide an external heating, the cell can be self-heated using Joule heating induced by the electrolyte during operation, due to its low conductivity (Spatocco and Sadoway, 2015).

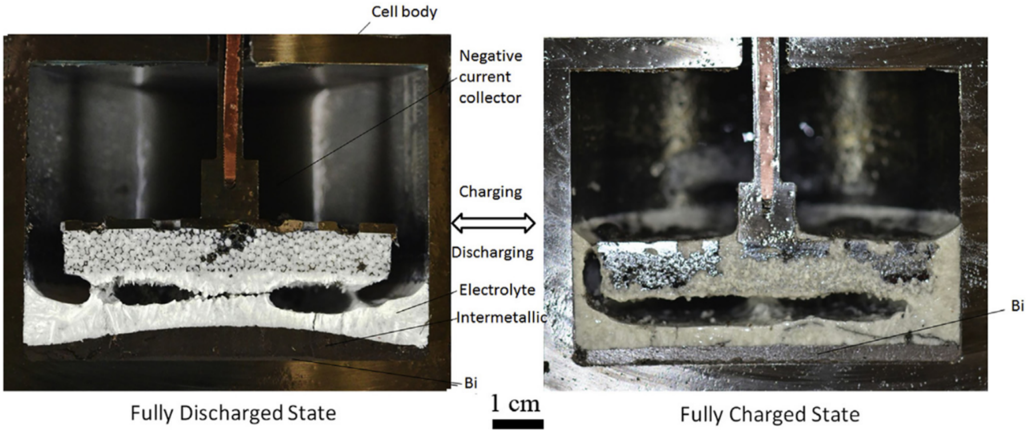

Figure 1.2 – Experimental setup of a Li||Bi LMB in a discharged (left) and charged (right) state. From Kelley and Weier (2018).

1.2.2 Advantages and developments

In the 1960s, the idea of using these stably-stratified three-layer cells has emerged for energy storage (Cairns and Shimotake (1969)), since they offer high current densities. Yet, they were abandoned afterwards, likely because of the need of mobile batteries (Kim et al. (2013a)). Because they are fully liquid, LMBs should not be put into motion: the interfaces could be deformed during motion and this could lead to a short circuit when both the top and the bottom electrodes enter in contact. Around 2011, the group of Donald Sadoway (MIT) has re-initiated research on LMB technology because of their capacity to answer the issue of massive energy storage. They have shown that LMBs could be a cheaper solution.

For stationary energy storage applications, LMBs have many advantages compared to other electrochemical cells. First, they can be significantly cheaper than classical batteries. A Li||Pb-Sb setup from GroupSadoway has a power cost of 283 $\$\mathrm{kW^{-1}}$ and an energy cost of 84 $\$\mathrm{kWh^{-1}}$ (Spatocco and Sadoway, 2015). This answers demands of power and energy costs lower than 1000 $\$\mathrm{kW^{-1}}$ and 100 $\$\mathrm{kWh^{-1}}$, respectively (see section §1.1). In comparison, a Li-ion battery has a minimal power cost of 1800 $\$\mathrm{kW^{-1}}$ and a minimal energy cost of 900 $\$\mathrm{kWh^{-1}}$ (Spatocco and Sadoway, 2015). Furthermore, this setup is not the cheapest that can be used. Indeed, LMBs can be built with earth-abundant materials, i.e. low cost materials (see section §1.2.3 for more details about the materials). The manufacturing is also not expensive because simple: the materials are poured into a vessel which is sealed, and the battery is heated. This is much more straightforward that other technologies which need finer procedures (Spatocco and Sadoway, 2015), such as Li-ion batteries in which the solid electrodes are often thin roles up blades.
In addition, LMBs are liquid cells. Liquid metal electrodes allow high exchange current densities of $\mathcal{O}(10^1)\mathrm{A\,cm^{-2}}$ compared to other types of electrodes (such as oxygen or hydrogen electrodes). Coupled with liquid electrolytes, the liquid-liquid interfaces allow more efficient charge transfer

and then higher current densities than other types of interfaces, usually around 1 $\mathrm{A\,cm^{-2}}$ and up to 13 $\mathrm{A\,cm^{-2}}$ (Cairns and Shimotake (1969)). Solid-liquid and solid-solid interfaces are subjected to degradation after a large amount of charge-discharge cycles, which is detrimental for the battery life-time. Such degradation cannot occur with liquid-liquid interfaces, hence we expect that the life-time is significantly increased and that much more charge-discharge cycles are allowed. For instance, the Li||Pb-Sb setup from GroupSadoway previously cited can support up to 10000 cycles, as compared to Li-ion batteries which can support up to 6000 cycles only (Spatocco and Sadoway, 2015).
Moreover, LMBs are also scalable and modular. Cells can be easily connected to form a platform in order to reach the desired amount of energy stored (https://ambri.com).
Finally, we must stress that LMBs are not only a concept. A calcium-antimony battery platform is already commercialized by Ambri (https://ambri.com). This platform is composed of several cells providing 1 kWh of energy which are connected in parallel. This makes the platform scalable to large-scale needs. It can support multiple charge-discharge cycles and safety is ensured. It is also self-heated. This platform offers a life-time of over 20 years. The materials chosen (calcium is one of the most earth-abundant materials) and the simple manufacturing make this battery much cheaper than Li-ion batteries, non-toxic and easily recyclable.

1.2.3 Materials suitable for LMBs

The metals that can be chosen to build an LMB must verify particular properties. For instance, they must remain liquid during operation. Then, their melting temperature should be quite low so that not too much energy is spent to heat the battery. They have to be good conductors as well (better than the electrolyte). Then, these materials are separated in two categories, the materials appropriate for the negative electrode and the ones for the positive electrode. This separation is realized mainly regarding their electronegativity: a metal with a low electronegativity is a good electron donor, when a metal with a high electronegativity is a good electron acceptor. The higher the electronegativity difference between anode and cathode metals are, the higher the cell voltage. After this selection, several couples of metals are suitable to make LMBs. In figure 1.3, we show in red the metals that can be used for the negative electrode and in blue the ones for the positive electrode. Moreover, metals should also be selected regarding their earth-abundance and their cost (Kim et al. (2013a)). A table of kilowatt hour costs regarding the materials is given in Spatocco and Sadoway (2015). This eliminates a lot of possible couples which would cost more than 300 $\$\mathrm{kWh^{-1}}$ and would then not be competitive. Another condition is the maximum annual energy storage available, which must be high enough to answer production demand. Lithium-based cells provide a too low energy storage (0.0071 TWh), when calcium- and sodium-based cells are able to store a large amount of energy (38.1 TWh and 111.50 TWh, respectively) (Spatocco and Sadoway, 2015). Sodium-based LMBs are the most preferable regarding their operation temperature, compared to calcium-based LMBs.

Several cells using different materials have been developed: Li||Pb (Cairns et al., 1967), Mg||Sb (Bradwell et al., 2012), Ca||Bi (Kim et al., 2013b), Li||Pb-Sb (Wang et al., 2014), Li||Bi (Ning et al., 2015), Na||Zn (Xu et al., 2016), Na||Bi (Weier et al., 2017) or Ca||Sb (Ouchi et al. (2014), https://ambri.com), for example. The last one is commercialized.

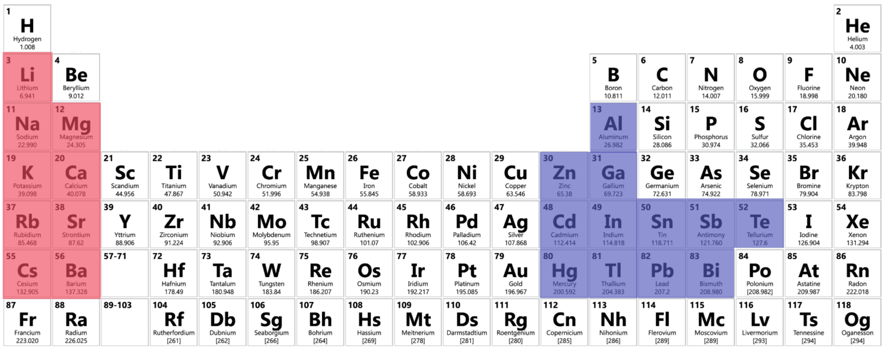

Figure 1.3 – Metals suitable to build the electrodes of an LMB. In red the metals for the negative electrode and in blue the ones for the positive electrode. Inspired by Kim et al. (2013a).

1.2.4 Challenges on liquid metal batteries

LMBs face several challenges. First, the cell design is not straightforward. The first LMBs setups considered were a superposition of three full liquid layers as schematized in figure 1.1. However, the system has to be insulated from its environment. The fluid container must be hermetically sealed. But it must be a good insulator too, so that the metal electrodes are not connected through this container - which would lead to a short circuit. The vessel could be made of ceramics which is an efficient insulator, but it is also really expensive, which does not meet the need for a low-cost system (Spatocco and Sadoway, 2015). Another solution to this issue is to place the upper liquid metal A in a metal retainer, which could be nickel spirals (Personnettaz et al., 2019), wire loops (Weier et al., 2017) or foams (Wang et al., 2014; Weber et al., 2019). Foams are porous solid usually made of steel (figure 1.4). These metal retainers retain the metal A by capillarity. This allows the use of a negative electrode whose radius is lower than the radius of the other layers. Thus, the upper metal is isolated from the vessel. Despite the fact that the capacity of the cell is limited in this setup, this setup is actually more realistic and more often used in experiments. Moreover, the high temperature of the cell makes it more vulnerable to corrosion (Kim et al., 2013a). It is then not easy to find a combination of materials which limits this phenomenon.

Moreover, no matter what the materials are, LMBs have always a low cell voltage, usually under 1 V (Kim et al. (2013a)), and, like any other battery, are subjected to voltage losses. The cell potential E_{cell} can be decomposed like (Vetter, 1967)

$$E_{\text{cell}} = E_{\text{cell,eq}} \pm (\eta_{\Omega} + \eta_{\text{mt}} + \eta_{\text{ct}}) \tag{1.2.4}$$

where $E_{\text{cell,eq}}$ is the equilibrium cell potential, η_{Ω} is the overpotential due to ohmic losses, η_{mt} the overpotential due to mass transfer and η_{ct} the overpotential due to charge transfer (induced by electrochemical reactions). The + sign is used during charge and the − sign during discharge. These overpotentials characterize a decrease in potential due to the different phenomena that affect the battery out of equilibrium, and they should remain as low as possible.

The equilibrium cell potential $E_{\text{cell,eq}}$ is measured with no applied current, when the cell has reached an equilibrium and the alloy is homogeneous. This potential depends on the alloy composition (i.e. on the concentration of A in the alloy). It is actually the maximal potential reachable by the cell.

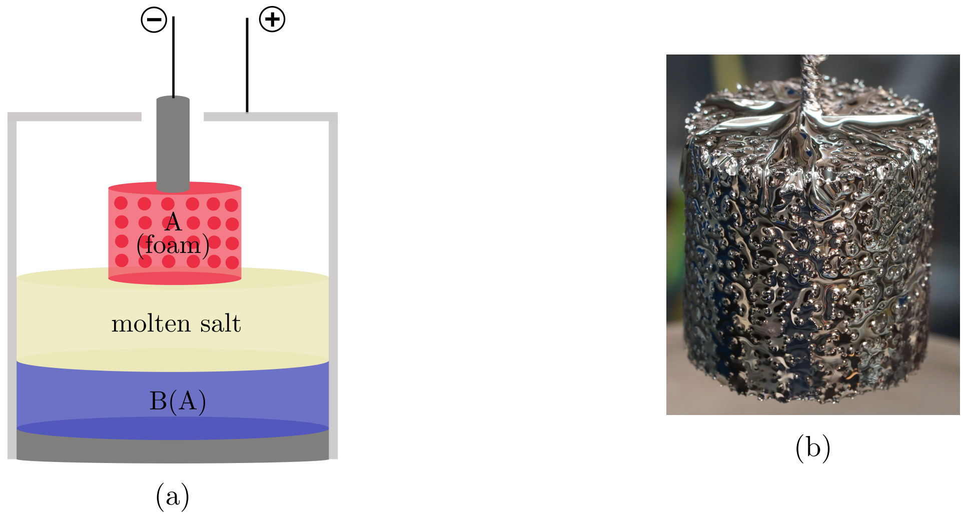

(a)

(b)

Figure 1.4 – (a) Scheme of the foam setup of an LMB: the metal of the negative electrode is contained in a foam. The cell is in a metallic container. (b) A foam used by the LMB team of HZDR.

η_{ct} is due to the activation barrier at the interfaces. Newhouse and Sadoway (2017) have shown that for Li||Bi and Mg||Sb LMBs, the measured exchange current densities are 10 times higher than the operating current density. These high exchange current densities make that η_{ct} is negligible in LMBs (Kim et al., 2013a; Newhouse and Sadoway, 2017).

η_{Ω} is due to ionic and electronic currents. It increases with the current and the thickness of the electrolyte, and decreases with its electrical conductivity. It can be reduced by using thin electrolytes or by modifying the electrolyte composition, and by reducing the applied current. This last modification is less desirable since LMBs are desired to operate with high current densities.

η_{mt} is due to the inhomogeneity of the alloy. The diffusion coefficient of light metal A in the alloy B(A) is typically really low. Hence, during charge and discharge, the diffusion process is slow. Thus, especially at high current densities, i.e. when the discharge/charge process is fast, light metal A accumulates just below the electrolyte-alloy interface (see figure 1.5). This inhomogeneity in the alloy is not desirable. First, η_{mt}, which is directly related to the composition of the surface of the alloy, increases with this inhomogeneity, which directly affects the cell potential. The cell performance is reduced. Second, it can lead to the formation of solid intermetallic phases, when the local concentration of metal A in the alloy is above a critical value. Even though certain types of batteries can operate with these solid phases (Li||Bi LMB, Ning et al. (2015)), they can be harmful for other batteries (Ca||Bi LMB, Kim et al. (2013b)). In order to limit the inhomogeneity in the alloy, ways to homogenize it have to be found. An idea is to produce an intense enough flow in the alloy. According to Weber et al. (2020), this idea has emerged already 60 years ago. However, if this is flow too intense, the interface can deform and the cell can be short-circuited. A compromise has to be realized considering the flow intensity.

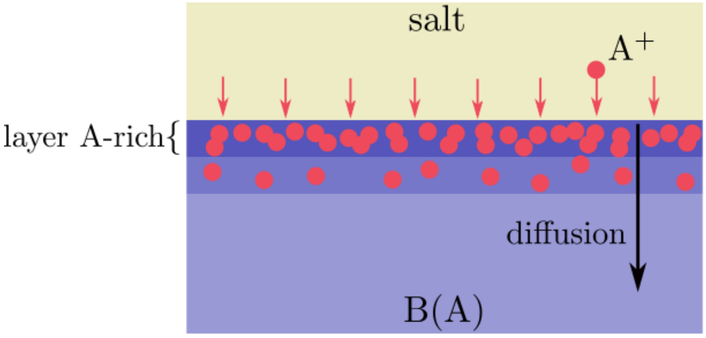

Figure 1.5 – Scheme of the slow diffusion in the alloy and the accumulation of A at the top of the alloy.

1.3 Simulations of liquid metal batteries

Experimental works are needed to study real setups. Post-mortem analysis can be easily performed which gives information about the final state of the cell - if short circuits have occurred, if intermetallic phases have formed... However, these experiments are expensive and, because of the hostile experimental environment (high temperature of the system, electrochemical reactions,...), it is not possible to observe the battery's interior during operation, since the interior must be isolated from the environment. Thus, only few measurable quantities are accessible during experiments. For instance, one can measure the current and the cell potential during operation, but the internal state such as the local alloy composition remains inaccessible. Moreover, flow measurements with the UDV (Ultrasound Doppler Velocimetry) method requires temperature lower than 230 °C (Weier et al., 2017), which is lower than the operating temperature of an LMB, above 350°C (see section §1.2.1). PIV (particle image velocimetry) is not possible because liquid metals are opaque (Ashour et al., 2018). This is why numerical work is essential to understand what is occurring in LMBs' interior. These numerical investigations require accurate models for LMBs, which are not easy to develop.

1.3.1 Difficulties of simulating liquid metal batteries

An LMB is a complex multi-physical system. It is above all an electrochemical cell, in which electrochemical reactions occur. The cell is subjected to mass transport, since the species are migrating during operation. The heating of the cell induces heat transport. Local variations of temperature and concentration can cause phase changes. During operation, charge transfer occurs and the electrical current induces a magnetic field. In large cells, the induced Lorentz force can drive flows and magnetohydrodynamic instabilities. The electrical potential of the cell can vary locally and depends on the alloy composition. In addition, the system is multiphase and the interfaces can deform. All of these phenomena make LMBs non-trivial to model.
Moreover, the material properties are not always available, particularly those of the alloy. There is a lack of experimental data for a lot of couples used in real LMBs.
Furthermore, the numerical implementation of relevant quantities is not straightforward. For instance, as said in section §1.2.4, the cell potential is a sum of the equilibrium cell potential and overpotentials. The way to compute these overpotentials must be well-defined and accurate.

To conclude, accurately modeling an LMB is not straightforward. The models can be sometimes simplified, but should not neglect relevant phenomena. Which models should be used and which simplifications can be done? We present in the next sections the different generations of models that are available in the literature.

1.3.2 Flows and magnetohydrodynamics instabilities

The first studies on LMBs were mainly interested in the flows and magnetohydrodynamics instabilities that can appear during operation. The goal was twofold: determine whether these flows and instabilities can be detrimental to the battery or not by leading to short circuits, and estimate the mixing efficiency of these flows in the alloy phase. The earliest models have supposed fluid layers of constant composition (density, conductivity...) for simplification. Four main flow types have been studied: the Tayler instability, the Metal Pad Roll instability, the thermal convection and the electrovortex flow. These flows are not specific to LMBs, they have been already studied in other types of systems. We summarize in this section the literature on this topic. A schematic representation of some of these flows and instabilities in LMBs is shown in figure 1.6.

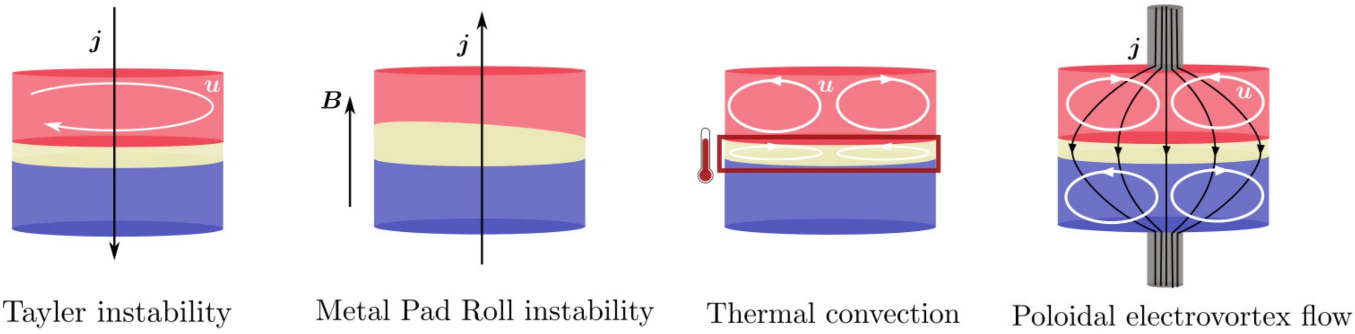

Figure 1.6 – Schematic representation of the flows and instabilities in liquid metal batteries.

Tayler instability

The Tayler instability is a magnetohydrodynamic instability, also present in astrophysics (Tayler, 1973; Vandakurov, 1972). We consider an axial current density distribution J which goes through a liquid conductor. This current induces an azimuthal magnetic field b_θ. The interaction between J and b_θ creates a radial Lorentz force. Usually, this force can be balanced by a magnetic pressure and does not act on the system. However, this system is sensitive to small perturbations and becomes unstable under certain conditions, particularly when the current density is above a critical value, and a flow is driven. The instability threshold can be defined using the Hartmann number

$$Ha = \frac{\mu_0 J R^2}{2}\left(\frac{\sigma}{\rho\nu}\right)^{1/2} \tag{1.3.1}$$

where μ_0 is the magnetic permeability of vacuum, J is the characteristic current density, R is the characteristic length of the system, and σ, ρ, ν are the electrical conductivity, the density and the viscosity of the fluid, respectively. When Ha is above a critical value ($Ha > 20$, Kelley and Weier (2018)), the system can become unstable. In LMBs, this flow appears mainly in the top electrode, which has the highest conductivity and the lowest density.

First, it was thought that the Tayler instability could induce a limitation of the size of the LMBs (Stefani et al., 2011). Several studies have been conducted in order to find means to avoid the appearance of this instability in LMBs (Stefani et al., 2011; Weber et al., 2013, 2014, 2015). For instance, Weber et al. (2014) have studied the suppression of this instability by using axial and transverse magnetic fields. Weber et al. (2015) have shown that using lower conductivities of the current collectors reduce the instability. Moreover, the aspect ratio of the cylinder (the ratio between the height and the radius) impacts significantly the critical current: the lower the aspect ratio, the higher the critical current. Herreman et al. (2015) have shown that Tayler instability can lead to short circuits only in very large cells. For a unitary aspect ratio, the critical radius for the appearance of the instability is 43 cm, and short circuits can appear for radius larger than 3 m. For lower aspect ratio, this critical size is even larger. Because realistic LMBs' sizes, in the order of $O(10^{-2} - 10^{-1})$ m, are much lower than this critical size, the Tayler instability is likely negligible in LMBs.

Metal Pad Roll instability

The Metal Pad Roll (MPR) instability is a classical instability in magnetohydrodynamics. The principle is the following: we consider a system of two superposed layers of liquid metal surrounded by a weak vertical magnetic field $\boldsymbol{B_z}$. A current $\boldsymbol{I}$ is applied and runs vertically through these layers. When the interface is slightly deformed, the current distribution is modified, and a horizontal perturbed current density $\boldsymbol{j}$ appears. This current interacts with $\boldsymbol{B_z}$ and creates a Lorentz force. This force can amplify a rotating wave at the interface. If other forces such as capillarity, viscous or gravity forces cannot balance the Lorentz force, the wave motion amplifies. This so-called metal pad roll instability has been a lot investigated in aluminium reduction cells (Bojarevics and Romerio (1994); Davidson and Lindsay (1998); Gerbeau et al. (2006)), which are two-layer systems used to produce aluminium. A parameter β_s for the appearance of the MPR instability in a two-layer system has been given by Sele (1977):

$$\beta_s = \frac{IB_z}{\Delta\rho g \mathcal{H}_1 \mathcal{H}_2} \tag{1.3.2}$$

where $\mathcal{H}_1$ and $\mathcal{H}_2$ are the heights of the layers, g the gravity coefficient and $\Delta\rho$ the density difference between the layers. The MPR instability appears when β_s is above a critical value. Herreman et al. (2019a) have provided an improved stability theory for such a system. The MPR instability can appear in three-layer systems too, such as LMBs, where waves can appear at both interfaces. This can cause short circuits if the wave motion is too intense.
Several theoretical and numerical studies have been realized on this topic in three-layer domains (Herreman et al. (2019a, 2023); Horstmann et al. (2018); Weber et al. (2017a,b); Weier et al. (2021); Zikanov (2015, 2018)).

The first study on Metal Pad Roll applied to LMBs has been realized by Zikanov (2015). This study suggested that the MPR instability could exist in LMBs and should be further investigated. A numerical work by Weber et al. (2017b) has highlighted that the appearance of the Metal Pad Roll instability depends on several parameters such as the materials, the current density, the size and the shape of the cell. For example, it is particularly detrimental in Mg||Sb liquid metal batteries, in large cells and in cells subjected to high current densities. Short circuits are not expected in small cells with shallow layers. In a three-layer system, both interfaces can be significantly deformed if the density differences at each interface are of the same order of magnitude. We can observe in this case either symmetrically or anti-symmetrically coupled interfacial waves (Horstmann et al., 2018). However, in most LMBs, the density difference between the top-layer and the electrolyte is much smaller that the density difference between the electrolyte and the bottom layer. In this case, only the upper interface moves and the bottom interface remains at rest. The three-layer LMB system mostly behaves as a two-layer system. This has been numerically observed by Herreman et al. (2019a); Weber et al. (2017a,b). Herreman et al. (2023) have extended the stability theory to a three-layer system and have theoretically confirmed this observation.

Thermal convection

Differences of temperature appear in LMBs. During operation, Joule effect is heating up the electrolyte, that has an electrical conductivity much lower than those of the liquid metals ($\mathcal{O}(10^2)$ vs $\mathcal{O}(10^6)\,\mathrm{Sm}^{-1}$). Electrochemical reactions can also locally modify the temperature (Personnettaz et al., 2018). This heating near the interfaces drives convective flows.

The first experiment to study thermal convection in LMBs was done by Kelley and Sadoway (2014). The authors have studied a single liquid metal electrode heated from the bottom, and have shown that a quite intense flow appears in the electrode. This work has been numerically modeled a few years later by Ashour et al. (2018); Beltrán (2017); Weber et al. (2018b). The first numerical study of thermal convection applied to LMBs was realized by Shen and Zikanov (2015). They have shown that the main source of heat in an LMB is the electrolyte, which creates an important Joule effect due to its low conductivity. Thus, in the bottom electrode, the temperature increases with the vertical coordinate z. In the top electrode, it is the contrary: the temperature decreases with z. In the electrolyte, the temperature does not vary monotonously: it increases with z at the bottom of the electrolyte, and decreases with z at the top of the electrolyte. Therefore, since the density decreases with the temperature, thermal convection drives a flow only in the electrolyte and in the top electrode, but not in the bottom electrode which is stably stratified. This result, confirmed by Personnettaz et al. (2022), proves that thermal convection is not able to mix the alloy phase. Personnettaz et al. (2018) have investigated the thermal convection due to electrochemical reactions. This electrochemical heating increases the cell temperature up to 30%, compared to the Joule heating. This could induce a flow in the bottom electrode but the conditions for the appearance of such a flow have not been well investigated. In addition, the flow is dominant in the negative electrode, but it is not intense enough to lead to short circuits. Because the temperature distribution in the electrolyte is more complex than in the electrodes, the appearance of flow in the electrolyte depends on its thickness. Shen and Zikanov (2015), Personnettaz et al. (2022) and Köllner et al. (2017) have shown that thermal convection in the electrolyte appears more easily in thick electrolytes. Using thin enough electrolytes limits heating and hence convective fluid motion.

Electrovortex flow

The electrovortex flow (EVF) has been thoroughly investigated in and outside of the context of LMBs. We consider a thin current collector connected to a larger cylinder containing liquid metal. A current $\boldsymbol{j}$ goes through the cylinder via the current collectors. Because the current collectors are thinner than the cylinder, the current distribution is non-uniform. This current induces a magnetic field $\boldsymbol{b}$ such as $\nabla \times \boldsymbol{b} = \mu_0 \boldsymbol{j}$. Supposing axisymmetry, $b_r = b_z = 0$. The interaction between this current and the induced magnetic field creates a Lorentz force $\boldsymbol{j} \times \boldsymbol{b}$ which contains a radial part which cannot be compensated by the pressure. This radial part of the Lorentz force drives a poloidal flow, which is called electrovortex flow. When an external vertical magnetic field $\boldsymbol{B}_z$ is added to the system, an azimuthal Lorentz force $-j_r B_z \boldsymbol{e}_\theta$ is created. Thus, a toroidal swirl motion is driven as well, the resulting flow is called swirling electrovortex flow. These electrovortex flows always appear in non-uniform current distributions, there is no threshold of appearance. The books of Bojarevics et al. (1989) and Davidson (2001) give an overview of the topic.

EVFs have been studied in several fluid domains: semi-infinite planes, cylinders and hemispheres for example. The work on hemispherical geometries has been motivated by the arc welding process, where a current goes through an electrode in contact with a molten metal.

Fluid motion has been observed in the liquid metal and could affect the welding process.

The earliest studies have been realized by Hunt and Malcolm (1968) and Hunt and Stewartson (1969), who have studied the flow in a horizontally finite domain confined between two planes. Two identical conducting electrodes of a finite diameter are connected to the fluid and a vertical magnetic field is imposed. They have conducted experiments and an asymptotic analysis of the flow. This has motivated many studies.
In a first series of studies, the current comes radially from a point source in a semi-infinite domain (figure 1.7a) (Lundquist (1969); Shercliff (1970)). Analytical solutions have been proposed for inviscid fluids (Shercliff, 1970) and for viscous fluids (Sozou, 1971).
Later, other studies have been conducted in an hemisphere where the current comes from a point source located on the flat side of the hemisphere (figure 1.7b), and provide analytical solutions (Andrews and Craine, 1978; Atthey, 1980; Sozou and Pickering, 1976).
Then studies have been realized in a finite cylinder, connected to an electrode (figure 1.7c). Vlasyuk (1987) has studied the effect of the electrode radius on the flow. Chudnovskii (1989a,b) has proposed a theoretical model of the EVF intensity as a function of different parameters, such as the applied current and the electrode radius. Scaling laws were proposed and verified to describe the non-swirling EVF. A non-dimensionalized number has been introduced to characterize the changes of regimes

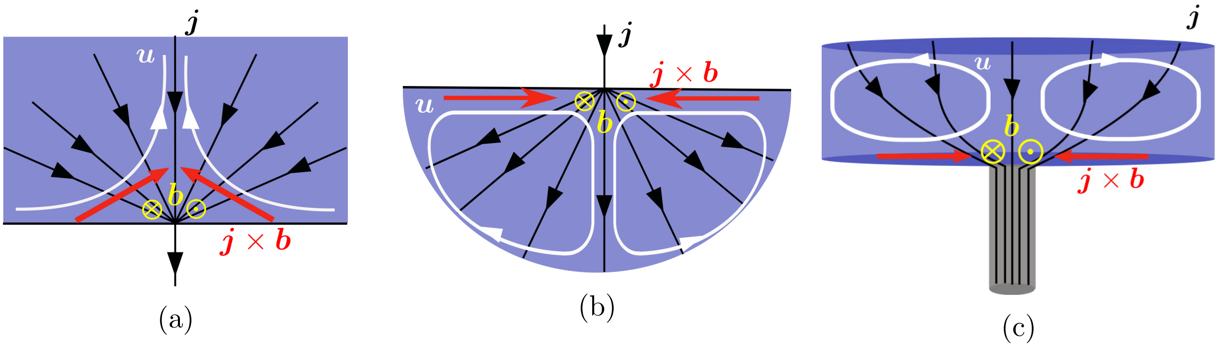

(a) (b) (c)

Figure 1.7 – Different geometries for the study of EVF (a) semi-infinite plane (b) hemisphere (c) cylinder.

$$S = \frac{\mu_0 \pi J^2 R^4}{4\rho\nu^2} \tag{1.3.3}$$

where μ_0 is the magnetic permeability of vacuum, J the imposed current density in the cylinder, R the radius of the cylinder, ρ the mass density and ν the viscosity of the liquid metal. It has been shown that, for low magnetic Prandtl number $P_m = \sigma\mu_O\nu$ - where σ is the electrical conductivity of the fluid - the flow's velocity U varies like S for low S and like $\sqrt{S}$ for large S (Bojarevics et al. (1989); Herreman et al. (2019b)). Bojarevics et al. (1989) have improved these scaling laws by fitting the dependency with the electrode radius R_w:

$$Re = \begin{cases} S(10^{1+5R_w})^{-1/2} & \text{for } S < 10^3 \\ \sqrt{S}(10^{3-5R_w})^{1/3} & \text{for } S > 10^5 \end{cases} \tag{1.3.4}$$

where $Re = UR/\nu$ is the Reynolds number. Nowadays, these non-swirling EVF are still of interest. Kazak (2013); Kazak and Semko (2011, 2012) have conducted numerical studies of EVF in an hemisphere connected to one or two electrodes.

For the swirling EVF, Millere et al. (1980) have conducted the earliest numerical study and have analyzed the flow structure. They have provided boundary conditions for the current density at the electrode-cylinder interface. Bojarevics et al. (1981) have noticed that significant swirl is observed in laboratory models of EVF that do not have externally imposed magnetic fields. They have conducted a numerical study of swirling EVF in a semi-infinite domain, where the current comes from a point source. This work has been extended by Bojarevičs and Shcherbinin (1983) and it was proposed that vorticity stretching was a source of the swirl amplification. Davidson (1992) has extensively analyzed the swirling EVF induced by a rotating magnetic field in different geometries, such as a cylinder or an hemisphere, and has provided theory and scaling laws. The swirl motion has been more precisely explained by Davidson et al. (1999), who has proved that a weak magnetic field is sufficient to generate swirl motion. This mechanism is also named as poloidal suppression, because the swirl motion gradually suppresses the poloidal motion and becomes dominant in the flow. Nowadays, these swirling EVFs are still of interest. Kharicha et al. (2015); Vinogradov et al. (2018) have conducted experimental studies of swirling EVF induced by the Earth's magnetic field in an hemisphere. More recently, Kolesnichenko et al. (2020) studied the swirling EVF in a different experimental setup. In a cylinder, the current is injected through a thin hole at the bottom of the cylinder and is evacuated by the lateral sides. The surface of the metal is free. This experimental and numerical study confirms the mechanism of poloidal flow suppression by weak magnetic fields introduced by Davidson et al. (1999). The suppression mechanism is indeed slow in time.
In chapter 3, we investigate the structure and the flow regimes of the swirling EVF in a symmetrically electrically connected cylinder.

Considering the ingredients which drive EVFs, we can easily imagine them to appear in LMBs. Indeed, the solid current collectors are usually thinner than the container which creates a non-uniform current distribution. The EVF appears then naturally during operation, and seems quite easy to control. It is therefore a good candidate for the mixing of the alloy phase. This is the main motivation of most studies that were conducted on EVFs in LMBs. These studies have been realized both with and without modeling mass transport. The first investigation of the mixing efficiency of the EVF in the alloy phase was experimental, coupling electrovortex flow and thermal convection in an electrode (Kelley and Sadoway, 2014). Weber et al. (2015) have shown that EVF is possible in LMBs, and can prevent the Tayler instability from appearing. Weber et al. (2018a) have numerically studied EVF in the same experimental setup as Zhilin et al. (1986), and have obtained a good agreement between the experimental and numerical results. Ashour et al. (2018) have numerically and experimentally investigated both thermal convection and EVF in the same setup as Kelley and Sadoway (2014). They have concluded that the flow intensity can be high enough to efficiently mix the cell. Weber et al. (2018b) have used the same setup too, to conduct a numerical study of thermal convection and EVF in an electrode. They have compared two types of EVF, an horizontal one and a vertical one - the way they are driven depends of the current supply, when the current leaves the electrode at the bottom of the cell or at the lateral sides. They have moreover examined the impact of the Earth's magnetic field on the flow. They have shown that the vertical EVF is damped by thermal convection, unlike the horizontal EVF which is barely affected. The interaction of the vertical flow with the Earth's magnetic field induces a swirl and a poloidal flow reduction is observed. For the horizontal EVF, the flow structure is modified but no flow is observed. They suggest that, even though the vertical EVF has a lower velocity than the horizontal EVF, it is expected to better enhance mass transfer. Herreman et al. (2019b) have conducted a numerical study of EVF in a single, a two- and a three-layer system. They have shown that the flow can become three-dimensional for high S. For a two- or three-layer system, deformations of the interfaces are observed. Moreover, they have shown that under certain conditions, the EVF can become so intense that it is able to short-circuit the LMB. An estimation of the maximal deformation as a function of the applied current and the radius of the cell is provided. For instance, in a Mg||Sb battery, current above 10 $\mathrm{kA\,m^{-2}}$ leads to short circuit if the cell radius is above 5 cm. Liu et al. (2020) have experimentally and numerically investigated the swirling EVF in a three-layer cylinder. The experimental and numerical results match, and the external magnetic field affects strongly the EVF structure.

1.3.3 Mass transport and enhanced mixing

In section §1.3.2, we have seen that some authors, like Ashour et al. (2018), have concluded that EVF can be intense enough to mix the alloy, and others, like Herreman et al. (2019b), have shown that EVF can be so intense that short circuits appear. Generally, it was shown that thermal convection has no effect on the mixing of the alloy phase, unlike EVF which seems quite efficient to mix the alloy. However, most studies on flows in LMBS have been realized without considering that an LMB is an electrochemical cell, i.e. that species are being transported into or away from the alloy during operation. In reality, the alloy composition and properties - such as density, conductivity, viscosity - are not constant during operation, they are modified at each instant. This mass transport and the way it modifies the material properties has been ignored in a lot of studies, although it can significantly impact the flow.

The first mass transport models for LMBs are very recent. The effect of thermal convection on the concentration in the alloy has been investigated by Barriga (2013), and Ashour et al. (2018) studied the influence of EVF on the concentration. However, these works have both modeled the concentration as a passive scalar, i.e. its potential influence on the velocity or density fields was not taken into account. Kelley and Weier (2018) have suggested that solutal convection, driven by concentration differences in the alloy, could be generated in a charging LMB. The first study modeling an active mass transport was realized by Personnettaz et al. (2019). They study a discharge-charge cycle of a Li||Bi LMB and model the local variations of the alloy composition. These variations create density differences inside the alloy, since the zones of the alloy richer in Li are lighter than the ones containing less Li. This induces solutal buoyancy. During discharge, Li is arriving in the alloy by the top. Then the top of the alloy is enriched with Li and becomes lighter than the bottom. In this case, no flow is driven and a stable stratification appears at the top of the alloy (figure 1.8 left). During charge, Li is removed from the alloy. Therefore the top of the alloy becomes poorer in Li and heavier than the bottom of the alloy. After a certain time, the system is destabilized and plums form close to the alloy-electrolyte interface. A solutal flow is driven, which is intense enough to mix the alloy (figure 1.8 right). This work of Personnettaz et al. (2019) has shown that solutal buoyancy has a major effect in LMBs.

Figure 1.8 – Effect of solutal buoyancy in LMBs: scheme of the concentration distribution of light metal A in the alloy during discharge and charge.

Mass transport can also significantly influence the EVF. The studies detailed in section §1.3.2 have led to the conclusion that non-swirling EVF can be intense enough to mix the alloy.

However, in Herreman et al. (2020), we have conducted a study coupling solutal buoyancy and non-swirling electrovortex flow. This work has shown that during discharge, the EVF cannot pierce through the light stratified layer at the top of the alloy and gradually vanishes. An estimation of the minimal velocity to mix the alloy has shown that EVF would be able to efficiently mix the alloy in a realistic setup with a size in the order of cm, if the current density is larger that 330 $\mathrm{kA\,m^{-2}}$. For more realistic current densities, the radius should be larger than 1.1m. This shows that previous conclusions of section §1.3.2 are drastically changed: non-swirling EVF are not able to mix the alloy in LMBs. During charge, solutal convection dominates the EVF. Further details on this study are given in chapter 2.
A way to counteract the buoyancy effects during discharge is to add an external magnetic field, which drives a swirling EVF. This flow is efficient to mix the alloy. This has been shown in a study by Weber et al. (2020) and confirmed by Herreman et al. (2021). Even low magnetic fields, of the order of few mT, are enough to drive a flow intense enough.
Personnettaz et al. (2020) have studied the effects of different current distributions in the positive electrode of a Li||Bi battery during charge. It was shown that the current distribution has a negligible effect on the solutal convection and on the cell performance. The flow and concentration distributions are modified only at short times. Personnettaz et al. (2022) have compared thermal convection and solutal convection during charge. They have shown that thermal convection appears 10 times later than solutal convection, and that solutal convection has a strong capacity of mixing of the positive electrode, unlike thermal convection which is not able to mix the alloy. Therefore, no external mixing is needed during charge, solutal convection, which appears naturally and rapidly, homogenizes very efficiently the alloy.

1.3.4 Electrical potential distribution

The cell potential is a quantity that is of direct interest to battery manufacturing but its computation is not straightforward. The electrical potential distribution in an LMB is actually quite complex and can display sharp variations. At an interface between two chemical phases which transport free charges, electric charges are created. Thus, electroneutrality, which is respected in the bulk, is not valid anymore close to the interface. The electrical potential φ and the currents vary locally close to this interface, and electrochemical reactions are impacted (Lück and Latz, 2016). In the particular case of electrode-electrolyte interfaces, a structure named electrochemical double layer (EDL) is created when an electronic conductor (here the electrodes) is in contact with a ionic conductor (here the electrolyte). Due to chemical interactions, ions are absorbed at the interface: this is the first layer, called surface charge. Then, ions with an opposite charge are attracted by this first layer by coulombian interactions and create a second layer: the diffusive layer. See figure 1.9a for a scheme of the EDL. This induces a continuous variation of potential at the interface. Lück and Latz (2016) have presented a theoretical model for the electrochemical double layer at an electrolyte-electrode interface. In their model, the EDL is not spatially resolved. The quantities of the EDL are associated to the local corresponding quantities in the bulk, at the interface. This allows them to use a macroscopic approach, where the continuous variation of the electrical potential in the EDL is approximated by a jump in potential. See figure 1.9b for a scheme of the modeled jump in potential at an interface.

LMBs are also subjected to variations of potential at each electrode-electrolyte interface, where EDLs exist. Yet, the electrical potential influences directly the currents. Thus, the current distribution can be modified. Since the flux of metal A into the alloy is directly linked to the current density at the alloy-electrolyte interface, this could significantly impact the concentra-

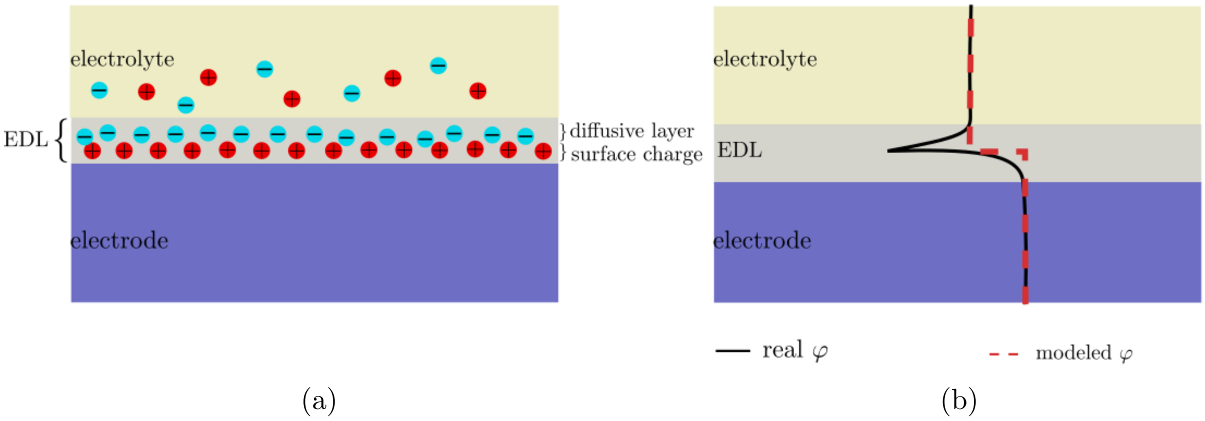

(a) (b)

Figure 1.9 – (a) Scheme of the electrochemical double layer. (b) Simplification of the variation of electrical potential in the electrochemical double layer EDL (black line) by a jump in potential (red dashed line).

tion distribution in the alloy.

In LMBs, local variations of potential due to the EDL appear at each electrode-electrolyte interface. The first study which has considered this phenomenon was realized by Weber et al. (2019). In their model, the EDL is not spatially resolved, like in Lück and Latz (2016), and the variation of potential at the interfaces is approximated by two jumps. Moreover, all phases are considered electrically neutral. The simplified electrical potential distribution in the cell chosen by Weber et al. (2019) shows that, at equilibrium - i.e. when no current is applied -, the only contributions to the cell voltage are these two jumps. This can be easily understood: when the cell is at equilibrium, the overpotentials of equation (1.2.4) are zero. The only source of potential is due to electrochemical mechanisms and to local variations of potential at the interfaces. However, it is not easy to determine the value of each jump separately. They can be theoretically determined by using the Nernst equation (Duczek et al., 2023):

$$\begin{aligned}
\varphi_{\text{jump}}^{\text{n-e}} &= \varphi_0 + \frac{\mathcal{R}T}{n_e F}\ln\frac{a_{\mathrm{A}^{n_e^+}}}{a_{\mathrm{A}}} && \text{at the negative electrode-electrolyte interface} \\
\varphi_{\text{jump}}^{\text{e-p}} &= \varphi_0 + \frac{\mathcal{R}T}{n_e F}\ln\frac{a_{\mathrm{A}^{n_e^+}}}{a_{\mathrm{A(in\,B)}}} && \text{at the positive electrode-electrolyte interface}
\end{aligned}$$

where φ_0 is the standard potential, $\mathcal{R}$ is the universal gas constant, T the temperature, and $a_{\mathrm{A}^{n_e^+}}$, a_{A}, and $a_{\mathrm{A(in\,B)}}$ are the activities of $\mathrm{A}^{n_e^+}$, A and A(in B), respectively. However, this requires to know the activities of the chemical components, which are not always available.

Since the foam composition does not vary during the battery operation, the jump at the negative electrode-electrolyte interface remains constant. Its impact on the current is likely not significant. When this upper jump is neglected, only the jump at the alloy-electrolyte interface is considered in the model. This jump depends on the local molar fraction of A in the alloy $x|_{\text{alloy-electrolyte}}$ at this interface. In this case, the value of the jump can be easily related to the equilibrium potential $E_{\text{cell,eq}}$. We have then:

$$\varphi_{\text{jump}}(x|_{\text{alloy-electrolyte}}) = E_{\text{cell,eq}}(x|_{\text{alloy-electrolyte}}).$$

This equilibrium potential is experimentally known. Weber et al. (2019) have only modeled the jump at the alloy-electrolyte interface. It is an approximation, but in their study, numerical results were in accordance with the experimental results, which validates the relevance of this model.

Only a few studies focused on LMBs and taking into account this jump exist (Duczek et al. (2023); Weber et al. (2019, 2020)). Weber et al. (2019) have implemented the jump in their model and conducted a numerical and experimental study, by ignoring the flow. Simulations and experiments yield similar results. Weber et al. (2020) have added the swirling electrovortex flow in this model and studied its effect. They have concluded, like Herreman et al. (2021), that swirling EVF is efficient to mix the alloy. Duczek et al. (2023) have proposed a 1D electrochemical model where the two jumps are taken into account. A detailed work on electrochemical properties is realized and they model the concentration migration in the electrolyte, without flow.

To summarize, it is necessary to stress that the electrical potential is a local variable which can influence significantly the currents and concentration in the cell in LMBs. The jump in potential induces a new coupling between the electrical problem and the mass transport, which makes them coupled in two ways: the material flux in the alloy is defined by the electrical current at the alloy-electrolyte interface; the electrical potential jumps at this interface, and this jump is directly related to the local concentration. However, in all of the studies previously described in sections §1.3.2 and §1.3.3, the electrical potential of the cell was computed in post-processing from the internal state of the cell. But ignoring this jump in numerical models is not self-consistent, since the electrical distribution is modified, and then the cell potential too. Results and conclusions of the previous studies about enhanced mixing and cell performance could be modified with an improved model. We investigate this topic in chapters 4, 5 and 6.

1.4 Outline of the thesis

This thesis is organized as follows.

In chapter 2, we present two studies that were initiated in internships preceding this PhD. First we present a study about the effect of solutal buoyancy on electrovortex flow in liquid metal batteries. We show that, during discharge and charge, solutal buoyancy dominates the EVF and cannot be neglected in the models, and that the EVF is not able to mix the alloy during discharge. In a second part of the chapter, we focus on another study about droplets detachment in liquid metal batteries. We show, by studying different setups, that, under certain conditions, droplets can form in the negative (top) electrode and detach, until falling into the positive electrode. In certain cases, short circuits are observed.

In chapter 3, we extend the studies of section §1.3.2 and characterize the swirling EVF by conducting a parametric study. We use a symmetrical setup, so that the flow obtained is similar to the von Kármán flow. We analyze the influence of several parameters on the flow structure and intensity, and provide scaling laws for the flow intensity.

In chapter 4, we focus on improving our model for LMBs by adding the jump in potential at the alloy-electrolyte interface. We propose a new magnetic field-based interface condition to model a jump in potential at an interface without the electrical potential variable. In order to validate this condition, we develop two solvers, one based on the electrical potential, using the classical interface condition, and the other based on the magnetic field, using the new interface condition. We validate these solvers and show that they are indeed equivalent.

In chapter 5, we use the magnetic field-based interface condition to improve our model for LMBs by considering the jump at the alloy-electrolyte interface. We examine how much the jump in potential affects the current and the concentration distributions, and how wrong the results of the previous studies - like those described in section §1.3.3 - are. We show that the jump in potential impacts slightly the alloy composition and moderately the ohmic losses.

In chapter 6, we show that the jump in potential can locally modify the surface tension at

the alloy-electrolyte interface, which can drive electrocapillary flows. We investigate how these flows affect the alloy composition, and show that they are significantly affected by the solutal buoyancy.
In chapter 7, we summarize the results and give perspectives for future work.

Chapter 2

Pre-thesis contributions

2.1 Introduction

Before this PhD, I have done two internships on the topic of liquid metal batteries, and this research led to two articles described here. During my M2 internship at LISN between March and July 2019, we studied the effect of solutal buoyancy on electrovortex flows (EVFs) in liquid metal batteries. This study is a basis for part of the work realized during this PhD. In my second internship at HZDR (Helmholtz-Zentrum Dresden-Rossendorf) in Dresden, Germany, between September 2019 and July 2020, we studied the droplets detachment during the operation of an LMB. This work was supervised by Norbert Weber and Tom Weier.

2.2 Solutal buoyancy vs electrovortex flow in liquid metal batteries

2.2.1 Motivation

Mixing the alloy phase can be useful to limit the drop of the cell potential. Electro-vortex flow is a natural candidate to enhance mixing in the alloy. Several studies have concluded that the driven EVF can be quite intense, but not all studies have modeled mass transport, which is really non negligible in LMBs, as solutal buoyancy seems to have a major effect on the alloy composition and on the flow. During discharge, a light stratified layer forms at the top of the alloy. Then, how does solutal buoyancy affect EVF? Is EVF still able to mix efficiently the alloy? What is the minimal flow's intensity for an efficient mixing? During charge, a very efficient mixing occurs by solutal convection in presence of solutal buoyancy. How does this solutal convection interact with EVF?

To answer these questions, we have modeled and performed numerical simulations of EVF in presence of solutal buoyancy effects. The results of this work are gathered in Herreman et al. (2020). We detail the model in section §2.2.2, and the findings in sections §2.2.3 and §2.2.4.

2.2.2 Model and material properties

The material properties of the alloy in LMBs are not always available. This is why we got interested in the Li||Pb cell. This LMB is likely not marketable, because lead is toxic and then not easy to handle. A lithium-based battery also provides a too low annual energy storage. However, this cell is really well adapted to fundamental studies, as we know the electrochemical properties of the Li-Pb alloy, which have been a lot studied for nuclear fusion reactors (De Les Valls et al., 2008; Martelli et al., 2019; Schulz, 1991).

The Li||Pb cell is composed of three liquid layers, schematized in figure 2.1a. The current collectors are here supposed to be wires made of copper whose electrical conductivity is $\sigma_{\mathrm{Cu}} = 5.8 \cdot 10^7\,\mathrm{Sm}^{-1}$. In the simulations, we only solve evolution equations in the alloy layer and the bottom wire. We denote R, $\mathcal{H}$ and R_w the radius of the alloy, the height of the alloy and the radius of the wire, respectively. A scheme of the setup used for the simulations is represented in figure 2.1b.

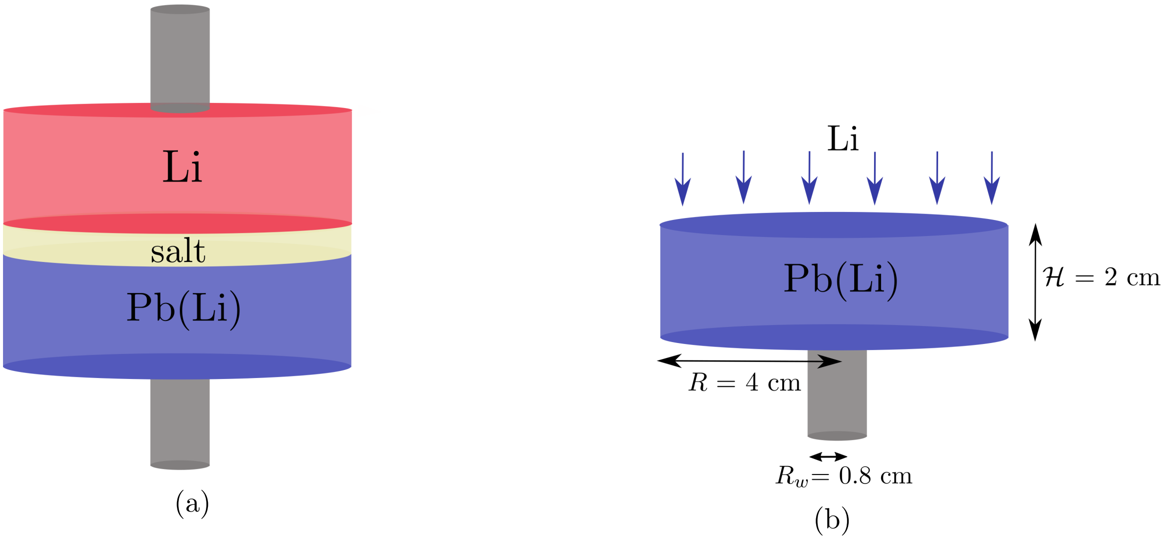

Figure 2.1 – (a) Three liquid layer battery setup. (b) Scheme of the setup used for the simulations. Only the alloy and the bottom wire are modeled.

Material properties of the Li-Pb alloy

We assume that the alloy in the battery evolves around the eutectic mixture, i.e. the composition of the Li-Pb alloy with the lowest melting point. This eutectic mixture has a molar fraction of lithium equal to 0.17. While the battery is charging or discharging, the composition of the alloy varies, and so do the material properties. We do not have information about the dependence of the viscosity ν and the electrical conductivity of the alloy σ, on its composition. From Khairulin et al. (2017b), we get that the variation of the coefficient diffusion D with the concentration of Li in the alloy is actually not significant. In our model, we will consider D, ν and σ equal to those of the eutectic at 500°C (Khairulin et al., 2017b; Martelli et al., 2019):

$$D = 8 \cdot 10^{-9}\,\mathrm{m^2 s^{-1}}, \quad \nu = 1.44 \cdot 10^{-7}\,\mathrm{m^2 s^{-1}}, \quad \sigma = 7.39 \cdot 10^5\,\mathrm{Sm^{-1}}.$$

The mass density of the alloy varies significantly during operation, and cannot be approximated as being constant. The density of the eutectic alloy is $\rho_* = 9543\,\mathrm{kg\,m^{-3}}$. In an experimental study, Khairulin et al. (2017a) measured the variation of the density of Li-Pb alloys. A linear fit on these data-points as a function of the molar concentration of Li, c, yields the following law:

$$\rho(c) = \rho_* - \mathcal{M}_{\mathrm{Li}}\chi(c - c_*), \quad \text{with} \quad \chi = 15.1. \tag{2.2.1}$$

$c_* = 9365\,\mathrm{mol\,m^{-3}}$ is the molar concentration of lithium in the eutectic alloy. This fit was used in Herreman et al. (2020). It can be noticed that the coefficient χ is quite large, and this suggests that density variations can be large.

In most of the previous studies, the field used to track the local composition of the alloy is the molar fraction of Li in the alloy, denoted x in our model. The fields x, c and ρ are connected by the fundamental relation

$$x = \left[1 + \frac{\mathcal{M}_{\mathrm{Li}}}{\mathcal{M}_{\mathrm{Pb}}}\left(\frac{\rho}{c\mathcal{M}_{Li}} - 1\right)\right]^{-1}.$$

where $\mathcal{M}_{\mathrm{Li}} = 6.941 \cdot 10^{-3}\,\mathrm{kg\,mol^{-1}}$ is the molar mass of Li and $\mathcal{M}_{\mathrm{Pb}} = 207.2 \cdot 10^{-3}\,\mathrm{kg\,mol^{-1}}$ is the molar mass of Pb. Injecting the fit (2.2.1) for ρ, this leads to the relation

$$x = \left[1 + \frac{\mathcal{M}_{Li}}{\mathcal{M}_{Pb}}\left(\frac{\rho_0}{c\mathcal{M}_{Li}} - \chi - 1\right)\right]^{-1} \tag{2.2.2}$$

that connects x and c. Here $\rho_0 = 10525\,\mathrm{kg\,m^{-3}}$ is the extrapolated density of pure lead, from the fit (2.2.1). This value is quite close to the real density of pure lead, equal to $10433\,\mathrm{kg\,m^{-3}}$.

Equations

The molar concentration field in the alloy satisfies an advection-diffusion equation

$$\partial_t c + \boldsymbol{u} \cdot \boldsymbol{\nabla} c = D \nabla^2 c. \tag{2.2.3}$$

Here $\boldsymbol{u}$ is the velocity of the mixture, and we assume D to be constant.
The governing field equations for the velocity derive from a Boussinesq model. The magnetic field is solution of the induction equation. Hence, we also solve in the alloy

$$\begin{aligned}
\rho_*(\partial_t \boldsymbol{u} + (\boldsymbol{u}\cdot\boldsymbol{\nabla})\boldsymbol{u}) &= -\boldsymbol{\nabla} p - \rho(c) g \boldsymbol{e}_z + \boldsymbol{\nabla}\cdot(\rho_* \nu (\boldsymbol{\nabla} u + (\boldsymbol{\nabla} u)^T) + \boldsymbol{j} \times \boldsymbol{b} && \text{(2.2.4a)}\\
\partial_t \boldsymbol{b} &= \boldsymbol{\nabla} \times (\boldsymbol{u} \times \boldsymbol{b}) + (\mu_0 \sigma)^{-1} \nabla^2 \boldsymbol{b}, && \text{(2.2.4b)}\\
\boldsymbol{\nabla}\cdot\boldsymbol{u} = 0, \qquad & \boldsymbol{\nabla}\cdot\boldsymbol{b} = 0. && \text{(2.2.4c)}
\end{aligned}$$

We denote μ_0 the magnetic permeability of vacuum, p the pressure field, g the gravity, $\boldsymbol{j}$ the current density and $\boldsymbol{b}$ the magnetic field.
In the wire, there is no flow and only the magnetic field is to be solved

$$\partial_t \boldsymbol{b} = (\mu_0 \sigma_{\mathrm{Cu}})^{-1} \boldsymbol{b}, \quad \boldsymbol{\nabla}\cdot\boldsymbol{b} = 0. \tag{2.2.5}$$

In the model, we fix the total electrical current I that is running through the cell. This electrical current also defines the material flux of lithium that enters the alloy at its top:

$$D \partial_z c|_\Sigma = \frac{J}{n_e F}. \tag{2.2.6}$$

J is the current density related to I in our model such as $J = I/(\pi R^2)$. We suppose a homogeneous current density at the top surface of the alloy. This condition is not fully realistic and is modified in chapters 4, 5 and 6. $F = 96485\,\mathrm{sA\,mol^{-1}}$ is the Faraday constant, $n_e = 1$ the number of charges carried by lithium ions and the index Σ corresponds to the localization of the alloy-electrolyte interface. No-slip boundary conditions are applied for the velocity.
The simulations start with the eutectic alloy, $c = c_*$ everywhere and $\boldsymbol{u} = \boldsymbol{0}$.
The problem is numerically solved using the code SFEMaNS. Details about this code are given in chapters 3, 4 and 5.
One can remark that we solve the full MHD problem in this case, which is not necessary regarding the low values of the magnetic Reynolds number. However, these equations were already implemented in SFEMaNS, and the simulations that we show below only take a few hours. We have thus chosen to not modify the equations.

Ideal and worst scenarios

Our goal is to examine how much the EVF can mix the alloy. In order to measure the effect of EVF on the alloy composition, we compare our numerical results with two scenarios, that we name the ideal scenario and the worst scenario.
The ideal scenario for the battery corresponds to the case of a perfectly mixed alloy. In this case, the concentration is homogeneous and only time-dependent. We suppose that the mixing is instantaneous and ignore how this is done. The evolution equation is then

$$\partial_t c = \nabla \cdot (D \nabla c). \tag{2.2.7}$$

After having integrated this equation on the volume and used the Green-Ostrogradski formula, we can find the following analytical solution for the concentration

$$c^{\text{ideal}}(t) = c_* + \frac{J}{n_e F \mathcal{H}} t. \tag{2.2.8}$$

In the worst scenario, there is no flow and diffusion is the only transfer mechanism. Since diffusion is really weak, this process is inefficient and the inhomogeneity close to the alloy-electrolyte interface is very large. In this case, the concentration depends only on z and t and is solution of (2.2.3) with $\boldsymbol{u} = \boldsymbol{0}$. The expression

$$c^{\text{diff}}(z,t) = c_* + 2\frac{J}{n_e F}\sqrt{\frac{t}{D}}\,\text{ierfc}\left(\frac{\mathcal{H} - z}{2\sqrt{Dt}}\right) \tag{2.2.9}$$

is an approximated analytical solution of this diffusion problem for short times ($t \ll \mathcal{H}^2/D$). The goal of the mixing is to be as close as possible to the ideal scenario.

Computing the potential of the cell

In this study, the potential of the cell E_{cell} is computed by post-processing using the equilibrium potential function $\Phi(x)$, corrected by ohmic losses. In the alloy, the main contribution for the potential is due to the surface where the molar fraction x is locally higher than in the bulk. We use the following formula to compute the cell potential:

$$E_{\text{cell}} = \Phi(\langle x \rangle_\Sigma) + \eta_\Omega \tag{2.2.10}$$

where $\langle x \rangle_\Sigma$ is the averaged molar fraction at the alloy-electrolyte interface. This average is an approximation, and we will see later in chapter 5 that this approximation is not consistent.
The ohmic losses η_Ω occur mainly in the electrolyte that we do not solve. We estimate that

$$\eta_\Omega = \frac{J \mathcal{H}_e}{\sigma_{\text{e}}}. \tag{2.2.11}$$

We fix, somehow arbitrarily, the height of the electrolyte $\mathcal{H}_e = 1$ cm and $\sigma_{\text{e}} = 187\,\text{S}\text{m}^{-1}$ is a realistic electrical conductivity for the electrolyte.
The equilibrium potential depends on the molar fraction of lithium in the alloy x. From the experimental study of Gasior and Moser (2001), we can deduce that a linear fit is applicable in the range $x \in [0.17, 0.60]$:

$$\Phi(x) = \alpha - \beta(x - x_*), \qquad \text{with } \alpha = 0.614\,\text{V}, \quad \beta = 0.598\,\text{V}. \tag{2.2.12}$$

Here $x_* = 0.17$ is the molar fraction of lithium at the eutectic mixture (see Herreman et al. (2020) for more details).

We aim to assess how mixing improves the cell potential with respect to the diffusive case and how close we can get to the ideal scenario. For this purpose, we define the ideal potential $E_{\text{cell}}^{\text{ideal}}$, when the alloy is homogeneous, such as

$$E_{\text{cell}}^{\text{ideal}} = \Phi(x^{\text{ideal}}) + \eta_{\Omega} \tag{2.2.13}$$

where x^{ideal} is the molar fraction in an homogeneous alloy. This formula can be analytically computed by using equations (2.2.8) and (2.2.2) to compute x^{ideal}.

Another potential that can be considered is the one of the worst scenario, when the flow is absent and only diffusion acts. It can be computed such as

$$E_{\text{cell}}^{\text{diff}} = \Phi(x^{\text{diff}}) + \eta_{\Omega} \tag{2.2.14}$$

where x^{diff} is the molar fraction at the alloy-electrolyte interface in the pure diffusion case, which is constant at the surface. x^{diff} is determined by using equations (2.2.9) and (2.2.2).

The mass transfer overpotential η_{mt}, defined in equation (1.2.4) of chapter 1, measures the variation of the cell potential due to local inhomogeneity in the alloy. In this study, it corresponds to the difference between the observed cell potential and the ideal potential

$$\eta_{\text{mt}} = |E_{\text{cell}} - E_{\text{cell}}^{\text{ideal}}| = |\Phi(\langle x \rangle_{\Sigma}) - \Phi(x^{\text{ideal}})| \tag{2.2.15}$$

In the pure diffusion scenario, η_{mt} is the difference between $E_{\text{cell}}^{\text{diff}}$ and $E_{\text{cell}}^{\text{ideal}}$. In the ideal scenario, η_{mt} is zero.

2.2.3 Discharge

In this section, we focus on discharging cells. We first conduct a study without considering buoyancy and compare these results to a configuration with solutal buoyancy present. In all simulations, we have a non-swirling EVF that is stirring the alloy.

Electrovortex flow without buoyancy

We run three simulations with three currents, $I = 0.25, 2.5, 25\,\text{A}$ and no solutal buoyancy. We show in figure 2.2 the velocity field and the molar fraction field at a fixed instant for each current. We notice that for low currents, the flow cannot mix the alloy: the concentration profile is close to the diffusive solution. In contrast, for high currents, the flow is intense enough to mix the alloy. In figure 2.3, we plot the surface averaged molar fraction $\langle x \rangle_{\Sigma}$, the potential E_{cell} and the overpotential η_{mt} as a function of time for the three currents (solid lines). We compare these profiles with the worst scenario, i.e. the pure diffusive case (dashed lines). This allows us to measure how mixing is impacting the battery. For low currents, the EVF does not bring real improvements of these quantities compared to the pure diffusive case, the dashed and solid lines are almost superposed. For high currents, the surface averaged molar fraction is significantly reduced and this also keeps E_{cell} higher. Overall, the mass transfer overpotential remains quite low with respect to the dominant ohmic losses.

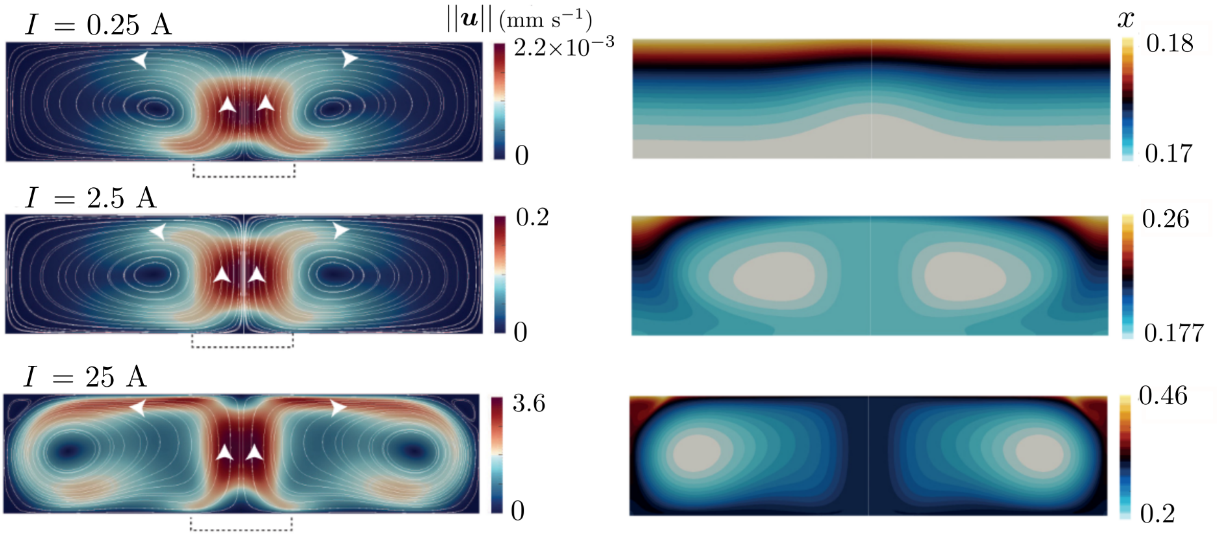

Figure 2.2 – Snapshots of the magnitude of the velocity (left) and the molar fraction distribution (right) for three currents: (top) $I = 0.25$ A, t = 5556 s, (middle) $I = 2.5$ A, t = 6111 s, (bottom) $I = 25$ A, t = 2889 s.

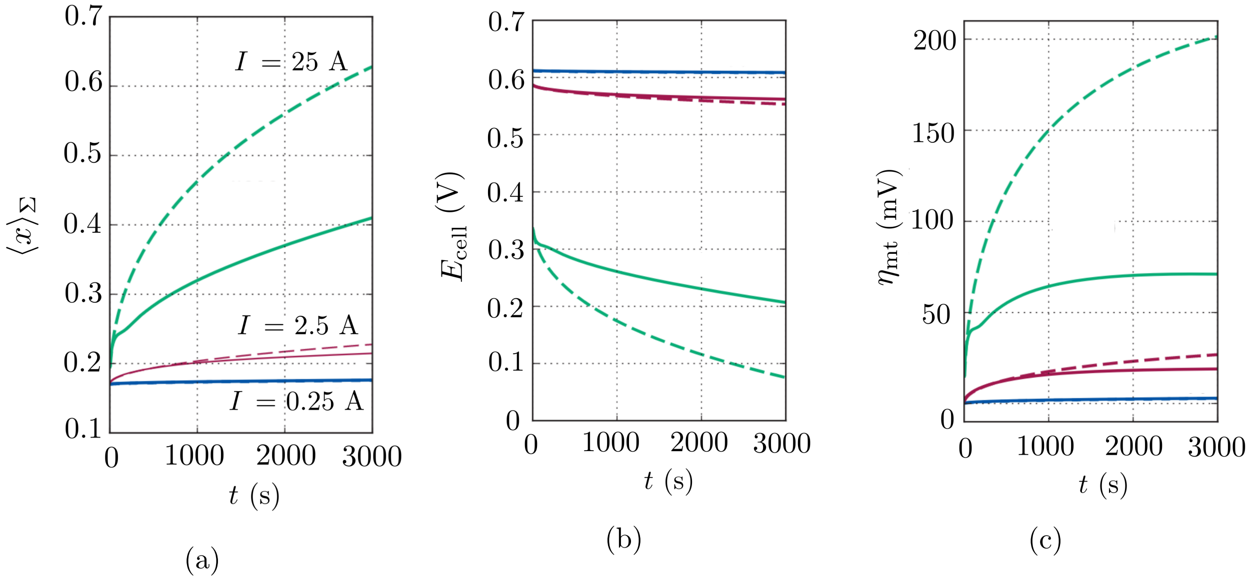

Figure 2.3 – Comparison of the pure diffusion case and the numerical results with EVF for three currents, $I = 0.25$ A (blue), $I = 2.5$ A (red), $I = 25$ A (green) as a function of time. (a) Averaged molar fraction at the alloy-electrolyte interface. (b) Potential of the cell. (c) Mass transfer overpotential.

Effect of solutal buoyancy on Electrovortex flow

When the buoyancy term is active in the equations, the flow is drastically modified. Even with the highest current $I = 25$ A, the EVF is not intense enough to counteract buoyancy. An EVF is certainly present in the bulk, but it never pierces through a stagnant buoyant layer, forming at the top of the alloy. As time evolves, the flow is progressively crushed by the thickening stagnant layer. This can be seen in figure 2.4, where we represent the molar fraction in the alloy and streamlines of the flow at different times for $I = 25$ A. In the stagnant layer, there is almost no flow, so diffusion dominates the mass transport. Hence we retrieve the same alloy composition as in the pure diffusion case in the presence of solutal buoyancy. Consequently, the solutal buoyancy has a major impact on the flow and on the battery: the flow cannot longer mix the alloy.

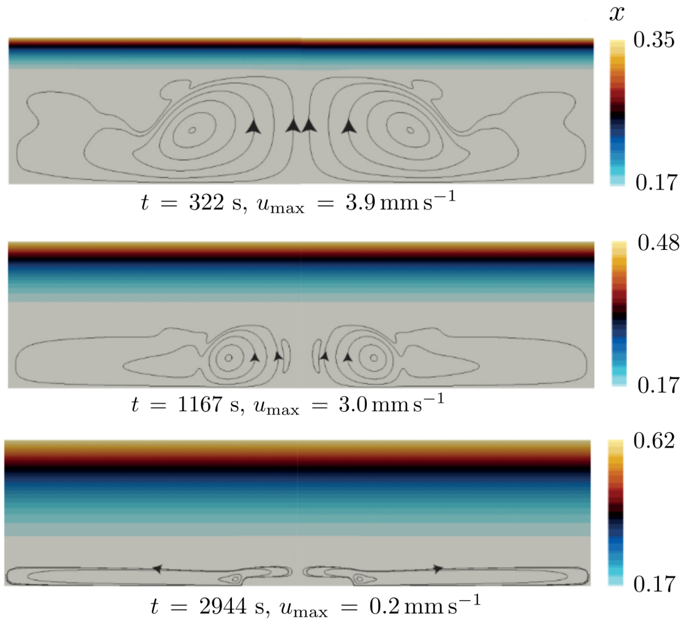

$t = 322$ s, $u_{\max} = 3.9\,\mathrm{mm\,s^{-1}}$

$t = 1167$ s, $u_{\max} = 3.0\,\mathrm{mm\,s^{-1}}$

$t = 2944$ s, $u_{\max} = 0.2\,\mathrm{mm\,s^{-1}}$

Figure 2.4 – Snapshots of the molar fraction field and streamlines of the velocity (black lines) for $I = 25$ A, at different times.

Criteria for an efficient mixing

Our simulations have shown that, for the currents studied, the EVF is not able to mix the alloy of an LMB. We aim to theoretically estimate the minimal flow intensity required to blend efficiently the alloy.

We introduce two reference velocities: U_p, the minimal flow intensity necessary to pierce the buoyant layer, and U_m, the minimal flow intensity needed to mix the alloy. We can distinguish three flow regimes:

- $U \ll U_p$: this means that the flow cannot pierce the buoyant layer and has no impact at all on the mixing.
- $U_p \ll U \ll U_m$: the flow is able to pierce the buoyant layer and impacts the molar fraction distribution in the alloy, but its influence is moderate and finite in time.
- $U_m \ll U$: the mixing is efficient at all times.

Thus, the EVF mixes efficiently the alloy if $U_m \ll U$.

It is possible to estimate the dependency of U_p and U_m as a function of control parameters, which is done in details in Herreman et al. (2020). To pierce the buoyant layer, the flow, which develops during an advection time, has to be intense enough to bring parcels of heavier fluid in the bulk through the buoyant layer and up to the top of the alloy. Using the diffusive solution and a balance between the kinetic energy of the flow and the work required to bring heavier parcels of fluid to the top of the alloy, this yields

$$U_p = \left(\frac{2J\mathcal{M}_{\mathrm{Li}}\chi g\mathcal{H}}{\rho_* F}\right)^{1/3}.$$

The flow can mix efficiently the alloy if its intensity is high enough to bring lighter parcels of fluid from the top of the alloy into the bulk. Using the maximal density difference between the bulk and the top of the alloy, and a balance between the kinetic energy of the flow and the work required to bring lighter parcels of fluid from the top of the alloy into the bulk, this yields

$$U_m = \left(\frac{4J\mathcal{M}_{\mathrm{Li}}\chi g}{F\rho_*}\right)^{2/5}\frac{\mathcal{H}^{3/5}}{(\pi D)^{1/5}}.$$

If we apply the formula for U_m to our model, really high currents are required to develop intense enough EVF for mixing efficiently the alloy ($J > 330\,\mathrm{kA\,m^{-2}}$ i.e. $I > 1650$ A). These currents are not realistic. Using a realistic current density for LMBs ($J = 10\,\mathrm{kA\,m^{-2}}$), we estimate that the radius of the setup should be greater than 1.1 m to reach this U_m scale, this is far from the actual setups. We conclude from this study that non-swirling EVFs are likely not able to mix efficiently the alloy in LMBs.

In these estimations, we did not consider the dependency on the wire radius R_w, whose value impacts the intensity of the EVF. Moreover, swirling EVF, driven when an external magnetic field is applied, creates more intense flows and could modify these conclusions.

2.2.4 Charge

In this study, we have also investigated charging cells. In simulations, this corresponds to a negative current density. We expect the development of solutal convection due to solutal buoyancy. We show in figure 2.5a the velocity field and the molar fraction field at three times with $I = 0.22\,\mathrm{A}$. At the beginning, the EVF appears progressively in the bulk. After a critical time, we retrieve the same observations as Personnettaz et al. (2019). Heavier plums form at the top of the alloy and drop down. This solutal convection flow mixes very efficiently the alloy. Notice also how this convective flow dominates the EVF that is not visible anymore. Figure 2.5b shows that the resulting molar fraction field obtained is clearly three-dimensional after a certain time.

The efficiency of mixing by solutal convection can be seen in figure 2.6, where the evolution of $\langle x\rangle_\Sigma$, E_{cell} and η_{mt} with time is plotted, and compared to the ideal scenario (homogeneous alloy, dot-dashed lines) and to the worst scenario (pure diffusion, dashed lines). Here, $I = 22\,\mathrm{A}$. We find that $\langle x\rangle_\Sigma$, E_{cell} and η_{mt} remain close to the values of the ideal scenario, confirming the very intense mixing.

In the article, we obtain a theoretical estimation of the intensity of the driven flow, using a balance between the kinetic energy of the flow and the gravitational potential energy:

$$U \sim \left(\frac{\chi J\mathcal{M}_{\mathrm{Li}} g}{F\rho_*}\right)^{1/5}\frac{\mathcal{H}^{3/5}}{D^{1/5}}. \tag{2.2.16}$$

The PhD thesis of Personnettaz (2022) investigates further the solutal convection in LMBs.

In summary, during charge, solutal buoyancy has a major influence on the flow. Even for low charging currents, an intense solutal convection flow develops and dominates the EVF.

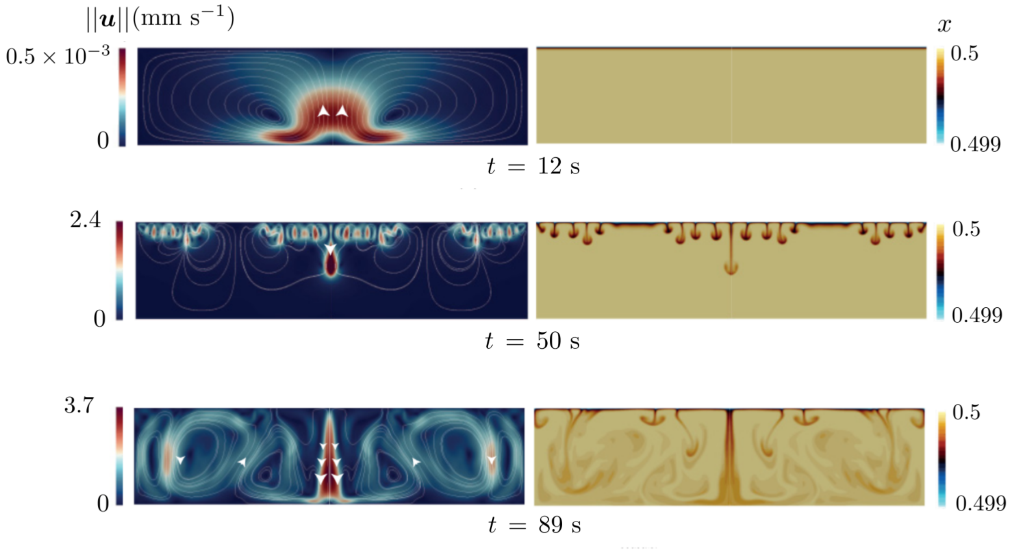

(a)

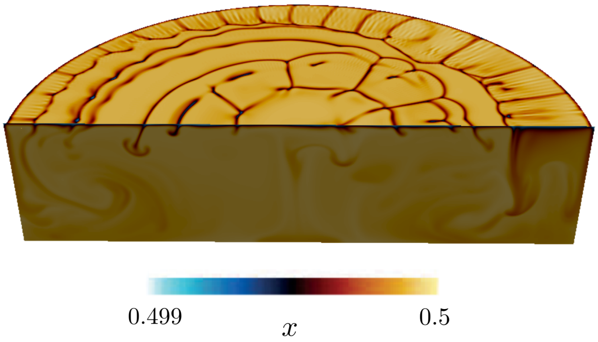

(b)

Figure 2.5 – (a) Snapshots of the velocity (left) and molar fraction (right) fields for I = 0.22 A, at different times. (b) Snapshot of the three-dimensional molar fraction for I = 0.22 A and t = 300 s.

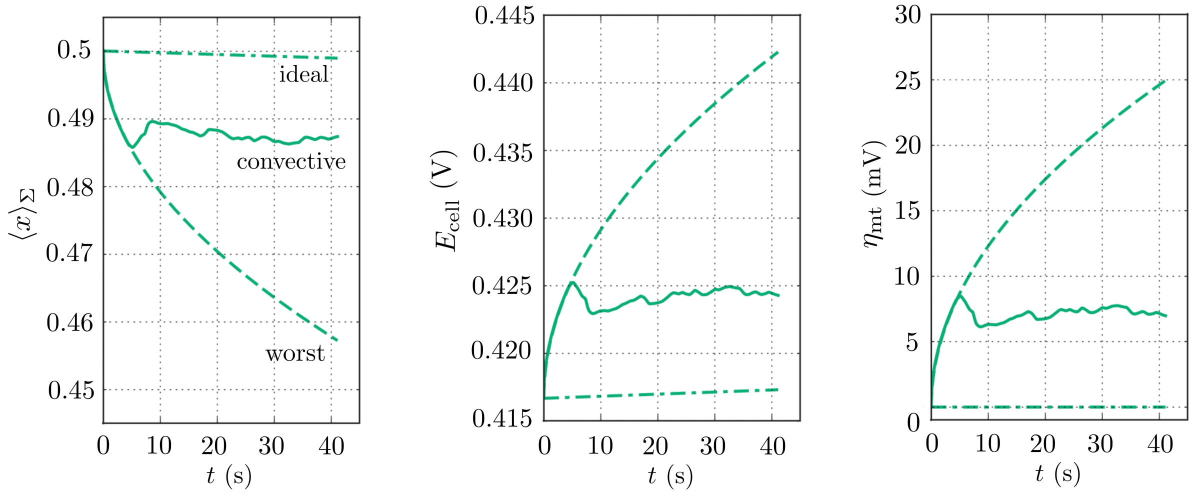

(a)

(b)

(c)

Figure 2.6 – Comparison of the worst scenario i.e. pure diffusion (dashed lines), the numerical results with the convective flow (solid lines), and the ideal scenario i.e. homogeneous alloy (dot-dashed lines) for $I = 22$ A as a function of time. (a) Averaged molar fraction at the alloy-electrolyte interface. (b) Potential of the cell. (c) Mass transfer overpotential.

2.2.5 Conclusion and perspectives

In this section, we have studied the effect of solutal buoyancy on EVF and on the alloy composition, during discharge and charge.

During discharge, we have shown that the EVF is not intense enough to pierce the light stratified layer at the top of the alloy, and has no effect on the mixing. The diffusion process dominates the EVF due to the solutal buoyancy. We have found three regimes of flows, and estimated the minimal flow required to efficiently mix the alloy. This has shown that EVF can efficiently mix the alloy in a small cell for non-realistic current densities. For realistic current densities, the EVF can mix only in very large cells. We deduce then that the EVF cannot be used for the mixing process in realistic LMBs, which are quite small.

During charge, solutal convection appears and mixes efficiently the alloy. This phenomenon dominates the EVF which is not visible after a short time, and is clearly three-dimensional. We have been able to theoretically estimate a scaling law for the flow intensity, which is consistent with the numerical simulations.

Therefore, this study has shown that non-swirling EVF is dominated by solutal buoyancy during both charge and discharge.

We have concluded from this internship that non-swirling EVFs cannot mix the alloy. But what happens when we consider swirling EVFs in discharge instead? Herreman et al. (2021) have studied the effect of swirling EVF on the mixing of the alloy in discharging cells. We recall that the swirling EVF is driven by an external vertical magnetic field. In practice, this magnetic field of magnitude B can be for instance induced by a solenoid placed around the LMB. This magnetic field adds an azimuthal component to the flow. The swirling EVF is actually very efficient for the mixing, even with low magnetic field. Figures 2.7a and 2.7b show the averaged molar fraction at the surface of the alloy and the molar fraction distribution in the alloy for different magnetic fields. We remark that even a weak magnetic field influences the flow. For higher magnetic fields, the mixing is really efficient since $\langle x \rangle_\Sigma$ becomes almost constant with time. Hence, these results are promising findings to answer the issue of mixing of the alloy. In this study, it is interesting to notice that the flow velocity varies like

$$U \sim \left(\frac{JB}{\rho_*}\right)^{2/3} \frac{R}{\nu^{1/3}}. \tag{2.2.17}$$

We try to understand the origin of this scaling law in chapter 3.

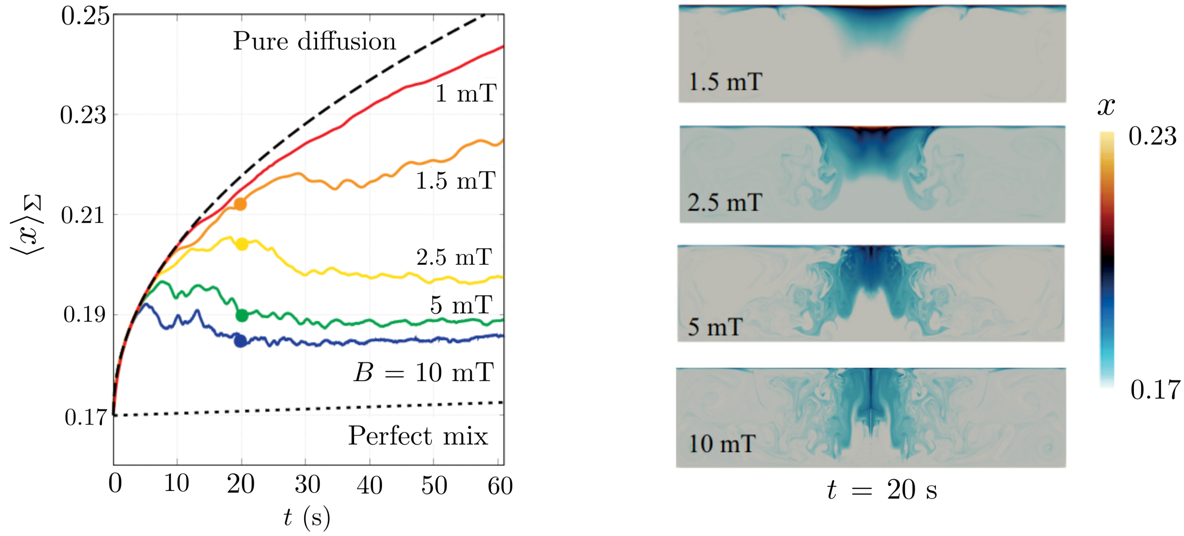

(a)

(b)

Figure 2.7 – I = 25 A. (a) Surface averaged molar fraction as a function of time for different magnetic fields. (b) Snapshots of the molar fraction distribution for different magnetic fields at t=20 s. Adapted from Herreman et al. (2021).

Furthermore, in this study, we have computed the cell potential in post-processing using approximations. This computation does not consider the complex electrical potential distribution in LMBs, like the jump in potential at the alloy-electrolyte interface. In chapters 4 and 5, we provide a better model for E_{cell}, taking into account this jump.

2.3 Droplets detachment in liquid metal batteries

2.3.1 Motivation

In HZDR (Helmholtz-Zentrum Dresden-Rossendorf), experiments are conducted on liquid metal batteries. During experimental studies, issues arise that are not encountered in numerical simulations. For instance, droplets and localized short circuits have been observed. In setups where the negative electrode is not fully liquid and is a metal retainer, the liquid metal of the negative electrode is maintained by capillarity in this retainer. However, Walsh et al. (1971) have reported that a low wettability of the metal retainer could lead to droplet formation.

In a setup where the metal retainer is a wire loop (figure 2.8a), droplets can been seen at the bottom of the loop, maybe because of a low wettability. In figure 2.8b, the negative collector in a solid foam. We can notice that intermetallic solid phases have formed on this foam. These intermetallic phases appear when the concentration of Li in the alloy exceeds a certain value, they do not form in pure lithium. Then, they could not have formed at the bottom of the foam. A possible explanation could be that due to a low wetting, a droplet has formed at the bottom of the foam and is entered in contact with the alloy, leading to a short circuit. This metal bridge between the two metallic phases might lead to the formation of intermetallic phases which attach to the foam. Figure 2.8c shows the experimentally measured cell potential $\boldsymbol{E}_{\text{cell}}$ as a function of time during three charge-discharge cycles (the first, the 20th and the 25th cycle), measured in a Li||Bi LMB. A typical charge-discharge cycle for an LMB consists of a first rest phase where no current is applied ($\boldsymbol{I} = 0$). Then, a positive current is applied during the charge phase. Later, the current is turned off during another rest phase, and a negative current is applied for the discharge phase. Finally, the current is once more turned off. On this graph, we can observe a sudden short drop of the cell potential after several cycles, during discharge. This could be explained by non-faraidic transfer of lithium from the negative (top) electrode into the positive (bottom) electrode, i.e. a droplet transfer. If such a transfer occurs, the concentration of lithium in the alloy locally increases close to the alloy-electrolyte interface, which decreases locally the potential. Since the total cell potential is directly linked to the potential at the surface of the alloy, the cell potential is reduced too.

In LMBs where the three layers are fully liquid, short circuits can be due to short-wave instabilities which deform the interfaces. These deformations might be amplified by the Lorentz force, until a short circuit occurs.

We are interested in understanding the amplification of the deformations in a fully liquid LMB, and the detachment of droplets in LMBs made with a metal retainer. These phenomena could lead to short circuits, which can be detrimental to LMBs. The results and details of this investigation can be found in Bénard et al. (2021). We summarize the study in the next paragraphs.

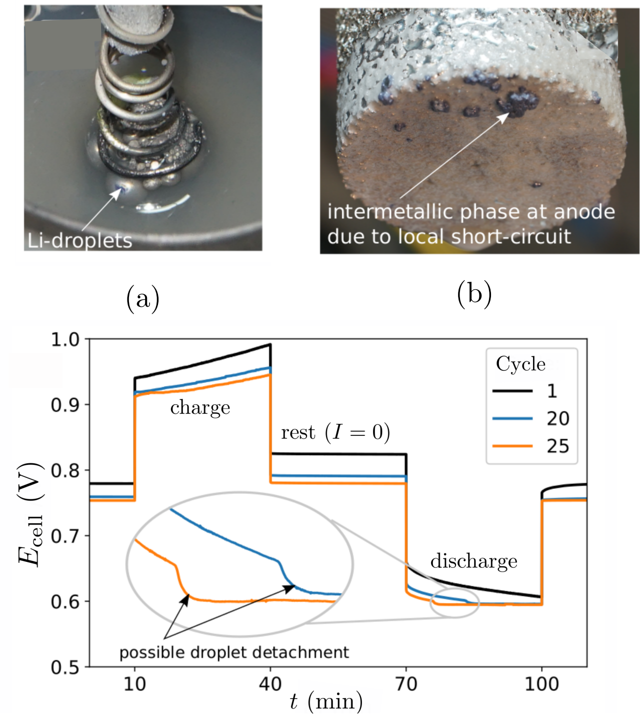

(a) (b)

(c)

Figure 2.8 – (a) Droplets in a spiral setup of an LMB. (b) Intermetallic phases observed on a foam. (c) Charge-discharge cycle of the cell potential vs time for different cycles.

2.3.2 Cases investigated

We study two types of LMB setups: a setup where the three phases are liquid (like in figure 1.1a), which will be called the three-layer setup, and a setup where the lithium of the negative electrode is contained in a foam, which will be called the foam setup.
In the three-layer setup, short-wave instabilities can deform the interfaces. These local deformations could be amplified if the current is high enough, until a possible short circuit occurs.
In the foam setup, an insufficient wetting could lead to the formation of droplets at the bottom of the foam in the electrolyte. These droplets could deform due to local forces, until a detachment and a local short circuit occur.

In order to analyze both situations, we conduct numerical studies in a Li||Bi LMB. The radius of the cell is R = 5 cm, the heights of the negative electrode, of the electrolyte and of the positive electrode are $\mathcal{H}_n$ = 4.5 cm, $\mathcal{H}_e$ = 1 cm, $\mathcal{H}_p$=4.5 cm, respectively. The external current collectors are not modeled in the setup and are replaced by simplified boundary conditions on the current. The negative (top) electrode of the LMB is either full liquid (figure 2.9a) or full solid to model the foam (figure 2.9b).
We add an initial perturbation to the system to model the deformation of the droplet in order to investigate the detachment process. In the three-layer setup, the perturbation is modeled by a hemispherical deformation of the negative electrode-electrolyte interface (figure 2.9a). Without the Lorentz force, we expect this deformation to flatten out due to gravity and capillarity. With the Lorentz force, this deformation might amplify. In the foam setup, the initial perturbation is an hemispherical liquid droplet, fixed at the bottom of the solid foam (figure 2.9b). Without the Lorentz force, we expect the droplet to stay at equilibrium below the foam. With the Lorentz force, the droplet might deform and detach. The radius of the perturbation is denoted ϵ.

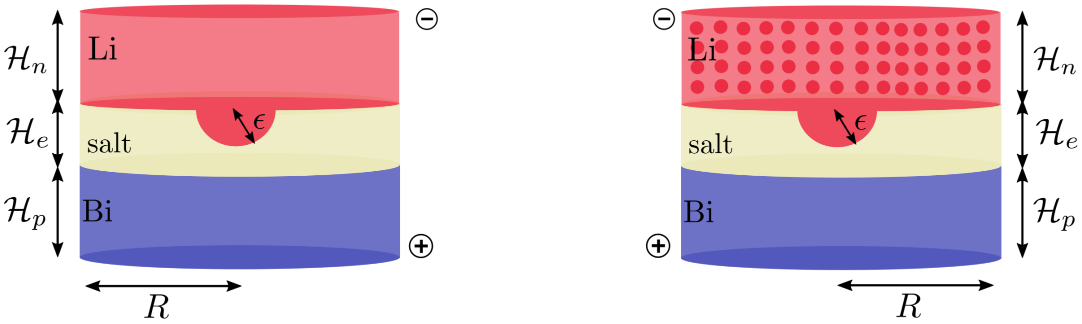

(a) (b)

Figure 2.9 – Schemes of the studied setups. (a) Three-layer setup, with an hemispherical deformation of the negative electrode-electrolyte interface. The phases are fully liquid. (b) Foam setup, with a liquid droplet at the bottom of the foam. The foam is solid and the other phases are liquid.

We focus on the discharge case. We fix a uniform current density $\boldsymbol{J}$ at the bottom and at the top of the cell. The model is multiphase, the phases are solved with a volume-of-fluid method. The positive electrode is considered as made of pure Bi, and the negative electrode is considered as made of pure Li, both in the three-layer and in the foam setups. The potential φ is solved with the Laplace equation. The current density $\boldsymbol{j}$ is deduced from φ. The magnetic field $\boldsymbol{b}$ is solved with the induction equation. The velocity is computed using the Navier-Stokes equations, where two external forces, the Lorentz force $\boldsymbol{f}_{\mathrm{L}}$ and the surface tension force $\boldsymbol{f}_{\mathrm{st}}$, are applied. Mass transfer is not modeled here. The model of the droplet in the foam setup requires to know the contact angle between the droplet and the foam, which depends on numerous parameters, like the materials, the surface roughness and the temperature. The surface of the foam is porous, which means that the contact angle can change depending on the porosity. Thus, the contact angle is unknown in our case. We will arbitrarily fix it to 90°.

In an already existing multiphase solver of OpenFOAM, we have added the induction and the Laplace equations, as well as the Lorentz force in the Navier-Stokes equation and the computation of the current density. To avoid oscillations of the droplets in the foam setup, we have added an algorithm which smooths the phase fraction field. Only axisymmetric simulations are conducted. Equations and more details about the model can be found in Bénard et al. (2021).

2.3.3 Three-layer setup

In the three-layer setup, we use a deformation of the negative (top) electrode-electrolyte interface as an initial perturbation. This deformation is taken as hemispherical for simplicity and is placed at the center of the LMB. We can remark that in this case, the initial state is not at equilibrium.

In figure 2.10, we focus on an initial perturbation with a radius ϵ = 8 mm and study the influence of the current density. The insert graph shows the distance d, which represents the minimal distance between the negative electrode and the positive electrode, as a function of time. When $d = 0$, both metallic phases have entered in contact. When $J = 4.4\,\mathrm{A\,cm^{-2}}$, we observe a re-stabilization of the system, d increases with time. This can be seen on the top snapshots of figure 2.10 too, where the three phases are represented. Gravity and surface tension re-stabilize the system by acting on the interface, generating a flow represented by velocity arrows.

When $J = 10\,\mathrm{A\,cm^{-2}}$, we observe a destabilization of the system. The deformation deviates the current lines (in blue on the snapshots). This deviation increases locally the Lorentz force (arrows on the bottom snapshots), which is predominant at the upper right corner of the deformation. This Lorentz force is high enough to counteract surface tension forces, therefore a droplet is cut. The induced flow drives the droplet downwards into the positive electrode. In this case d reaches 0, but no short circuit is observed.
These observations suggest that a critical current density exists. We have determined the critical current density J_c for different perturbation radii. We have observed that J_c decreases when ϵ increases. For $\epsilon = 9$ mm, $J_c = 4.1\,\mathrm{A\,cm^{-2}}$. This current density could be used in LMBs, but such a large initial deformation is really unlikely, this could require a very intense flow to distort the interface as much. For smaller and more likely perturbation sizes, the critical current density is not realistic. Moreover, no short circuit is observed. This means that, in the three-layer setup, droplet transfers are unlikely. Even though a droplet transfer can occur, it requires either a too large initial deformation or a too large electrical current.

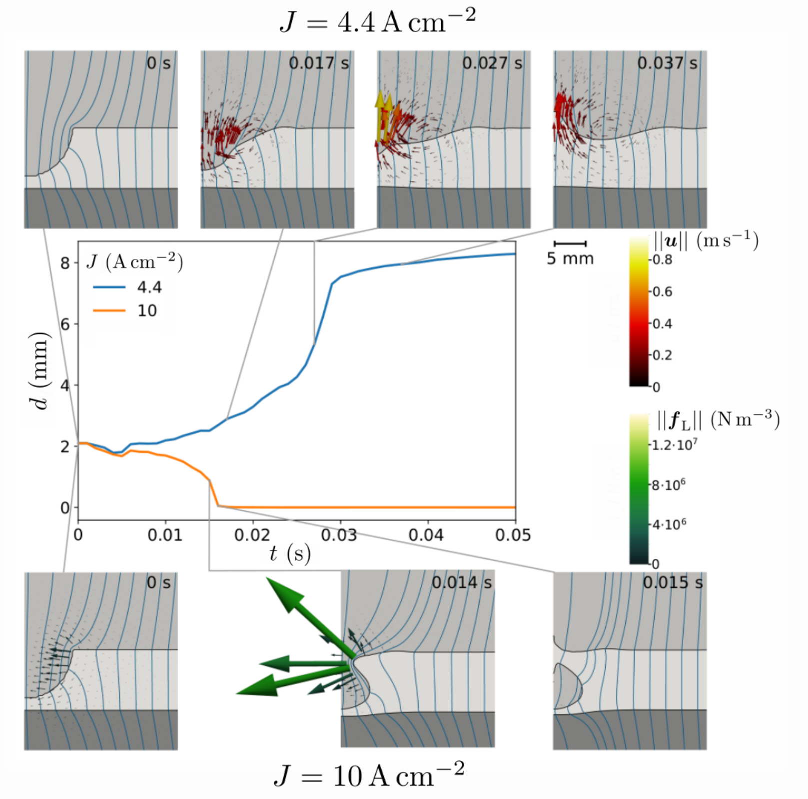

Figure 2.10 – Study of the three-layer setup for $\epsilon = 8$ mm. On the insert graph is plotted d as a function of time for $J = 4.4$, $10\,\mathrm{A\,cm^{-2}}$. The snapshots represent a zoom on the three phases at different times as indicated. Only a meridian plane is displayed with the symmetry axis on the left. The top snapshots are for $J = 4.4\,\mathrm{A\,cm^{-2}}$ and the arrows represent the velocity vectors $\boldsymbol{u}$. The bottom snapshots are for $J = 10\,\mathrm{A\,cm^{-2}}$ and the arrows represent the Lorentz force vectors $\boldsymbol{f}_\mathrm{L}$. The blue lines are streamlines of the current.

In order to understand better the detachment process and the forces involved, we have conducted a theoretical analysis to determine the critical current density. This analysis is based on the assumption that the detachment is due to the competition between the surface tension force, whose characteristic magnitude is denoted F_st, and the Lorentz force, whose characteristic magnitude is denoted F_L. The deformation induces a perturbed current, which deviates from the purely vertical applied current. This perturbed current creates a radial part in the Lorentz force, which acts on the detachment of the droplet. The magnitude of this radial Lorentz force is directly linked to the magnitude of the perturbed current which can be estimated as a function of the size of the deformation. This estimation has been done in Bénard et al. (2021), as well as the estimation of F_{st}. A non-dimensionalized parameter β which characterizes the competition between the surface tension and the Lorentz forces has been determined:

$$\beta = \frac{F_{\mathrm{L}}}{F_{\mathrm{st}}} = \frac{\mu_0 J^2 \pi^2 R^4}{\gamma_{\mathrm{n-e}}} \frac{\epsilon}{(3\mathcal{H}_e - 2\epsilon)^2} \tag{2.3.1}$$

where μ_0 is the magnetic permeability of vacuum and $\gamma_{\mathrm{n-e}}$ the surface tension between the electrolyte and the negative (top) electrode. When $\beta > \beta_c \simeq 37$, a droplet detachment is observed in our simulations. This non-dimensional parameter seems to be a good criterion to describe the detachment process in the three-layer system.

2.3.4 Foam setup

In the foam setup, the liquid lithium is contained in a solid foam. We suppose that liquid droplets can be formed below the negative (top) electrode due to an insufficient wetting. We do not know the exact equilibrium shape of this droplet. In order to determine this shape, we first add an initial hemispherical droplet at the bottom of the solid foam and at the center of the LMB. We suppose a contact angle between the droplet and the foam of 90°. We then run a first simulation without any Lorentz force until the droplet takes its equilibrium shape. We finally conduct the study from this equilibrium state. We can remark that, contrary to the three-layer setup, the initial state is at equilibrium.

Figure 2.11a shows a plot of the distance d as a function of time for different current densities, and $\epsilon = 6$ mm. The critical current density J_c is equal to $3.5\,\mathrm{A\,cm^{-2}}$. For $J < J_c$, oscillations of the droplet are observed, but no detachment occurs. For $J > J_c$, we observe a droplet detachment but no short circuit. This can be seen on the snapshots of figure 2.11a too, which are represented for $J = 3.5\,\mathrm{A\,cm^{-2}}$.
Figure 2.11b shows a plot of the distance d as a function of time for different current densities, and $\epsilon = 8$ mm. The critical current density J_c is equal to $2.45\,\mathrm{A\,cm^{-2}}$. For $J < J_c$, we observe oscillations but no detachment. For J slightly above J_c, we observe first several oscillations before the droplet detaches. This can be seen on the snapshots of figure 2.11b too, which are represented for $J = 2.5\,\mathrm{A\,cm^{-2}}$. In this case, a short circuit is observed at $t = 0.272$ s. For $J > J_c$, the droplet detaches immediately, no oscillations are observed.
We can remark that critical current densities are much lower than in the three-layer setup, for an identical size of the perturbation. These critical current densities can be reached in LMBs.

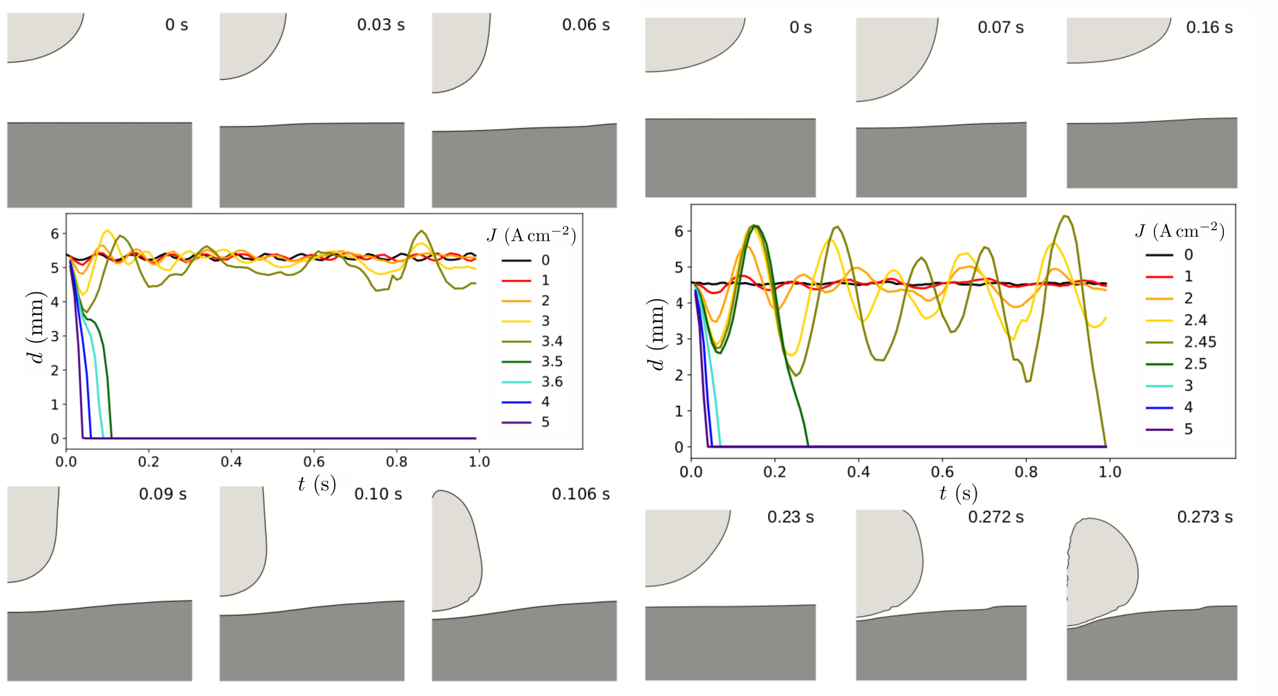

(a)

(b)

Figure 2.11 – Snapshots of the detachment process and distance d, minimal distance between the top and the bottom electrode, as a function of time for different current densities. The snapshots are a zoom on the three liquid phases, the solid foam is not visible. (a) $\epsilon = 6$ mm. Snapshots are represented for $J = 3.5\,\mathrm{A\,cm^{-2}}$. (b) $\epsilon = 8$ mm. Snapshots are represented for $J = 2.5\,\mathrm{A\,cm^{-2}}$.

2.3.5 Conclusion

To conclude this study, the droplet detachment process is due to the Lorentz force which, for high enough current density, dominates the surface tension force, and pinches the droplet. In the three-layer setup, a critical current always exists depending on the size of the deformation, above which a droplet detaches. But this current is not realistic for reasonable deformation sizes. Thus, no droplet detachment is expected in this case. In the foam case, the critical current is more realistic in real LMBs, and short circuit can happen.

However, our model uses simplifications. The simulations conducted are purely axisymmetric. In the foam case, we suppose a contact angle of 90°, but this value was taken arbitrarily. In all of our simulations, the droplet is initially present, we did not study how it forms. Moreover, the droplet volume can vary during operation. Although our model clearly has its limitations, this study provides a first explanation to the observation of droplets and local short circuits in LMBs.

A perspective of this work would be the understanding of the droplet formation below the foam. This would allow us to examine how droplets can appear at the bottom of the foam, and to better model the shape of these droplets.

Chapter 3

Numerical study of swirling electrovortex flows in a cylinder

In this chapter, we present the work published in the article Bénard et al. (2022) in Journal of Fluid Mechanics *in September 2022.*

3.1 Introduction

The swirling electrovortex flow has been thoroughly investigated in and outside the context of LMBs (Bojarevics et al., 1989; Davidson, 2001). Much attention went to the estimation of scaling laws for the intensity of the flow. The work of Davidson et al. (1999) about swirling EVF has suggested the following scaling laws for swirling EVF (see appendix A of Bénard et al. (2022)):

$$U \sim \left(\frac{JBR}{\rho}\right)^{5/9} \left(\frac{R}{\nu}\right)^{1/9}. \tag{3.1.1}$$

Another study realized by Herreman et al. (2021) on the mixing of the alloy of LMBs by swirling electrovortex flow has suggested the existence of a so called boundary layer regime, where the velocity varies like

$$U \sim \left(\frac{JB}{\rho}\right)^{2/3} \frac{R}{\nu^{1/3}} \tag{3.1.2}$$

which is different from the findings of Davidson et al. (1999). Herreman et al. (2021) have explained that the forcing by the Lorentz force is the largest at the rim of the electrical contact between the electrode and the cylinder, where this force is actually singular. This indicates that this regime is controlled by the boundary layer. However, the origin of this regime was not so clear to us. We wonder then what are the conditions of the existence of the boundary layer regime described by equation (3.1.2). Moreover, both above scaling laws have been determined without considering the induction effects, which cannot be neglected for high magnetic fields. How these scaling laws are modified when the induction-less approximation is not valid anymore?

With the numerical code SFEMaNS, we are able to conduct three-dimensional direct simulations. Previously, a lot of numerical simulations were realized using axisymmetric approximation, as this is significantly less costly. Although axisymmetry is sometimes exact, this approximation is certainly not always valid. How does three-dimensionality affect the flow and does it influence the scaling laws?

To answer these questions, we conduct a magnetohydrodynamic study in a cylinder filled with

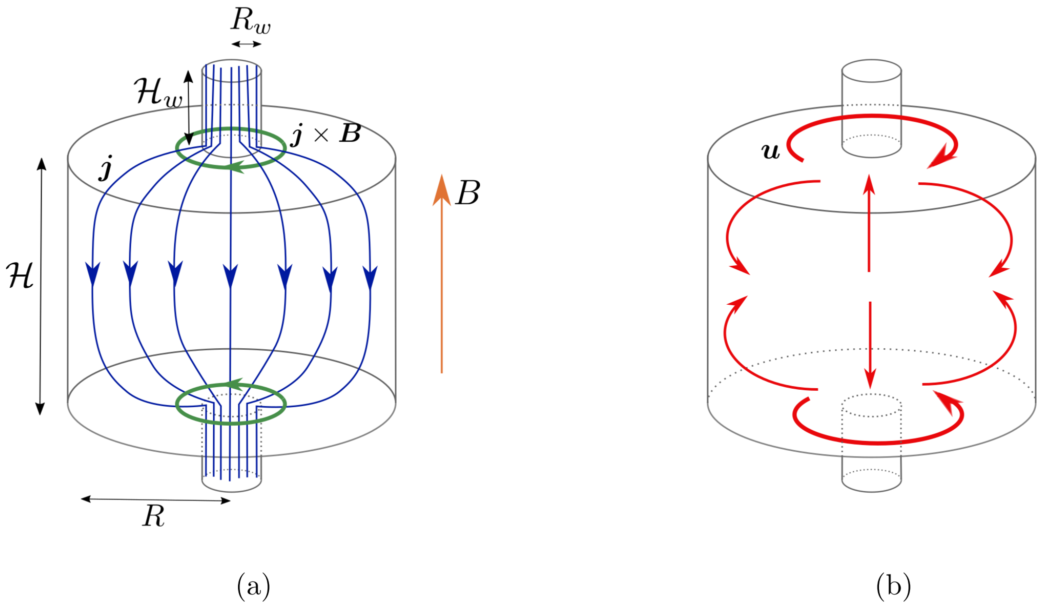

Figure 3.1 – Scheme of the setup used and of the induced swirling EVF. (a) An electrical current is driven through solid copper wires in a cylinder filled with liquid GaInSn and surrounded by a vertical magnetic field $\boldsymbol{B}$. The current density lines are deviated as shown by the blue lines. The Lorentz force $\boldsymbol{j} \times B\boldsymbol{e}_z$ is mainly azimuthal, localized near the electrical contact. (b) Swirling flow driven, mainly azimuthal and structurally similar to a von Kármán flow.

a single liquid metal. Unlike the setup of Herreman et al. (2021), this fluid domain is symmetrically connected to two thin solid electrodes (see figure 3.1a) at the top and bottom of the cylinder. Due to this wiring, we expect an azimuthal Lorentz force $\boldsymbol{j} \times \boldsymbol{b}$ near the top and bottom of the cylinder, with opposite directions and identical magnitude. The swirling electrovortex flow driven is thus expected to be counter-rotating (see figure 3.1b). We have chosen this setup as it should drive a similar flow to the well-known von Kármán flow, investigated by many teams (Berhanu et al. (2007); Monchaux et al. (2007); Nore et al. (2003, 2004)). In this way we can compare the electrovortex flow to the classical counter-rotating von Kármán flow. Our principal aims are to better characterize the different flow regimes of this counter-rotating electrovortex flow and how the flow intensity varies with the different control parameters. Moreover, most of the studies realized in the literature use axisymmetric simulations. By running both axisymmetric and three-dimensional simulations, we are able to analyze differences between them and this allows us to estimate whether axisymmetric simulations can be a good approximation or not.
We begin by describing the model used in the study. Then we show the results of axisymmetric and three-dimensional parametric studies by varying the current, the magnetic field and the viscosity and we identify scaling laws. Finally, we investigate how the geometry influences the flow, before concluding on the results of the chapter.

3.2 Model

We study a cylinder filled with Galistan (GaInSn) liquid metal. We denote $\mathcal{H}$ the height of the cylinder and R its radius. This cylinder is electrically connected to two identical copper wires, one at the top of the cylinder and one at the bottom of the cylinder as shown in figure 3.1a. We denote R_w and $\mathcal{H}_w$ the radius and the height of the wires, respectively. An external vertical magnetic field $\boldsymbol{B} = B\boldsymbol{e}_z$ is applied and a current I is imposed. We will denote $J = I/(\pi R^2)$ the corresponding current density. This current density is nearly that found at the mid-plane. Although I is the actual control parameter and not J, we will often use J to describe the value of the applied current in our study. The system is described by cylindrical coordinates (r, θ, z). The plane $z = 0$ corresponds to the equatorial, mid-plane of the cylinder.
In the cylinder, we impose the magnetohydrodynamics equations:

$$\begin{aligned}
\rho(\partial_t \boldsymbol{u} + (\boldsymbol{u}\cdot\boldsymbol{\nabla})\boldsymbol{u}) &= -\boldsymbol{\nabla} p + \rho\nu(\boldsymbol{\nabla} u + (\boldsymbol{\nabla} u)^T) + \boldsymbol{j}\times\boldsymbol{b}, && (3.2.1a)\\
\partial_t \boldsymbol{b} &= \boldsymbol{\nabla}\times(\boldsymbol{u}\times\boldsymbol{b}) + (\mu_0\sigma^{-1})\boldsymbol{\nabla}\times\boldsymbol{j}, && (3.2.1b)\\
\boldsymbol{\nabla}\cdot\boldsymbol{u} &= 0, && (3.2.1c)\\
\boldsymbol{\nabla}\cdot\boldsymbol{b} &= 0. && (3.2.1d)
\end{aligned}$$

$\boldsymbol{u}$ is the velocity of the fluid, p the pressure, $\boldsymbol{j} = (\nabla\times\boldsymbol{b})/\mu_0$ the current density and $\boldsymbol{b}$ the magnetic field. We denote ρ, ν and σ the density, the kinematic viscosity and the conductivity of the GaInSn, respectively. From Plevachuk et al. (2014), at a temperature $T = 303$ K, we have

$$\rho = 6345 \text{ kg m}^{-3}, \quad \nu = 3.2\cdot 10^{-7}\text{ m}^2\text{ s}^{-1}, \quad \sigma = 3.24\cdot 10^{6}\text{ S m}^{-1}. \tag{3.2.2}$$

μ_0 is the magnetic permeability of vacuum. In the solid wires, the magnetic induction equation fixes

$$\begin{aligned}
\partial_t \boldsymbol{b}_w &= (\mu_0\sigma_{\text{Cu}})^{-1}\nabla^2\,\boldsymbol{b}_w, && (3.2.3a)\\
\boldsymbol{\nabla}\cdot\boldsymbol{b}_w &= 0, && (3.2.3b)
\end{aligned}$$

where $\boldsymbol{b}_w$ is the magnetic field in the wires, and $\sigma_{\text{Cu}} = 5.96\cdot 10^{7}$ S m^{-1} their conductivity.
On the boundaries of the fluid domain we impose no-slip boundary conditions for the velocity. The fluid is initially at rest.
In SFEMaNS, the electrical boundary conditions need to be imposed through the magnetic field, and this can be done using Ampère's law. At any radial coordinate a, we have

$$b_\theta|_{r=a} = \frac{1}{a}\int_0^a \mu_0 j_z r dr. \tag{3.2.4}$$

This yields for instance at $r = R$

$$b_\theta|_{r=R} = \mu_0 J R/2. \tag{3.2.5}$$

Applying this to other boundaries leads to the following boundary conditions. On the insulating part of the liquid domain, we have:

$$\begin{aligned}
&b_z|_{r=R} = B, && b_\theta|_{r=R} = \mu_0 J R/2, && && (3.2.6a)\\
&b_r|_{z=\pm\mathcal{H}/2} = 0, && b_\theta|_{z=\pm\mathcal{H}/2} = \mu_0 J R^2/(2r), && \forall r \in [R_w, R]. && (3.2.6b)
\end{aligned}$$

On the insulating part of the wires, we have:

$$b_{w,z}|_{r=R_w} = B, \quad b_{w,\theta}|_{r=R_w} = \mu_0 J R^2/(2R_w). \tag{3.2.7}$$

At the top and bottom of the wires, we have:

$$b_{w,r}|_{z=\pm(\mathcal{H}/2+\mathcal{H}_w)} = 0, \quad b_{w,\theta}|_{z=\pm(\mathcal{H}/2+\mathcal{H}_w)} = \mu_0 J R^2 r/(2R_w^2) \qquad \forall r \in [0, R_w]. \tag{3.2.8}$$

These conditions are exact for axisymmetric simulations and a suitable approximation for three-dimensional simulations for low magnetic Reynolds numbers, as shown in Herreman et al. (2019b). In our simulations, the magnetic Reynolds number remains always low.

The transmission conditions at the interfaces between the cylinder and the wires, i.e. the continuity of the tangential magnetic and electrical field, are

$$\boldsymbol{e}_z \times (\boldsymbol{b} - \boldsymbol{b}_w)|_{z=\pm\mathcal{H}/2} = 0, \quad \boldsymbol{e}_z \times (\boldsymbol{j}/\sigma) - (\boldsymbol{j}_w/\sigma_w))|_{z=\pm\mathcal{H}/2} = 0, \qquad \forall r \in [0, R_w],$$

where $\boldsymbol{j}_w$ is the current density in the wire.

To solve these equations, we use the numerical code SFEMaNS (Spectral/Finite Elements for Maxwell and Navier-Stokes). This code is written in Fortran 90 and is developed since 2001 in a long-term collaboration between LISN (ex-LIMSI) and TAMU (College Station, Texas). SFEMaNS was initially developed to study dynamo problems in axisymmetrical geometries. This code was already validated thoroughly and previously used to solve different magnetohydrodynamic problems (Guermond et al., 2007, 2009, 2011). As said in section §2.2.2, to avoid new developments, we solve in this chapter the full MHD problem, even though the magnetic Reynolds number remains low.

In SFEMaNS, the numerical method is based on a hybrid decomposition of the fields. Each field $\mathcal{A}$, scalar or vectorial, is decomposed according to a spectral representation in the azimuthal direction and a finite element representation in the meridian plane, such as

$$\mathcal{A}(r,z,\theta,t) \;=\; \sum_{m=0}^{M-1} \mathcal{A}_m^c(r,z,t)\cos(m\theta) \;+\; \sum_{m=1}^{M-1} \mathcal{A}_m^s(r,z,t)\sin(m\theta) \tag{3.2.9}$$

where M is the total number of Fourier modes. We further detail this decomposition and the finite element method in chapters 4 and 5.

In order to characterize the intensity of the flow, we will use the following global quantities:

$$u = \sqrt{\langle \|\boldsymbol{u}\|^2 \rangle_{\mathcal{V}}}, \quad u_{\max} = \max_{\boldsymbol{x}\in\mathcal{V}} \|\boldsymbol{u}(\boldsymbol{x},t)\|. \tag{3.2.10}$$

Here $\langle ... \rangle_{\mathcal{V}}$ means a volume average and $\|\boldsymbol{u}\|^2 = (u_r^2(\boldsymbol{x},t) + u_\theta^2(\boldsymbol{x},t) + u_z^2(\boldsymbol{x},t))$. $\mathcal{V}$ is the volume of the cylindrical fluid domain.

Denoting δ_{kl} the Kronecker symbol, we also define the following quantities for all $m \in \{0,\ldots,M-1\}$ in order to measure the modal content of the flow:

$$u_{\mathrm{m}} = \sqrt{0.5\langle (1+\delta_{m,0})\|\boldsymbol{u}_m^c\|^2 + (1-\delta_{m,0})\|\boldsymbol{u}_m^s\|^2 \rangle_{\mathcal{V}}}. \tag{3.2.11}$$

The toroidal and the poloidal parts of the axisymmetric component of the flow are measured with the following quantities:

$$u_{\mathrm{tor}} = \sqrt{\left\langle (u_{0,\theta}^c)^2 \right\rangle_{\mathcal{V}}}, \quad u_{\mathrm{pol}} = \sqrt{\left\langle (u_{0,r}^c)^2 + (u_{0,z}^c)^2 \right\rangle_{\mathcal{V}}}. \tag{3.2.12}$$

We finally denote time-averaged quantities by using overbars - $\overline{u}$ is the time-average of u for example.

3.3 Influence of J, B and ν on the flow

In this section, we study the influence of the current intensity, of the magnetic field and of the viscosity on the flow. We fix the geometry: R= 10 cm, $\mathcal{H}$ = 18 cm, R_w = 2 cm and $\mathcal{H}_w$ = 4 cm. The aspect ratio $\mathcal{H}/R = 1.8$ is the same used in the von Kármán Sodium experiment (Berhanu et al. (2007); Monchaux et al. (2007)).

3.3.1 Influence of the current density J, axisymmetric study

The external magnetic field is fixed such as $B = 1$ mT. We vary the current density in the range $[10^{-2}, 2000]$ A m^{-2}, equivalent to $I \in [3.1 \cdot 10^{-4}, 62.8]$ A. We first conduct purely axisymmetric simulations only. We use a non-uniform mesh. For $J \leq 50\,\mathrm{A\,m^{-2}}$, the non-constant mesh size h varies in the range $[0.0025, 0.005]$ m. For $J \geq 100\,\mathrm{A\,m^{-2}}$, $h \in [0.0005, 0.0025]$ m.
We show in figure 3.2a the time evolution of the rms velocity u for several current densities. We remark the existence of different states. For $J = 5,\ 10$ A m^{-2}, the velocity magnitude reaches a steady state. For $J = 50,\ 100$ A m^{-2}, the velocity magnitude reaches a non-steady state characterized with weak fluctuations. At some time, a transition occurs. The velocity decreases suddenly, fluctuations are larger. For $J = 500,\ 2000$ A m^{-2}, the velocity is unsteady and presents strong fluctuations after a short transient regime. The time-averaged velocity $\overline{u}$ increases with the current density J, as shown in figure 3.2b. For low J we observe a scaling $\overline{u} \sim J^1$. For intermediate J, the power-law $\overline{u} \sim J^{2/3}$ is merely visible over a decade. At high J, we can observe a power-law $\overline{u} \sim J^{1/2}$.
The ratio between the poloidal and toroidal velocities $u_{\mathrm{pol}}/u_{\mathrm{tor}}$ is plotted in figure 3.2c. The toroidal component always dominates the poloidal component. This ratio is really low for $J = 0.01$ A m^{-2}, and increases until reaching a maximum almost equal to 0.5 at $J = 5$ A m^{-2}. When J is higher, the ratio decreases and fluctuates around a plateau just below 0.4.

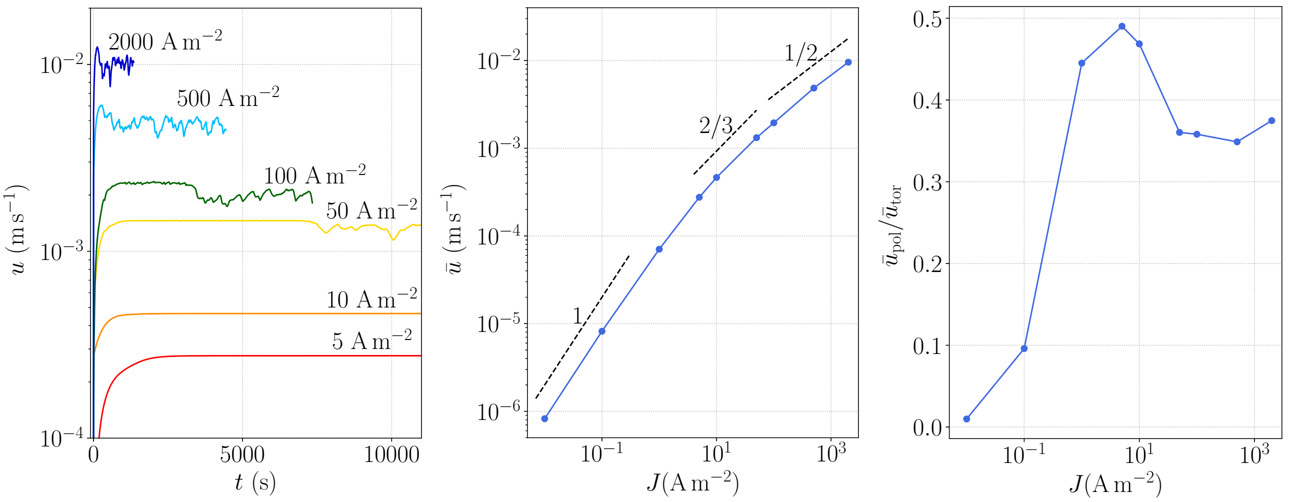

(a) (b) (c)

Figure 3.2 – Variable J, axisymmetric simulations. (a) Time evolution of the volume-averaged velocity u for different values of J. (b) Time- and space-averaged velocity $\bar{u}$ as a function of J (time average done after the transient). (c) Ratio $\overline{u}_{\mathrm{pol}}/\overline{u}_{\mathrm{tor}}$ as a function of J.

The spatial distribution of the flow can be seen in figure 3.3. Figures 3.3a and 3.3b represent the streamlines of the velocity, colored by the velocity magnitude, for two current densities. For $J = 5$ A m^{-2}, the flow is mainly azimuthal and steady. The flow is directed along the symmetry axis and to the electrical bottom and top wires. Then it comes back from the top and bottom walls to the equatorial plane following a spiral fashion around the vertical axis. This structure is $\boldsymbol{R}_\pi$-symmetric, which means that

$$\begin{pmatrix} u_r \\ u_\theta \\ u_z \end{pmatrix}(r,\theta,z) = \begin{pmatrix} u_r \\ -u_\theta \\ -u_z \end{pmatrix}(r,-\theta,-z). \tag{3.3.1}$$

This flow structure is similar to the von Kármán flow studied by Nore et al. (2003). For $J = 500\ \mathrm{A\,m^{-2}}$, the flow is turbulent and predominantly azimuthal. The $\boldsymbol{R}_\pi$-symmetry is broken.
The influence of the current density on the spatial structure of the velocity field is studied more precisely in figure 3.3c, where the velocity magnitude $||\boldsymbol{u}||$ is represented for different current densities in a meridional plane. For $J = 0.1\ \mathrm{A\,m^{-2}}$, the flow is steady and largest close to the electrical contacts with the wires. When J increases, the flow becomes more intense along the vertical axis. The flow is still $\boldsymbol{R}_\pi$-symmetric. From $J = 50\ \mathrm{A\,m^{-2}}$ the system is destabilized, the $\boldsymbol{R}_\pi$-symmetry is broken and the flow becomes "turbulent".

The different spatial structures observed highlight the existence of a symmetry-breaking bifurcation in the interval $[10,\ 50]\ \mathrm{A\,m^{-2}}$. Figure 3.4a shows the velocity magnitude at two instants for $J = 50\mathrm{A\,m^{-2}}$ before and after the bifurcation. At $t = 4000$ s the flow is strongest along the vertical axis and presents a $\boldsymbol{R}_\pi$-symmetry. At $t = 30000$ s, the flow is disorganized and unsteady, the $\boldsymbol{R}_\pi$-symmetry is broken.
We use this symmetry-breaking to determine the bifurcation threshold. We define the top (resp. bottom) energy E_{top} (resp. E_{bot}) as the volume-averaged magnetic energy computed in the top (resp. bottom) half of the cylinder. If $|E_{\mathrm{top}} - E_{\mathrm{bot}}|$ increases with time, the $\boldsymbol{R}_\pi$-symmetry is broken. We use this quantity to determine the threshold of the bifurcation. On the inset graph of figure 3.4b we plot $|E_{\mathrm{top}} - E_{\mathrm{bot}}|$ with time using a logarithmic scale, for $J = 50\,\mathrm{A\,m^{-2}}$. This difference increases linearly with time before reaching a plateau where it oscillates. From these data, we measure the growth rate λ_r, i.e. the slope of the linear part. In figure 3.4b, we show λ_r in blue points for different values of J. Close to the threshold, λ_r increases linearly with J. The points for $J > 90\ \mathrm{A\,m^{-2}}$ are far from the threshold, and deviate from this linear behavior. A linear interpolation of λ_r for low J (orange dashed line) yields the threshold $J_c = 17\,\mathrm{A\,m^{-2}}$.

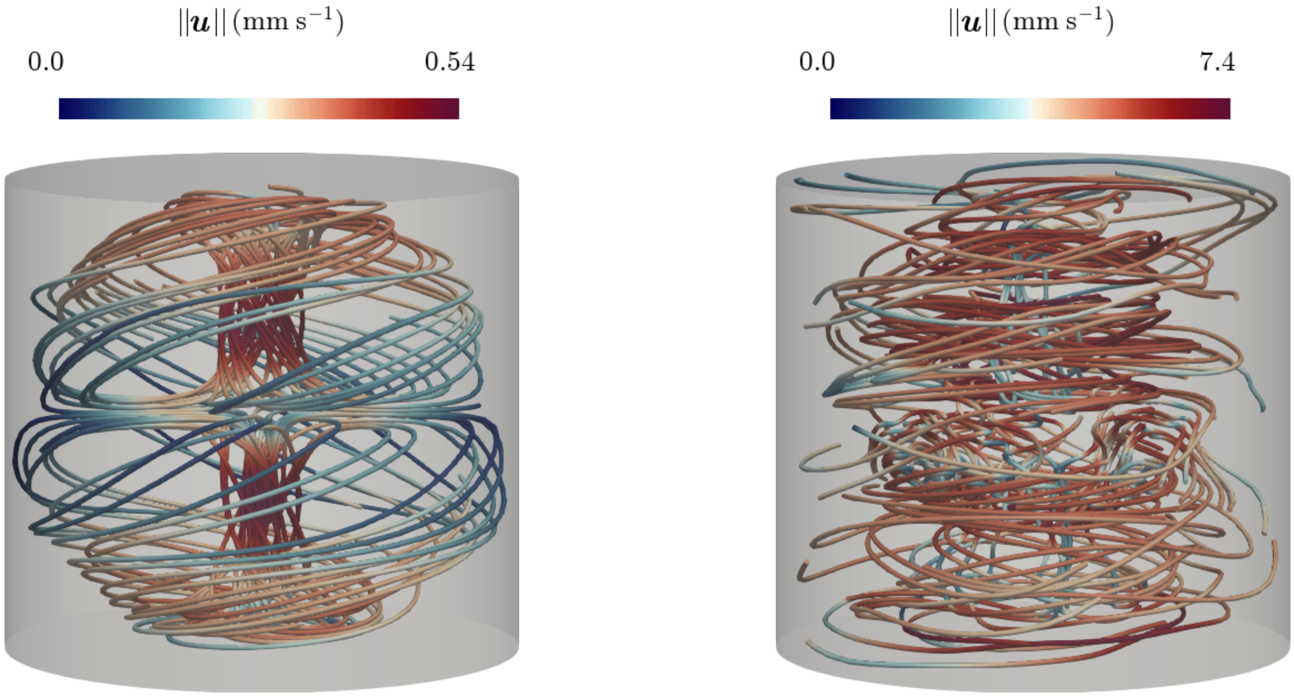

(a) $J = 5$ A m^{-2} (b) $J = 500$ A m^{-2}

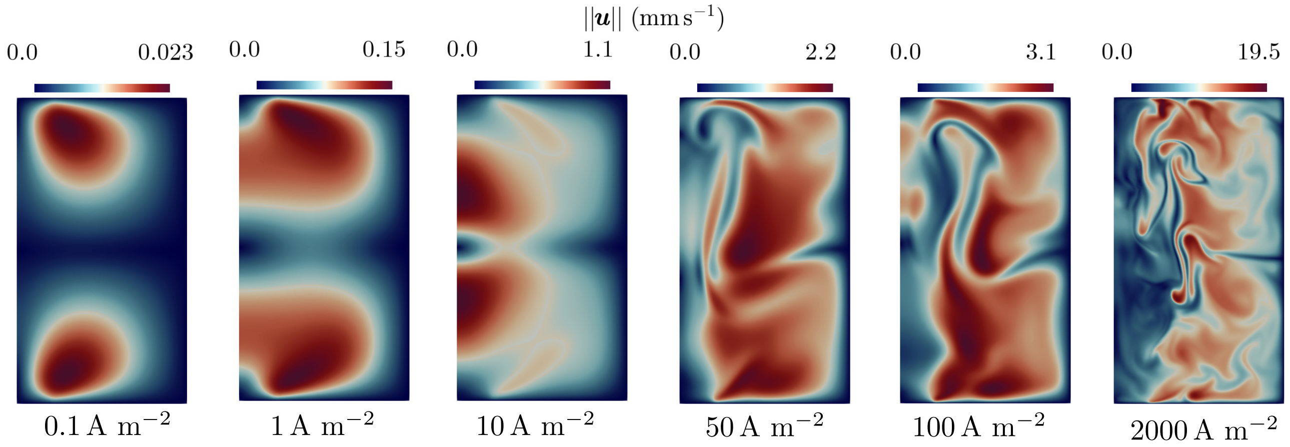

(c)

Figure 3.3 – Variable J. Axisymmetric simulations. Spatial structure of the flow. (a-b) Streamlines colored by the velocity magnitude in axisymmetric simulations for different values of J. (c) Transition of the axisymmetric flow as J increases, visualized by the velocity magnitude $\|\boldsymbol{u}\|$ in a meridian plane (the symmetry axis is on the left).

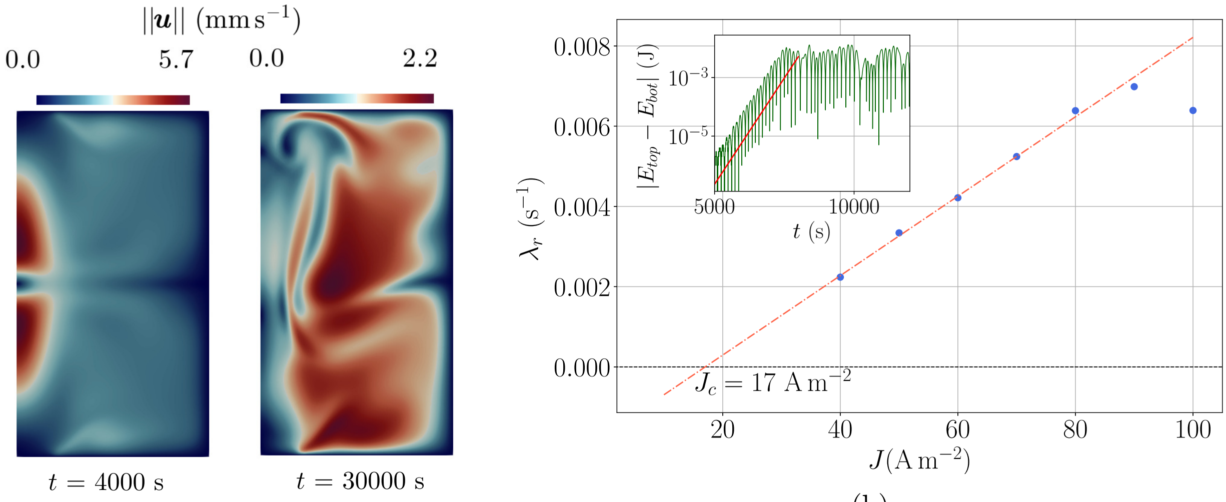

(a) (b)

Figure 3.4 – Determination of the threshold of unsteadiness. (a) Velocity distribution for $J = 50$ A m^{-2} at $t = 4000$ s and at $t = 30000$ s (b) On the inset graph is plotted the difference $|E_{\text{top}} - E_{\text{bot}}|$ for $J = 50$ A m^{-2}. The growth rate λ_r of this difference, which corresponds to the slope of the increasing part, is plotted in blue for different J. A linear fit of these values (orange dashed line) leads to the threshold $J_c = 17$ A m^{-2}.

3.3.2 Influence of the current density J, three-dimensional study

The unsteady behavior of the system for high enough current densities suggests a three-dimensional flow. Thus, we conduct three-dimensional simulations and compare them with axisymmetric simulations. We use $M = 20$, and show further why 20 modes are enough to conduct our study. The meshes are the same as in section §3.3.1.
In figure 3.5 are shown the time evolution of the volume-averaged velocity u as well as its modal components u_0, u_1, u_2 and u_3. For $J = 1$ A m^{-2}, the system remains axisymmetric. For $J = 5$ A m^{-2}, the three-dimensional behavior appears from $t = 8000$ s. The flow oscillates until it stabilizes at $t = 20000$ s. The mode 2 dominates the three-dimensional components. For $J = 10$ A m^{-2}, the mode 2 also dominates, but the three-dimensional behavior appears sooner, from $t = 2000$ s, and the system remains unsteady with large oscillations. For $J = 50$ A m^{-2}, the three-dimensional behavior appears very quickly and the flow is turbulent with large fluctuations. The modes are all non-zero. Even though the flow is clearly three-dimensional, the axisymmetric component remains dominant.

In order to compare axisymmetrical and three-dimensional simulations, we plot in figure 3.6a the mean velocities $\bar{u}$ obtained with axisymmetric and three-dimensional simulations, as a function of the current density. The flow becomes three-dimensional between 1 and 5 A m^{-2}. For high current densities, the law $\bar{u} \sim J^{1/2}$ or $\bar{u} \sim J^{5/9}$ can be observed. More precisely, a fit of the values give a slope of 0.51 for axisymmetric simulations, i.e. rather $\bar{u} \sim J^{1/2}$, and a slope equal to 0.55 for three-dimensional simulations, i.e. rather $\bar{u} \sim J^{5/9}$. For medium current densities the law $\bar{u} \sim J^{2/3}$ is not clearly visible. The three-dimensional rms velocity is always lower than the axisymmetric velocity, but remains of the same order of magnitude. This is shown more precisely in figure 3.6b, where the ratio between both quantities $\bar{u}_{3\text{D}}/\bar{u}_{\text{axi}}$ is represented. This ratio decreases with J until it fluctuates around a plateau from $J = 50$ A m^{-2}. The fact that this ratio remains slightly above 0.75 shows that axisymmetric simulations can give a reasonable order of magnitude of the flow intensity.

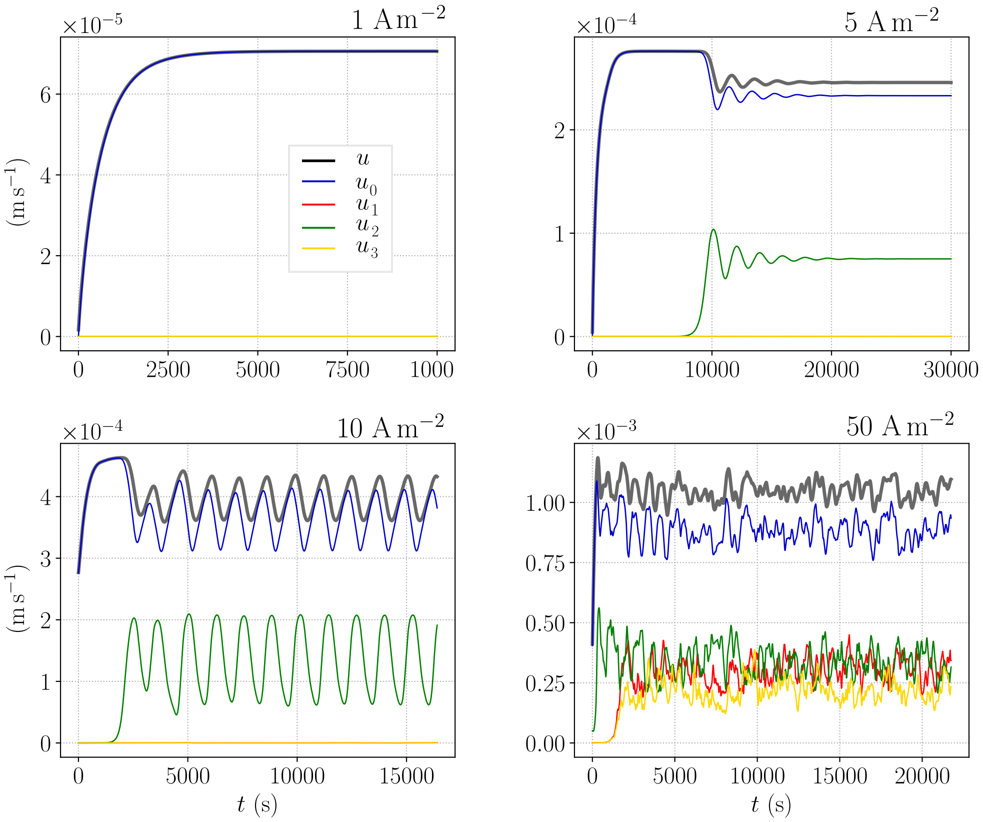

Figure 3.5 – Time evolution of u and modal content u_0, u_1, u_2, u_3 for different current densities J.

The spatial distribution of the three-dimensional flow is represented in figure 3.7, which shows the velocity magnitude on a meridian plane and a horizontal plane at $z = 8.8$ cm for three current densities. For $J = 5$ A m^{-2}, the flow is steady and presents a weak top-bottom asymmetry, unlike in the axisymmetric simulations. For $J = 50$ A m^{-2} and $J = 500$ A m^{-2}, the flow is clearly turbulent and three-dimensional. Notice that the low-velocity zone around the vertical axis visible in axisymmetric simulations (figure 3.3c) is completely absent in three-dimensional simulations.

For high current densities, the flow is turbulent and presents large fluctuations. Thus, we can wonder if 20 Fourier modes are enough to accurately represent the flow. For this reason, we have conducted a small convergence study using $M = 20$ to $M = 40$ and for three current densities, $J = 100$, 500 and 2000 A m^{-2}. In figure 3.8 we represent the time- and space-averaged modal kinetic energy $E_c = \overline{u^2}\mathcal{V}/2$ as a function of m for $M = 20$ and $M = 40$.
For $J = 100$ A m^{-2}, the spectra present small differences for $m \geq 15$. For $J = 500$ A m^{-2}, similar differences appear for $m \geq 10$. In both cases, the most energetic modes are well converged. Hence $M = 20$ is enough to properly represent the flow. For $J = 2000$ A m^{-2}, the spectra show more significant differences, particularly for the first modes. Thus, the use of 40 modes is preferable in this case. However, we see that the averaged velocity $\bar{u}$ is identical with 20 or 40 modes. The plots of figure 3.6 computed with $M = 20$ remain valid.

The first bifurcation observed in the three-dimensional simulations with increasing J is the breaking of axisymmetry. This happens in the range between $J = 1$ A m^{-2} and $J = 5$ A m^{-2}. The flow in the case $J = 5$ A m^{-2}, just after this bifurcation, is characterized in figure 3.9. This

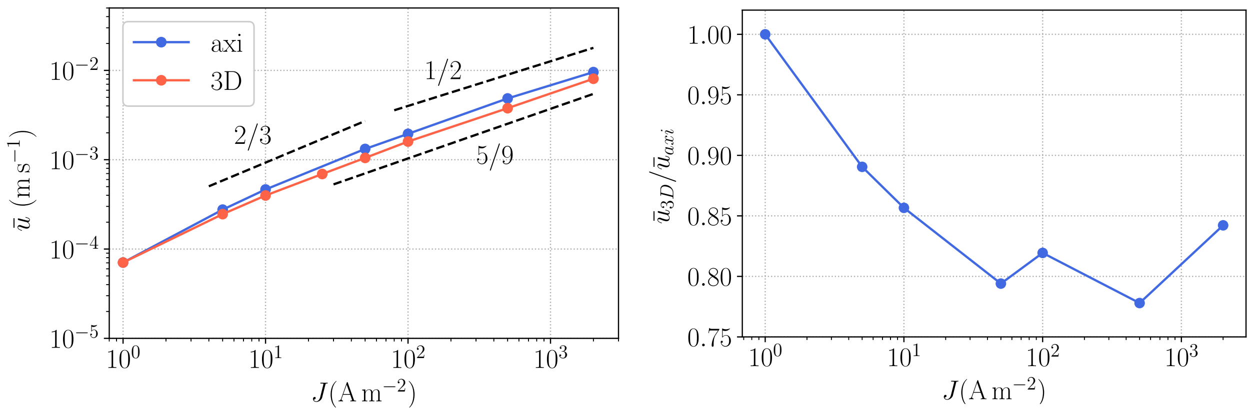

(a)

(b)

Figure 3.6 – (a) $\overline{u}$ as a function of J in axisymmetrical and three-dimensional simulations. (b) Ratio $\overline{u}_{\mathrm{3D}}/\overline{u}_{\mathrm{axi}}$ vs J.

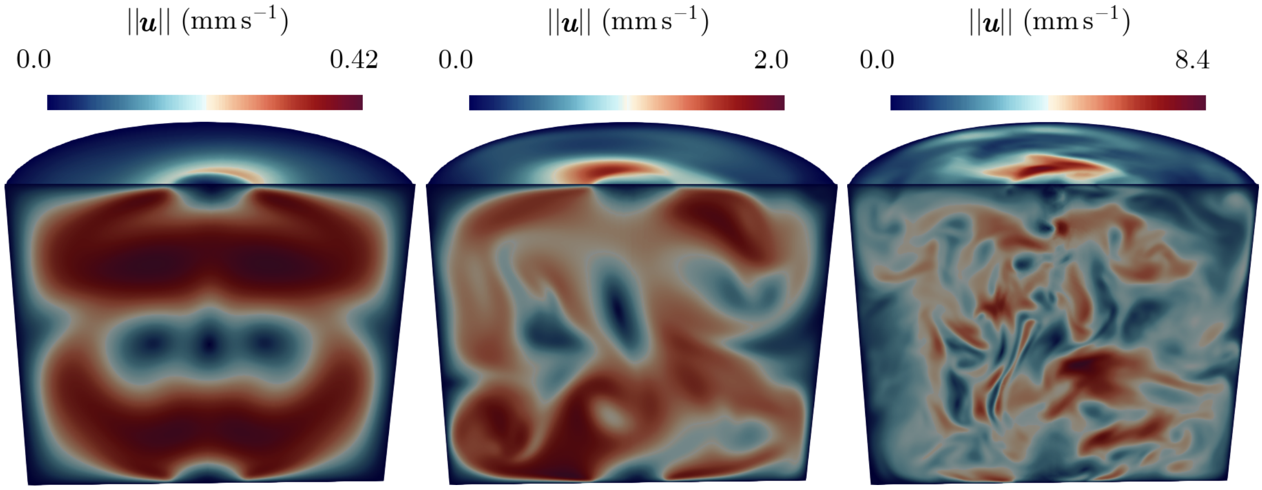

(a) $J = 5$ A m^{-2}

(b) $J = 50$ A m^{-2}

(c) $J = 500$ A m^{-2}

Figure 3.7 – Spatial distribution of the velocity magnitude $\|\boldsymbol{u}\|$ for $J = 5,\ 50,\ 500$ A m^{-2}.

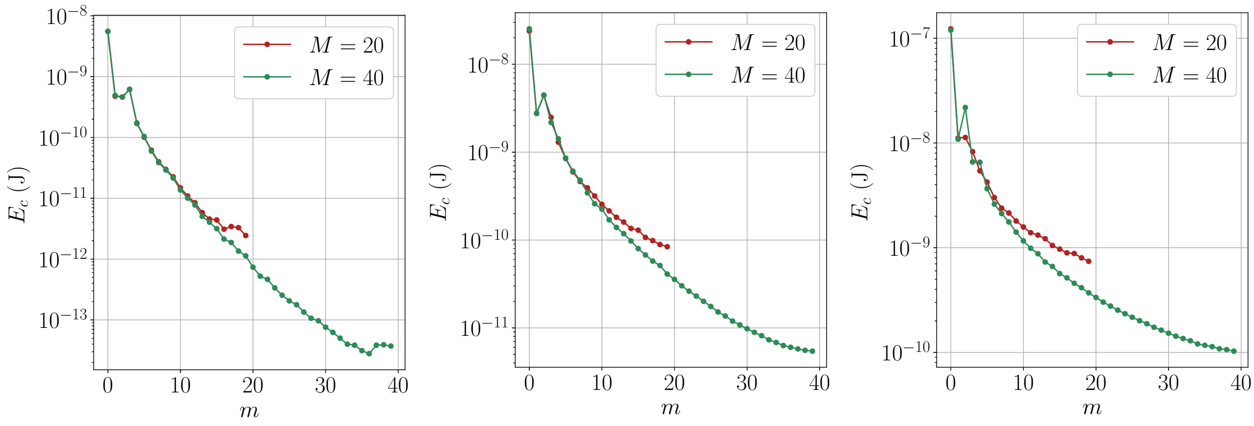

(a) $J = 100$ A m^{-2}

(b) $J = 500$ A m^{-2}

(c) $J = 2000$ A m^{-2}

Figure 3.8 – Spectra of the time-averaged kinetic energy in the statistically steady state as a function of the mode m for $J = 100,\ 500,\ 2000$ A m^{-2}, using $M = 20$ and $M = 40$.

flow is steady and three-dimensional. In figure 3.9a we show the vertical component of the velocity u_z on three horizontal planes at $z = -3$ cm, $z = 0$ cm and $z = 3$ cm. One can clearly see the dominance of the mode 2, and the R_π-symmetry, also visible in 3.9b. This flow is structurally very close to the counter-rotating von Kármán flow studied in Nore et al. (2003). This predominance of the mode 2 in the horizontal planes is due to two opposite vortices centered at $\theta = -\pi/2$ and $\theta = \pi/2$, separated by two opposite fronts centered at $\theta = 0$ and $\theta = \pi$ where the flow is drawn towards the center of the cylinder. These equatorial vortices are visible in figure 3.9c, where the velocity magnitude is plotted at $r = 0.8R$.
The second bifurcation in the simulations with increasing J is the appearance of the unsteadiness. This occurs between $J = 5$ A m^{-2} and $J = 10$ A m^{-2}. The flow oscillates but still remains R_π-symmetric. The mode 2 remains dominant.
The third and final bifurcation is the appearance of turbulence and the loss of the R_π symmetry, which happens between $J = 10$ A m^{-2} and $J = 50$ A m^{-2}.

We focus on the determination of the threshold of the first bifurcation, when the axisymmetry is broken. The velocity component of the two first three-dimensional modes u_1 and u_2 increases exponentially with time for $J = 5$ A m^{-2} (see the inset in figure 3.10). In figure 3.10 is plotted the growth rate λ of the modes 1 and 2 for $J = 1$ A m^{-2}, $J = 5$ A m^{-2} and $J = 10$ A m^{-2}. The growth rates for $J = 1$ A m^{-2} are negative because this case is axisymmetrical. We deduce from a linear fit between $J = 1$ A m^{-2} and $J = 5$ A m^{-2} the threshold $J_c^{3\mathrm{D}} = 2.5$ A m^{-2}, which is identical for both modes 1 and 2. This result is qualitatively similar to the findings of Nore et al. (2004) where it was shown that, for an aspect ratio of 1.8, modes 1 and 2 destabilize at the same threshold.

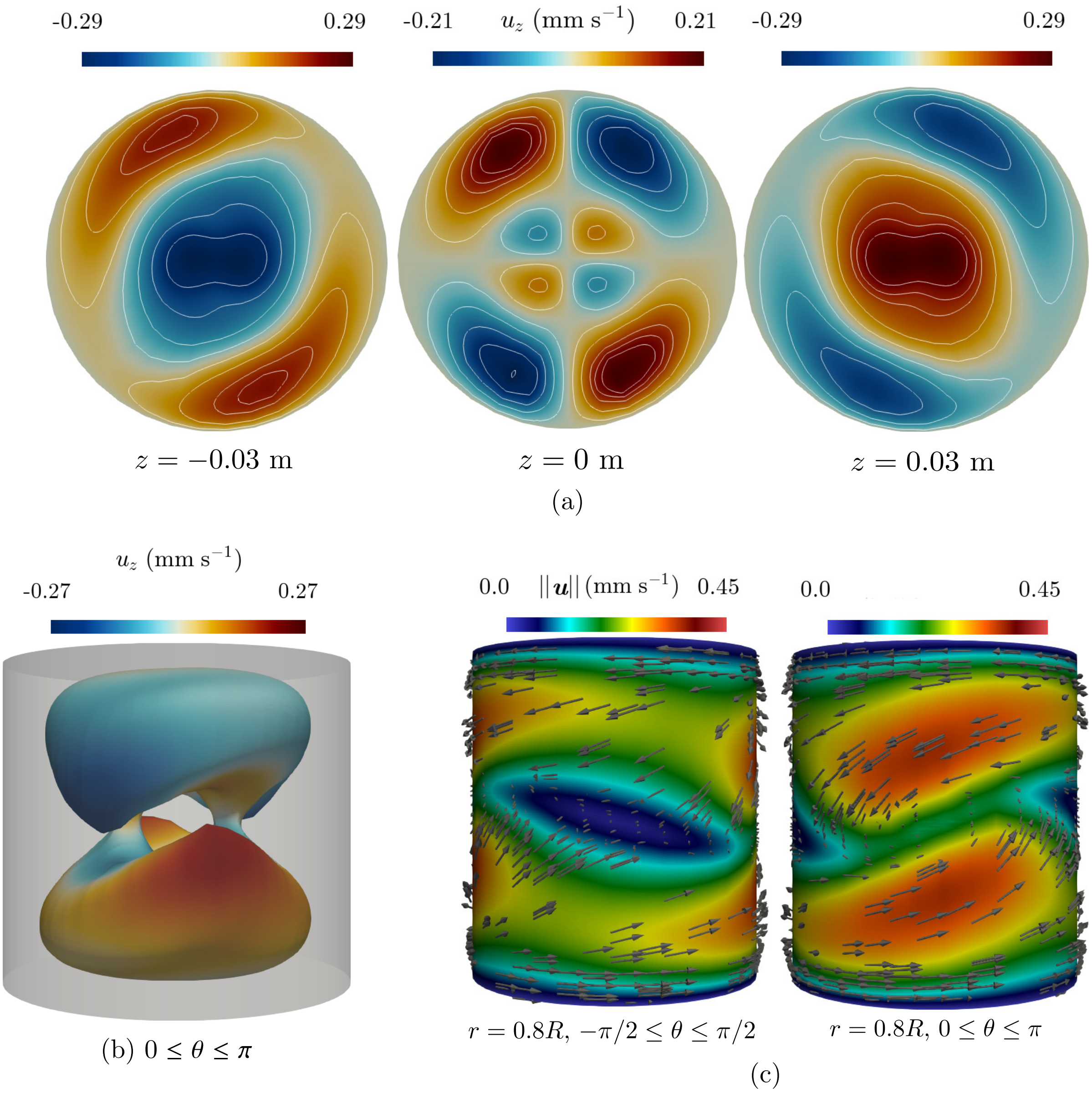

(a)

(b) $0 \leq \theta \leq \pi$

(c)

Figure 3.9 – Flow structure after the first bifurcation, for $J = 5$ A m^{-2}. (a) Vertical velocity u_z at $z = -0.03$ m, $z = 0$ m and $z = 0.03$ m. (b) Contour of $\|\boldsymbol{u}\|$ taken for $\|\boldsymbol{u}\| = 0.6\ \|\boldsymbol{u}\|_{\max}$ and colored by u_z. (c) $\|\boldsymbol{u}\|$ at $r = 0.8R$ and $-\pi/2 \leq \theta \leq \pi/2$ (left) and $0 \leq \theta \leq \pi$ (right).

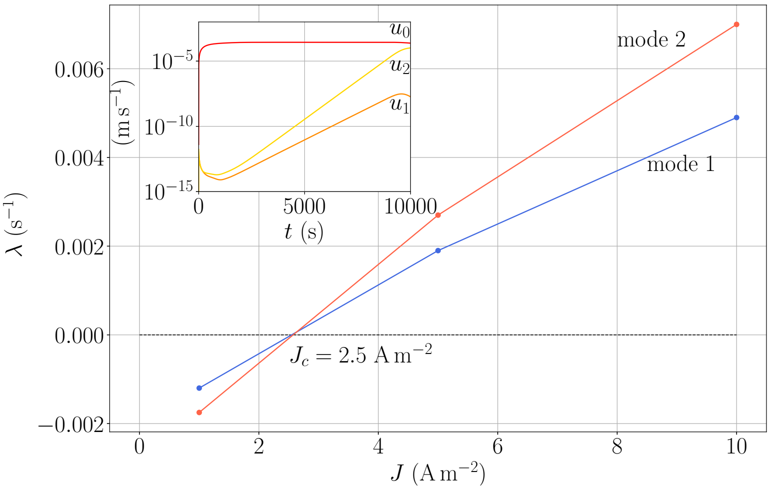

Figure 3.10 – Threshold of the first bifurcation i.e. the three-dimensionalization of the flow. Exponential growths of u_1, u_2 are shown in the inset for $J = 5$ A m^{-2}. The measured growth rates plotted as a function of J permit to locate the threshold of the first three-dimensional bifurcation near $J_c^{3D} \approx 2.5$ A m^{-2} for both modes $m = 1, 2$.

3.3.3 Influence of the magnetic field B

In a second series of simulations, we fix the current density at $J = 50$ A m^{-2}. We vary the external magnetic field magnitude B. We focus on axisymmetric simulations, and conduct only one three-dimensional simulation with $M = 20$ modes. For $B \leq 10^{-3}$ T, the mesh size h varies in the range $[0.0025, 0.005]$ m. For $2 \cdot 10^{-3}$T $\leq B \leq 5 \cdot 10^{-1}$ T, $h \in [0.0005, 0.0025]$ m. For $B = 1$ T, $h \in [0.001, 0.005]$ m.
In figure 3.11, we show the time- and volume-averaged velocity $\overline{u}$ as a function of B. This quantity increases with B following the law $\overline{u} \sim B^{2/3}$ until $B = 5 \cdot 10^{-4}$ T, then the law $\overline{u} \sim B^{1/2}$ is observed until $B = 2 \cdot 10^{-3}$ T. For higher B, the slope increases progressively, until a maximum is reached and the behavior is drastically modified. For the highest magnetic fields, the velocity decreases with B and we observe a law $\overline{u} \sim B^{-1}$.

Figure 3.12 shows snapshots of the current density distribution (left) and velocity field (right) for three magnetic fields between 10^{-3}, 10^{-2} and 10^{-1} T. When the magnetic field increases, the flow becomes steady and the current density lines are compressed. For the highest magnetic field studied, the flow and the current are concentrated in a thin vertical column whose borders are aligned with the boundaries of the wires. Outside of this column the velocity is zero. In this case, for high magnetic fields, the flow remains axisymmetric. We have conducted a three-dimensional simulation for $B = 10^{-1}$T which has shown that $\overline{u}$ is identical in both axisymmetric and three-dimensional simulations (it corresponds to the red point in figure 3.11). The three-dimensional modes ($m \neq 0$) are zero. Hence, high magnetic fields make the flow more axisymmetric and reduce drastically the flow intensity. The term $\sigma \boldsymbol{u} \times B\boldsymbol{e}_z$ in (3.2.1b), which corresponds to the induction effects, is the source of the reorganization of the current density and velocity distributions.
One can also notice that, unlike in duct flows (Hunt and Stewartson (1965); Moresco and Alboussiere (2004)), Hartmann boundary layers are not present at high magnetic field in our setup. Such layers are always localised near the solid boundaries of the domain and channel the electrical current for large Hartmann numbers, defined as

$$Ha = BR\left(\frac{\sigma}{\rho\nu}\right)^{1/2}. \tag{3.3.2}$$

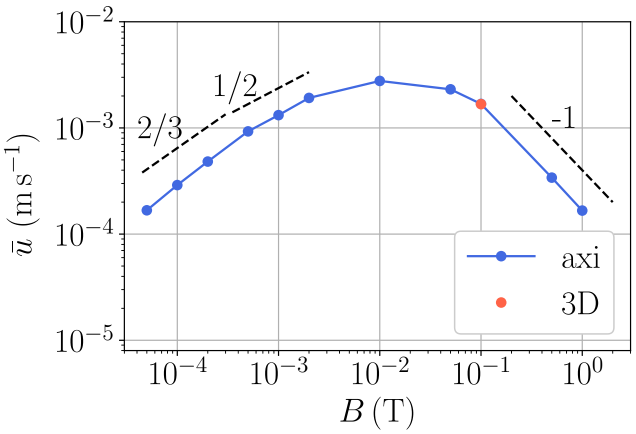

Figure 3.11 – Time- and volume-averaged velocity $\overline{u}$ as a function of $\boldsymbol{B}$.

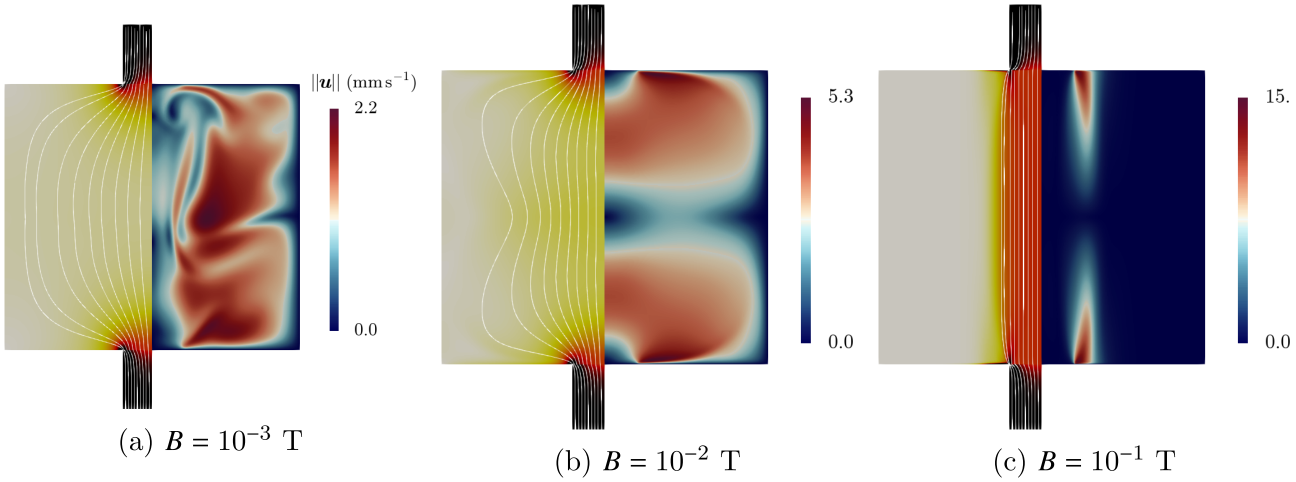

(a) $\boldsymbol{B} = 10^{-3}$ T

(b) $\boldsymbol{B} = 10^{-2}$ T

(c) $\boldsymbol{B} = 10^{-1}$ T

Figure 3.12 – Spatial representation of the current density (left) and of the velocity magnitude (right) for three magnetic fields. The current density is scaled from yellow to purple in the range $[0,\boldsymbol{J}_w]$ where $\boldsymbol{J}_w = 1250$ A m^{-2} is the imposed current density in the wires.

In our case, we have, for the three simulations reported in figure 3.12, $\boldsymbol{Ha} \approx 4, 40, 400$, for $\boldsymbol{B} = 10^{-3}, 10^{-2}, 10^{-1}$ T, respectively, and does effectively become large. Yet, in our setup, the configuration is different from the duct flows. The imposed current density and external magnetic field are parallel, unlike the case of duct flows where they are perpendicular. However, free Shercliff layers can be observed.

3.3.4 Influence of the viscosity ν

We study in this section the influence of the viscosity ν. We use the same geometry as in the previous sections. We fix $J = 50$ A m^{-2}, $B = 1$ mT, and we artificially vary the viscosity of the liquid metal. Usually, the viscosity of a liquid metal is between 10^{-7} and 10^{-6} m^{2}s^{-1}. Yet, in order to better understand the behavior of the flow, we extend the study to other non-realistic viscosities. We conduct only axisymmetric simulations. We vary the viscosity in the range $\nu \in [8 \cdot 10^{-8}, 3 \cdot 10^{-5}]\,\mathrm{m^2s^{-1}}$. The mesh size h varies in the range $[0.0025, 0.005]$ m for each value of viscosity.

We show in figure 3.13 the time- and volume-averaged velocity $\overline{u}$ as a function of the viscosity. The velocity decreases with ν. For small values of ν, it is not so clear if we observe the power-law $\overline{u} \sim \nu^{-1/9}$ or ν^0, but the flow magnitude is pretty independent of ν. For large viscosities, we observe the behavior $\overline{u} \sim \nu^{-1}$.

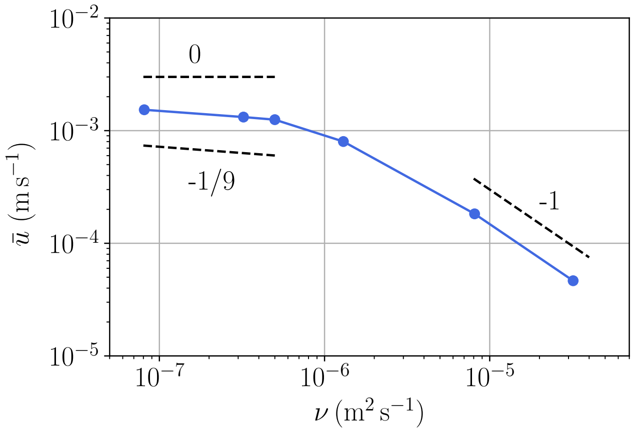

Figure 3.13 – Velocity $\bar{u}$ as a function of the viscosity ν.

3.3.5 Scaling laws

Let us now explain the scaling laws observed in figures 3.2b, 3.11 and 3.13. We first introduce the non-dimensional quantity $\Gamma = \mu_0 JR/B$ which is a ratio between the horizontal component of the magnetic field and the vertical magnetic field. For all simulated cases, we have $\Gamma \ll 1$. This means that the dominant part of the magnetic field is B and that the EVF is likely always swirling. We then introduce the typical scales for the velocity, the current density and the magnetic field: $[\boldsymbol{u}] = U$, $[\boldsymbol{j}] = J$ and $[\boldsymbol{b}] = B$.

We first describe the inductive regime for high magnetic fields. In this regime, the inductive term $\sigma(\boldsymbol{u} \times \boldsymbol{b})$ becomes dominant in Ohm's law. We conjecture that the flow saturates when this term balances the applied current density J. This yields:

$$U \sim \frac{J}{\sigma B} \tag{3.3.3}$$

which is in accordance with the observation $\bar{u} \sim B^{-1}$ for high B (figure 3.11).

When induction is not important, we can distinguish three flow regimes. The first regime corresponds to the Stokes regime where the viscous term dominates, valid for low velocities. Thus, a balance between the viscous and the Lorentz force terms from the Navier-Stokes equations (equation (3.2.1a)) is verified. We have then $[\nabla \cdot (\rho\nu(\nabla \boldsymbol{u} + (\nabla \boldsymbol{u})^{\mathrm{T}}))] \sim [\boldsymbol{j} \times \boldsymbol{b}]$. In this regime, the velocity fills the whole cell, the scale $[r] = R$ is then accurate. This yields the following relation:

$$U \sim \frac{JBR^2}{\rho\nu} \tag{3.3.4}$$

Thus, in this regime, the velocity varies like J and ν^{-1}. This is in agreement with our simulations where $\bar{u} \sim J^1$ and $\bar{u} \sim \nu^{-1}$ for low velocities. This regime has been also observed in duct flows (Poyé et al. (2020)).
A second regime is the inertial regime, valid for high velocities. In this regime, inertia dominates viscosity and balances the Lorentz force. We have then $[\rho(\boldsymbol{u} \cdot \boldsymbol{\nabla})\boldsymbol{u}] \sim [\boldsymbol{j} \times \boldsymbol{b}]$, which yields:

$$U \sim \left(\frac{JBR}{\rho}\right)^{1/2} \tag{3.3.5}$$

We recover the power-laws $\bar{u} \sim J^{1/2}$, $\bar{u} \sim B^{1/2}$ and $\bar{u} \sim \nu^0$ found in our simulations (figures 3.2b, 3.11 and 3.13). This regime has been already investigated by Bojarevics et al. (1989). Davidson (1992); Davidson et al. (1999) have proposed a finer approach to derive scaling laws of axisymmetric flows driven by azimuthal body forces. A reinterpretation of the scaling law proposed by Davidson et al. (1999) in the turbulent regime, by using the Lorentz force as the driving body force, yields

$$U \sim \left(\frac{JBR}{\rho}\right)^{5/9} \left(\frac{R}{\nu}\right)^{1/9} \tag{3.3.6}$$

(see appendix A of Bénard et al. (2022) for details on this reinterpretation). This explains the law $\bar{u} \sim J^{5/9}$, $\bar{u} \sim \nu^{-1/9}$ that could be observed in figures 3.2b and 3.13. However, it is difficult to determine which law for the inertial regime (3.3.5) or (3.3.6) is the most adapted in our case.
A third intermediate regime, that we call the boundary layer regime, can sometimes be observed. It exists when the viscous effects, the inertial effects and the Lorentz force have all the same intensity, which is possible because forcing principally occurs near the electrical contact, in the viscous boundary layer. The derivation of the scaling law for this regime is explained in Herreman et al. (2021). It is based on the z-component of the vorticity equation

$$\partial_t \omega_z + (\boldsymbol{u} \cdot \nabla)u_z \approx (\boldsymbol{\omega} \cdot \nabla)u_z + \rho B \partial_z j_z + \nu \partial_{zz} \omega_z. \tag{3.3.7}$$

If the viscous effects, the inertial effects and the Lorentz force have the same intensity, this yields the three-term balance

$$[(\boldsymbol{u} \cdot \nabla)\omega_z - (\boldsymbol{\omega} \cdot \nabla)u_z] \sim [\rho^{-1} B \partial_z j_z] \sim [\nu \partial_{zz}^2 \omega_z]. \tag{3.3.8}$$

This regime is mainly controlled by the flow in the boundary layer with thickness δ. We can then estimate the scales $[\partial_z] = \delta^{-1}$ and $[\partial_r] = R^{-1}$. We suppose $[u_r, u_\theta] = U$. We have then $[u_z] = U\delta R^{-1}$ due to incompressibility. Thus, $[\omega_r, \omega_\theta] = U\delta^{-1}$ and $[\omega_z] = UR^{-1}$ for the vorticity. From this, the three-term balance becomes

$$\frac{U^2}{R^2} \sim \frac{JB}{\rho\delta} \sim \frac{\nu U}{R\delta^2} \tag{3.3.9}$$

which yields, after having eliminated δ

$$U \sim \left(\frac{JB}{\rho}\right)^{2/3} \frac{R}{\nu^{1/3}}. \tag{3.3.10}$$

This scaling law has been observed by Poyé et al. (2020) in duct flows, and was explicitly visible in Herreman et al. (2021). However, in this symmetrically wired setup, with pairs of opposing wire electrodes, this scaling law is not so clearly observed or only in a short range of current densities. The flow driven in this setup is much more turbulent than that in Herreman et al. (2021). This likely implies that the boundary layer will also become more easily turbulent too. Since the three-term balance is based on a laminar boundary layer, it will then be easily broken. This regime can be also derived from the model of Davidson (1992), by supposing a laminar boundary layer and using a laminar friction law for the viscous stress (see Davidson et al. (2022)).

Until now, we have chosen to use a dimensional representation to stress the fact that varying J and varying B is not equivalent. In the induction-less regime previously defined, we can gather our results of flow intensity using a non-dimensional representation. In the inertial regime, we can define a Reynolds number

$$Re_{\text{in}} = \left(\frac{JB}{\rho}\right)^{1/2} \frac{R^{3/2}}{\nu} \tag{3.3.11}$$

based on the velocity scale for the inertial regime (3.3.5). We define an output Reynolds number $\overline{Re} = \overline{u}R/\nu$ based on the measured velocity from the axisymmetric simulations conducted. Because we focus on the induction-less regime, we only consider the data in the range $B \in [0, 2]$ mT for the simulations with varying B. In figure 3.14 is plotted $\overline{Re}$ as a function of Re_{in}. All the data are remarkably superposed on a single curve. At high Re_{in}, we observe that $\overline{Re} \sim Re_{\text{in}}$, which confirms the inertial scaling law.

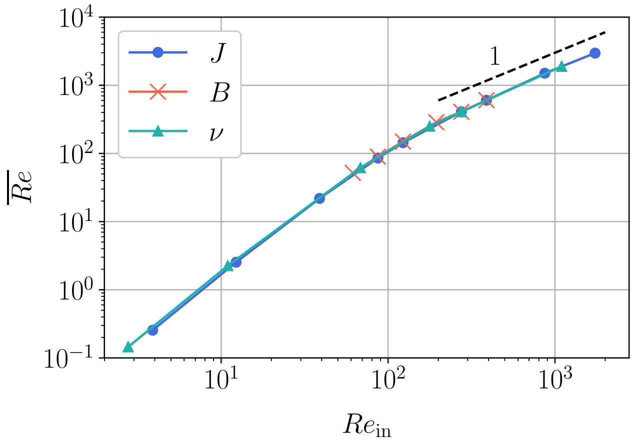

Figure 3.14 – Computed Reynolds number $\overline{Re} = \overline{u}R/\nu$ vs the input Reynolds numbers Re_{in} which is defined in (3.3.11).

3.3.6 Boundary layer

We want now to focus on the induction-less regimes, and more particularly on the boundary layer regime, in order to better understand it.

In order to characterize the transition between the three induction-less regimes, we define the velocities U_{St}, U_{BL} and U_{In} in the Stokes, the boundary layer and the inertial regime, respectively:

$$U_{\text{St}} = C_{\text{St}} \frac{JBR^2}{\rho\nu}, \quad U_{\text{BL}} = C_{\text{BL}} \left(\frac{JB}{\rho}\right)^{2/3} \frac{R}{\nu^{1/3}}, \quad U_{\text{In}} = C_{\text{In}} \left(\frac{JBR}{\rho}\right)^{1/2} \tag{3.3.12}$$

where we introduce C_{St}, C_{BL} and C_{In} which correspond to the multiplicative constants in the scaling laws. These constants are only geometrical dependent.

By looking closer to the behavior of the velocity with the current density, one can remark that the regime chosen by the system is the one which gives the lowest velocity. We show in figure 3.15a a graphical explanation, with constants C_{St}, C_{BL} and C_{In} chosen arbitrarily. This means

that the system is in the Stokes regime when $U_{\mathrm{St}} < U_{\mathrm{BL}}, U_{\mathrm{In}}$ and in the inertial regime when $U_{\mathrm{In}} < U_{\mathrm{BL}}, U_{\mathrm{St}}$. The particularity of the boundary layer regime is that it only exists when both conditions $U_{\mathrm{BL}} < U_{\mathrm{St}}$ and $U_{\mathrm{BL}} < U_{\mathrm{In}}$ are verified, i.e. when $C_{\mathrm{St}} C_{\mathrm{In}}^2 > C_{\mathrm{BL}}^3$. The existence of this regime depends thus on the geometry. In figure 3.15b is represented a case where the velocity will never be in the boundary layer regime.
This observation could be an explanation of why the boundary layer regime is not clearly visible in our simulations.

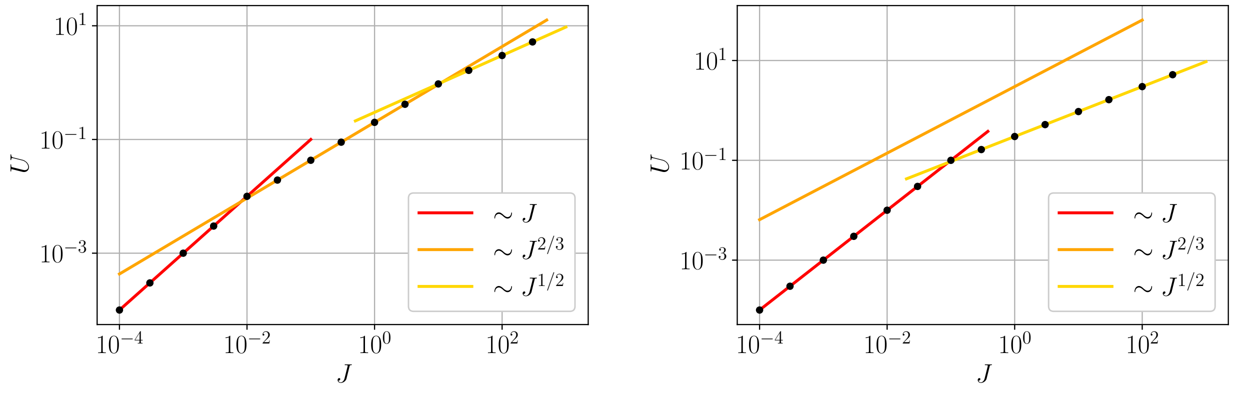

(a) (b)

Figure 3.15 – Representation of the velocity as a function of the current density with different values for the constants C_{St}, C_{BL} and C_{In}. The path followed by U when increasing J is represented by the black dots. (a) Case where all regimes are encountered. (b) Case where the boundary layer regime is not encountered.

The boundary layer regime is based on the fact that the system behavior is controlled by the flow in the boundary layer. In figure 3.16a we show the distribution of the injected power at the bottom of the cylinder for different current densities. The injected power is defined such as $P_{\mathrm{inj}} = \iiint_V (\boldsymbol{j} \times \boldsymbol{b}) \cdot \boldsymbol{u} d\tau$ and represents the power provided by the Lorentz force. It can be seen that the injected power is located really close to the electrical contact in each case, and the height of the zone where it takes its most significant values decreases with $\boldsymbol{J}$.
From the balance (3.3.9) we estimate the thickness of the boundary layer δ:

$$\delta \sim \left(\frac{\rho}{\nu B}\right) \nu^{2/3}. \tag{3.3.13}$$

For $J = 10$ A m^{-2}, we plot in figures 3.16b, 3.16c and 3.16d the toroidal and poloidal components of the velocities as well as the radial component of the vorticity, respectively, around the electrical contact and in a meridian plane. In this case, $\delta = 4$ mm. The toroidal velocity presents a bump for $r > 2$ cm close to the bottom, before becoming almost constant with z from $z = \delta$. The poloidal velocity presents the same behavior, it increases when z increases before being concentrated in a vertical column from $z = \delta$. The last figure, showing the radial vorticity, highlights that this vorticity is non-zero only in a layer with a thickness δ, i.e. in the boundary layer. All these observations confirm that δ is a relevant estimate of the thickness of this boundary layer.

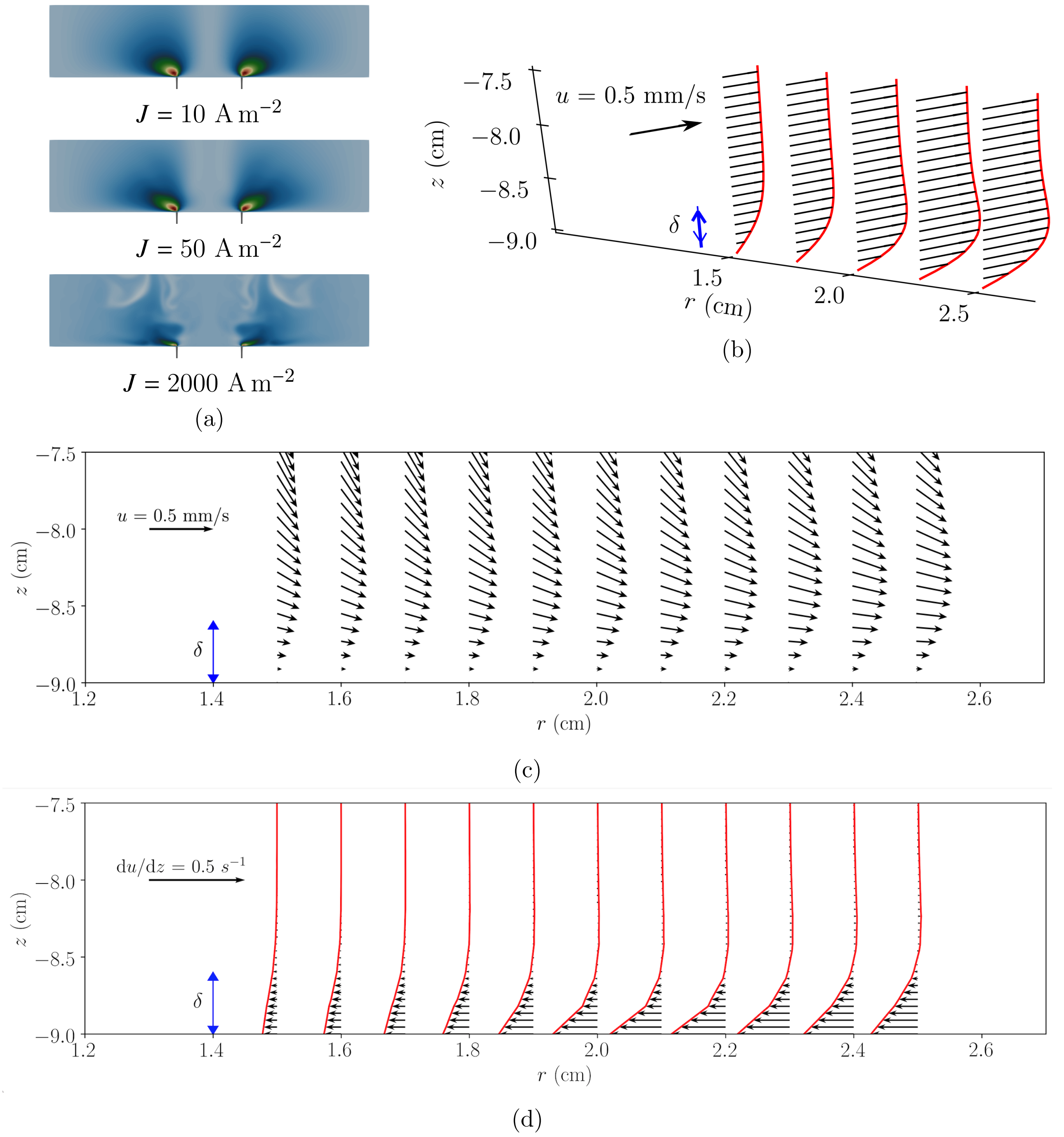

Figure 3.16 – Zoom on the flow in the bottom boundary layer. The electrical contact is at $r = 2$ cm. (a) Injected power field P_{inj} for different J, for $z \leq -4.5$ cm. The power is located close to the electrical contact and in the boundary layer. (b) Velocity u_θ in the meridian plane for $J = 10$ A m^{-2}. One can see the appearance of a bump close to the bottom when $r > 2$ cm. (c) Velocity u_{pol} in the meridian plane for $J = 10$ A m^{-2}. (d) Radial vorticity ω_r in the meridian plane for $J = 10$ A m^{-2}. The vorticity decreases with z and becomes almost zero from $z = \delta$. All of these profiles show that δ is an appropriate characteristic length for the height of the boundary layer.

3.4 Influence of the geometry

In this section, we modify the geometry of the setup and study its influence on the flow. We vary the radius of the wire and also the aspect ratio of the cylinder. We study in addition the influence of using asymmetrical wires like in Herreman et al. (2021). We fix the exterior magnetic field to 10^{-3} T and the viscosity to $3.23 \cdot 10^{-7}$ m^2 s^{-1}.

3.4.1 Influence of the wire radius R_w

We study first the impact of size of the wires' radius. We fix $R = 10$ cm, $\mathcal{H} = 18$ cm, $\mathcal{H}_w = 4$ cm, and vary R_w.
On figure 3.17a we show the velocity u as a function of time for four different ratios $R_w/R = 0.2, 0.4, 0.6, 0.8$. When R_w/R decreases, the velocity increases and the flow presents larger fluctuations. This can be also seen on the top of figure 3.17b, where we plot the time-averaged velocity $\bar{u}$ as a function of R_w/R for different current densities, between 5 and 2000 A m^{-2}. These curves have a similar behavior with R_w/R, the velocity increases when J increases and R_w/R decreases. It seems that the velocity converges to a constant when R_w/R approaches zero. The bottom of figure 3.17b shows that the evolution of $\bar{u}$ with J slightly differs when R_w/R varies, scaling laws are not identical.
The flow distribution for the different wire radii is shown on figure 3.18. We have conducted axisymmetric (top of figure 3.18) and three-dimensional simulations (bottom of figure 3.18) for four values of R_w/R. In axisymmetric simulations, there is a low-speed zone around the axis where the flow intensity is almost zero. This zone has the same width as the wires. Three-dimensional simulations give a different flow distribution. The low-speed region does not exist in three-dimensional simulations, the flow fills the whole cylinder and is more turbulent. The velocity magnitude remains equivalent in axisymmetrical and three-dimensional simulations, for the same wire radius.

We have observed that $\bar{u}$ depends on the ratio R_w/R. We now try to model this dependency. Laws are given by Bojarevics et al. (1989); Vlasyuk (1987) for non-swirling EVF, and a theoretical model has been realized by Chudnovskii (1989a). However, this model cannot be applied to swirling EVF. Thus, we determine theoretically an approximation of the torque exerted by the Lorentz force on the bottom half of the cylinder.
For this purpose, we use the torque balance of Davidson et al. (1999). We can approximate the Lorentz force by $-j_r B \boldsymbol{e}_\theta$. The axial torque balance between the Lorentz force and the viscous stress yields

$$\underbrace{\int_{\mathcal{V}} r j_r B \, dV}_{K} \approx \int_{d\mathcal{V}} r \tau_\theta \, dS. \tag{3.4.1}$$

We take $\mathcal{V}$ as the bottom half of the cylinder. If we suppose axisymmetry, Ampère's law yields $j_r \approx -\mu_0^{-1} \partial_z b_\theta$. Thus, the expression for the torque induced by the Lorentz force becomes

$$K = \frac{2\pi B}{\mu_0} \int_0^R \left(b_\theta|_{z=-\mathcal{H}/2} - b_\theta|_{z=0} \right) r^2 \, dr. \tag{3.4.2}$$

The radial integral can be numerically evaluated by using the computed values of the magnetic field. However, a theoretical approximation can also be obtained. Since we impose $\boldsymbol{j}|_{z=0} = J \boldsymbol{e}_z$ at the top of the cell, we have

$$b_\theta|_{z=0} = \frac{\mu_0 I r}{2\pi R^2}. \tag{3.4.3}$$

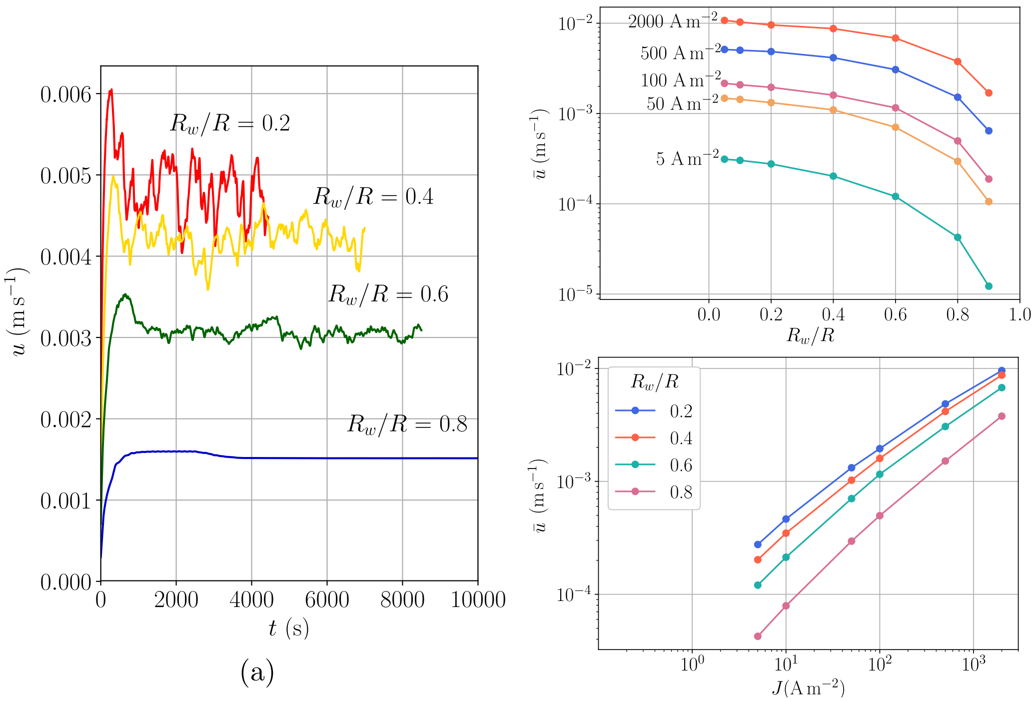

(a)

(b)

Figure 3.17 – (a) Evolution of the velocity $\boldsymbol{u}$ with time for different R_w/R and $J = 500$ A m^{-2}. (b) Time- and volume-averaged velocity $\bar{u}$ as a function of R_w/R for different J (top), as a function of J for different R_w/R (bottom).

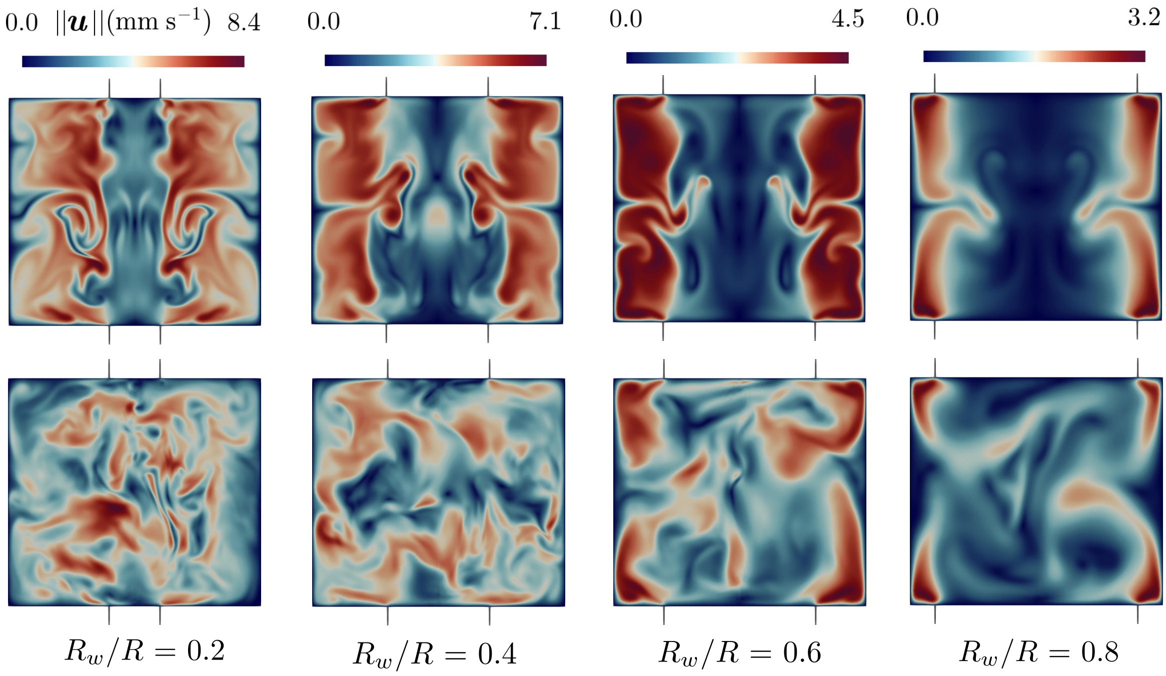

Figure 3.18 – Snapshots of the velocity distribution $\|\boldsymbol{u}\|$ for $J = 500$ A m^{-2} and different R_w/R. (top) axisymmetric simulations, (bottom) three-dimensional simulations. In axisymmetrical simulations we observe low speeds in a cylinder with radius R_w.

On the insulating part of the bottom surface, i.e. for $r \in [R_w, R]$, the magnetic field can be computed from the boundary conditions (3.2.6b). Then, using $I = J/\pi R^2$, this yields

$$\text{for } r \in [R_w, R], \quad b_\theta|_{z=-\mathcal{H}/2} = \frac{\mu_0 I}{2\pi r}. \tag{3.4.4a}$$

At the electrode-cylinder interface, i.e. for $r \in [0, R_w]$ we consider two limiting cases. Herreman et al. (2019b) have shown that the Millere approximation is well adapted if the connecting wire is very thin compared to R (see Millere et al. (1980)). Otherwise, if the connecting wire is thick, a uniform current density is a good approximation. We have then the two possible approximations:

$$\text{for } r \in [0, R_w], \quad b_\theta|_{z=-\mathcal{H}/2} = \frac{\mu_0 I}{2\pi} \begin{cases} \left(1 - \sqrt{1-(r/R_w)^2}\right)/r, & \text{(Millere)} \\ r/R_w^2, & \text{(uniform)}. \end{cases} \tag{3.4.4b}$$

We deduce two possible torques:

$$K = K_0 \begin{cases} 1 - (4R_w^2/3R^2), & \text{(Millere)} \\ 1 - R_w^2/R^2, & \text{(uniform)} \end{cases} \tag{3.4.5}$$

where $K_0 = (1/4)IBR^2$. We compare both expressions with the real torque that we can determine numerically from our simulations in figure 3.19a. For ratio R_w/R lower than 0.5, the Millere's approximation gives a good accuracy. Now that we have determined the torque, we are interested in the velocity. We do not know the dependency of the velocity with the torque, but we suppose that they are proportional:

$$U \approx U_0 \begin{cases} 1 - (4R_w^2/3R^2), & \text{(Millere)} \\ 1 - R_w^2/R^2, & \text{(uniform)}. \end{cases} \tag{3.4.6}$$

where we have chosen U_0 to be the maximum of U when $R_w/R \to 0$. It can be numerically determined by a fit of the data of figure 3.17b. We plot in figure 3.19b the quantity $\overline{u}/u_0$ as a function of R_w/R for $J > 100\,\mathrm{A\,m^{-2}}$, with the two theoretical profiles of (3.4.6). This simplistic model seems quite accurate for these current densities. Yet, for lower J, the quantity $\overline{u}/u_0$ seems to vary rather linearly with R_w/R (see Figure 3.19c) and the parabolic profile determined does not fit well the data. It would then require another model for this range of current density.

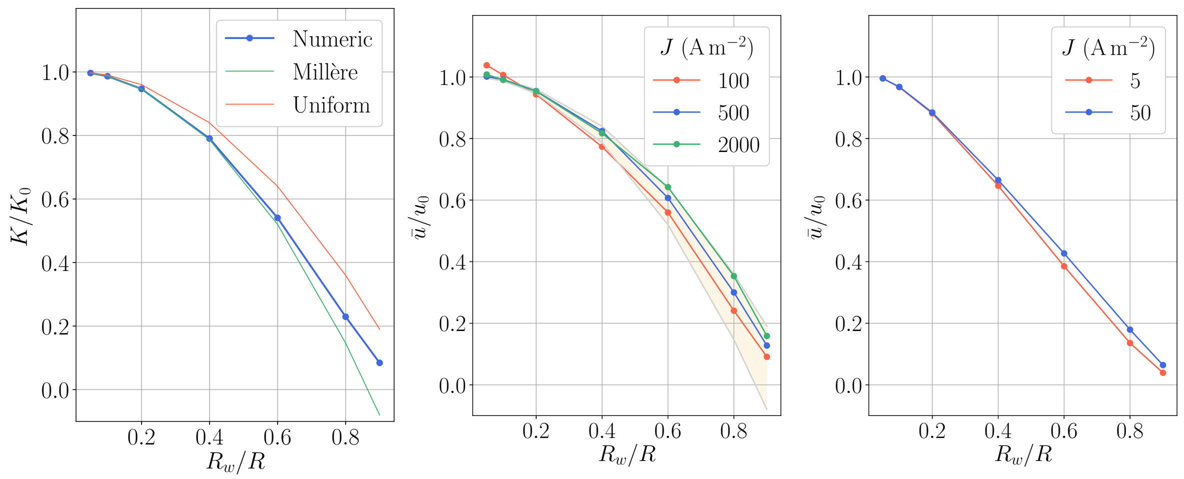

(a)

(b)

(c)

Figure 3.19 – (a) Normalized torque K/K_0 vs R_w/R. (b) Normalized velocity $\overline{u}/u_0$ vs R_w/R for high J. The orange zone corresponds to the zone between the two determined theoretical profiles, uniform and Millere. (c) Normalized velocity $\overline{u}/u_0$ for low J.

3.4.2 Influence of the height $\mathcal{H}$

We study the impact of the aspect ratio of the liquid metal domain. We fix $R = 10$ cm, $R_w = 2$ cm, $\mathcal{H}_w = 4$ cm, and vary $\mathcal{H}$.
We plot in figure 3.20a the time series of the velocity u for different aspect ratios $\mathcal{H}/R = 0.5, 1, 1.8$,and $J = 500$ A m^{-2}. This velocity increases with the aspect ratio, as well as the amplitude of the fluctuations. We present in figure 3.20b the velocities $\bar{u}$ and $\bar{u}_{\max}$ as a function of the current density for the three studied aspect ratios. We remark that $\bar{u}$ presents the same behavior for the three aspect ratios, where $\bar{u} \sim J^{1/2}$ for high current densities. However, the quantity $\bar{u}$ is computed using a volume average, then this quantity is probably not really relevant since the volume changes with the aspect ratio. This is why we show also the evolution of $\bar{u}_{\max}$ with J for the same aspect ratios. The observed behavior is significantly different, as the slope for high current densities changes with the aspect ratio. We still observe the law $\bar{u} \sim J^{1/2}$ for $\mathcal{H}/R = 1.8$ but the law is modified when $\mathcal{H}/R$ decreases. We observe rather $\bar{u} \sim J^{2/3}$ for $\mathcal{H}/R = 0.5$. This could be explained by the less turbulent flow for low aspect ratios, thus the laminar boundary layer scaling is the most accurate. Therefore, the validity of the scaling laws seems to depend on the aspect ratio.

Figure 3.21 shows the flow spatial distribution for two current densities, $J = 5$ A m^{-2} and $J = 500$ A m^{-2}, and for the three studied aspect ratios. For the lowest current density the flow is steady for each aspect ratio, and for the highest aspect ratio, the flow is turbulent. However, when $\mathcal{H}/R = 0.5$, the flow motion is concentrated close to the central vertical axis, for both current densities. This shows that the aspect ratio impacts the flow distribution in space, and also provides an explanation for the different behaviors observed between $\bar{u}$ and $\bar{u}_{\max}$, since the first quantity is influenced by the spatial distribution.

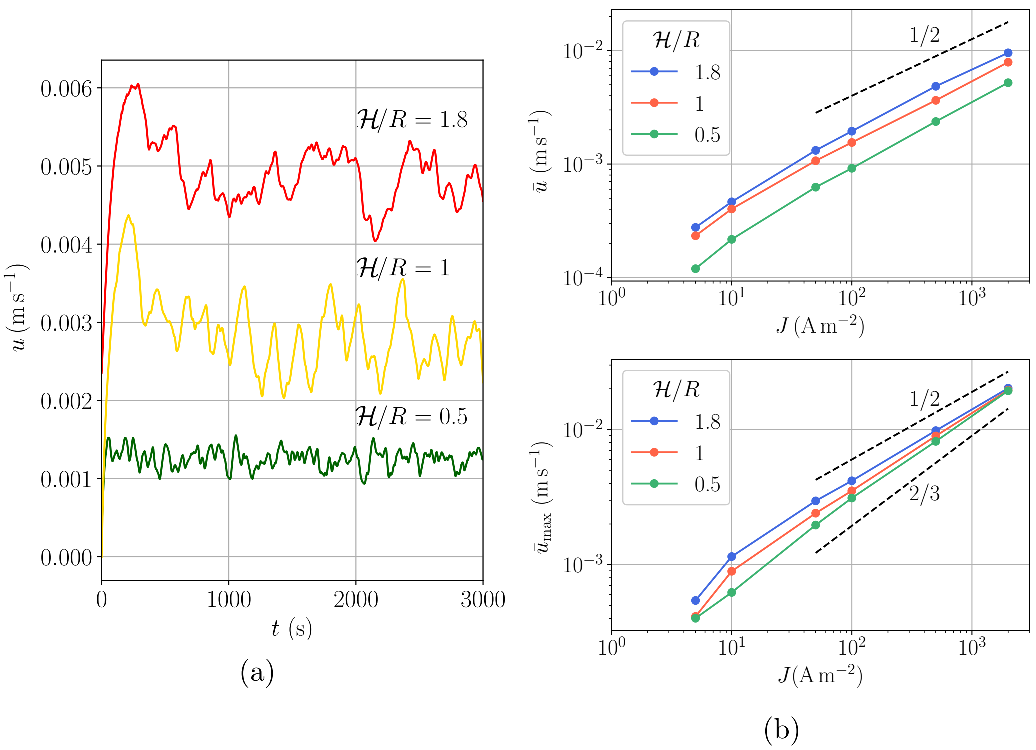

Figure 3.20 – (a) Volume-averaged velocity $\boldsymbol{u}$ for different aspect ratios and $\boldsymbol{J}$ = 500 A m^{-2}. (b) $\bar{u}$ (top) and $\bar{u}_{\max}$ (bottom) as a function of $\boldsymbol{J}$.

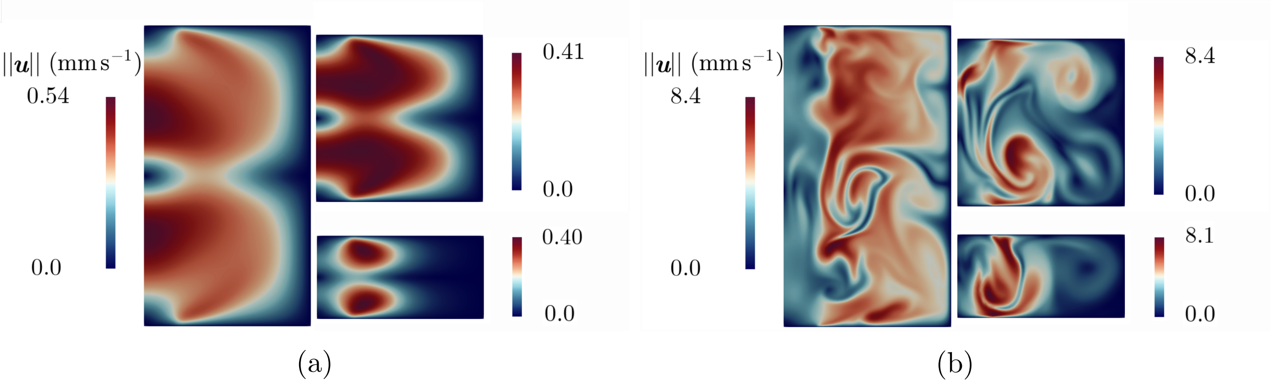

Figure 3.21 – Snapshots of $\|\boldsymbol{u}\|$ in a meridian plane for (a) $\boldsymbol{J}$ = 5 A m^{-2} and (b) $\boldsymbol{J}$ = 500 A m^{-2}.

3.4.3 Asymmetrical or symmetrical wires

In all of the previous series of simulations, the boundary layer regime was not really observable. In the study of Herreman et al. (2021), this regime was however clearly present over several decades. This is why we compare two configurations: the symmetrical configuration that we studied previously in this chapter with identical and symmetrical wires and an asymmetrical configuration like in Herreman et al. (2021), with only one wire at the bottom of the cell. We study two cells, whose radius remains R= 10 cm. The first cell is symmetrical with an aspect ratio $\mathcal{H}/R = 1$ and two symmetrical and identical wires at the top and at the bottom of the cell (figure 3.22a). In this cell, the mid-plane can be easily destabilized. The second cell is asymmetrical with an aspect ratio $\mathcal{H}/R = 0.5$, and with only one wire at the bottom (figure 3.22b). At the top of the cell, we fix no-slip boundary conditions for the velocity at the top of the cell and the current enters uniformly. The top of this cell corresponds to the mid-plane of the symmetrical cell, and the flow there is expected to be more stable. We fix $(R_w, \mathcal{H}_w) = (2, 4)$ cm in both setups. We conduct only axisymmetric simulations.

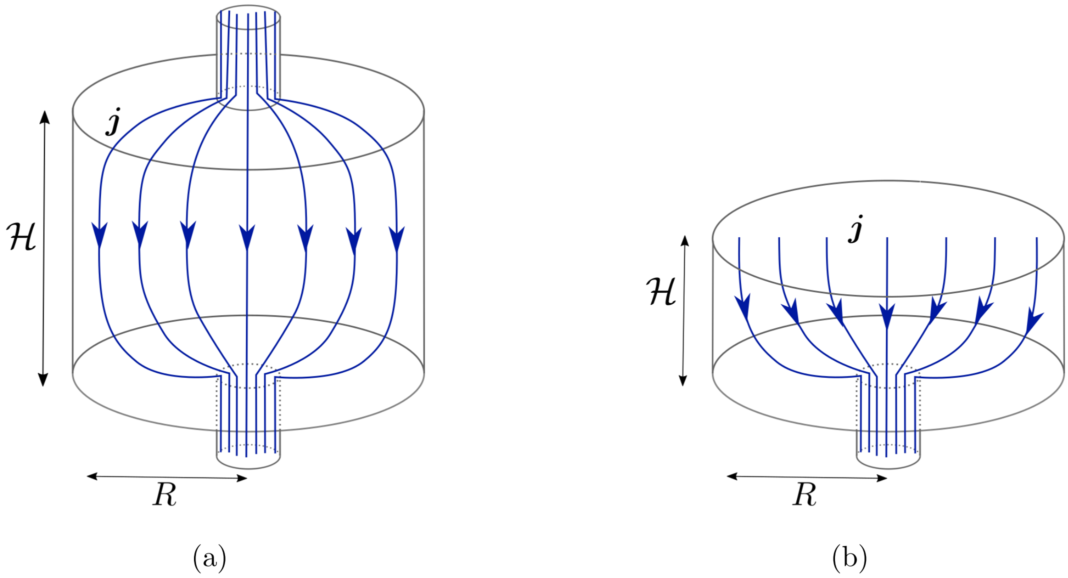

Figure 3.22 – Scheme of (a) the symmetrical and (b) the asymmetrical setups.

We show in figure 3.23a the velocity $\bar{u}$ as a function of J for both configurations. This velocity is always higher in the asymmetrical cell. We can notice that the law $\bar{u} \sim J^{1/2}$ that we can observe in the symmetrical cell does not exist in the asymmetrical cell where the law $\bar{u} \sim J^{2/3}$ is clearly visible. This is in accordance with the results of Herreman et al. (2021). Thus, the flow is really different in both configurations. The spatial distribution of the velocity can be seen in figure 3.23b for three current densities. For $J = 5$ A m^{-2}, the flow is laminar and similar in both configurations, with a slight difference near the axis where the velocity is almost zero in the asymmetrical cell. For $J = 500$ A m^{-2}, the structure is radically different: the flow is concentrated near the axis in the symmetrical cell, and fills the whole cell in the asymmetrical configuration. For $J = 500$ A m^{-2}, the flow is much more turbulent in the symmetrical configuration.

The difference between the symmetrical and asymmetrical setup can be explained by the fact that in the symmetrical cell, a mixing layer at the equatorial plane is present and is easily destabilized. This increases the level of turbulence, and highlights the fact that the laminar boundary layer regime requires a low turbulence level.

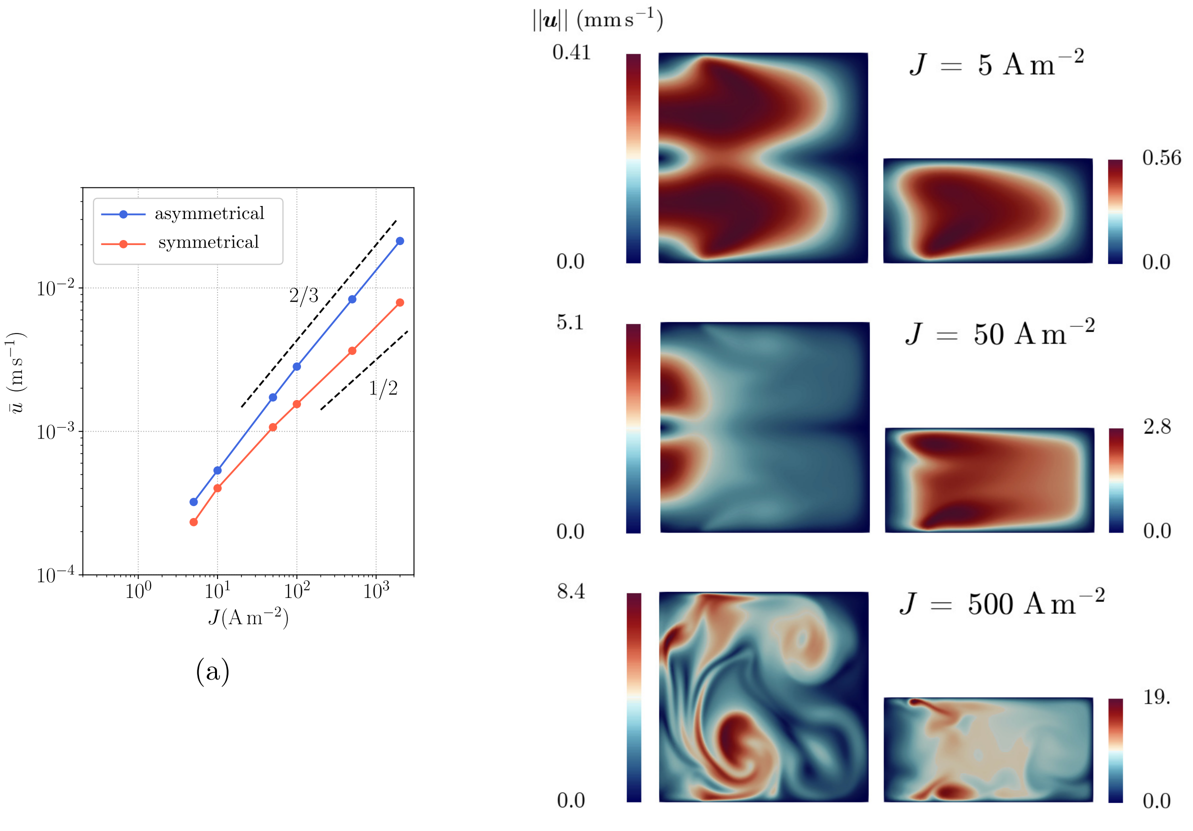

(a)

(b)

Figure 3.23 – Symmetrical and asymmetrical setups. (a) Time- and space-averaged magnitude of the velocity $\bar{u}$ as a function of J in both set-ups. (b) Snapshots of $\|\boldsymbol{u}\|$ in both setups.

3.5 Conclusion

In this chapter, we have numerically studied and characterized the swirling electrovortex flow in a cylinder filled of GaInSn liquid metal.

We have first conducted a parametric study by varying the parameters J, B and ν and by focusing on axisymmetric simulations. When varying J, we have found that, for low current densities, the flow remains steady and is mainly close to the electrical contacts. When J is above a critical value that we could determine, the flow becomes unstable and mixes the whole cell. The flow intensity U increases with J, following different regimes: $U \sim J$ for low current densities, $U \sim J^{2/3}$ for intermediate current densities and $U \sim J^{1/2}$ for high current densities. When varying B, if B remains below a critical value, the flow is turbulent and the flow intensity increases with the magnetic field following the laws $U \sim B^{2/3}$ then $U \sim B^{1/2}$ for higher B. But, when B is above a critical value, the flow decreases with B and becomes steady until it is concentrated in a line between the top and the bottom lids. In this regime, $U \sim B^{-1}$. When varying ν, we can find the following regimes, from low to high ν: $U \sim \nu^{-1/9}$ or ν^0 then $U \sim \nu^{-1}$. The parametric study has allowed us to highlight the existence of four different flow regimes:

- an inductive regime for high magnetic fields B where the induction term dominates. Here, the velocity varies like
$$U \sim \frac{J}{\sigma B},$$

- an inductive-less and viscous regime, for low velocities and large viscosities. Here, we have
$$U \sim \frac{JBR^2}{\rho \nu},$$
- an inductive-less and inertial regime, for high velocities. Here, we have
$$U \sim \left(\frac{JBR}{\rho}\right)^{1/2} \quad \text{or} \quad U \sim \left(\frac{JBR}{\rho}\right)^{5/9} \left(\frac{R}{\nu}\right)^{1/9}.$$
  There are two possible scaling laws in this regime, it is difficult to distinguish which one is the more adapted in the simulations.
- an inductive-less with laminar boundary layer, for intermediate velocities. Here, we have
$$\left(\frac{JB}{\rho}\right)^{2/3} \frac{R}{\nu^{1/3}}.$$
  This last regime was barely visible in the simulations.

We have then investigated how the geometry influences the flow intensity. When varying the radius of the wire R_w, we remark that the velocity increases when R_w/R decreases. It is quite difficult to model theoretically the variation of the velocity U with R_w/R, but we have proposed two possible scaling laws, depending of the way we model the interface conditions at the cylinder-wire interfaces. Surprisingly, these simplistic theoretical laws are quite accurate at high enough current densities. When varying the aspect ratio $\mathcal{H}/R$ of the cylinder, we have found that the smaller the aspect ratio is, the more the flow is concentrated in a small region close to the axis. For low aspect ratio, the flow is rather situated in the boundary layer regime, and for high aspect ratios, the inertial regime is the most accurate.

We compared an asymmetrical and a symmetrical cell, as represented in figure 3.22. We have shown that the flow is much less turbulent when the cell is asymmetric, and that the boundary layer regime is clearly visible in this case, contrary to the symmetrical cell, where we rather observe an inertial regime.

We have run three-dimensional simulations in the study of the parameter J. We have observed several bifurcations between different regimes. We have been able to determine the threshold of the first bifurcation. In the regime where the flow is three-dimensional and steady, this counter-rotating EVF is von Kármán like. We can therefore use electrodes to drive von Kármán flows without impellers.

When we compare axisymmetric with three-dimensional simulations, we have noticed that the spatial distribution of the flow can be significantly different. Yet, the mean velocity keeps in both cases the same order of magnitude. Thus, when one is only interested in the velocity intensity of the flow, axisymmetric simulations can be a good approximation. In addition, we retrieve the inertial regime in three-dimensional simulations, but the boundary layer regime is not visible at all.

In order to conclude on the boundary layer regime, this regime is not really observable in symmetrical setups. However, it seems to exist when the flow is not too turbulent, which is the case in the asymmetrical cell for instance. We suppose that the boundary layer regime requires a laminar boundary layer, and cannot be observed when the turbulence is too intense.

A perspective of this work would be the investigation of the transition between the boundary layer regime to the inertial regime. More particularly, it would be interesting to examine the structure of the boundary layer in order to understand the transition to turbulence in this layer. We could also extend this work to other types of geometries, such as an hemispherical setup.

Chapter 4

Modeling discontinuous electrical potential distributions with a magnetic field formulation

In this chapter, we present the work published in the article Bénard et al. (2023) in Comptes Rendus. Mécanique *in April 2023.*

4.1 Introduction

As said in chapter 1, variations of potential exist at the alloy-electrolyte interface in LMBs, due to the formation of an electrochemical double layer. These variations can be modeled by a jump in electrical potential on a macroscopic scale (Lück and Latz, 2016; Weber et al., 2019). The impact of this potential jump has not been well investigated: only a few studies focused on LMBs model this jump, and none of them gives information on the specific effect of this jump on the mixing process and on the cell potential. In this chapter, we improve our model for the LMB interior by considering this jump in electrical potential, and we will study how the electrical current and concentration distribution are affected.
As explained by Weber et al. (2019), there is a potential jump at each interface. The value of each of these jumps is not easy to determine and depends on the activity of the chemical components. The simplified model used by Weber et al. (2019) considers only one jump at the alloy-electrolyte interface, that varies locally with the composition of the alloy along the interface. Their numerical results were in accordance with experiments. Moreover, the lithium remains pure in the foam, no change in composition occurs at the foam-electrolyte interface. Therefore, the jump at the upper interface has likely no impact on the electrical current distribution. Because this model is quite simple, we have chosen it to perform our study.

The model used by Weber et al. (2019) is based on finite volumes and solves the electrical problem:

$$-\boldsymbol{\nabla}\cdot(\sigma\boldsymbol{\nabla}\varphi) \quad , \qquad \text{in all domains,} \tag{4.1.1a}$$

$$\varphi_{\text{alloy}} - \varphi_{\text{electrolyte}} = \varphi_{\text{jump}} \quad \text{at the alloy-electrolyte interface} \tag{4.1.1b}$$

where σ is the electrical conductivity of the domain and φ the electrical potential in the domain. Equation (4.1.1b) represents the imposition of the jump at the interface. Our goal is to implement this electrical problem in our solver, and more particularly the potential jump condition. However, the code SFEMaNS that we use to conduct our numerical studies is based on a magnetic field formulation, the electrical potential field is not explicitly available. Hence, how can we impose a discontinuity in the electrical potential at an interface without the potential variable φ?

In order to tackle this problem, two ideas emerge. The first idea is simply to develop a new numerical solver for the electrical problem, defined by equations (4.1.1a)-(4.1.1b). This solver can be used to solve the diffusion and electrical problems. However, we cannot use this solver to study EVF like in chapter 2: the Lorentz force term requires to know the magnetic field. This magnetic field can be computed by using Biot-Savart's law, as in the model of Weber et al. (2020), but the numerical development and evolution of this law are complex. A second idea is to provide an alternative magnetic field formulation. We then need to find an interface condition based on the magnetic field that is equivalent to the potential jump condition. In the existing code, we then need to program this new condition.

In this chapter, we first give details about meridional and azimuthal decomposition in the code SFEMaNS. Then we focus on the formulation in electrical potential by describing the electrical problem, the numerical developments realized and we validate our solver, denoted φ-solver. Later, we present the new magnetic field formulation and the new interface condition, by describing the equivalent magnetic problem, the numerical developments realized and we validate our solver, denoted $\boldsymbol{H}$-solver. Finally, we show that both formulations are indeed equivalent by comparing both solvers in different geometries.
We solve neither the concentration nor the velocity, we only focus on the electrical and magnetic problems. When not precised, the quantities in this chapter are non-dimensionalized.

4.2 Spectral and meridional decomposition in the numerical code SFEMaNS

In SFEMaNS, the numerical resolution is based on a hybrid decomposition of the fields. Each field is decomposed according to a spectral representation in the azimuthal direction and a finite element representation in the meridian plane. The geometry being axisymmetric, the cylindrical coordinates (r, θ, z) are always used.

For the spectral decomposition, a scalar field $\mathcal{A}(r, \theta, z)$ can be approximated by the following form

$$\mathcal{A}(r, \theta, z) \simeq \sum_{m=0}^{M-1} \mathcal{A}_h^{m,c}(r, z) \cos(m\theta) + \sum_{m=1}^{M-1} \mathcal{A}_h^{m,s}(r, z) \sin(m\theta). \tag{4.2.1}$$

$M \in \mathbb{N}$ is the number of Fourier modes used. The fields $\mathcal{A}_h^m$ only depend on r and z and must be now decomposed in the meridian plane.

We introduce the meridian section Ω^{2D} of a cylindrical domain Ω. Ω^{2D} is decomposed in non-overlapping triangles whose maximal size is denoted h. An example of a mesh can be seen in figure 4.1. A transformation is applied on each triangle to straighten this triangle in order to deal only with canonical triangles. The scalar fields $\mathcal{A}_h^{m,c}(r, z)$ and $\mathcal{A}_h^{m,s}(r, z)$ are approximated on nodes associated to the triangles by using polynomial decomposition with a degree n, which indicates the precision of the approximation. We say then that we use $\mathbb{P}_n$ finite elements (see figure 4.2). For example, the pressure is approximated on $\mathbb{P}_1$ finite elements, contrary to the velocity and the magnetic field which use $\mathbb{P}_2$ finite elements.

We denote N the number of nodes. We define a base of functions $(\psi_j)_{1 \leq j \leq N}$ adapted to the

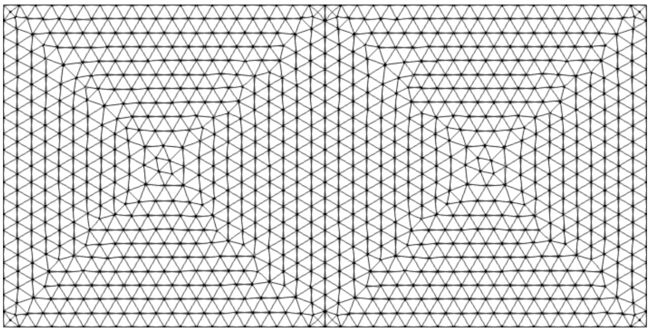

Figure 4.1 – Example of a mesh decomposed in finite elements. The domain has a height of 0.5 and a length of 1. The maximal size of the triangles is 0.025.

(a) (b)

Figure 4.2 – Nodes of a canonical triangle for different degrees of precision. (a) Element $\mathbb{P}_1$. (b) Element $\mathbb{P}_2$

mesh, which are chosen as Lagrange polynomials. Thus, $\mathcal{A}_h^{m,c}(r,z)$ can be decomposed on the base at a node x_i such as

$$\mathcal{A}_h^{m,c}(x_i) = \sum_{j=1}^{N} a_j \psi_j(x_i) \tag{4.2.2}$$

where a_j are coefficients. We can define a similar decomposition for $\mathcal{A}_h^{m,s}(r,z)$.

For vectorial fields, each component is approximated in the same way as a scalar field. For more details about finite element decomposition, see Ern and Guermond (2004).

4.3 Electrical potential φ formulation

In this section, we present the model of a jump of electrical potential on an interface using the potential variable φ. We implement the weak formulation in the code SFEMaNS and validate it by using a comparison with analytical solutions.

4.3.1 Problem description

We consider a cylindrical domain $\mathbf{\Omega}$, separated in two sub-domains $\mathbf{\Omega}_1$ and $\mathbf{\Omega}_2$. We denote its boundary $\Gamma = \partial\Omega$, and the interface between the domains Σ. We use a system of cylindrical coordinates. A sketch of the studied domain is shown in figure 4.3. The radius of the cylinder is R, the vertical coordinates of the bottom and top of the cylinder are z_0 and z_2, and the one of the interface z_1. We set $R = 0.5$, $z_0 = 0$, $z_1 = 0.5$, and $z_2 = 1$. The outward normal to a surface will be denoted $\boldsymbol{n}$.

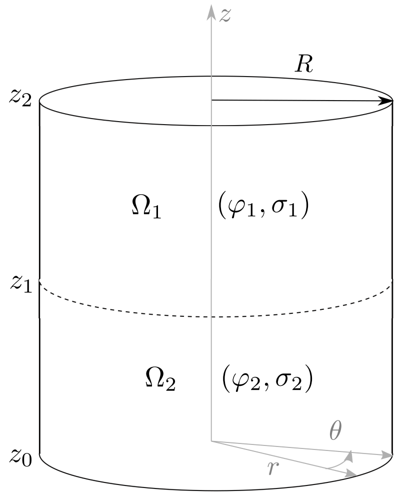

Figure 4.3 – Sketch of the cylindrical domain used for numerical investigations.

The electrical potential φ is solution, in each subdomain, of the equation $-\boldsymbol{\nabla} \cdot (\sigma \boldsymbol{\nabla} \varphi) = 0$, where σ is the electrical conductivity. On the interface, the normal component of the electrical current, equal to $-\sigma \boldsymbol{\nabla} \varphi \cdot \boldsymbol{n}$, is continuous. By denoting φ_1 and φ_2 the potential in the subdomains $\boldsymbol{\Omega}_1$ and $\boldsymbol{\Omega}_2$, respectively, and σ_1 and σ_2 the corresponding conductivities, this leads to $(\sigma_1 \boldsymbol{\nabla} \varphi_1 - \sigma_2 \boldsymbol{\nabla} \varphi_2) \cdot \boldsymbol{n} = 0$. We introduce a jump in potential φ_{jump} at the interface. We impose Dirichlet boundary conditions at the top and at the bottom of the cylinder ($\boldsymbol{\Gamma}_D$), and Neumann boundary conditions at the lateral border ($\boldsymbol{\Gamma}_N$), such as $\boldsymbol{\nabla} \varphi \cdot \boldsymbol{n} = 0$. The function for the Dirichlet boundary conditions is denoted g_D.

The final problem to solve is hence

$$-\boldsymbol{\nabla} \cdot (\sigma \boldsymbol{\nabla} \varphi) = 0 \qquad \text{in } \boldsymbol{\Omega}_1 \text{ and } \boldsymbol{\Omega}_2, \tag{4.3.1a}$$

$$\varphi_1 - \varphi_2 = \varphi_{\text{jump}} \qquad \text{on } \Sigma, \tag{4.3.1b}$$

$$(\sigma_1 \boldsymbol{\nabla} \varphi_1 - \sigma_2 \boldsymbol{\nabla} \varphi_2) \cdot \boldsymbol{n} = 0 \qquad \text{on } \Sigma. \tag{4.3.1c}$$

$$\varphi = g_D \quad \text{on } \boldsymbol{\Gamma}_D \qquad \text{and} \qquad \boldsymbol{\nabla} \varphi \cdot \boldsymbol{n} = 0 \quad \text{on } \boldsymbol{\Gamma}_N. \tag{4.3.1d}$$

4.3.2 Weak formulation

General weak formulation

The Dirichlet boundary conditions of (4.3.1d) are imposed strongly, and do not appear in the weak formulation. We determine the weak formulation for homogeneous Dirichlet boundary conditions, i.e. $g_D = 0$. We will see later how inhomogeneous boundary conditions are numerically applied.

The electrical potential φ is solution of the equation $-\boldsymbol{\nabla} \cdot (\sigma \boldsymbol{\nabla} \varphi) = 0$. We denote ψ the test functions. φ and ψ are in $L^2(\Omega)$ and continuous on each subdomain $\boldsymbol{\Omega}_i$. We have, for all ψ, on the domain $\boldsymbol{\Omega}_i$:

$$\begin{aligned} \int_{\Omega_i} -\boldsymbol{\nabla}\cdot(\sigma\boldsymbol{\nabla}\varphi)\psi &= 0 \\ \Longleftrightarrow \int_{\Omega_i} \boldsymbol{\nabla}\psi\cdot(\sigma\boldsymbol{\nabla}\varphi) - \int_{\Omega_i} \boldsymbol{\nabla}\cdot(\sigma\boldsymbol{\nabla}\varphi\,\psi) &= 0 \\ \Longleftrightarrow \int_{\Omega_i} \boldsymbol{\nabla}\psi\cdot(\sigma\boldsymbol{\nabla}\varphi) - \int_{\partial\Omega_i} \psi(\boldsymbol{n}\cdot\sigma\boldsymbol{\nabla}\varphi) &= 0. \end{aligned} \tag{4.3.2}$$

We sum (4.3.2) on $\boldsymbol{\Omega}$:

$$\int_{\Omega_1}\boldsymbol{\nabla}\psi\cdot(\sigma\boldsymbol{\nabla}\varphi)+\int_{\Omega_2}\boldsymbol{\nabla}\psi\cdot(\sigma\boldsymbol{\nabla}\varphi)-\int_{\Gamma_N}\psi(\boldsymbol{n}\cdot\sigma\boldsymbol{\nabla}\varphi)\;-\int_{\Sigma}(\psi_1(\boldsymbol{n}_1\cdot\sigma_1\boldsymbol{\nabla}\varphi_1)+\psi_2(\boldsymbol{n}_2\cdot\sigma_2\boldsymbol{\nabla}\varphi_2)) = 0 \tag{4.3.3}$$

where $\boldsymbol{n}_1$ and $\boldsymbol{n}_2$ are the outward normal to Σ relatively to $\boldsymbol{\Omega}_1$ and $\boldsymbol{\Omega}_2$. $\boldsymbol{n}$ is the outward normal to Σ such as $\boldsymbol{n}=\boldsymbol{n}_1$ and $\boldsymbol{n}=-\boldsymbol{n}_2$.
Because of the Neumann boundary condition (4.3.1d), $\psi(\boldsymbol{n}\cdot\sigma\boldsymbol{\nabla}\varphi)=0$ on Γ_N. We impose this boundary condition strongly, by directly setting $\int_{\Gamma_N}\psi(\boldsymbol{n}\cdot\sigma\boldsymbol{\nabla}\varphi)=0$.
We introduce the notations $[w]=w_1-w_2$ and $\{w\}=\frac{1}{2}(w_1+w_2)$.
We have

$$\psi_1(\boldsymbol{n}_1\cdot\sigma_1\boldsymbol{\nabla}\varphi_1)+\psi_2(\boldsymbol{n}_2\cdot\sigma_2\boldsymbol{\nabla}\varphi_2) = \psi_1(\boldsymbol{n}\cdot\sigma_1\boldsymbol{\nabla}\varphi_1)-\psi_2(\boldsymbol{n}\cdot\sigma_2\boldsymbol{\nabla}\varphi_2) = [\psi(\boldsymbol{n}\cdot\sigma\boldsymbol{\nabla}\varphi)],$$

and

$$[\psi(\boldsymbol{n}\cdot\sigma\boldsymbol{\nabla}\varphi)] = \{\boldsymbol{n}\cdot\sigma\boldsymbol{\nabla}\varphi\}[\psi]+[\boldsymbol{n}\cdot\sigma\boldsymbol{\nabla}\varphi]\{\psi\}.$$

However $[\boldsymbol{n}\cdot\sigma\boldsymbol{\nabla}\varphi]=(\sigma_1\boldsymbol{\nabla}\varphi_1-\sigma_2\boldsymbol{\nabla}\varphi_2)\cdot\boldsymbol{n}=0$ from (4.3.1c). Thus (4.3.3) leads to

$$\int_{\Omega_1}\boldsymbol{\nabla}\psi\cdot(\sigma\boldsymbol{\nabla}\varphi)+\int_{\Omega_2}\boldsymbol{\nabla}\psi\cdot(\sigma\boldsymbol{\nabla}\varphi)-\int_{\Sigma}\{\boldsymbol{n}\cdot\sigma\boldsymbol{\nabla}\varphi\}[\psi] = 0$$

which can be rewritten

$$\int_{\Omega_1}\boldsymbol{\nabla}\psi\cdot(\sigma\boldsymbol{\nabla}\varphi)\;+\;\int_{\Omega_2}\boldsymbol{\nabla}\psi\cdot(\sigma\boldsymbol{\nabla}\varphi)-\int_{\Sigma}\frac{1}{2}(\boldsymbol{n}_1\cdot\sigma_1\boldsymbol{\nabla}\varphi_1-\boldsymbol{n}_2\cdot\sigma_2\boldsymbol{\nabla}\varphi_2)\;(\psi_1-\psi_2) = 0. \tag{4.3.4}$$

In order to impose the jump at the interface Σ, i.e. equation (4.3.1b), we have to use a penalization term

$$c\int_{\Sigma}\frac{1}{h}(\varphi_1-\varphi_2)(\psi_1-\psi_2) = c\int_{\Sigma}\frac{1}{h}\varphi_{\text{jump}}(\psi_1-\psi_2) \tag{4.3.5}$$

where c is a constant which will be set to one. We remark that this jump is imposed weakly, which means that it is enforced in the weak formulation, unlike the boundary conditions.
All of this yields the following weak formulation

$$\begin{aligned} \int_{\Omega_1}\boldsymbol{\nabla}\psi\cdot(\sigma\boldsymbol{\nabla}\varphi)\;+\;\int_{\Omega_2}\boldsymbol{\nabla}\psi\cdot(\sigma\boldsymbol{\nabla}\varphi)-\int_{\Sigma}\frac{1}{2}(\boldsymbol{n}_1\cdot\sigma_1\boldsymbol{\nabla}\varphi_1-\boldsymbol{n}_2\cdot\sigma_2\boldsymbol{\nabla}\varphi_2)\;(\psi_1-\psi_2) \\ +\;c\int_{\Sigma}\frac{1}{h}(\varphi_1-\varphi_2)(\psi_1-\psi_2) = c\int_{\Sigma}\frac{1}{h}\varphi_{\text{jump}}(\psi_1-\psi_2). \end{aligned} \tag{4.3.6}$$

Weights

When electrical conductivities σ are very different, some of the terms of the weak formulation have to be balanced with weights (Ern and Guermond, 2021; Ern et al., 2009). We introduce the weights

$$\lambda = \frac{2\sigma_1\sigma_2}{\sigma_1+\sigma_2}, \quad \omega_1 = \frac{\sigma_2}{\sigma_1+\sigma_2}, \quad \omega_2 = \frac{\sigma_1}{\sigma_1+\sigma_2}. \tag{4.3.7}$$

The weak formulation (4.3.6) becomes hence

$$\begin{aligned}\int_{\Omega_1} \nabla\psi\cdot(\sigma\nabla\varphi) \ + \int_{\Omega_2} \nabla\psi\cdot(\sigma\nabla\varphi) - \int_{\Sigma}(\omega_1\boldsymbol{n}_1\cdot\sigma_1\nabla\varphi_1 - \omega_2\boldsymbol{n}_2\cdot\sigma_2\nabla\varphi_2)\ (\psi_1-\psi_2) \\ + c\int_{\Sigma}\frac{\lambda}{h}(\varphi_1-\varphi_2)(\psi_1-\psi_2) \ = \ c\int_{\Sigma}\frac{\lambda}{h}\varphi_{\text{jump}}(\psi_1-\psi_2).\end{aligned} \tag{4.3.8}$$

Numerics

We implement this weak formulation in the code SFEMaNS by introducing a new variable φ in the code. We present now how (4.3.8) is solved.
For each mode m, we denote for more simplicity φ_h the cosinus part of this mode. The process is the same for the sinus part. As said in section §4.2, we can write

$$\varphi_h(x_i) = \sum_{j=1}^{N} a_j\psi_j(x_i) \tag{4.3.9}$$

where x_i is a node. The coefficients a_j are unknown. We solve equation (4.3.8) for all $1 \le j \le N$, by replacing the test function ψ by ψ_j. This yields a linear system of N equations of the form $AX = B$, where A and B are known matrice and vector respectively and X is the unknown vector. This system is then solved numerically.

When inhomogeneous boundary conditions are imposed, like in our problem in equation (4.3.1d) where we impose $\varphi = g_D$, they are enforced strongly. The function g_D can be decomposed on the base: $g_D = \sum_{j=1}^{N} g_{D,j}\,\psi_j$. On each node of Γ_D, we have $a_j = g_{D,j}$. Thus in the linear system, we add for the nodes on Γ_D the condition $a_j = g_{D,j}$.

Solving the weak formulation (4.3.8) requires to solve many integrals. The Gauss quadrature is used to compute these integrals. The principle is to approximate the integral by the value of the function at certain points, called Gauss points. We denote l_G the number of Gauss points. An integral on a canonical triangle $\hat{K}$ is approximated by

$$\int_{\hat{K}} \varphi_h(r,z)drdz \ = \ \sum_{l=1}^{l_G} \hat{\omega}_l\varphi_h(\hat{x}_l) \tag{4.3.10}$$

where $\hat{\omega}_l$ are called the Gauss weights, and $(\hat{x}_l)$ are the Gauss points. The weights depend on the point considered and on the mesh we use.

4.3.3 Determination of analytical solutions

In order to validate the numerical solutions, we give as boundary conditions and initial condition a known solution of the problem. We are then expecting that the solver retrieves this solution. We can determine solutions of the problem by calculating analytical solutions. We are then looking for analytical solutions of the problem (4.3.1), before comparing them with numerical solutions.

Analytical solutions with $\varphi_{\text{jump}} = 0$

We are looking first for solutions of the equation $-\boldsymbol{\nabla}\cdot(\sigma\boldsymbol{\nabla}\varphi) = 0$ (4.3.1a). In a single domain with σ constant, this equation is equivalent to $\nabla^2\varphi = 0$, i.e.

$$\frac{\partial^2\varphi}{\partial r^2} + \frac{1}{r}\frac{\partial\varphi}{\partial r} + \frac{1}{r^2}\frac{\partial^2\varphi}{\partial\theta^2} + \frac{\partial^2\varphi}{\partial z^2} = 0. \tag{4.3.11}$$

There are solutions depending only on z, which take the form $\varphi = az+b$ with a and b constants.

We are now looking for more complex solutions that also depend on r and θ to test all the terms of this new formulation. We take an analytical solution with separable variables such as $\varphi(r,\theta,z) = \mathcal{R}(r)\Theta(\theta)\mathcal{Z}(z)$, where $\mathcal{R}$, Θ, and $\mathcal{Z}$ are functions. This yields, $\forall r,\theta,z$

$$\begin{aligned}
\mathcal{R}''(r)\Theta(\theta)\mathcal{Z}(z) + \frac{1}{r}\mathcal{R}'(r)\Theta(\theta)\mathcal{Z}(z) + \frac{1}{r^2}\mathcal{R}(r)\Theta''(\theta)\mathcal{Z}(z) + \mathcal{R}(r)\Theta(\theta)\mathcal{Z}''(z) &= 0.\\
\iff \mathcal{R}''(r) + \frac{1}{r}\mathcal{R}'(r) + \frac{1}{r^2}\mathcal{R}(r)\frac{\Theta''(\theta)}{\Theta(\theta)} + \mathcal{R}(r)\frac{\mathcal{Z}''(z)}{\mathcal{Z}(z)} &= 0.
\end{aligned}$$

We denote $\frac{\Theta''(\theta)}{\Theta(\theta)} = -m^2$ and $\frac{\mathcal{Z}''(z)}{\mathcal{Z}(z)} = k^2$ where m is an integer and k a real number. Hence

$$\mathcal{R}''(r) + \frac{1}{r}\mathcal{R}'(r) + \frac{m^2}{r^2}\mathcal{R}(r) + k^2\,\mathcal{R}(r) = 0, \tag{4.3.13a}$$

$$\Theta''(\theta) + m^2\,\Theta(\theta) = 0, \tag{4.3.13b}$$

$$\mathcal{Z}''(z) - k^2\,\mathcal{Z}(z) = 0. \tag{4.3.13c}$$

Because of the cylindrical shape of the domain, the function Θ is necessarily periodic, i.e. $m^2 > 0$, and the solutions of (4.3.13b) take the form $\Theta(\theta) = e^{\pm im\theta}$.
We choose $k^2 > 0$ so that the solutions of (4.3.13c) are non-periodic: $\mathcal{Z}(z) = e^{\pm kz}$.
For the equation (4.3.13a), the solutions are Bessel functions $\mathcal{R}(r) = J_m(kr)$.
Thus, the solutions of equation (4.3.11) are

$$\varphi(r,z,\theta) = e^{im\theta}J_m(kr)\;e^{\pm kz}. \tag{4.3.14}$$

The integer m corresponds to the mode we choose for the following numerical tests.

Moreover, the Neumann boundary condition (4.3.1d) $\boldsymbol{\nabla}\varphi\cdot\boldsymbol{n} = 0$ on the lateral border has to be verified. We must choose k such that, for a given m, $J'_m(kR) = 0$. Thus we can take $k = \kappa'_{m1}/R$, where κ'_{m1} is the first zero of J'_m. Every linear combination of $e^{\pm kz}$ is a solution of (4.3.13c), we can use the functions sinh and cosh to impose the chosen Dirichlet boundary conditions at the top and at the bottom of the cylinder.

Analytical solutions with $\varphi_{\text{jump}} \neq 0$

In a case with a non-zero jump in electrical potential, the solutions take the same form as the ones in the last paragraph with $\varphi_{\text{jump}} = 0$ in $\boldsymbol{\Omega}_1$ and $\boldsymbol{\Omega}_2$. At the interface Σ, equations (4.3.1b) and (4.3.1c) have to be also verified.
For a solution depending only on z, analytical solutions of the problem can be written as:

$$\begin{aligned} \varphi_1(z) &= az+b, && \text{for } z \leq z_1, \\ \varphi_2(z) &= dz+e, && \text{for } z > z_1. \end{aligned} \tag{4.3.15}$$

d must be equal to $(\sigma_1/\sigma_2)a$ to verify (4.3.1c). The other constants should be chosen so that $\varphi_{\text{jump}} = (\varphi_1(z) - \varphi_2(z))_{|z=z_1} = (a-d)z_1 + (b-e)$ is non zero (equation (4.3.1b)).
For a solution depending also on r and θ, the analytical solutions take the form

$$\begin{aligned} \varphi_1(r,z,\theta) &= e^{im\theta}\ J_m(kr)\ e^{\pm kz}, z \leq z_1 \\ \varphi_2(r,z,\theta) &= (\sigma_1/\sigma_2)\ e^{im\theta}\ J_m(kr)\ e^{\pm kz}, z > z_1. \end{aligned} \tag{4.3.16}$$

Here, $\varphi_{\text{jump}} = (1-\sigma_1/\sigma_2)e^{im\theta}\ J_m(kr)\ e^{\pm kz}$, which is non zero at $z = z_1$.

4.3.4 Numerical investigations

In this section we validate our solver in the domain $\boldsymbol{\Omega}$ defined in section §4.3.1 by comparing the numerical solutions with analytical solutions found in section §4.3.3. The tests are done for a solution depending only on z and then for solutions depending on r and θ too, with different Fourier modes (m= 0,1 or 2), in two cases, first without a jump (single domain) and then with a jump on the interface Σ. The values of κ'_{m1} are in these cases $\kappa'_{01} = 3.8317059702, \kappa'_{11} = 1.841183781200789, \kappa'_{21} = 3.054236935206724$. We define the relative error in L^2-norm of φ

$$\xi_\varphi = \frac{\|\varphi_{\text{num}} - \varphi_{\text{ex}}\|_2}{\|\varphi_{\text{ex}}\|_2}, \tag{4.3.17}$$

where φ_{num} is the numerical solution and φ_{ex} the analytical solution. This error is expected to vary like $O(h^3)$, where h is the mesh size, because $\mathbb{P}_2$ finite elements are used (Brenner and Scott, 2008; Ern and Guermond, 2004).

Tests without jump

The first set of tests is done for a case with no interface and then no jump. The electrical conductivity is $\sigma = 1$. We run the following tests:

- **Test 0** (mode $m = 0$, variable z only) :
  $\varphi_{\text{ex}}(z) = \ az + b$ with $a = 5/(z_2 - z_0)$, $\beta = 5 - z_2 a$, as imposed by (4.3.14) and so that $\varphi_{\text{ex}}(z = z_0) = 0$.
- **Test 1** (mode $m = 0$) :
  $\varphi_{\text{ex}}(r,z) = J_0(kr)\sinh(k(z+z_0))$ with $k = \kappa'_{01}/R$.
- **Test 2** (mode $m = 1$) :
  $\varphi_{\text{ex}}(r,z,\theta) = e^{i\theta}\ J_1(kr)\sinh(k(z+z_0))$ with $k = \kappa'_{11}/R$.
- **Test 3** (mode $m = 2$) :
  $\varphi_{\text{ex}}(r,z,\theta) = e^{2i\theta}\ J_2(kr)\cosh(k(z-z_2))$ with $k = \kappa'_{21}/R$.

We report the relative error ξ_φ in table 4.1.
For test 0, ξ_φ is really low and almost equal to the zero-machine, which is an expected result for a linear solution. For the other tests, the error varies like $O(h^3)$, which can also be seen in figure 4.4. These results validate the numerical solver.

h	Test 0	Test 1	Test 2	Test 3
0.1	$1.29 \cdot 10^{-15}$	$6.12 \cdot 10^{-4}$	$5.21 \cdot 10^{-5}$	$2.58 \cdot 10^{-4}$
0.05	$2.20 \cdot 10^{-15}$	$5.87 \cdot 10^{-5}$	$4.55 \cdot 10^{-6}$	$1.77 \cdot 10^{-5}$
0.025	$1.77 \cdot 10^{-15}$	$5.06 \cdot 10^{-6}$	$4.11 \cdot 10^{-7}$	$1.70 \cdot 10^{-6}$
0.0125	$4.57 \cdot 10^{-15}$	$4.37 \cdot 10^{-7}$	$3.55 \cdot 10^{-8}$	$1.51 \cdot 10^{-7}$
0.00625	$3.58 \cdot 10^{-14}$	$3.80 \cdot 10^{-8}$	$3.11 \cdot 10^{-9}$	$1.35 \cdot 10^{-8}$

Table 4.1 – Relative error ξ_φ for different mesh sizes h for $\varphi_{\text{jump}} = 0$.

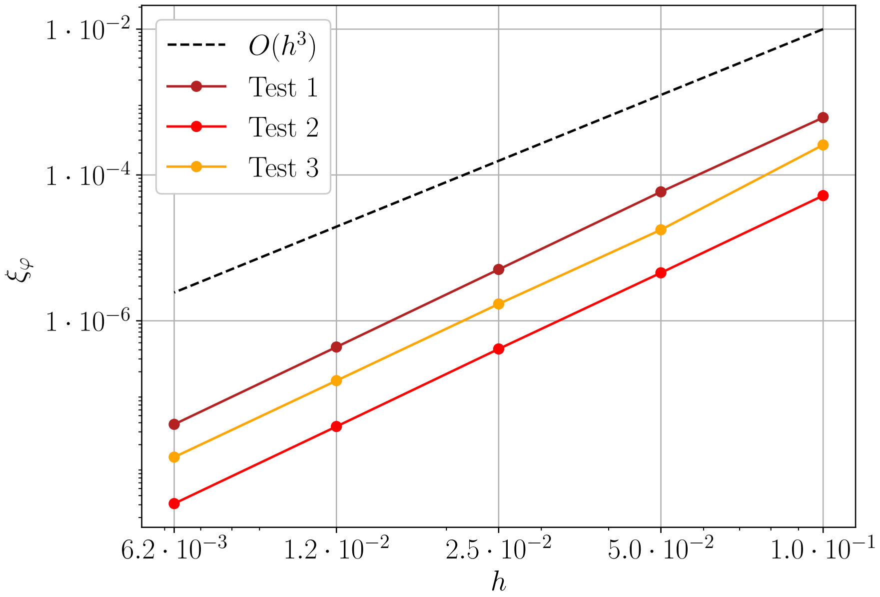

Figure 4.4 – Order of convergence of ξ_φ when $\varphi_{\text{jump}} = 0$ as a function of mesh size h for the different tests. The dashed line represents the theoretical order of convergence h^3.

Tests with jump

The second set of tests is done for a case with an interface and a jump in electrical potential. The electrical conductivities are $\sigma_1 = 10^4$ and $\sigma_2 = 1$. We run the following tests

- **Test 4** (mode $m = 0$, variable z only) :
  $\varphi_{ex,1}(z) = az + b$, for $z \leq z_1$
  $\varphi_{ex,2}(z) = dz + e$, for $z > z_1$
  with $a = \frac{4\sigma_2}{\sigma_2(z_1 - z_0) - \sigma_1(z_1 - z_2)}$, $b = az_0$, $d = (\sigma_1/\sigma_2)a$, $e = 5 - dz_2$, as imposed by (4.3.16).
  Value of the jump: $\varphi_{\text{jump}} = b$.
- **Test 5** (mode $m = 0$) :
  $\varphi_{ex,1}(r, z) = J_0(kr)\ \sinh(k(z + z_0))$, for $z \leq z_1$
  $\varphi_{ex,2}(r, z) = J_0(kr)\ (\sigma_1/\sigma_2)\ \sinh(k(z + z_0))$, for $z > z_1$
  with $k = \kappa'_{01}/R$.
  Value of the jump: $\varphi_{\text{jump}} = J_0(kr)\ (\sigma_1/\sigma_2 - 1)\ \sinh(k(z_1 + z_0))$.
- **Test 6** (mode $m = 1$) :
  $\varphi_{ex,1}(r, z, \theta) = e^{i\theta}\ J_1(kr)\ \sinh(k(z + z_0))$, for $z \leq z_1$
  $\varphi_{ex,2}(r, z, \theta) = e^{i\theta}\ J_1(kr)\ (\sigma_1/\sigma_2)\ \sinh(k(z + z_0))$, for $z > z_1$
  with $k = \kappa'_{11}/R$.
  Value of the jump: $\varphi_{\text{jump}} = e^{i\theta}\ J_1(kr)\ (\sigma_1/\sigma_2 - 1)\ \sinh(k(z_1 + z_0))$.

- **Test 7** (mode $m = 2$) :
  $\varphi_{ex,1}(r, z, \theta) = e^{2i\theta}\ J_2(kr)\ \cosh(k(z - z_2))$, for $z \leq z_1$
  $\varphi_{ex,2}(r, z, \theta) = e^{2i\theta}\ J_2(kr)\ (\sigma_1/\sigma_2)\ \cosh(k(z - z_2))$, for $z > z_1$
  with $k = \kappa'_{21}/R$.
  Value of the jump: $\varphi_{\text{jump}} = e^{2i\theta}\ J_2(kr)\ (\sigma_1/\sigma_2 - 1)\ \cosh(k(z_1 - z_2))$.

h	Test 4	Test 5	Test 6	Test 7
0.1	$3.56 \cdot 10^{-16}$	$6.48 \cdot 10^{-4}$	$2.30 \cdot 10^{-4}$	$4.77 \cdot 10^{-3}$
0.05	$1.32 \cdot 10^{-15}$	$7.38 \cdot 10^{-5}$	$3.46 \cdot 10^{-5}$	$7.21 \cdot 10^{-4}$
0.025	$5.25 \cdot 10^{-15}$	$8.14 \cdot 10^{-6}$	$4.70 \cdot 10^{-6}$	$1.10 \cdot 10^{-4}$
0.0125	$6.57 \cdot 10^{-15}$	$8.92 \cdot 10^{-7}$	$5.95 \cdot 10^{-7}$	$1.47 \cdot 10^{-5}$
0.00625	$1.17 \cdot 10^{-14}$	$1.05 \cdot 10^{-7}$	$7.57 \cdot 10^{-8}$	$1.92 \cdot 10^{-6}$

Table 4.2 – Relative error ξ_φ for different mesh sizes h for $\varphi_{\text{jump}} \neq 0$.

For test 4, ξ_φ is really low and reaches almost the zero-machine, which is an expected result for a linear solution. For the other tests, the error varies like $O(h^3)$, that we can also see in figure 4.5. These results validate the numerical solver.

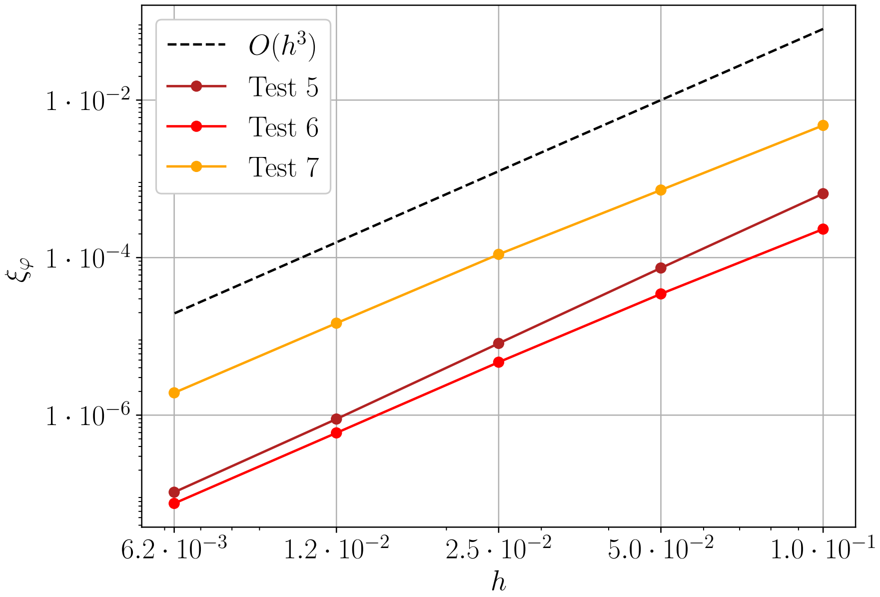

Figure 4.5 – Order of convergence of ξ_φ when $\varphi_{\text{jump}} \neq 0$ as a function of mesh size h for the different tests. The dashed line represents the theoretical order of convergence h^3.

4.4 Magnetic field $\boldsymbol{H}$ formulation

In this section, we present a new formulation using the magnetic field $\boldsymbol{H}$ to model a jump in potential on an interface. The relation between $\boldsymbol{H}$ and the usual magnetic field $\boldsymbol{B}$ is $\boldsymbol{B} = \mu_0 \boldsymbol{H}$. We implement the weak formulation in the code SFEMaNS and validate it by comparing with analytical solutions.

4.4.1 Problem description

Equation on $\boldsymbol{H}$

We consider the same problem as in section §4.3.3.
In the magnetostatic approximation, the classical equations for the magnetic field $\boldsymbol{H}$ are

$$\begin{aligned} \boldsymbol{\nabla} \times \left(\frac{\boldsymbol{\nabla} \times \boldsymbol{H}}{\sigma} \right) &= \boldsymbol{0}, && (4.4.1a) \\ \boldsymbol{\nabla} \cdot (\mu \boldsymbol{H}) &= \boldsymbol{0}. && (4.4.1b) \end{aligned}$$

where μ is the magnetic permeability.
From equation (4.3.1a), one can retrieve (4.4.1a). Indeed, the electrical current is $\boldsymbol{j} = -\sigma \boldsymbol{\nabla} \varphi$. Thus, $\boldsymbol{\nabla} \times \left(\frac{\boldsymbol{j}}{\sigma} \right) = 0$. However, $\boldsymbol{j} = \boldsymbol{\nabla} \times \boldsymbol{H}$. This yields $\boldsymbol{\nabla} \times \left(\frac{\boldsymbol{\nabla} \times \boldsymbol{H}}{\sigma} \right) = 0$.

Extension to discontinuous distributions of electrical potential

We aim now to adapt this formulation to discontinuous electrical potential at the interface Σ. In each subdomain Ω_1 and Ω_2, $\boldsymbol{j}_1 = -\sigma_1 \boldsymbol{\nabla} \varphi_1$ and $\boldsymbol{j}_2 = -\sigma_2 \boldsymbol{\nabla} \varphi_2$. Then on the interface Σ, $(\boldsymbol{j}_1/\sigma_1 - \boldsymbol{j}_2/\sigma_2) \times \boldsymbol{n} = -\boldsymbol{\nabla}_T(\varphi_1 - \varphi_2) \times \boldsymbol{n}$, where the index T is for the tangential part of the gradient. We know that $\boldsymbol{\nabla} \times \boldsymbol{H} = \boldsymbol{j}$. This finally yields:

$$\boldsymbol{n} \times \left(\frac{\boldsymbol{\nabla} \times \boldsymbol{H}_1}{\sigma_1} \right) - \boldsymbol{n} \times \left(\frac{\boldsymbol{\nabla} \times \boldsymbol{H}_2}{\sigma_2} \right) = -\boldsymbol{n} \times \boldsymbol{\nabla}_T(\varphi_1 - \varphi_2) \qquad (4.4.2)$$

By denoting $\boldsymbol{E} = \left(\frac{\boldsymbol{\nabla} \times \boldsymbol{H}}{\sigma} \right)$ the electrical field, we have shown that a discontinuous electrical potential distribution is equivalent to a discontinuity in the tangential component of the electrical field. The jump in $\left(\frac{\boldsymbol{\nabla} \times \boldsymbol{H}}{\sigma} \right)$ is denoted $\left(\frac{\boldsymbol{\nabla} \times \boldsymbol{H}}{\sigma} \right)_{\text{jump}}$ in the following.

Final problem

Two other conditions must be verified for the magnetic field on the interface, the continuity of the tangential components of $\boldsymbol{H}$ and the continuity of the normal component of $\mu \boldsymbol{H}$.
We impose Dirichlet boundary conditions $\boldsymbol{H}_D$ on all the borders Γ_D.

The final problem to solve is

$$\begin{aligned}
\boldsymbol{\nabla} \times \left(\frac{\boldsymbol{\nabla} \times \boldsymbol{H}}{\sigma} \right) &= \mathbf{0} && \text{in } \boldsymbol{\Omega}_1 \text{ and } \boldsymbol{\Omega}_2, && (4.4.3a)\\
\boldsymbol{\nabla} \cdot (\mu \boldsymbol{H}) &= \mathbf{0} && \text{in } \boldsymbol{\Omega}_1 \text{ and } \boldsymbol{\Omega}_2, && (4.4.3b)\\
\left(\frac{\boldsymbol{\nabla} \times \boldsymbol{H}_1}{\sigma_1} - \frac{\boldsymbol{\nabla} \times \boldsymbol{H}_2}{\sigma_2} \right) \times \boldsymbol{n} &= \left(\frac{\boldsymbol{\nabla} \times \boldsymbol{H}}{\sigma} \right)_{\text{jump}} \times \boldsymbol{n} && \text{on } \Sigma, && (4.4.3c)\\
(\boldsymbol{H}_1 - \boldsymbol{H}_2) \times \boldsymbol{n} &= \mathbf{0} && \text{on } \Sigma, && (4.4.3d)\\
\mu(\boldsymbol{H}_1 - \boldsymbol{H}_2) \cdot \boldsymbol{n} &= 0 && \text{on } \Sigma. && (4.4.3e)\\
\boldsymbol{H} &= \boldsymbol{H}_D && \text{on } \Gamma_D. && (4.4.3f)
\end{aligned}$$

4.4.2 Weak formulation

General weak formulation

In the volume

In order to find the weak formulation of equation (4.4.3a), we integrate (4.4.1a) on $\boldsymbol{\Omega}_i$ (i=1 or 2) after having multiplied it by a test function $\boldsymbol{v}$. $\boldsymbol{H}$ and $\boldsymbol{v}$ are in $L^2(\boldsymbol{\Omega})$ and continuous on each domain $\boldsymbol{\Omega}_i$. This gives:

$$\int_{\Omega_i} \left(\boldsymbol{\nabla} \times \frac{\boldsymbol{\nabla} \times \boldsymbol{H}}{\sigma} \right) \cdot \boldsymbol{v} \; dV = 0. \tag{4.4.4}$$

However $\left(\boldsymbol{\nabla} \times \frac{\boldsymbol{\nabla}\times\boldsymbol{H}}{\sigma} \right) \cdot \boldsymbol{v} \;=\; \epsilon_{ijk} \partial_j \left(\frac{\boldsymbol{\nabla}\times\boldsymbol{H}}{\sigma} \right)_k v_i$, where ϵ_{ijk} is the Levi-Civita symbol.

And $\epsilon_{ijk} \partial_j \left(\frac{\boldsymbol{\nabla}\times\boldsymbol{H}}{\sigma} \right)_k v_i \;=\; \underbrace{\partial_j \left(\epsilon_{ijk} \left(\frac{\boldsymbol{\nabla} \times \boldsymbol{H}}{\sigma} \right)_k v_i \right)}_{\text{(i)}} - \underbrace{\epsilon_{ijk} \left(\frac{\boldsymbol{\nabla} \times \boldsymbol{H}}{\sigma} \right)_k \partial_j v_i}_{\text{(ii)}}.$

On one hand

$$\text{(i)} = \partial_j \left(\epsilon_{ijk} \left(\frac{\boldsymbol{\nabla} \times \boldsymbol{H}}{\sigma} \right)_k v_i \right) = \partial_j \left(\left(\frac{\boldsymbol{\nabla} \times \boldsymbol{H}}{\sigma} \right) \times \boldsymbol{v} \right)_j = \boldsymbol{\nabla} \cdot \left(\left(\frac{\boldsymbol{\nabla} \times \boldsymbol{H}}{\sigma} \right) \times \boldsymbol{v} \right).$$

which gives, from Green-Ostrogradski formula,

$$\int_{\Omega_i} \boldsymbol{\nabla} \cdot \left(\left(\frac{\boldsymbol{\nabla} \times \boldsymbol{H}}{\sigma} \right) \times \boldsymbol{v} \right) dV = \int_{\partial\Omega_i} \left(\left(\frac{\boldsymbol{\nabla} \times \boldsymbol{H}}{\sigma} \right) \times \boldsymbol{v} \right) \cdot \boldsymbol{n}_i dS,$$

where $\boldsymbol{n}_i$ is the outward normal of $\partial\boldsymbol{\Omega}_i$. On the other hand

$$\text{(ii)} = \epsilon_{ijk} \left(\frac{\boldsymbol{\nabla} \times \boldsymbol{H}}{\sigma} \right)_k \partial_j v_i = \left(\frac{\boldsymbol{\nabla} \times \boldsymbol{H}}{\sigma} \right)_k \epsilon_{ijk} \partial_j v_i = \left(\frac{\boldsymbol{\nabla} \times \boldsymbol{H}}{\sigma} \right)_k \cdot (-\boldsymbol{\nabla} \times \boldsymbol{v})_k = - \left(\frac{\boldsymbol{\nabla} \times \boldsymbol{H}}{\sigma} \right) \cdot (\boldsymbol{\nabla} \times \boldsymbol{v}).$$

Hence

$$\int_{\Omega_i} \left(\boldsymbol{\nabla} \times \frac{\boldsymbol{\nabla} \times \boldsymbol{H}}{\sigma} \right) \cdot \boldsymbol{v} \; dV = 0 \iff \int_{\Omega_i} \left(\frac{\boldsymbol{\nabla} \times \boldsymbol{H}}{\sigma} \right) \cdot (\boldsymbol{\nabla} \times \boldsymbol{v}) dV + \int_{\partial\Omega_i} \left(\left(\frac{\boldsymbol{\nabla} \times \boldsymbol{H}}{\sigma} \right) \times \boldsymbol{v} \right) \cdot \boldsymbol{n}_i dS = 0.$$

By summing this on $\boldsymbol{\Omega}$ and using the relation $\left(\left(\frac{\boldsymbol{\nabla}\times\boldsymbol{H}}{\sigma} \right) \times \boldsymbol{v} \right) \cdot \boldsymbol{n}_i = \left(\boldsymbol{n}_i \times \left(\frac{\boldsymbol{\nabla}\times\boldsymbol{H}}{\sigma} \right) \right) \cdot \boldsymbol{v}$, we obtain

$$\begin{aligned}
\int_{\Omega_1} \left(\frac{\boldsymbol{\nabla} \times \boldsymbol{H}}{\sigma} \right) \cdot (\boldsymbol{\nabla} \times \boldsymbol{v}) dV + \int_{\Omega_2} \left(\frac{\boldsymbol{\nabla} \times \boldsymbol{H}}{\sigma} \right) \cdot (\boldsymbol{\nabla} \times \boldsymbol{v}) dV + \int_{\Sigma} \boldsymbol{n}_1 \times \left(\frac{\boldsymbol{\nabla} \times \boldsymbol{H}}{\sigma} \right) \cdot \boldsymbol{v}_1 dS \\
+ \int_{\Sigma} \boldsymbol{n}_2 \times \left(\frac{\boldsymbol{\nabla} \times \boldsymbol{H}}{\sigma} \right) \cdot \boldsymbol{v}_2 dS = 0.
\end{aligned}$$

We define the normal $\boldsymbol{n}$ at the interface such as $\boldsymbol{n} = \boldsymbol{n}_1$ and $\boldsymbol{n} = -\boldsymbol{n}_2$. This yields

$$\int_{\Omega_1} \left(\frac{\nabla \times \boldsymbol{H}}{\sigma}\right) \cdot (\nabla \times \boldsymbol{v}) dV \ + \int_{\Omega_2} \left(\frac{\nabla \times \boldsymbol{H}}{\sigma}\right) \cdot (\nabla \times \boldsymbol{v}) dV + \int_{\Sigma} \left[\boldsymbol{n} \times \left(\frac{\nabla \times \boldsymbol{H}}{\sigma}\right) \cdot \boldsymbol{v}\right] dS = 0.$$

$\left[\boldsymbol{n} \times \left(\frac{\nabla\times\boldsymbol{H}}{\sigma}\right) \cdot \boldsymbol{v}\right]$ can be rewritten as $\left[\left(\frac{\nabla\times\boldsymbol{H}}{\sigma}\right) \cdot (\boldsymbol{v} \times \boldsymbol{n})\right]$.

We have

$$\left[\left(\frac{\nabla \times \boldsymbol{H}}{\sigma}\right) \cdot (\boldsymbol{v} \times \boldsymbol{n})\right] = \left\{\frac{\nabla \times \boldsymbol{H}}{\sigma}\right\} \cdot [\boldsymbol{v} \times \boldsymbol{n}] \ + \left[\frac{\nabla \times \boldsymbol{H}}{\sigma}\right] \cdot \{\boldsymbol{v} \times \boldsymbol{n}\}.$$

Thus (4.4.5) becomes

$$\begin{aligned}\int_{\Omega_1} \left(\frac{\nabla \times \boldsymbol{H}}{\sigma}\right) \cdot (\nabla \times \boldsymbol{v}) dV \ + \int_{\Omega_2} \left(\frac{\nabla \times \boldsymbol{H}}{\sigma}\right) \cdot (\nabla \times \boldsymbol{v}) dV + \int_{\Sigma} \left\{\frac{\nabla \times \boldsymbol{H}}{\sigma}\right\} \cdot [\boldsymbol{v} \times \boldsymbol{n}] dS \\ + \int_{\Sigma} \left[\frac{\nabla \times \boldsymbol{H}}{\sigma}\right] \cdot \{\boldsymbol{v} \times \boldsymbol{n}\} dS = 0\end{aligned}$$

with $\boldsymbol{n} = \boldsymbol{n}_1$ and $\boldsymbol{n} = -\boldsymbol{n}_2$, $[\boldsymbol{v} \times \boldsymbol{n}] = \boldsymbol{v}_1 \times \boldsymbol{n}_1 + \boldsymbol{v}_2 \times \boldsymbol{n}_2$ and $\{\boldsymbol{v} \times \boldsymbol{n}\} = \frac{1}{2}(\boldsymbol{v}_1 \times \boldsymbol{n}_1 - \boldsymbol{v}_2 \times \boldsymbol{n}_2)$. Therefore

$$\begin{aligned}\int_{\Omega_1} \left(\frac{\nabla \times \boldsymbol{H}}{\sigma}\right) \cdot (\nabla \times \boldsymbol{v}) dV \ + \int_{\Omega_2} \left(\frac{\nabla \times \boldsymbol{H}}{\sigma}\right) \cdot (\nabla \times \boldsymbol{v}) dV \\ + \int_{\Sigma} \frac{1}{2} \left(\frac{\nabla \times \boldsymbol{H}_1}{\sigma_1} \ + \ \frac{\nabla \times \boldsymbol{H}_2}{\sigma_2}\right) \cdot (\boldsymbol{v}_1 \times \boldsymbol{n}_1 + \boldsymbol{v}_2 \times \boldsymbol{n}_2) dS \\ + \int_{\Sigma} \frac{1}{2} \left(\frac{\nabla \times \boldsymbol{H}_1}{\sigma_1} - \frac{\nabla \times \boldsymbol{H}_2}{\sigma_2}\right) \cdot (\boldsymbol{v}_1 \times \boldsymbol{n}_1 - \boldsymbol{v}_2 \times \boldsymbol{n}_2) dS \ = \ 0.\end{aligned} \tag{4.4.5}$$

Terms of continuity

In order to ensure the continuity of $\boldsymbol{H} \times \boldsymbol{n}$ and $\mu\boldsymbol{H} \cdot \boldsymbol{n}$ at the interface (equations (4.4.3d) and (4.4.3e)), $\boldsymbol{H}$ must verify

$$\beta_3 \int_{\Sigma} \frac{1}{h} (\boldsymbol{H}_1 \times \boldsymbol{n}_1 \ + \ \boldsymbol{H}_2 \times \boldsymbol{n}_2) \cdot (\boldsymbol{v}_1 \times \boldsymbol{n}_1 \ + \ \boldsymbol{v}_2 \times \boldsymbol{n}_2) dS \ = 0 \tag{4.4.6}$$

and

$$\beta_1 \int_{\Sigma} \frac{1}{h} (\mu_1 \boldsymbol{H}_1 \cdot \boldsymbol{n}_1 \ + \ \mu_2 \boldsymbol{H}_2 \cdot \boldsymbol{n}_2)(\mu_1 \boldsymbol{v}_1 \cdot \boldsymbol{n}_1 \ + \ \mu_2 \boldsymbol{v}_2 \cdot \boldsymbol{n}_2) dS \ = \ 0 \tag{4.4.7}$$

where β_1 and β_3 are penalty coefficients.

Imposition of the jump

Our first attempt to impose the jump in $\left(\frac{\nabla\times\boldsymbol{H}}{\sigma}\right)_{\text{jump}}$ (equation (4.4.3c)) was, as in the electrical potential case, to use a penalty term such as

$$\frac{c}{h} \int_{\Sigma} \left(\frac{\nabla \times \boldsymbol{H}_1}{\sigma_1} \times \boldsymbol{n} - \frac{\nabla \times \boldsymbol{H}_2}{\sigma_2} \times \boldsymbol{n}\right) \cdot (\boldsymbol{v}_1 - \boldsymbol{v}_2) \ dS \ = \ \frac{c}{h} \int_{\Sigma} \left(\frac{\nabla \times \boldsymbol{H}}{\sigma}\right)_{\text{jump}} \times \boldsymbol{n} \cdot (\boldsymbol{v}_1 - \boldsymbol{v}_2) \ dS$$

i.e.

$$c \int_{\Sigma} \frac{1}{h} \left(\frac{\nabla \times \boldsymbol{H}_1}{\sigma_1} - \frac{\nabla \times \boldsymbol{H}_2}{\sigma_2}\right) \cdot (\boldsymbol{v}_1 \times \boldsymbol{n}_1 + \boldsymbol{v}_2 \times \boldsymbol{n}_2) \ dS \ = \ c \int_{\Sigma} \frac{1}{h} \left(\frac{\nabla \times \boldsymbol{H}}{\sigma}\right)_{\text{jump}} \cdot (\boldsymbol{v}_1 \times \boldsymbol{n}_1 + \boldsymbol{v}_2 \times \boldsymbol{n}_2) \ dS.$$

However, by looking on the continuity term (4.4.6), both terms have the same form relatively to the test functions: $\boldsymbol{v}_1 \times \boldsymbol{n}_1 + \boldsymbol{v}_2 \times \boldsymbol{n}_2$. This means that numerically, these terms cannot be distinguished and the code will read

$$\int_\Sigma \frac{1}{h}\left(c\left(\frac{\nabla\times\boldsymbol{H}_1}{\sigma_1} - \frac{\nabla\times\boldsymbol{H}_2}{\sigma_2}\right) + \beta_3(\boldsymbol{H}_1\times\boldsymbol{n}_1 \ + \ \boldsymbol{H}_2\times\boldsymbol{n}_2)\right)\cdot(\boldsymbol{v}_1\times\boldsymbol{n}_1 + \boldsymbol{v}_2\times\boldsymbol{n}_2)\ dS$$
$$= c\int_\Sigma \frac{1}{h}\left(\frac{\nabla\times\boldsymbol{H}}{\sigma}\right)_{\text{jump}}\cdot(\boldsymbol{v}_1\times\boldsymbol{n}_1 + \boldsymbol{v}_2\times\boldsymbol{n}_2)\ dS$$

which enforces

$$\frac{1}{h}\left(c\left(\frac{\nabla\times\boldsymbol{H}_1}{\sigma_1} - \frac{\nabla\times\boldsymbol{H}_2}{\sigma_2}\right) + \beta_3(\boldsymbol{H}_1\times\boldsymbol{n}_1 \ + \ \boldsymbol{H}_2\times\boldsymbol{n}_2)\right) = \frac{c}{h}\left(\frac{\nabla\times\boldsymbol{H}}{\sigma}\right)_{\text{jump}}. \tag{4.4.8}$$

After having implemented this method, it was shown that the code is not able to impose the desired jump and the numerical solution is not continuous at the interface.
We have then to impose the jump in another way. We finally impose it strongly, that is to say we replace the term $\int_\Sigma \frac{1}{2}\left(\frac{\nabla\times\boldsymbol{H}_1}{\sigma_1} - \frac{\nabla\times\boldsymbol{H}_2}{\sigma_2}\right)\cdot(\boldsymbol{v}_1\times\boldsymbol{n}_1 - \boldsymbol{v}_2\times\boldsymbol{n}_2)dS$ by $\int_\Sigma \frac{1}{2}\left(\frac{\nabla\times\boldsymbol{H}}{\sigma}\right)_{\text{jump}}\cdot(\boldsymbol{v}_1\times\boldsymbol{n}_1 - \boldsymbol{v}_2\times\boldsymbol{n}_2)dS$.
This term is now known, we pass it to the right-hand side.

This yields

$$\int_{\Omega_1}\left(\frac{\nabla\times\boldsymbol{H}}{\sigma}\right)\cdot(\nabla\times\boldsymbol{v})dV \ + \ \int_{\Omega_2}\left(\frac{\nabla\times\boldsymbol{H}}{\sigma}\right)\cdot(\nabla\times\boldsymbol{v})dV$$
$$+\int_\Sigma \frac{1}{2}\left(\frac{\nabla\times\boldsymbol{H}_1}{\sigma_1} + \frac{\nabla\times\boldsymbol{H}_2}{\sigma_2}\right)\cdot(\boldsymbol{v}_1\times\boldsymbol{n}_1+\boldsymbol{v}_2\times\boldsymbol{n}_2)dS = -\int_\Sigma \frac{1}{2}\left(\frac{\nabla\times\boldsymbol{H}}{\sigma}\right)_{\text{jump}}\cdot(\boldsymbol{v}_1\times\boldsymbol{n}_1-\boldsymbol{v}_2\times\boldsymbol{n}_2)dS. \tag{4.4.9}$$

Divergence and magnetic pressure
In order to ensure $\nabla\cdot(\mu\boldsymbol{H}) = 0$ (equation (4.4.3b)), a magnetic pressure p_m has been implemented in SFEMaNS to control the divergence. p_m is a solution of

$$-\nabla\cdot(h^{2(1-a)}\nabla p_m) \ = -\nabla\cdot(\mu\boldsymbol{H}) \qquad \text{in } \Omega_1 \ \text{ and } \ \Omega_2. \tag{4.4.10}$$

where a is a constant between 0 and 1. In the weak formulation, where we denote q a test function related to p_m, this is translated by

$$\beta_1\left(\int_{\Omega_1}\mu\nabla p_m\cdot\boldsymbol{v}dV - \int_{\Omega_1}\mu\boldsymbol{H}\cdot\nabla q dV + \int_{\Omega_1}h^{2(1-a)}\nabla p_m\cdot\nabla q dV + \int_{\Omega_1}h^{2a}\nabla\cdot(\mu\boldsymbol{H})\nabla\cdot(\mu\boldsymbol{v})dV\right)$$
$$+\beta_1\left(\int_{\Omega_2}\mu\nabla p_m\cdot\boldsymbol{v}dV - \int_{\Omega_2}\mu\boldsymbol{H}\cdot\nabla q dV + \int_{\Omega_2}h^{2(1-a)}\nabla p_m\cdot\nabla q dV + \int_{\Omega_2}h^{2a}\nabla\cdot(\mu\boldsymbol{H})\nabla\cdot(\mu\boldsymbol{v})dV\right) = 0. \tag{4.4.11}$$

Dirichlet boundary conditions
The Dirichlet boundary conditions (equation (4.4.3f)) are enforced weakly, i.e. in the weak formulation, unlike the code with φ. They are imposed on $\boldsymbol{H}\times\boldsymbol{n}$. This is written

$$\int_{\Gamma_D}\frac{1}{\sigma}\boldsymbol{\nabla}\times\boldsymbol{H}\cdot(\boldsymbol{v}\times\boldsymbol{n})dS+\beta_3\int_{\Gamma_D}h^{-1}(\boldsymbol{H}\times\boldsymbol{n})\cdot(\boldsymbol{v}\times\boldsymbol{n})dS=\beta_3\int_{\Gamma_D}h^{-1}(\boldsymbol{H}_D\times\boldsymbol{n})\cdot(\boldsymbol{v}\times\boldsymbol{n})dS. \tag{4.4.12}$$

$\mu\boldsymbol{H}\cdot\boldsymbol{n}$ is constrained by the code on the boundaries via the divergence equation (4.4.3b).

Final weak formulation
Using all the previous calculations, the final weak formulation can be written as

$$\begin{aligned}
&\int_{\Omega_1}\left(\frac{\boldsymbol{\nabla}\times\boldsymbol{H}}{\sigma}\right)\cdot(\boldsymbol{\nabla}\times\boldsymbol{v})dV+\int_{\Omega_2}\left(\frac{\boldsymbol{\nabla}\times\boldsymbol{H}}{\sigma}\right)\cdot(\boldsymbol{\nabla}\times\boldsymbol{v})dV+\int_{\Sigma}\left(\frac{\boldsymbol{\nabla}\times\boldsymbol{H}_1}{\sigma_1}+\frac{\boldsymbol{\nabla}\times\boldsymbol{H}_2}{\sigma_2}\right)\cdot(\boldsymbol{v}_1\times\boldsymbol{n}_1+\boldsymbol{v}_2\times\boldsymbol{n}_2)dS\\
&+\beta_1\left(\int_{\Omega_1}\mu\boldsymbol{\nabla}p_m\cdot\boldsymbol{v}dV-\int_{\Omega_1}\mu\boldsymbol{H}\cdot\boldsymbol{\nabla}qdV+\int_{\Omega_1}h^{2(1-a)}\boldsymbol{\nabla}p_m\cdot\boldsymbol{\nabla}qdV+\int_{\Omega_1}h^{2a}\boldsymbol{\nabla}\cdot(\mu\boldsymbol{H})\boldsymbol{\nabla}\cdot(\mu\boldsymbol{v})dV\right)\\
&+\beta_1\left(\int_{\Omega_2}\mu\boldsymbol{\nabla}p_m\cdot\boldsymbol{v}dV-\int_{\Omega_2}\mu\boldsymbol{H}\cdot\boldsymbol{\nabla}qdV+\int_{\Omega_2}h^{2(1-a)}\boldsymbol{\nabla}p_m\cdot\boldsymbol{\nabla}qdV+\int_{\Omega_2}h^{2a}\boldsymbol{\nabla}\cdot(\mu\boldsymbol{H})\boldsymbol{\nabla}\cdot(\mu\boldsymbol{v})dV\right)\\
&\qquad+\beta_3\int_{\Sigma}\frac{1}{h}(\boldsymbol{H}_1\times\boldsymbol{n}_1\ +\ \boldsymbol{H}_2\times\boldsymbol{n}_2)\cdot(\boldsymbol{v}_1\times\boldsymbol{n}_1\ +\ \boldsymbol{v}_2\times\boldsymbol{n}_2)dS\\
&\qquad+\beta_1\int_{\Sigma}\frac{1}{h}(\mu\boldsymbol{H}_1\cdot\boldsymbol{n}_1\ +\ \mu\boldsymbol{H}_2\cdot\boldsymbol{n}_2)(\mu\boldsymbol{v}_1\cdot\boldsymbol{n}_1\ +\ \mu\boldsymbol{v}_2\cdot\boldsymbol{n}_2)dS\\
&\qquad+\int_{\Gamma_D}\frac{1}{\sigma}(\boldsymbol{\nabla}\times\boldsymbol{H})\cdot(\boldsymbol{v}\times\boldsymbol{n})dS+\beta_3\int_{\Gamma_D}h^{-1}(\boldsymbol{H}\times\boldsymbol{n})\cdot(\boldsymbol{v}\times\boldsymbol{n})dS=\\
&-\int_{\Sigma}\left(\frac{\boldsymbol{\nabla}\times\boldsymbol{H}}{\sigma}\right)_{\text{jump}}\cdot(\boldsymbol{v}_1\times\boldsymbol{n}_1-\boldsymbol{v}_2\times\boldsymbol{n}_2)dS+\beta_3\int_{\Gamma_D}h^{-1}(\boldsymbol{H}_D\times\boldsymbol{n})\cdot(\boldsymbol{v}\times\boldsymbol{n})dS.
\end{aligned} \tag{4.4.13}$$

Weights

The weights have to be applied to the term $\left[\boldsymbol{n}\times\left(\frac{\boldsymbol{\nabla}\times\boldsymbol{H}}{\sigma}\right)\cdot\boldsymbol{v}\right]$ in the weak formulation (4.4.5). The weights in this case are

$$\tau_1=\frac{(1/\sigma_2)}{(1/\sigma_1)+(1/\sigma_2)}=\frac{\sigma_1}{\sigma_1+\sigma_2},\qquad \tau_2=\frac{(1/\sigma_1)}{(1/\sigma_1)+(1/\sigma_2)}=\frac{\sigma_2}{\sigma_1+\sigma_2}. \tag{4.4.14}$$

We have

$$\begin{aligned}
&\left[\boldsymbol{n}\times\left(\frac{\boldsymbol{\nabla}\times\boldsymbol{H}}{\sigma}\right)\cdot\boldsymbol{v}\right]=\boldsymbol{n}\times\left(\frac{\boldsymbol{\nabla}\times\boldsymbol{H}_1}{\sigma_1}\right)\cdot\boldsymbol{v}_1-\boldsymbol{n}\times\left(\frac{\boldsymbol{\nabla}\times\boldsymbol{H}_2}{\sigma_2}\right)\cdot\boldsymbol{v}_2\\
=\ &\boldsymbol{n}\times\left(\tau_1\frac{\boldsymbol{\nabla}\times\boldsymbol{H}_1}{\sigma_1}+\tau_2\frac{\boldsymbol{\nabla}\times\boldsymbol{H}_2}{\sigma_2}\right)\cdot(\boldsymbol{v}_1-\boldsymbol{v}_2)\ +\ \boldsymbol{n}\times\left(\frac{\boldsymbol{\nabla}\times\boldsymbol{H}_1}{\sigma_1}-\frac{\boldsymbol{\nabla}\times\boldsymbol{H}_2}{\sigma_2}\right)\cdot(\tau_2\boldsymbol{v}_1-\tau_1\boldsymbol{v}_2)\\
=\ &\boldsymbol{n}\times\left(\tau_1\frac{\boldsymbol{\nabla}\times\boldsymbol{H}_1}{\sigma_1}+\tau_2\frac{\boldsymbol{\nabla}\times\boldsymbol{H}_2}{\sigma_2}\right)\cdot(\boldsymbol{v}_1-\boldsymbol{v}_2)\ +\ \boldsymbol{n}\times\left(\frac{\boldsymbol{\nabla}\times\boldsymbol{H}}{\sigma}\right)_{\text{jump}}\cdot(\tau_2\boldsymbol{v}_1-\tau_1\boldsymbol{v}_2).
\end{aligned}$$

The final weak formulation with weights is hence

$$
\begin{aligned}
&\int_{\Omega_1}\left(\frac{\boldsymbol{\nabla}\times\boldsymbol{H}}{\sigma}\right)\cdot(\boldsymbol{\nabla}\times\boldsymbol{v})dV+\int_{\Omega_2}\left(\frac{\boldsymbol{\nabla}\times\boldsymbol{H}}{\sigma}\right)\cdot(\boldsymbol{\nabla}\times\boldsymbol{v})dV\\
&\qquad+\underbrace{\int_{\Sigma}\left(\tau_1\frac{\boldsymbol{\nabla}\times\boldsymbol{H}_1}{\sigma_1}+\tau_2\frac{\boldsymbol{\nabla}\times\boldsymbol{H}_2}{\sigma_2}\right)\cdot(\boldsymbol{v}_1\times\boldsymbol{n}_1+\boldsymbol{v}_2\times\boldsymbol{n}_2)dS}_{(*)}\\
&+\beta_1\left(\int_{\Omega_1}\mu\boldsymbol{\nabla}p_m\cdot\boldsymbol{v}dV-\int_{\Omega_1}\mu\boldsymbol{H}\cdot\boldsymbol{\nabla}qdV+\int_{\Omega_1}h^{2(1-a)}\boldsymbol{\nabla}p_m\cdot\boldsymbol{\nabla}qdV+\int_{\Omega_1}h^{2a}\boldsymbol{\nabla}\cdot(\mu\boldsymbol{H})\boldsymbol{\nabla}\cdot(\mu\boldsymbol{v})dV\right)\\
&+\beta_1\left(\int_{\Omega_2}\mu\boldsymbol{\nabla}p_m\cdot\boldsymbol{v}dV-\int_{\Omega_2}\mu\boldsymbol{H}\cdot\boldsymbol{\nabla}qdV+\int_{\Omega_2}h^{2(1-a)}\boldsymbol{\nabla}p_m\cdot\boldsymbol{\nabla}qdV+\int_{\Omega_2}h^{2a}\boldsymbol{\nabla}\cdot(\mu\boldsymbol{H})\boldsymbol{\nabla}\cdot(\mu\boldsymbol{v})dV\right)\\
&\qquad+\beta_3\int_{\Sigma}\frac{1}{h}(\boldsymbol{H}_1\times\boldsymbol{n}_1\;+\;\boldsymbol{H}_2\times\boldsymbol{n}_2)\cdot(\boldsymbol{v}_1\times\boldsymbol{n}_1\;+\;\boldsymbol{v}_2\times\boldsymbol{n}_2)dS\\
&\qquad+\beta_1\int_{\Sigma}\frac{1}{h}(\mu\boldsymbol{H}_1\cdot\boldsymbol{n}_1\;+\;\mu\boldsymbol{H}_2\cdot\boldsymbol{n}_2)(\mu\boldsymbol{v}_1\cdot\boldsymbol{n}_1\;+\;\mu\boldsymbol{v}_2\cdot\boldsymbol{n}_2)dS\\
&\qquad+\int_{\Gamma_D}\frac{1}{\sigma}(\boldsymbol{\nabla}\times\boldsymbol{H})\cdot(\boldsymbol{v}\times\boldsymbol{n})dS+\beta_3\int_{\Gamma_D}h^{-1}(\boldsymbol{H}\times\boldsymbol{n})\cdot(\boldsymbol{v}\times\boldsymbol{n})dS=\\
&-\underbrace{\int_{\Sigma}\left(\frac{\boldsymbol{\nabla}\times\boldsymbol{H}}{\sigma}\right)_{\text{jump}}\cdot(\tau_2\boldsymbol{v}_1\times\boldsymbol{n}_1-\tau_1\boldsymbol{v}_2\times\boldsymbol{n}_2)dS}_{(*)}+\beta_3\int_{\Gamma_D}h^{-1}(\boldsymbol{H}_D\times\boldsymbol{n})\cdot(\boldsymbol{v}\times\boldsymbol{n})dS.
\end{aligned}
\tag{4.4.15}
$$

Numerics

Most of the terms of this weak formulation were already present in SFEMaNS. During this thesis, we have implemented the terms modeling the jump and the weights, i.e. the terms indicated by (∗) in formulation (4.4.15). The numerical decomposition and solving process is similar to that presented in section §4.3.

4.4.3 Determination of analytical solutions

In order to validate the numerical solutions, we need to compare them to analytical solutions. We are looking for solutions to the problem (4.4.3).

Analytical solutions with $\left(\frac{\nabla\times\boldsymbol{H}}{\sigma}\right)_{\textbf{jump}} = 0$

In a single domain, we are looking for solutions of the system $\begin{cases} \nabla\times(\nabla\times\boldsymbol{H}) &= \boldsymbol{0}, \\ \nabla\cdot\boldsymbol{H} &= \boldsymbol{0}, \end{cases}$ which is equivalent to

$$\left(\triangle - \frac{1}{r^2}\right)H_r \;-\; \frac{2}{r^2}\partial_\theta H_\theta \;=\; 0, \tag{4.4.16a}$$

$$\left(\triangle - \frac{1}{r^2}\right)H_\theta \;+\; \frac{2}{r^2}\partial_\theta \;=\; 0, \tag{4.4.16b}$$

$$\triangle H_z \;=\; 0, \tag{4.4.16c}$$

$$\left(\partial_r + \frac{1}{r}\right)H_r \;+\; \frac{1}{r}\partial_\theta H_\theta \;+\; \partial_z H_z \;=\; 0. \tag{4.4.16d}$$

Let $H_+ = H_r + iH_\theta$ and $H_- = H_r - iH_\theta$. Thus $H_r = (H_+ + H_-)/2$ et $H_\theta = (H_+ - H_-)/2i$.

Hence

$$(4.4.16a){+}i(4.4.16b) \Rightarrow \left(\triangle - \frac{1}{r^2}\right)(H_r{+}iH_\theta) + 2\frac{\partial_\theta}{r^2}(iH_r{-}H_\theta) \;=\; 0 \;\Rightarrow \left(\triangle - \frac{1}{r^2}\right)H_+ + 2i\frac{\partial_\theta}{r^2}H_+ \;=\; 0$$

$$(4.4.16a){-}i(4.4.16b) \Rightarrow \left(\triangle - \frac{1}{r^2}\right)(H_r{-}iH_\theta) - 2\frac{\partial_\theta}{r^2}(iH_r{+}H_\theta) \;=\; 0 \;\Rightarrow \left(\triangle - \frac{1}{r^2}\right)H_- - 2i\frac{\partial_\theta}{r^2}H_- \;=\; 0$$

which leads to

$$\left(\partial^2_{rr} + \frac{1}{r}\partial_r + \frac{\partial^2_{\theta\theta}}{r^2} + \partial^2_{zz} - \frac{1}{r^2} + 2i\frac{\partial_\theta}{r^2}\right)H_+ \;=\; 0,$$

$$\left(\partial^2_{rr} + \frac{1}{r}\partial_r + \frac{\partial^2_{\theta\theta}}{r^2} + \partial^2_{zz} - \frac{1}{r^2} - 2i\frac{\partial_\theta}{r^2}\right)H_- \;=\; 0,$$

$$\left(\partial^2_{rr} + \frac{1}{r}\partial_r + \frac{\partial^2_{\theta\theta}}{r^2} + \partial^2_{zz}\right)H_z \;=\; 0.$$

We take solutions with separable variables such as $(H_+, H_-, H_z) = e^{im\theta}(h_+, h_-, h_z)$ with $h_+ = A_+\mathcal{R}_+(r)\mathcal{Z}_+(z)$, $h_- = A_-\mathcal{R}_-(r)\mathcal{Z}_-(z)$, $h_z = A_z\mathcal{R}_z(r)\mathcal{Z}_z(z)$, where A_+, A_-, A_z are constants and $\mathcal{R}_+$, $\mathcal{R}_-$, $\mathcal{R}_z$, $\mathcal{Z}_+$, $\mathcal{Z}_-$, $\mathcal{Z}_z$ are functions.

We solve then

$$\left(\partial^2_{rr} + \frac{1}{r}\partial_r - \frac{m^2}{r^2} + \partial^2_{zz} - \frac{1}{r^2} - 2\frac{m}{r^2}\right)h_+ \;=\; 0,$$

$$\left(\partial^2_{rr} + \frac{1}{r}\partial_r - \frac{m^2}{r^2} + \partial^2_{zz} - \frac{1}{r^2} + 2\frac{m}{r^2}\right)h_- \;=\; 0,$$

$$\left(\partial^2_{rr} + \frac{1}{r}\partial_r - \frac{m^2}{r^2} + \partial^2_{zz}\right)h_z \;=\; 0.$$

i.e.

$$\begin{aligned}
\left(\partial^2_{rr} + \frac{1}{r}\partial_r - \frac{(m+1)^2}{r^2} + \partial^2_{zz}\right) h_+ &= 0,\\
\left(\partial^2_{rr} + \frac{1}{r}\partial_r - \frac{(m-1)^2}{r^2} + \partial^2_{zz}\right) h_- &= 0,\\
\left(\partial^2_{rr} + \frac{1}{r}\partial_r - \frac{m^2}{r^2} + \partial^2_{zz}\right) h_z &= 0.
\end{aligned}$$

We choose $\mathcal{Z}_+(z), \mathcal{Z}_-(z), \mathcal{Z}_z(z) = e^{kz}$.
Thus $\mathcal{R}_+(r) = J_{m+1}(kr)$, $\mathcal{R}_-(r) = J_{m-1}(kr)$ et $\mathcal{R}_z(r) = J_m(kr)$ where J are Bessel functions.

Hence we find

$$\begin{aligned}
H_+ &= A_+ \, J_{m+1}(kr)\; e^{kz}\; e^{im\theta}\\
H_- &= A_- \, J_{m-1}(kr)\; e^{kz}\; e^{im\theta}\\
H_z &= A_z \, J_m(kr)\; e^{kz}\; e^{im\theta}.
\end{aligned}$$

To find a relation between the constants A, we inject the result in the divergence equation (4.4.16d), which gives

$$\begin{aligned}
&\left(\partial_r + \frac{1}{r}\right) H_r + \frac{1}{r}\partial_\theta H_\theta + \partial_z H_z = 0\\
\Rightarrow &\left(\partial_r + \frac{1}{r}\right) \frac{(H_+ + H_-)}{2} + \frac{1}{r}\partial_\theta \frac{(H_+ - H_-)}{2i} + \partial_z H_z = 0\\
\Rightarrow &\frac{1}{2}\left(\partial_r + \frac{1}{r} + \frac{1}{ir}\partial_\theta\right) H_+ + \frac{1}{2}\left(\partial_r + \frac{1}{r} - \frac{1}{ir}\partial_\theta\right) H_- + \partial_z H_z = 0\\
\Rightarrow &\frac{1}{2}\left(\partial_r + \frac{1}{r} + \frac{m}{r}\right) h_+ + \frac{1}{2}\left(\partial_r + \frac{1}{r} - \frac{m}{r}\right) h_- + \partial_z h_z = 0\\
\Rightarrow &\frac{1}{2}\left(\partial_r + \frac{m+1}{r}\right) h_+ + \frac{1}{2}\left(\partial_r - \frac{m-1}{r}\right) h_- + \partial_z h_z = 0\\
\Rightarrow &\frac{1}{2}\left(\partial_r + \frac{m+1}{r}\right) A_+ J_{m+1}(kr) + \frac{1}{2}\left(\partial_r - \frac{m-1}{r}\right) A_- J_{m-1}(kr) + A_z k J_m(kr) = 0.
\end{aligned}$$

Using the relations

$$\begin{aligned}
\left(\partial_r + \frac{m+1}{r}\right) J_{m+1}(kr) &= kJ_m(kr),\\
\left(\partial_r - \frac{m-1}{r}\right) J_{m-1}(kr) &= -kJ_m(kr),
\end{aligned}$$

we find

$$\frac{A_+}{2} - \frac{A_-}{2} + A_z = 0 \Rightarrow A_z = \frac{A_- - A_+}{2}.$$

We obtain finally the following complex solutions

$$\begin{aligned}
H_r &= \frac{A_+ \, J_{m+1}(kr) + A_- J_{m-1}(kr)}{2} e^{kz}\; e^{im\theta}\\
H_\theta &= \frac{A_+ \, J_{m+1}(kr) - A_- J_{m-1}(kr)}{2i} e^{kz}\; e^{im\theta}\\
H_z &= \frac{A_- - A_+}{2} J_m(kr)\; e^{kz}\; e^{im\theta}
\end{aligned}$$

and, after having taken the real part, we get the solution

$$H_r = \frac{A_+ \, J_{m+1}(kr) + A_- J_{m-1}(kr)}{2} e^{kz} \cos(m\theta) \tag{4.4.24a}$$

$$H_\theta = \frac{A_+ \, J_{m+1}(kr) - A_- J_{m-1}(kr)}{2} e^{kz} \sin(m\theta) \tag{4.4.24b}$$

$$H_z = \frac{A_- - A_+}{2} J_m(kr) \; e^{kz} \cos(m\theta) \tag{4.4.24c}$$

where m is the mode we choose for the following numerical tests. A_+ and A_- can be chosen arbitrarily.

Analytical solutions with $\left(\frac{\nabla\times\boldsymbol{H}}{\sigma}\right)_{\text{jump}} \neq 0$

In a case with a non-zero jump in $\left(\frac{\nabla\times\boldsymbol{H}}{\sigma}\right)_{\text{jump}}$, the solutions take the same form as the ones in the last paragraph with $\left(\frac{\nabla\times\boldsymbol{H}}{\sigma}\right)_{\text{jump}} = 0$ in Ω_1 and Ω_2. At the interface Σ, equations (4.4.3c), (4.4.3d) and (4.4.3e) have to be also verified. We set μ to a constant in the whole domain Ω, this means that $\boldsymbol{H}_1 = \boldsymbol{H}_2$ at the interface.

Thus, at the interface

$$\frac{\nabla\times\boldsymbol{H}_1}{\sigma_1} - \frac{\nabla\times\boldsymbol{H}_2}{\sigma_2} = \nabla\times\boldsymbol{H}_1\left(\frac{1}{\sigma_1} - \frac{1}{\sigma_2}\right)$$

because $\boldsymbol{H}_1 = \boldsymbol{H}_2$. This means that, if we choose $\sigma_1 \neq \sigma_2$ and $\boldsymbol{H}_1 = \boldsymbol{H}_2 = \boldsymbol{H}$ where $\boldsymbol{H}$ is the solution (4.4.24), it verifies at the interface $\boldsymbol{H}_1 = \boldsymbol{H}_2$ and the jump is non-zero. This is the solution that we choose for the following.
In order to find the value of the jump, we calculate $\nabla\times\boldsymbol{H}$ with the solution (4.4.24). Using properties of Bessel functions, this gives

$$\nabla \times \boldsymbol{H} = \left| \begin{array}{l} \dfrac{ke^{kz}\sin(m\theta)}{4}(A_+ + A_-)(J_{m-1}(kr) - J_{m+1}(kr)) \\ \dfrac{ke^{kz}\cos(m\theta)}{4}(A_+ + A_-)(J_{m+1}(kr) + J_{m-1}(kr)) \\ \dfrac{ke^{kz}\sin(m\theta)}{2}(A_+ + A_-)J_m(kr) \end{array} \right. . \tag{4.4.25}$$

Hence we have $\left(\frac{\nabla\times\boldsymbol{H}}{\sigma}\right)_{\text{jump}} = \nabla\times\boldsymbol{H}\left(\frac{1}{\sigma_1} - \frac{1}{\sigma_2}\right)_{|\Sigma}$ where $\nabla \times \boldsymbol{H}$ is equal to (4.4.25).

4.4.4 Numerical investigations

In this section we validate our solver in the domain $\boldsymbol{\Omega}$ defined in section §4.3.1 by comparing the numerical solution with analytical solutions found in section §4.4.3.
The tests are done using solution (4.4.24)

$$\begin{aligned}
H_r &= \frac{A_+\, J_{m+1}(kr) + A_- J_{m-1}(kr)}{2} e^{kz}\, \cos(m\theta)\\
H_\theta &= \frac{A_+\, J_{m+1}(kr) - A_- J_{m-1}(kr)}{2} e^{kz}\, \sin(m\theta)\\
H_z &= \frac{A_- - A_+}{2} J_m(kr)\; e^{kz}\, \cos(m\theta)
\end{aligned}$$

for different Fourier modes (m= 0,1 or 2), in two cases, first without a jump (single domain) and then with a jump on the interface Σ. We fix $A_+ = 2$ and $A_- = 1$. We define the relative error in L^2-norm of $\boldsymbol{H}$

$$\xi_{\boldsymbol{H}} = \frac{\|\boldsymbol{H}_{\text{num}} - \boldsymbol{H}_{\text{ex}}\|_2}{\|\boldsymbol{H}_{\text{ex}}\|_2}, \tag{4.4.27}$$

where $\boldsymbol{H}_{\text{num}}$ is the numerical solution and $\boldsymbol{H}_{\text{ex}}$ the analytical solution. This error is expected to vary like $O(h^3)$, like in the case with the φ-solver (section §4.3.4).
In the following we denote by κ_{m1} the first root of the Bessel function J_m. The numerical tests presented in this section use κ_{01}, κ_{11} and κ_{21} whose values are

$$\kappa_{01} = 2.4048255577, \quad \kappa_{11} = 3.8317059702, \quad \kappa_{21} = 5.1356223018.$$

We precise that, for $m = 0$, we need J_{-1} which is equal to $-J_1$.

Tests without jump

The first set of tests is done for a case with no interface and then no jump. The electrical conductivity is $\sigma = 1$, and the magnetic permeability $\mu = 1$. We run the following tests

- **Test 1**: mode $m = 0$, $k = \kappa_{01}$.
- **Test 2**: mode $m = 1$, $k = \kappa_{11}$.
- **Test 3**: mode $m = 2$, $k = \kappa_{21}$.

We report the relative error $\xi_{\boldsymbol{H}}$ in table 4.3.

h	Test 1	Test 2	Test 3
0.1	$3.18 \cdot 10^{-2}$	$1.56 \cdot 10^{-2}$	$3.59 \cdot 10^{-2}$
0.05	$5.88 \cdot 10^{-3}$	$2.79 \cdot 10^{-3}$	$6.51 \cdot 10^{-3}$
0.025	$9.27 \cdot 10^{-4}$	$4.08 \cdot 10^{-4}$	$9.50 \cdot 10^{-4}$
0.0125	$1.40 \cdot 10^{-4}$	$5.54 \cdot 10^{-5}$	$1.30 \cdot 10^{-4}$
0.00625	$2.07 \cdot 10^{-5}$	$7.33 \cdot 10^{-6}$	$1.73 \cdot 10^{-5}$

Table 4.3 – Relative errors $\xi_{\boldsymbol{H}}$ for different mesh sizes h for $\left(\frac{\nabla\times\boldsymbol{H}}{\sigma}\right)_{\text{jump}} = 0$.

For each test, the error $\xi_{\boldsymbol{H}}$ varies like $O(h^3)$, that we can also see in figure 4.6. These results validate the numerical solver.

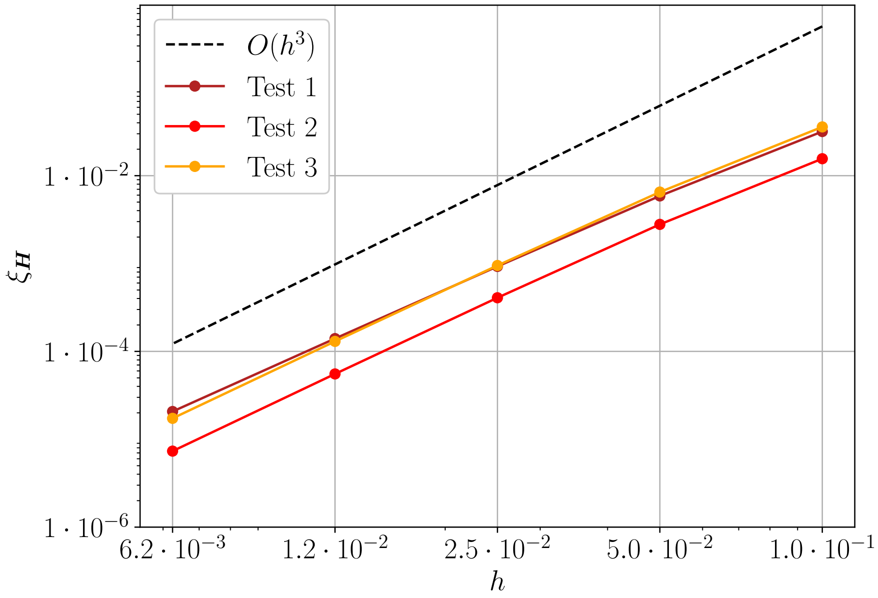

Figure 4.6 – Order of convergence of $\xi_{\boldsymbol{H}}$ when $\left(\frac{\nabla\times\boldsymbol{H}}{\sigma}\right)_{\text{jump}} = 0$ as a function of the mesh size h for different tests. The dashed line represents the theoretical order of convergence h^3.

Tests with jump

The second set of tests is done for a case with an interface and a jump of the tangential components of the electrical current. The electrical conductivities are $\sigma_1 = 10^4$ and $\sigma_2 = 1$, and the magnetic permeability $\mu = 1$. The jump is fixed to $\left(\frac{\nabla\times\boldsymbol{H}}{\sigma}\right)_{\text{jump}} = \nabla\times\boldsymbol{H}\left(\frac{1}{\sigma_1} - \frac{1}{\sigma_2}\right)_{|\Sigma}$. We run the following tests:

- **Test 4**: mode $m = 0$, $k = \kappa_{01}$.
- **Test 5**: mode $m = 1$, $k = \kappa_{11}$.
- **Test 6**: mode $m = 2$, $k = \kappa_{21}$.

We report the relative error $\xi_{\boldsymbol{H}}$ in table 4.4.

h	Test 4	Test 5	Test 6
0.1	$3.53 \cdot 10^{-1}$	$4.53 \cdot 10^{-2}$	$3.93 \cdot 10^{-2}$
0.05	$3.18 \cdot 10^{-2}$	$4.22 \cdot 10^{-3}$	$6.82 \cdot 10^{-3}$
0.025	$2.29 \cdot 10^{-3}$	$4.63 \cdot 10^{-4}$	$9.79 \cdot 10^{-4}$
0.0125	$2.10 \cdot 10^{-4}$	$5.74 \cdot 10^{-5}$	$1.31 \cdot 10^{-4}$
0.00625	$2.38 \cdot 10^{-5}$	$7.46 \cdot 10^{-6}$	$1.74 \cdot 10^{-5}$

Table 4.4 – Relative errors $\xi_{\boldsymbol{H}}$ for different mesh sizes h for $\left(\frac{\nabla\times\boldsymbol{H}}{\sigma}\right)_{\text{jump}} \neq 0$.

For each test, the error $\xi_{\boldsymbol{H}}$ varies like $O(h^3)$, that we can also see in figure 4.7. These results validate the numerical solver.

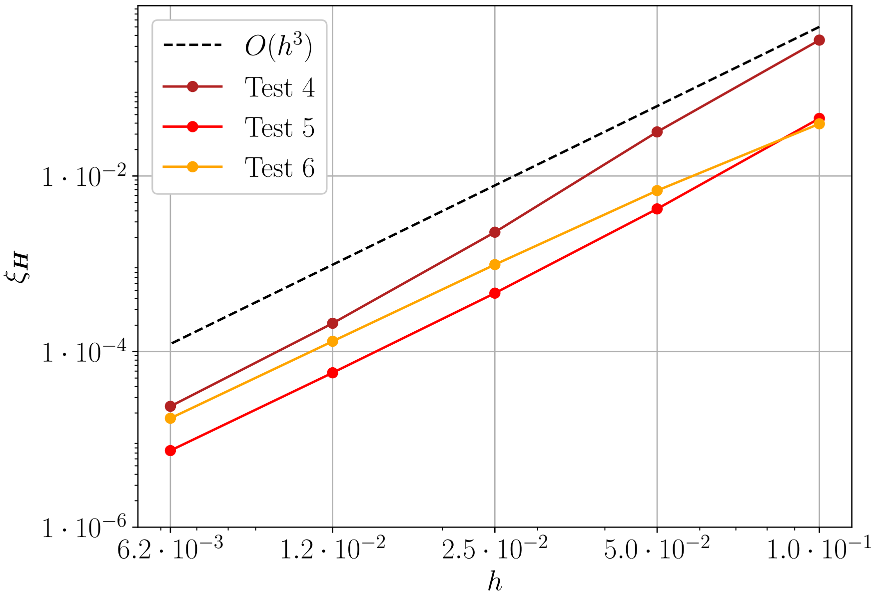

Figure 4.7 – Order of convergence of $\xi_{\boldsymbol{H}}$ when $\left(\frac{\nabla\times\boldsymbol{H}}{\sigma}\right)_{\text{jump}} \neq 0$ as a function of the mesh size h for different tests. The dashed line represents the theoretical order of convergence h^3.

4.5 Comparison between both formulations

In this section, we show that both formulations are equivalent. For this purpose, we compare the electrical current obtained, which should be the same. We first determine equivalent analytical solutions in order to validate the numerical solutions. We validate our solver first in a cylinder like in sections §4.3.4 and §4.4.4. Then we extend our validation in an LMB setup.

4.5.1 Determination of equivalent analytical solutions

Analytical solutions without jump

We found in section §4.3.3 the following analytical solution for the problem in φ

$$\varphi(r,\theta,z) = J_m(kr)e^{im\theta}e^{kz}.$$

We want to find the equivalent magnetic field $\boldsymbol{H}$. We know that the electrical current $\boldsymbol{j}$ verifies $\boldsymbol{j} = \nabla\times\boldsymbol{H}$ and $\boldsymbol{j} = -\sigma\nabla\varphi$. Thus $\boldsymbol{H}$ must verify

$$\nabla\times\boldsymbol{H} = -\sigma\nabla\varphi, \tag{4.5.1a}$$
$$\nabla\cdot\boldsymbol{H} = 0. \tag{4.5.1b}$$

$\boldsymbol{H}$ can be written such as $\boldsymbol{H} = \nabla\times(\mathcal{T}\boldsymbol{e}_z)$ with $\mathcal{T}$ a scalar.
First $\nabla\cdot\boldsymbol{H} = \nabla\cdot(\nabla\times(\mathcal{T}\boldsymbol{e}_z)) = 0$, therefore (4.5.1b) is verified.
Then let us calculate $(\nabla\times\boldsymbol{H})\cdot\boldsymbol{e}_z$.
On one hand $(\nabla\times\boldsymbol{H})\cdot\boldsymbol{e}_z = (\nabla\times\nabla\times(\mathcal{T}\boldsymbol{e}_z))\cdot\boldsymbol{e}_z = (-\nabla^2(\mathcal{T}\boldsymbol{e}_z)+\nabla(\partial_z\mathcal{T}))\cdot\boldsymbol{e}_z = -\nabla_T^2\mathcal{T}$ (where ∇_T^2 is the tangential laplacian).
On the other hand $(\nabla\times\boldsymbol{H})\cdot\boldsymbol{e}_z = -\sigma\partial_z\varphi$.
Hence $\mathcal{T}$ is solution of $\nabla_T^2\mathcal{T} = \sigma\partial_z\varphi$.

Let us take $\mathcal{T}$ as $\mathcal{T} = AJ_m(kr)e^{im\theta}e^{kz}$ where A is a constant. This yields

$$\nabla_T^2\mathcal{T} = \frac{1}{r}\partial_r(r\partial_r\mathcal{T})+\frac{1}{r^2}\partial^2_{\theta\theta}\mathcal{T} = Ae^{im\theta}e^{kz}\left(\partial^2_{rr}J_m(kr)+\frac{1}{r}\partial_rJ_m(kr)-\frac{m^2}{r^2}J_m(kr)\right) = -k^2AJ_m(kr)e^{im\theta}e^{kz}.$$

However $\sigma \partial_z \varphi = \sigma k J_m(kr) e^{im\theta} e^{kz}$.
This leads to $A = -\dfrac{\sigma}{k}$ and thus $\mathcal{T} = -\dfrac{\sigma}{k} J_m(kr) e^{im\theta} e^{kz}$.

We deduce $\boldsymbol{H}$ from $\mathcal{T}$:

$$\boldsymbol{H} = \boldsymbol{\nabla} \times (\mathcal{T} \boldsymbol{e}_z) = -\frac{\sigma}{2} e^{im\theta} e^{kz} \left| \begin{array}{l} i(J_{m+1}(kr) + J_{m-1}(kr)) \\ J_{m+1}(kr) - J_{m-1}(kr) \\ 0 \end{array} \right.$$

and, after having taken the real part of this solution,

$$\boldsymbol{H} = -\frac{\sigma}{2} e^{kz} \left| \begin{array}{l} -(J_{m+1}(kr) + J_{m-1}(kr)) \sin(m\theta) \\ (J_{m+1}(kr) - J_{m-1}(kr)) \cos(m\theta) \\ 0 \end{array} \right. . \tag{4.5.2}$$

This solution of the magnetic field problem is equivalent to the electrical potential $\varphi(r, \theta, z) = J_m(kr) e^{im\theta} e^{kz}$.

Analytical solutions with jump

In a case with $\varphi_{\text{jump}} \neq 0$, an analytical solution of the problem in φ is (see equation (4.3.16)):

$$\left\{ \begin{array}{l} \varphi_1(r, \theta, z) = J_m(kr) e^{im\theta} e^{kz}, \\ \varphi_2(r, \theta, z) = \dfrac{\sigma_1}{\sigma_2} J_m(kr) e^{im\theta} e^{kz}. \end{array} \right.$$

$$\varphi_{\text{jump}} = \left(1 - \frac{\sigma_1}{\sigma_2}\right) J_m(kr) e^{im\theta} e^{kH}.$$

The equivalent solution for the magnetic field $\boldsymbol{H}$ must be continuous at the interface and must verify

$$\left(\frac{\boldsymbol{\nabla} \times \boldsymbol{H}_1}{\sigma_1} - \frac{\boldsymbol{\nabla} \times \boldsymbol{H}_2}{\sigma_2} \right) \times \boldsymbol{e}_z = -\boldsymbol{\nabla}_T (\varphi_1 - \varphi_2) \times \boldsymbol{e}_z \quad \text{on } \Sigma. \tag{4.5.3}$$

In each subdomain, we define $\mathcal{T}_1$ and $\mathcal{T}_2$ such as $\boldsymbol{H}_1 = \boldsymbol{\nabla} \times (\mathcal{T}_1 \boldsymbol{e}_z)$ and $\boldsymbol{H}_2 = \boldsymbol{\nabla} \times (\mathcal{T}_2 \boldsymbol{e}_z)$.
From the last section, we can find $\mathcal{T}_1$ and $\mathcal{T}_2$ from φ_1 and φ_2

$$\left\{ \begin{array}{l} \mathcal{T}_1(r, \theta, z) = -\dfrac{\sigma_1}{k} J_m(kr) e^{im\theta} e^{kz}, \\ \mathcal{T}_2(r, \theta, z) = -\dfrac{\sigma_2}{k} \dfrac{\sigma_1}{\sigma_2} J_m(kr) e^{im\theta} e^{kz} = -\dfrac{\sigma_1}{k} J_m(kr) e^{im\theta} e^{kz}. \end{array} \right.$$

We remark that $\mathcal{T}_1 = \mathcal{T}_2$, that we will denote $\mathcal{T}$. Then $\boldsymbol{H}$ is indeed continuous on Σ.
We now show that this solution respects (4.5.3).
On one hand

$$-\boldsymbol{\nabla}(\varphi_1 - \varphi_2) \times \boldsymbol{e}_z = -\left(1 - \frac{\sigma_1}{\sigma_2}\right) e^{im\theta} e^{kz_1} \left| \begin{array}{l} \dfrac{im}{r} J_m(kr) \\ -k J_m'(kr) \\ 0 \end{array} \right.$$

On the other hand

$$\begin{aligned}
\left(\frac{\nabla\times \boldsymbol{H}_1}{\sigma_1} - \frac{\nabla\times \boldsymbol{H}_2}{\sigma_2}\right)\times \boldsymbol{e}_z &= \left| \begin{array}{l} \frac{1}{r}\left(\frac{1}{\sigma_1}\partial_\theta\partial_z\mathcal{T} - \frac{1}{\sigma_2}\partial_\theta\partial_z\mathcal{T}\right)\\ -\frac{1}{\sigma_1}\partial_r\partial_z\mathcal{T}+\frac{1}{\sigma_2}\partial_r\partial_z\mathcal{T}\\ 0\end{array}\right. \\
&= \left| \begin{array}{l} \frac{1}{r}\left(\frac{1}{\sigma_1} - \frac{1}{\sigma_2}\right) im(-\sigma_1)J_m(kr)e^{im\theta}e^{kz}\\ \left(\frac{1}{\sigma_2} - \frac{1}{\sigma_1}\right) k(-\sigma_1)J'_m(kr)e^{im\theta}e^{kz}\\ 0\end{array}\right. \\
&= -\left(1-\frac{\sigma_1}{\sigma_2}\right)e^{im\theta}e^{kz}\left| \begin{array}{l} \frac{im}{r}J_m(kr)\\ -kJ'_m(kr)\\ 0.\end{array}\right.
\end{aligned}$$

Hence we have indeed (4.5.3) for $z = z_1$ at the interface.
We deduce $\boldsymbol{H}$ from $\mathcal{T}$ like in the previous section. Therefore, the solution

$$\boldsymbol{H} = -\frac{\sigma_1}{2}e^{kz}\left| \begin{array}{l} -(J_{m+1}(kr)+J_{m-1}(kr))\sin(m\theta)\\ (J_{m+1}(kr)-J_{m-1}(kr))\cos(m\theta)\\ 0\end{array}\right. \tag{4.5.4}$$

is equivalent to the problem (4.5.3).

4.5.2 Numerical investigations in a cylinder

In this section, we show that the two solvers are equivalent (i.e. they give the same electrical current) in the domain $\boldsymbol{\Omega}$ defined in section §4.3.1. We study two cases, a case without a jump (single domain) and then a case with a jump on the interface Σ. Here we compare the numerical solutions with the analytical solutions found in section §4.5.1. To compare the results, we define two relative errors in L^2-norm of the electrical current $\boldsymbol{j}$

$$\zeta_\varphi = \frac{\|\boldsymbol{j}_\varphi - \boldsymbol{j}_{\text{ex}}\|_2}{\|\boldsymbol{j}_{\text{ex}}\|_2}, \zeta_{\boldsymbol{H}} = \frac{\|\boldsymbol{j}_{\boldsymbol{H}} - \boldsymbol{j}_{\text{ex}}\|_2}{\|\boldsymbol{j}_{\text{ex}}\|_2}, \tag{4.5.5}$$

where $\boldsymbol{j}_\varphi$ is the numerical electrical current obtained with the $\varphi-$solver, $\boldsymbol{j}_{\boldsymbol{H}}$ the numerical electrical current obtained with the $\boldsymbol{H}-$solver, and $\boldsymbol{j}_{\text{ex}}$ the analytical solution. These errors are expected to vary like $O(h^2)$. We will show this by calculating the rate of convergence defined by

$$\text{rate} = \log\left(\frac{\zeta_i - \zeta_{i-1}}{h_i - h_{i-1}}\right) \tag{4.5.6}$$

where ζ is equal to ζ_φ or $\zeta_{\boldsymbol{H}}$, and i is an index. The rate is expected to be around 2.

Tests in a cylinder without jump

The first set of tests is done in the cylinder $\boldsymbol{\Omega}$ for a case with no interface and then no jump. The electrical conductivity is $\sigma = 1$, and the magnetic permeability $\mu = 1$. We use the analytical solution with no jump from section §4.5.1 defined as follows

$$\varphi(r,\theta,z) = J_m(kr)e^{im\theta}e^{kz}$$

$$\boldsymbol{H} = -\frac{\sigma}{2} e^{kz} \left| \begin{array}{l} -(J_{m+1}(kr) + J_{m-1}(kr))\sin(m\theta) \\ (J_{m+1}(kr) - J_{m-1}(kr))\cos(m\theta) \\ 0 \end{array} \right. .$$

We run the following tests

- **Test 1**: mode $m = 0$, $k = \kappa'_{01}$.
- **Test 2**: mode $m = 1$, $k = \kappa'_{11}$.
- **Test 3**: mode $m = 2$, $k = \kappa'_{21}$.

We report the relative errors ζ_φ and $\zeta_{\boldsymbol{H}}$ in three tables 4.5, 4.6, 4.7 which gather the rates and the relative errors for the tests 1, 2 and 3, respectively.

	φ-solver		$\boldsymbol{H}$-solver	
h	ζ_φ	Rate	$\zeta_{\boldsymbol{H}}$	Rate
0.1	$1.34 \cdot 10^{-2}$	-	$1.02 \cdot 10^{-2}$	-
0.05	$4.37 \cdot 10^{-3}$	1.62	$7.53 \cdot 10^{-3}$	2.30
0.025	$1.22 \cdot 10^{-3}$	1.84	$1.55 \cdot 10^{-3}$	2.28
0.0125	$3.07 \cdot 10^{-4}$	1.99	$3.70 \cdot 10^{-4}$	2.07
0.00625	$7.72 \cdot 10^{-5}$	1.99	$9.14 \cdot 10^{-5}$	2.01

Table 4.5 – Case with no jump, test 1 ($m = 0$). Rate of convergence and relative errors ζ_φ and $\zeta_{\boldsymbol{H}}$ for different mesh sizes h.

	φ-solver		$\boldsymbol{H}$-solver	
h	ζ_φ	Rate	$\zeta_{\boldsymbol{H}}$	Rate
0.1	$3.50 \cdot 10^{-3}$	-	$6.70 \cdot 10^{-3}$	-
0.05	$9.52 \cdot 10^{-4}$	1.88	$1.61 \cdot 10^{-3}$	2.06
0.025	$2.48 \cdot 10^{-4}$	1.94	$3.80 \cdot 10^{-4}$	2.08
0.0125	$6.29 \cdot 10^{-5}$	1.98	$9.34 \cdot 10^{-5}$	2.02
0.00625	$1.57 \cdot 10^{-5}$	2.00	$2.27 \cdot 10^{-5}$	2.04

Table 4.6 – Case with no jump, test 2 ($m = 1$). Rate of convergence and relative errors ζ_φ and $\zeta_{\boldsymbol{H}}$ for different mesh sizes h.

	φ-solver		$\boldsymbol{H}$-solver	
h	ζ_φ	Rate	$\zeta_{\boldsymbol{H}}$	Rate
0.1	$6.42 \cdot 10^{-3}$	-	$1.47 \cdot 10^{-2}$	-
0.05	$1.88 \cdot 10^{-3}$	1.77	$3.41 \cdot 10^{-3}$	2.11
0.025	$5.41 \cdot 10^{-4}$	1.80	$7.94 \cdot 10^{-4}$	2.10
0.0125	$1.37 \cdot 10^{-4}$	1.98	$1.97 \cdot 10^{-4}$	2.01
0.00625	$3.46 \cdot 10^{-5}$	1.99	$4.91 \cdot 10^{-5}$	2.00

Table 4.7 – Case with no jump, test 3 ($m = 2$). Rate of convergence and relative errors ζ_φ and $\zeta_{\boldsymbol{H}}$ for different mesh sizes h.

All the errors vary like $O(h^2)$, as shown by the values of the rates which are around 2. Moreover, the solutions converge to the same limit. This shows that the two solvers give equivalent results.

Tests in a cylinder with jump

The second set of tests is done in the cylinder $\boldsymbol{\Omega}$ for a case with an interface and a jump. The electrical conductivities are $\sigma_1 = 10^4$ and $\sigma_2 = 1$, and the magnetic permeability $\mu = 1$. We use the analytical solution with a jump from section §4.5.1:

$$\begin{cases} \varphi_1(r,\theta,z) = J_m(kr)e^{im\theta}e^{kz}, \\ \varphi_2(r,\theta,z) = \dfrac{\sigma_1}{\sigma_2} J_m(kr)e^{im\theta}e^{kz} \end{cases}$$

$$\varphi_{\text{jump}} = \left(1 - \frac{\sigma_1}{\sigma_2}\right) J_m(kr)e^{im\theta}e^{kH}$$

$$\boldsymbol{H} = -\frac{\sigma_1}{2}e^{kz} \left| \begin{array}{l} -(J_{m+1}(kr) + J_{m-1}(kr))\sin(m\theta) \\ (J_{m+1}(kr) - J_{m-1}(kr))\cos(m\theta) \\ 0 \end{array} \right.$$

We run the following tests

- **Test 4**: mode $m = 0$, $k = \kappa'_{01}$.
- **Test 5**: mode $m = 1$, $k = \kappa'_{11}$.
- **Test 6**: mode $m = 2$, $k = \kappa'_{21}$.

We report the relative errors ζ_φ and $\zeta_{\boldsymbol{H}}$ in three tables 4.8, 4.9, 4.10 which gather the rates and the relative errors for the tests 4, 5 and 6, respectively.

	φ-solver		$\boldsymbol{H}$-solver	
h	ζ_φ	Rate	$\zeta_{\boldsymbol{H}}$	Rate
0.1	$1.34 \cdot 10^{-2}$	-	$3.72 \cdot 10^{-2}$	-
0.05	$4.37 \cdot 10^{-3}$	1.62	$7.54 \cdot 10^{-3}$	2.30
0.025	$1.22 \cdot 10^{-3}$	1.84	$1.55 \cdot 10^{-3}$	2.28
0.0125	$3.07 \cdot 10^{-4}$	1.99	$3.70 \cdot 10^{-4}$	2.06
0.00625	$7.72 \cdot 10^{-5}$	1.99	$9.14 \cdot 10^{-5}$	2.02

Table 4.8 – Case with jump, test 4 ($m = 0$). Rate of convergence and relative errors ζ_φ and $\zeta_{\boldsymbol{H}}$ for different mesh sizes h.

	φ-solver		$\boldsymbol{H}$-solver	
h	ζ_φ	Rate	$\zeta_{\boldsymbol{H}}$	Rate
0.1	$3.52 \cdot 10^{-3}$	-	$1.63 \cdot 10^{-2}$	-
0.05	$9.53 \cdot 10^{-4}$	1.89	$2.62 \cdot 10^{-3}$	2.64
0.025	$2.48 \cdot 10^{-4}$	1.94	$3.40 \cdot 10^{-4}$	2.95
0.0125	$6.28 \cdot 10^{-5}$	1.98	$6.97 \cdot 10^{-5}$	2.29
0.00625	$1.57 \cdot 10^{-5}$	2.00	$1.70 \cdot 10^{-5}$	2.04

Table 4.9 – Case with jump, test 5 ($m = 1$). Rate of convergence and relative errors ζ_φ and $\zeta_{\boldsymbol{H}}$ for different mesh sizes h.

All the errors vary like $O(h^2)$, as shown by the values of the rates which are around 2. Moreover, the solutions converge to the same limit. This shows that the two solvers give equivalent results. In figure 4.8 are shown snapshots of results obtained with the test 4 ($m = 0$ and a jump in electrical potential) on a meridian plane, for $h = 0.025$. In figure 4.8a, we display the azimuthal component of the magnetic field (all the other components are zero) and the current

	φ-solver		$\boldsymbol{H}$-solver	
h	ζ_φ	Rate	$\zeta_{\boldsymbol{H}}$	Rate
0.1	$6.43 \cdot 10^{-3}$	-	$2.14 \cdot 10^{-2}$	-
0.05	$1.88 \cdot 10^{-3}$	1.77	$3.88 \cdot 10^{-3}$	2.46
0.025	$5.41 \cdot 10^{-4}$	1.80	$7.79 \cdot 10^{-4}$	2.31
0.0125	$1.37 \cdot 10^{-4}$	1.98	$1.88 \cdot 10^{-4}$	2.05
0.00625	$3.46 \cdot 10^{-5}$	1.99	$4.69 \cdot 10^{-5}$	2.00

Table 4.10 – Case with jump, test 6 ($m = 2$). Rate of convergence and relative errors ζ_φ and $\zeta_{\boldsymbol{H}}$ for different mesh sizes h.

density obtained with the $\boldsymbol{H}$-solver. Figure 4.8b shows the electrical potential and the current density obtained with the φ-solver. The current density field is identical for both formulations. We remark that the electrical potential presents indeed a jump at the interface, whereas the magnetic field is continuous.

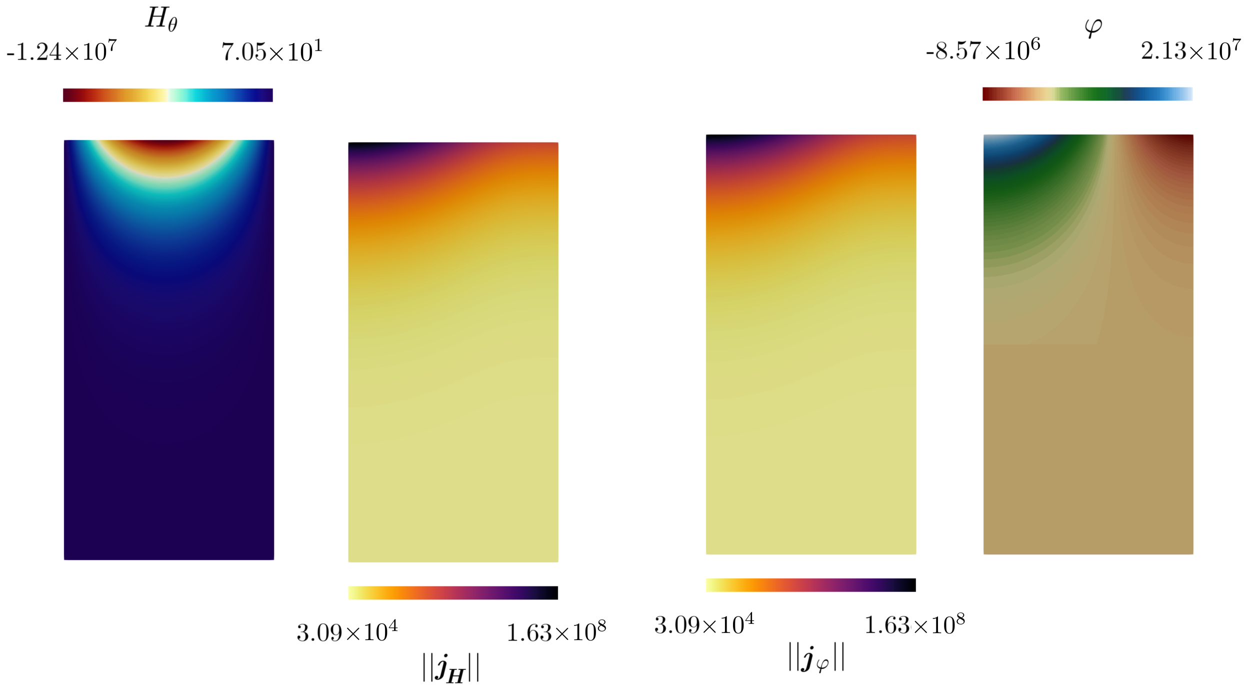

(a)

(b)

Figure 4.8 – Snapshots of fields obtained with both solvers represented on a meridian plane. (a) $\boldsymbol{H}$-solver, left: magnetic field H_θ and right: current density. (b) φ-solver, left: current density and right: electrical potential φ.

4.5.3 Numerical investigations in a liquid metal battery

In order to validate our solvers in a geometry that we will use afterwards, we now compare both formulations in a Li||Pb LMB setup, solving neither the concentration nor the velocity. We choose a setup really similar to the one studied by Weber et al. (2019), where the lithium is contained in a foam. The only differences with the original setup are that we do not model the side walls for simplicity, and we choose a cylindrical foam (and not spherical at the bottom). The current collectors are made of copper, we recall that $\sigma_{\mathrm{Cu}} = 5.8 \cdot 10^7\,\mathrm{Sm}^{-1}$. The negative electrode (the foam) is composed of steel and lithium. The electrical conductivity of pure lithium is $\sigma_{\mathrm{Li}} = 2.7 \cdot 10^6\,\mathrm{Sm}^{-1}$ and the conductivity of steel is equal to $1.5 \cdot 10^6\,\mathrm{Sm}^{-1}$. These two values have the same order of magnitude. Hence, the electrical conductivity of the negative electrode can be approximated by σ_{Li}. We take the same conductivity for the alloy and the electrolyte as in section §2.2.2, $\sigma = 7.39 \cdot 10^5\,\mathrm{Sm}^{-1}$ and $\sigma_e = 187\,\mathrm{Sm}^{-1}$. A scheme of the setup is shown in figure 4.9a, where the dimensions of the setup are given. We denote the height of the whole cell $\mathcal{H}_{\mathrm{cell}}$, its radius R and the radius of the top current collector R_w. The vertical coordinate z is set to 0 at the bottom of the cell. In figure 4.9b is represented a meridian plane of the battery which is used for the representation of snapshots in the following because the simulations are axisymmetric. The colored lines represent the profiles used for figures 4.10b and 4.11b. The mesh is non-uniform, the mesh size h varies in the range $[0.00025, 0.0005]$ m.

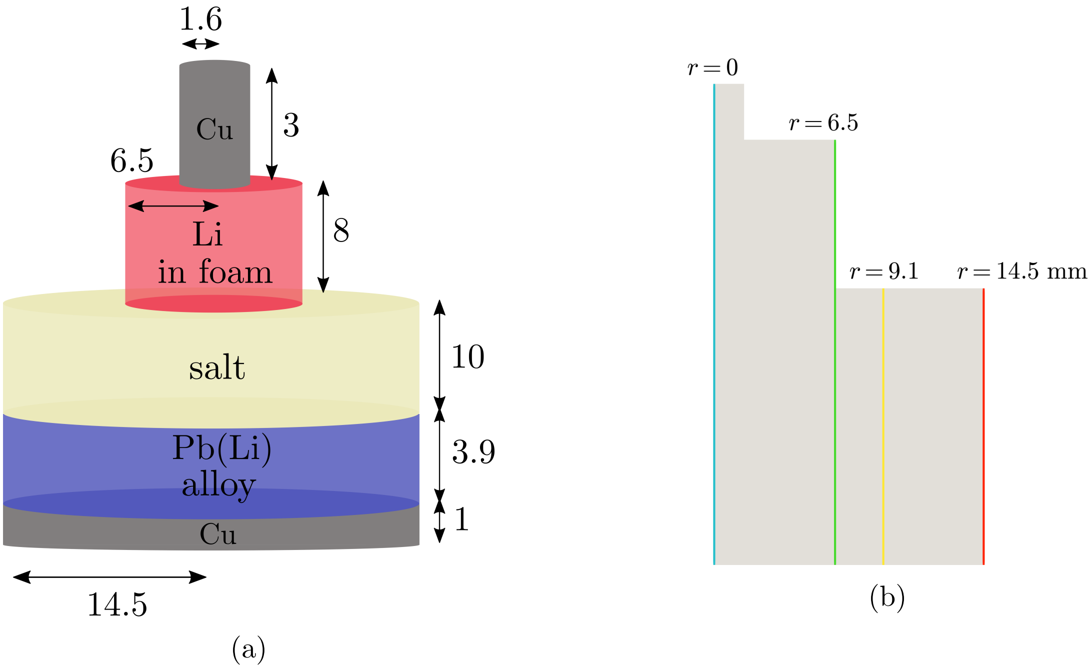

(a) (b)

Figure 4.9 – (a) Scheme of the LMB setup used for the comparison between both formulations. The dimensions are in mm. (b) Scheme of a meridian plane of the setup with colored lines used for the profiles in figures 4.10b and 4.11b.

We study two cases, a case with a constant jump in electrical potential and a case with a jump in electrical potential depending in r.
For the potential, we solve the following problem

$$-\nabla \cdot (\sigma_i \nabla \varphi) = 0 \quad \text{in all domains,} \tag{4.5.7a}$$

$$\varphi_{\mathrm{alloy}} - \varphi_{\mathrm{electrolyte}} = \varphi_{\mathrm{jump}} \quad \text{at the alloy-electrolyte interface} \tag{4.5.7b}$$

where σ_i are the different conductivities of the domains. We impose a constant potential at the bottom of the cell. We fix the electrical current $I = 1$ A. We impose no flux of current at the lateral border. This yields the following boundary conditions

$$\begin{aligned}
-\sigma_{\mathrm{w}}\, \partial_z \varphi|_{z=\mathcal{H}_{\mathrm{cell}}} &= \frac{I}{\pi R_w^2}, && (4.5.8a)\\
\partial_n \varphi|_{r\geq R_w, z>0} &= 0, && (4.5.8b)\\
\varphi|_{z=0} &= 0 && (4.5.8c)
\end{aligned}$$

where σ_{w} is the electrical conductivity of the current collectors.
For the magnetic field,

$$\begin{aligned}
\boldsymbol{\nabla} \times \left(\frac{\boldsymbol{\nabla} \times \boldsymbol{H}}{\sigma_i} \right) &= \mathbf{0} && \text{in all domains,} && (4.5.9a)\\
\boldsymbol{\nabla} \cdot (\mu \boldsymbol{H}) &= \mathbf{0} && \text{in all domains,} && (4.5.9b)\\
\left(\frac{\boldsymbol{\nabla} \times \boldsymbol{H}_{\mathrm{alloy}}}{\sigma} - \frac{\boldsymbol{\nabla} \times \boldsymbol{H}_{\mathrm{electrolyte}}}{\sigma_e} \right) \times \boldsymbol{n} &= \left(\frac{\boldsymbol{\nabla} \times \boldsymbol{H}}{\sigma} \right)_{\mathrm{jump}} \times \boldsymbol{n} && \text{at the alloy-electrolyte interface.} && (4.5.9c)
\end{aligned}$$

Here, $\mu = \mu_0$ the permeability of vacuum and σ_e the conductivity of the electrolyte.
In order to be able to compare both solvers, we have to find equivalent boundary conditions for the magnetic field.
At the bottom, $\varphi|_{z=0} = 0$ for all $\{r, \theta\}$ means that $\partial_r \varphi|_{z=0} = 0$ i.e. $-j_r\, \sigma_{\mathrm{Cu}}^{-1}|_{z=0} = 0$ and $\partial_\theta \varphi|_{z=0} = 0$ i.e. $-r\, j_\theta\, \sigma_{\mathrm{Cu}}^{-1}|_{z=0} = 0$. Thus $\boldsymbol{j} \times \boldsymbol{n}|_{z=0} = \mathbf{0}$ i.e. $(\boldsymbol{\nabla} \times \boldsymbol{H}) \times \boldsymbol{n}|_{z=0} = \mathbf{0}$.
On the other borders, Dirichlet boundary conditions for the magnetic field can be found using Ampère's law at a radial coordinate a (like in chapter 3):

$$H_\theta|_{r=a} = \frac{1}{a} \int_0^a j_z r dr \qquad (4.5.10)$$

This yields

$$H_\theta|_{z=\mathcal{H}_{\mathrm{cell}}} = \frac{I}{2\pi R_w^2} r, \qquad H_\theta|_{r\geq R_w, z>0} = \frac{I}{2\pi r}. \qquad (4.5.11)$$

We use hence the following boundary conditions for $\boldsymbol{H}$, equivalent to equations (4.5.8):

$$\begin{aligned}
H_\theta|_{z=\mathcal{H}_{\mathrm{cell}}} &= \frac{I}{2\pi R_w^2} r, && (4.5.12a)\\
H_\theta|_{r\geq R_w, z>0} &= \frac{I}{2\pi r}, && (4.5.12b)\\
(\boldsymbol{\nabla} \times \boldsymbol{H}) \times \boldsymbol{n}|_{z=0} &= \mathbf{0} && (4.5.12c)
\end{aligned}$$

and $H_r = H_z = 0$ on all borders.

Tests with a constant jump in electrical potential

We first study a simple case where the jump in potential is constant, $\varphi_{\text{jump}} = 0.8$ V for all $\boldsymbol{r}$ at the alloy-electrolyte interface. The equivalent jump for the magnetic field is $\left(\frac{\boldsymbol{\nabla}\times\boldsymbol{H}}{\sigma}\right)_{\text{jump}} = \boldsymbol{0}$. The results are gathered in figure 4.10. Using the φ-solver, we show in figure 4.10a a snapshot of the obtained electrical potential. We remark the constant jump of 0.8 V at the alloy-electrolyte interface. This jump can also be noticed in figure 4.10b, where we plot the electrical potential as a function of z at different radii $\boldsymbol{r}$. The profile along the z-axis is coherent with the profile obtained by Weber et al. (2019) in a Li||Bi battery. Figure 4.10c shows streamlines of the electrical current $\boldsymbol{j}$ computed with the two solvers. These streamlines are colored by the amplitude of j_z. This figure highlights that the electrical current obtained with both formulations is identical as expected.

Tests with a jump in electrical potential depending on r

Secondly we study a case where the jump in potential depends on r such as $\varphi_{\text{jump}} = J_0(kr)$ (in V), where $k = \kappa'_{01}/R$. The equivalent jump for the magnetic field is $\left(\frac{\boldsymbol{\nabla}\times\boldsymbol{H}}{\sigma}\right)_{\text{jump}} = -kJ'_0(kr)\boldsymbol{e}_r$. The results are gathered in figure 4.11. Using the φ-solver, we show in figure 4.11a a snapshot of the obtained electrical potential. We remark that the jump varies with $\boldsymbol{r}$ at the alloy-electrolyte interface. This jump can also be noticed in figure 4.11b, where we plot the electrical potential as a function of z at different radii $\boldsymbol{r}$. Figure 4.11c shows streamlines of the electrical current $\boldsymbol{j}$ computed with the two solvers. These streamlines are colored by the amplitude of j_z. This figure highlights that the electrical current obtained with both formulations is identical as expected. We can notice the current loop due to the change of sign of the jump along the interface.

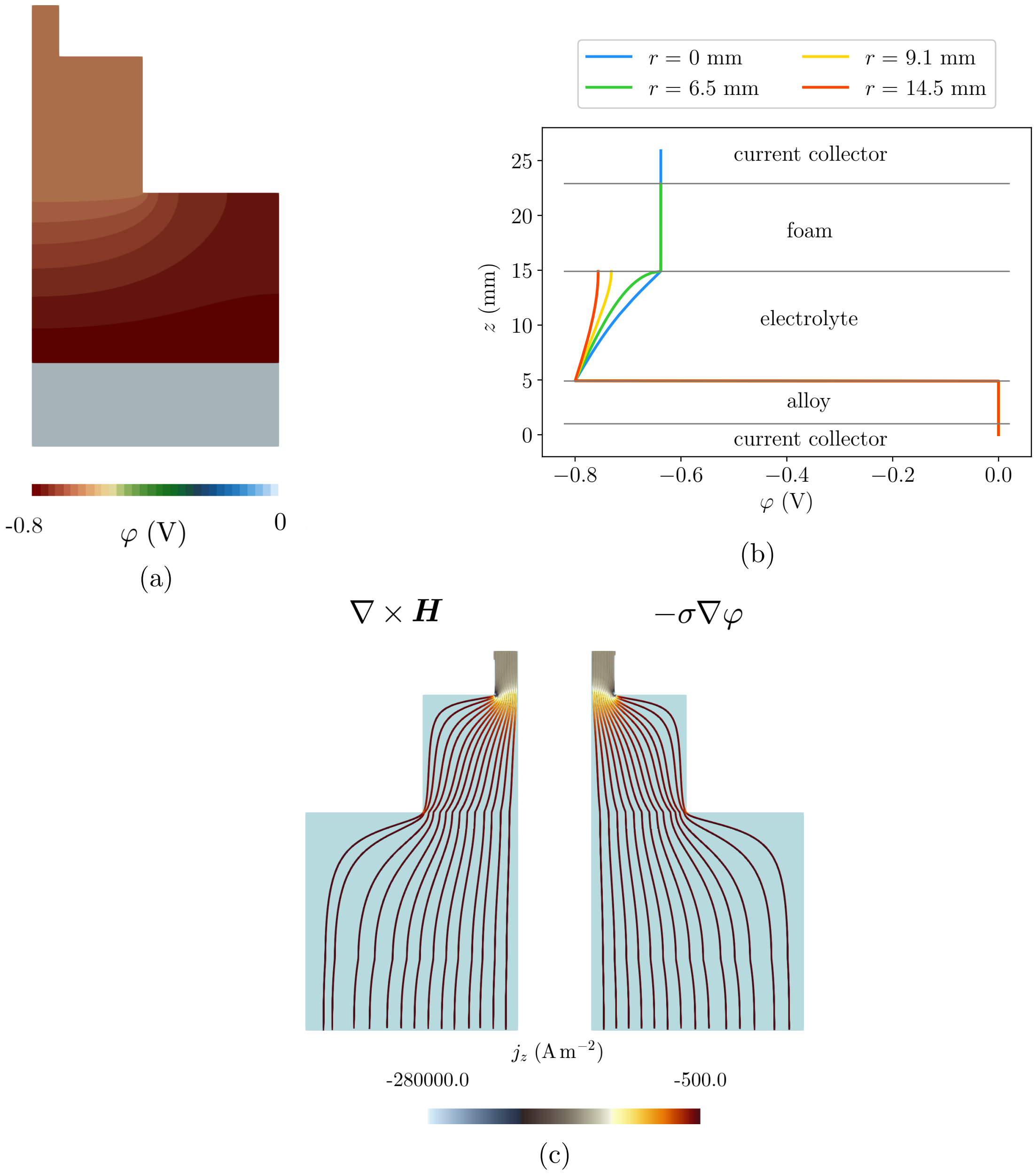

Figure 4.10 – Case with a constant jump in electrical potential φ_{jump} = -0.8 V. (a) Snapshot of the electrical potential φ in a meridian plane. (b) Profile of the electrical potential vs z at different radii $\boldsymbol{r}$, defined in figure 4.9b. (c) Streamlines of the current density $\boldsymbol{j}$ colored with amplitude of j_z using both formulations, in a meridian plane: (left) $\boldsymbol{H}$-solver (right) φ-solver.

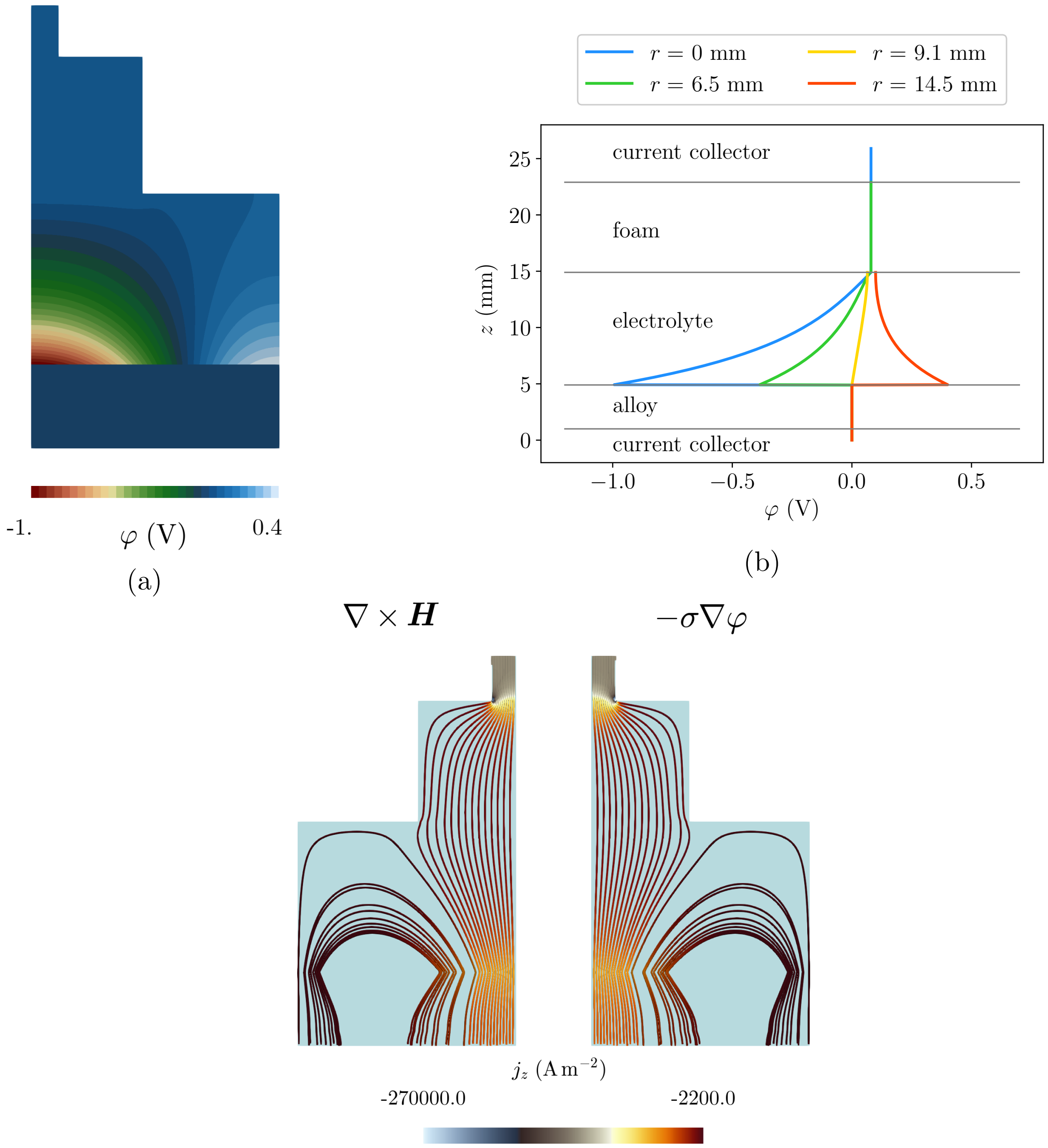

(a)

(b)

(c)

Figure 4.11 – Case with a jump in electrical potential φ_{jump} = - $J_0(kr)$ (in V). (a) Snapshot of the electrical potential φ in a meridian plane. (b) Profile of the electrical potential vs z at different radii r, defined in figure 4.9b. (c) Streamlines of the current density $\boldsymbol{j}$ colored with amplitude of j_z using both formulations, in a meridian plane: (left) $\boldsymbol{H}$-solver; (right) φ-solver.

4.6 Conclusion

In this chapter, we have proposed a new magnetic field based formulation to model discontinuous electrical potential distributions. Indeed, a jump in electrical potential φ_{jump} can be linked to a jump in the tangential components of the rotational of the magnetic field $\left(\frac{\boldsymbol{\nabla}\times\boldsymbol{H}}{\sigma}\right)_{\text{jump}}$ with the formula

$$\boldsymbol{n}\times\left(\frac{\boldsymbol{\nabla}\times\boldsymbol{H}}{\sigma}\right)_{\text{jump}} = -\boldsymbol{n}\times\boldsymbol{\nabla}_T(\varphi_{\text{jump}}). \tag{4.6.1}$$

We have developed a finite element code solving the electrical problem and validated it in a cylinder subdivided in one or two domains, by comparing the numerical solutions to analytical solutions. Then, we have implemented the magnetic field-based interface condition (4.6.1) in a finite element code solving the magnetic problem and validated it in the same cylinder, using the same method for the validation. We have finally shown that both formulations are equivalent by comparing the current density obtained in both cases with analytical solutions, in the cylinder as well as in a liquid metal battery setup.

Now that these developments are realized, it is necessary to extend the study by adding the concentration and the velocity to be able to analyze the impact of the jump in electrical potential on the concentration and current distributions. This work is done in chapter 5.

Chapter 5

Influence of the electrical potential on the alloy composition and on the cell potential

5.1 Introduction

In an LMB, the electrical potential distribution is complex. A jump in electrical potential appears at the alloy-electrolyte interface. This jump has been ignored in most of the studies, and has been considered only recently in a few studies (Duczek et al., 2023; Weber et al., 2019, 2020). These latter do not provide comparison with other simulations without jump in potential, therefore, the impact of the potential jump on the current and concentration distributions, as well as on the cell potential, is not easy to distinguish from other physical phenomena.

Our goal is to understand the effect of the jump in potential on the alloy composition. We consider an LMB setup with a foam electrode, which is a setup more often used in the experiments than the three-liquid layer setup. The foam has a thinner radius than the alloy. During discharge, the material flux in the alloy is inhomogeneous at the alloy-electrolyte interface and we expect a higher concentration close to the axis than on the lateral borders (figure 5.1).

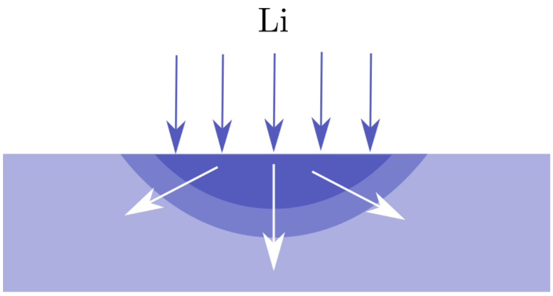

Figure 5.1 – Scheme of the diffusion process in the alloy in a foam setup.

The effects of the EVF and the solutal buoyancy, that we have already studied in this thesis, are also different from chapter 2 due to the foam. The thinner current collector is above the alloy, and not below like in section §2.2. The EVF is then induced in the opposite direction, and brings the lithium towards the axis (figure 5.2a). The buoyancy term impacts the vertical velocity and depends on local densities in the alloy. Because the alloy-electrolyte interface is not homogeneous, the alloy density is lower at the center - richer in lithium - than on the sides. Thus, the vertical velocity is directed downwards everywhere with a higher amplitude on the sides. We expect an almost homogeneous alloy in the radial direction (figure 5.2b).

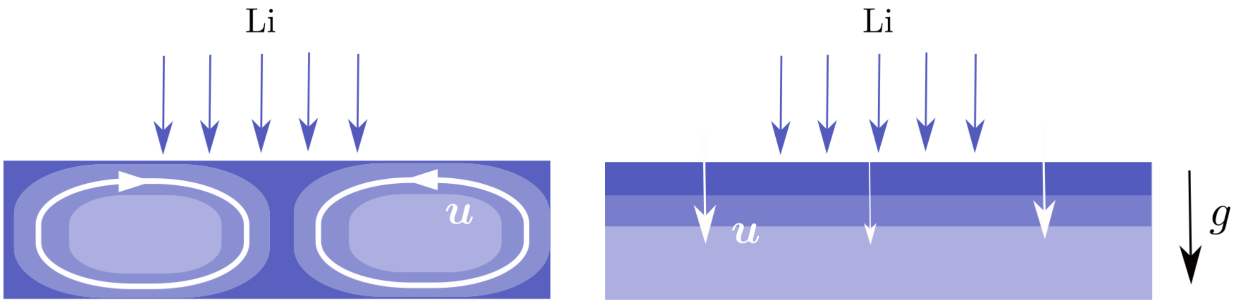

(a) (b)

Figure 5.2 – Scheme of the (a) EVF and (b) buoyancy effects in the alloy in a foam setup.

Now we wish to understand how the potential jump influences the alloy. A scheme of the process is shown on figure 5.3. Since the electrical potential (red line) is almost homogeneous in the alloy, it varies only in the electrolyte. The inhomogeneity of the alloy-electrolyte interface yields an inhomogeneity of the potential jump along the interface. The jump in electrical potential decreases with the molar fraction. We expect then a lower jump at the center ($\varphi_{\text{jump},-}$) than on the sides ($\varphi_{\text{jump},+}$). Therefore, the electrical potential in the electrolyte just above the interface alloy-electrolyte is higher at the center (φ_+) than on the borders (φ_-). A radial current j_r is then induced, directed from the axis to the sides. The current distribution in the electrolyte is modified and the vertical current j_z decreases on the axis and increases on the borders. Thus, an homogenization of the material flux, proportional to j_z, occurs.

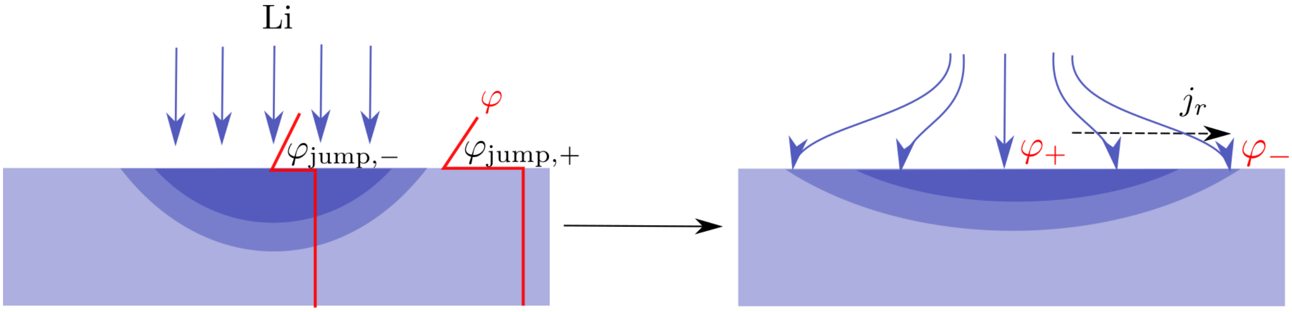

Figure 5.3 – Scheme of the current redistribution and the homogenization of the alloy by the potential jump.

We expect therefore a redistribution of the current in the electrolyte and of the material flux due to the potential jump. How much does this redistribution impact the alloy composition? Do the conclusions of enhanced mixing by flows (section §1.3.3) remain valid?
We have seen in chapter 1 that the jump defines the electrical potential distribution and consequently the total potential of the cell. In section §2.2 of chapter 2, we have ignored the potential jump and computed the cell potential in post-processing from the surface averaged molar fraction. This computation is not self-consistent. The cell potential is affected by local variations of the potential at the alloy-electrolyte interface and taking a surface average ignores these local variations. Is a self-consistent way of computation significantly different from the post-processed computation from the surface averaged molar fraction? How much does the potential jump impact the cell potential?

In chapter 4, we have found a new magnetic field-based interface condition to model the jump at the alloy-electrolyte interface. Now that we have developed this formulation, we can improve our solver by coupling the potential jump along the alloy-electrolyte interface to the local alloy concentration. In our model, we will solve the magnetic field, the flow and the concentration. We first present the new model used in this chapter. Then, we present some numerical details on the development of the concentration variable in SFEMaNS, that we call the c-solver. Later, we compare the φ-solver with the results of Weber et al. (2019) and validate the $\boldsymbol{H}$-solver coupled with the c-solver, using the φ-solver. Once this is done, we conduct a study on the effect of the potential jump. We compare simulations with and without jump, in a small and a larger LMB setups, and study the effect of the jump on the flow and the alloy composition. We also compare different ways of computation of the cell potential.

5.2 Model

We consider a cylindrical Li||Pb liquid metal battery and use the same setup as in section §4.5.3 of chapter 4. The lithium in the negative electrode is contained in a foam, considered as solid and composed of pure lithium in the simulations. The current collectors are assumed to be made of copper that has an electrical conductivity $\sigma_{\mathrm{Cu}} = 5.8 \cdot 10^{-7}\,\mathrm{S\,m^{-1}}$. The material properties of the Li-Pb alloy are given in section §2.2.2 of chapter 2.

We study two different setups, with different dimensions but a similar shape, shown in figure 5.4. We denote $\boldsymbol{R}$ and $\boldsymbol{R}_w$ the radius of the cell and the radius of the upper current collector, respectively, and $\mathcal{H}_{\mathrm{cell}}$ the total height of the cell. The vessel which contains the phases (light grey on the sketch) is not modeled.

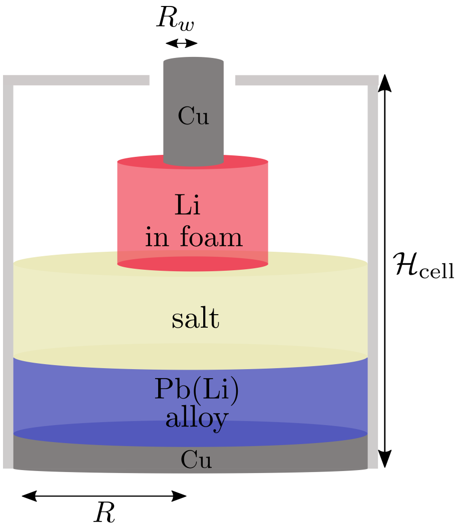

Figure 5.4 – Sketch of the LMB setups. Dimensions are specified below.

5.2.1 Electrical potential formulation with concentration

We first develop a model which solves the electrical potential variable φ and the concentration c. Solving the velocity requires to compute the Lorentz force $\boldsymbol{j} \times \boldsymbol{b}$. While the current density $\boldsymbol{j}$ can be easily computed from the electrical potential φ, obtaining the magnetic field $\boldsymbol{b}$ from the current density $\boldsymbol{j}$ is not trivial. Biot-Savart's law gives $\boldsymbol{b}$ from $\boldsymbol{j}$, but its computation is not easy. Therefore, we do not solve the velocity in this formulation.

This model will allow us to reproduce the results of Weber et al. (2019), without any flow, and to compare its results with the ones of our magnetic field-based model described in section §5.2.2.

The electrical potential formulation is based on the formulation in φ defined in chapter 4. The electrical potential φ is then solution in all domains of the equation

$$\nabla \cdot (\sigma_i \boldsymbol{\nabla} \varphi) = 0 \tag{5.2.1}$$

where σ_i are the different electrical conductivities of the domains.
We fix the total current I. This yields the same boundary conditions as in section §4.5.3:

$$\begin{aligned} \sigma_{\mathrm{Cu}} \partial_z \varphi|_{z=\mathcal{H}_{\mathrm{cell}}} &= \frac{I}{\pi R_w^2}, && (5.2.2a) \\ \partial_n \varphi|_{r>R_w} &= 0, && (5.2.2b) \\ \varphi|_{z=0} &= 0. && (5.2.2c) \end{aligned}$$

At the alloy-electrolyte interface, the jump in electrical potential is imposed as:

$$\varphi_{\mathrm{alloy}} - \varphi_{\mathrm{electrolyte}} = \varphi_{\mathrm{jump}}. \tag{5.2.3}$$

φ_{jump} is a function of the local molar fraction of lithium at the interface $x|_\Sigma$,

$$\varphi_{\mathrm{jump}} = \Phi(x|_\Sigma) \tag{5.2.4}$$

where Φ is the open-circuit voltage. We remind that

$$\Phi(x) = \alpha - \beta(x - x_*) \tag{5.2.5}$$

where $x_* = 0.17$, $\alpha = 0.614$ V and $\beta = 0.598$ V. The jump induces a new coupling between the potential and the molar fraction, absent in chapter 2. We will talk about the jump coupling in what follows.
The concentration c of lithium in the alloy is solution of the diffusion equation

$$\partial_t c \ = \ D \nabla^2 c \tag{5.2.6}$$

where $D = 8 \cdot 10^{-9}\,\mathrm{m}^2\mathrm{s}^{-1}$ is the diffusion coefficient. At the alloy-electrolyte interface, denoted Σ, the material flux depends here on the local electrical current density:

$$D \partial_z c|_\Sigma \ = \ -\frac{j_z}{n_e F} \tag{5.2.7}$$

where F is the Faraday constant. Unlike in section §2.2.2, the current density at the alloy-electrolyte interface is not homogeneous. It is computed as $\boldsymbol{j} = -\sigma \boldsymbol{\nabla} \varphi$. The material flux is zero at the other boundaries of the alloy ($\partial_n c = 0$).

5.2.2 Magnetic field formulation with concentration and velocity

We develop a second model which solves the magnetic field variable $\boldsymbol{b}$, the concentration c and the velocity $\boldsymbol{u}$. Unlike the previous model based on the electrical potential, the Lorentz force can be easily computed since $\boldsymbol{j} = \mu_0^{-1} \nabla \times \boldsymbol{b}$.
This model will be compared to the previous model with the electrical potential, and will be

used to conduct the studies of this chapter.

The magnetic field based formulation in this model is described in chapter 4. This model, unlike in section §2.2, uses the magnetostatic approximation. In our simulations, the velocity and thus the magnetic Reynolds number remain low. The magnetostatic approximation is then valid, which is consistent with the models used in the literature of liquid metal batteries (Personnettaz et al. (2020); Weber et al. (2018b, 2019) for instance).

In all domains, the magnetic field $\boldsymbol{H}$ is solution of the equations

$$\begin{aligned} \boldsymbol{\nabla} \times \left(\frac{\boldsymbol{\nabla} \times \boldsymbol{H}}{\sigma_i} \right) &= \boldsymbol{0}, && (5.2.8a) \\ \boldsymbol{\nabla} \cdot \boldsymbol{H} &= 0 && (5.2.8b) \end{aligned}$$

where σ_i are the different electrical conductivities of the domains.

The equivalent magnetic field boundary conditions are (see section §4.5.3)

$$\begin{aligned} H_\theta|_{z=\mathcal{H}_{\text{cell}}} &= \frac{I}{2\pi R_w^2} r, && (5.2.9a) \\ H_\theta|_{r>R_w} &= \frac{I}{2\pi r}, && (5.2.9b) \\ (\boldsymbol{\nabla} \times \boldsymbol{H}) \times \boldsymbol{n}|_{z=0} &= \boldsymbol{0}. && (5.2.9c) \end{aligned}$$

In axisymmetric simulations, $H_r = H_z = 0$ everywhere.

In chapter 4, we have shown that a jump in electrical potential is equivalent to a jump in the tangential component of the electrical field $\boldsymbol{E} = \left(\frac{\boldsymbol{\nabla} \times \boldsymbol{H}}{\sigma}\right)$. Hence, at the alloy-electrolyte interface Σ

$$\left(\frac{\boldsymbol{\nabla} \times \boldsymbol{H}}{\sigma} \right)_{\text{jump}} \times \boldsymbol{n} = -\boldsymbol{\nabla}_T(\varphi_{\text{jump}}) \times \boldsymbol{n} = -\boldsymbol{\nabla}(\Phi(x|_\Sigma)) \times \boldsymbol{n}. \qquad (5.2.10)$$

In the alloy, we solve the concentration field c as well as the velocity field $\boldsymbol{u}$. c is solution of the advection-diffusion equation

$$\partial_t c + \boldsymbol{u} \cdot \boldsymbol{\nabla} c = D \nabla^2 c. \qquad (5.2.11)$$

The material flux of Li at the alloy-electrolyte interface is the same as in the model with the electrical potential:

$$D \partial_z c|_\Sigma = -\frac{j_z}{n_e F} \qquad (5.2.12)$$

At the other boundaries of the alloy, this flux is zero. The current density $\boldsymbol{j}$ is this time computed as $\boldsymbol{j} = \boldsymbol{\nabla} \times \boldsymbol{H}$.

The flow field $\boldsymbol{u}$ is solution of the Boussinesq model

$$\begin{aligned} \rho_*(\partial_t \boldsymbol{u} + (\boldsymbol{u} \cdot \boldsymbol{\nabla})\boldsymbol{u}) &= -\boldsymbol{\nabla} p - \rho(c) g \boldsymbol{e}_z + \boldsymbol{\nabla} \cdot (\rho_* \nu (\boldsymbol{\nabla} u + (\boldsymbol{\nabla} u)^T) + \boldsymbol{j} \times \boldsymbol{b} && (5.2.13a) \\ \nabla \cdot \boldsymbol{u} &= 0 && (5.2.13b) \end{aligned}$$

where p is the pressure, g the gravity, μ_0 the magnetic permeability of vacuum, and $\boldsymbol{b} = \mu_0 \boldsymbol{H}$ the magnetic field. We recall that the density $\rho(c)$ of the alloy depends on the concentration c through the constitutive law (see section §2.2.2)

$$\rho(c) = \rho_* - \chi \mathcal{M}_{\text{Li}}(c - c_*). \qquad (5.2.14)$$

Here, $\rho_* = 9543 \, \text{kg} \, \text{m}^{-3}$, $\chi = 15.1$ and $c_* = 9365 \, \text{mol} \, \text{m}^{-3}$.

In real LMBs, the electrolyte is subject to fluid motion. Yet, modeling also the flow in the

electrolyte requires a multiphase model. Combining the mass transfer model with a multiphase approach is quite difficult to do, therefore we decided to neglect the flow in the electrolyte. At the alloy-electrolyte interface, we then impose free-slip boundary conditions. This approximation is not necessarily better than the no-slip boundary conditions that were used in section §2.2.2, but these conditions allow more fluid motion near the interface. On the other borders of the alloy, no-slip boundary conditions are used.
The simulations start with the eutectic alloy, $c = c_*$ and $\boldsymbol{u} = \boldsymbol{0}$.

5.2.3 Computation of the electrical potential using the magnetic field

The electrical potential of the cell E_{cell} is the difference between the potentials at the top and the bottom of the cell. In the φ-solver, $E_{\text{cell}} = \varphi_{\text{bot}} - \varphi_{\text{top}}$, where φ_{top} (resp. φ_{bot}) is the potential at the top (resp. bottom) of the cell. In the $\boldsymbol{H}$-solver, the potential variable is not directly accessible, but it can be computed from the current density. Indeed, in each domain, we still have $\boldsymbol{j} = -\sigma_i \nabla\varphi$. Thus, integrating $\sigma_i^{-1}\boldsymbol{j}$ along a line gives the electrical potential φ. The line the most accessible is the vertical axis. If the vertical coordinate z is above the alloy-electrolyte interface, the discontinuity due to the jump has to be taken into account. We can then deduce, the potential on the axis as given by:

$$\varphi(z) = \begin{cases} \int_0^z -\dfrac{\boldsymbol{j}}{\sigma_i}\cdot \boldsymbol{e}_z dz & \text{if } z \text{ is below } \Sigma, \\ \int_0^z -\dfrac{\boldsymbol{j}}{\sigma_i}\cdot \boldsymbol{e}_z dz \; - \; \varphi_{\text{jump}}|_{r=0} & \text{otherwise} \end{cases}$$

Since the potential is constant at the top and at the bottom of the cell, we deduce the cell potential:

$$E_{\text{cell}} = \varphi_{\text{bot}} - \varphi_{\text{top}} = \varphi_{\text{jump}}|_{r=0} - \int_0^{\mathcal{H}_{\text{cell}}} -\frac{\boldsymbol{j}}{\sigma_i}\cdot \boldsymbol{e}_z dz \tag{5.2.15}$$

Because of the high electrical conductivities of the metals, the electrical potential is almost constant in these layers, i.e. the ohmic losses are very little. Therefore, we can focus on the ohmic losses in the electrolyte η_Ω only. Hence, E_{cell} can be approximated by

$$E_{\text{cell}} \simeq \varphi_{\text{jump}}|_{r=0} - \eta_\Omega. \tag{5.2.16}$$

where $\eta_\Omega = \int_{\text{electrolyte}} -\dfrac{\boldsymbol{j}}{\sigma_i}\cdot \boldsymbol{e}_z dz.$
Considering the formula (1.2.4) of chapter 1, we notice that $\varphi_{\text{jump}}|_{r=0} = E_{\text{cell,eq}} - \eta_{\text{mt}}$.
To compute the mass transfer overpotential, we need to know $E_{\text{cell,eq}}$. It corresponds to the cell potential in the ideal scenario, when the alloy is everywhere perfectly blended and homogeneous. We can compute $E_{\text{cell,eq}} = \Phi(\langle x\rangle_{\mathcal{V}})$, where $\langle x\rangle_{\mathcal{V}}$ is the averaged molar fraction on the volume. Hence, η_{mt} is computed such as:

$$\eta_{\text{mt}} = |E_{\text{cell}} - E_{\text{cell,eq}} + \eta_\Omega|. \tag{5.2.17}$$

5.3 Numerical development in SFEMaNS: adding the concentration variable

Before this PhD, the concentration variable c was not explicitly present in SFEMaNS. In the previous studies realized, we have used the analogous temperature variable to compute the concentration. Indeed, temperature and concentration are both solutions of an advection-diffusion equation and so we could use this solver. However, it could be interesting in the future to be able to compute both the temperature and the concentration. Therefore, we have chosen to add in SFEMaNS the concentration field by developing a c-solver.

5.3.1 Temporal advancement in SFEMaNS

Unlike the problem studied in chapter 4, the problem we want to solve is now time-dependent. In SFEMaNS, for the temporal advancement, the solver uses a constant time-step δt. At each iteration the time t is incremented by δt. We denote t_n the time after n iterations. The time derivatives are decomposed according to the second-order Backward Difference Formula (BDF2). After having discretized the concentration and velocity variables (the discretized variables are denoted with the index h), this yields at t_{n+1}

$$\partial_t c_h^{n+1} = \frac{3c_h^{n+1} - 4c_h^n + c_h^{n-1}}{2\delta t} + O(\delta t^2), \qquad \partial_t \boldsymbol{u}_h^{n+1} = \frac{3\boldsymbol{u}_h^{n+1} - 4\boldsymbol{u}_h^n + \boldsymbol{u}_h^{n-1}}{2\delta t} + O(\delta t^2).$$

where c_h^{n+1}, c_h^n, c_h^{n-1} (resp. $\boldsymbol{u}_h^{n+1}$, $\boldsymbol{u}_h^n$, $\boldsymbol{u}_h^{n-1}$) are the concentration (resp. the velocity) at the times t_{n+1}, t_n, t_{n-1}, respectively. We recall that we use the magnetostatic approximation, there is no time derivative for the magnetic field.

The use of an implicit scheme improves the numerical stability. Equation (5.2.11) becomes at t_{n+1}

$$\frac{3c_h^{n+1}}{2\delta t} + D\nabla^2 c_h^{n+1} = \frac{4c_h^n - c_h^{n-1}}{2\delta t} - \boldsymbol{u}_h^{*,n+1}\boldsymbol{\nabla} c_h^{*,n+1}. \tag{5.3.1}$$

Equation (5.2.13a) is first rewritten as

$$\partial_t \boldsymbol{u} + (\boldsymbol{u}\cdot\boldsymbol{\nabla})\boldsymbol{u} = -\boldsymbol{\nabla}\hat{p} + 2\nu\boldsymbol{\nabla}\cdot(\boldsymbol{\nabla}^S\boldsymbol{u}) - \boldsymbol{f}_\rho + \boldsymbol{f}_L \tag{5.3.2}$$

where we denote $\boldsymbol{f}_L = \boldsymbol{j}\times\mu_0\boldsymbol{H}/\rho_*$ the Lorentz force, $\boldsymbol{f}_\rho = (\rho(c)/\rho_*)g\boldsymbol{e}_z$ the buoyancy term and $\hat{p} = p/\rho_* + 1/2\,\boldsymbol{u}^2$ a modified pressure. We also denote

$$\boldsymbol{\nabla}^S\boldsymbol{u} = \frac{1}{2}(\boldsymbol{\nabla}\boldsymbol{u} + (\boldsymbol{\nabla}\boldsymbol{u})^T).$$

This yields at t_{n+1}

$$\frac{3\boldsymbol{u}_h^{n+1}}{2\delta t} - 2\nu\boldsymbol{\nabla}\cdot(\boldsymbol{\nabla}^S\boldsymbol{u}_h^{n+1}) = \frac{4\boldsymbol{u}_h^n - \boldsymbol{u}_h^{n-1}}{2\delta t} - \boldsymbol{\nabla}\hat{p}^n - (\boldsymbol{u}_h^{*,n+1}\cdot\boldsymbol{\nabla})\boldsymbol{u}_h^{*,n+1} - \boldsymbol{f}_{\rho,h}^{*,n+1} + \boldsymbol{f}_{L,h}^{*,n+1}. \tag{5.3.3}$$

The unknown variables in the right-hand side are approximated such as

$$\begin{aligned} c_h^{n+1} &= c_h^{*,n+1} \quad \text{with} \quad c_h^{*,n+1} = 2c_h^n - c_h^{n-1},\\ \boldsymbol{u}_h^{n+1} &= \boldsymbol{u}_h^{*,n+1} \quad \text{with} \quad \boldsymbol{u}_h^{*,n+1} = 2\boldsymbol{u}_h^n - \boldsymbol{u}_h^{n-1},\\ \boldsymbol{H}_h^{n+1} &= \boldsymbol{H}_h^{*,n+1} \quad \text{with} \quad \boldsymbol{H}_h^{*,n+1} = 2\boldsymbol{H}_h^n - \boldsymbol{H}_h^{n-1}. \end{aligned}$$

The velocity equation is solved with a prediction-correction method, which ensures a weak velocity divergence. This method has been first proposed by Timmermans et al. (1996), then adapted and validated by Guermond and Shen (2004).
We now detail the time-marching algorithm. The domains where each variable is solved are denoted Ω_c, $\Omega_{\boldsymbol{u}}$ and $\Omega_{\boldsymbol{H}}$ for the variables c, $\boldsymbol{u}$ and $\boldsymbol{H}$, respectively. First, both the fields at t_0 and t_1 are initialized with the given initial condition. Then, for $n > 1$, at t_n, the concentration field c_h^n is solved on Ω_c using $u_h^{*,n}$ and $\boldsymbol{H}_h^{*,n}$. Later, c_h^n is mapped on $\Omega_{\boldsymbol{u}}$, so that c_h^n is known on $\Omega_{\boldsymbol{u}}$. The velocity $\boldsymbol{u}_h^n$ is determined using c_h^n and $\boldsymbol{H}_h^{*,n}$. Finally, c_h^n is mapped on $\Omega_{\boldsymbol{H}}$ and the magnetic field is updated using c_h^n. The last step is to increment t_n by δt, and the same process is realized at t_{n+1}.
During this thesis, we have implemented this algorithm in the solver.

5.3.2 Validation of the c-solver

For the validation of the c-solver, we compare numerical solutions to analytical solutions. We focus on a case without flow.
Equation (5.2.11) becomes without velocity

$$\partial_t c = D\nabla^2 c. \tag{5.3.5}$$

A simple solution of this equation is

$$c(z,t) = \mathrm{e}^{-Dk^2 t}\cos(kz) \tag{5.3.6}$$

where k is a constant.
We are looking for a simple test in a cylinder with a radius R and a height $\mathcal{H}$, where material flux g is imposed at the top of a domain ($\partial_z c_{|z=\mathcal{H}} = g$), and the flux is zero on the other borders ($\partial_n c = 0$).
With solution (5.3.6), at $z = 0$, $\partial_z c = 0$ for all k. At $r = R$, $\partial_r c = 0$ is always verified because the solution does not depend on r. At $z = \mathcal{H}$, $\partial_z c_{|z=\mathcal{H}} = -k\mathrm{e}^{-Dk^2 t}\sin(k\mathcal{H})$. We impose then the flux $g = -k\mathrm{e}^{-Dk^2 t}\sin(k\mathcal{H})$ at $z = \mathcal{H}$.

For the numerical tests, we use non-dimensional variables. We consider a cylinder with a height $\mathcal{H} = 0.5$ and a radius $R = 1$. The diffusion coefficient is fixed to $D = 10^{-2}$. We fix $k = \pi/(2\mathcal{H})$.
We define the relative error in L^2-norm of c

$$\xi_c = \frac{||c_{\text{num}} - c_{\text{ex}}||_2}{c_{\text{ex}}} \tag{5.3.7}$$

where c_{num} is the numerical solutions and c_{ex} the analytical one. The error is expected to vary like $O(h^3) + O(\delta t^2)$ where h is the mesh-size and δt the time-step.

We run a first series of tests where we fix $\delta t = 10^{-4}$ and vary h. The relative errors ξ_c are reported in table 5.1a at two different times $t = 5\cdot 10^{-3}$ and $t = 5\cdot 10^{-2}$.
For both times t, we find that the error ξ_c varies like $O(h^3)$ (see figure 5.5a).

We run a second test where we fix $h = 0.0125$ and vary δt. The relative errors ξ_c are reported in table 5.1b at $t = 1$. The error ξ_c varies like $O(\delta t^2)$ for large δt, and becomes constant when δt becomes lower than a certain value. That can also be seen in figure 5.5b. For low δt, the error is dominated by the spatial error in $O(h^3)$, which explains why it becomes independent of δt. Notice that the limit reached when δt decreases is equal to ξ_c when $h = 0.0125$ in table 5.1a.
These results validate the c-solver.

h	$t = 5 \cdot 10^{-3}$	$t = 5 \cdot 10^{-2}$
0.1	$5.60 \cdot 10^{-6}$	$1.60 \cdot 10^{-5}$
0.05	$1.04 \cdot 10^{-6}$	$1.84 \cdot 10^{-6}$
0.025	$1.35 \cdot 10^{-7}$	$1.67 \cdot 10^{-7}$
0.0125	$1.46 \cdot 10^{-8}$	$1.52 \cdot 10^{-8}$
0.00625	$1.34 \cdot 10^{-9}$	$1.34 \cdot 10^{-9}$

(a)

δt	$t = 1$
1×10^{0}	$2.21 \cdot 10^{-4}$
5×10^{-1}	$6.43 \cdot 10^{-5}$
1×10^{-1}	$3.11 \cdot 10^{-6}$
5×10^{-2}	$7.96 \cdot 10^{-7}$
1×10^{-2}	$3.58 \cdot 10^{-8}$
5×10^{-3}	$1.72 \cdot 10^{-8}$
1×10^{-3}	$1.52 \cdot 10^{-8}$
5×10^{-4}	$1.52 \cdot 10^{-8}$
1×10^{-4}	$1.52 \cdot 10^{-8}$

(b)

Table 5.1 – (a) Relative errors ξ_c for different mesh-sizes h with $\delta t = 10^{-4}$. (b) Relative errors ξ_c for different time steps δt with $h = 0.0125$.

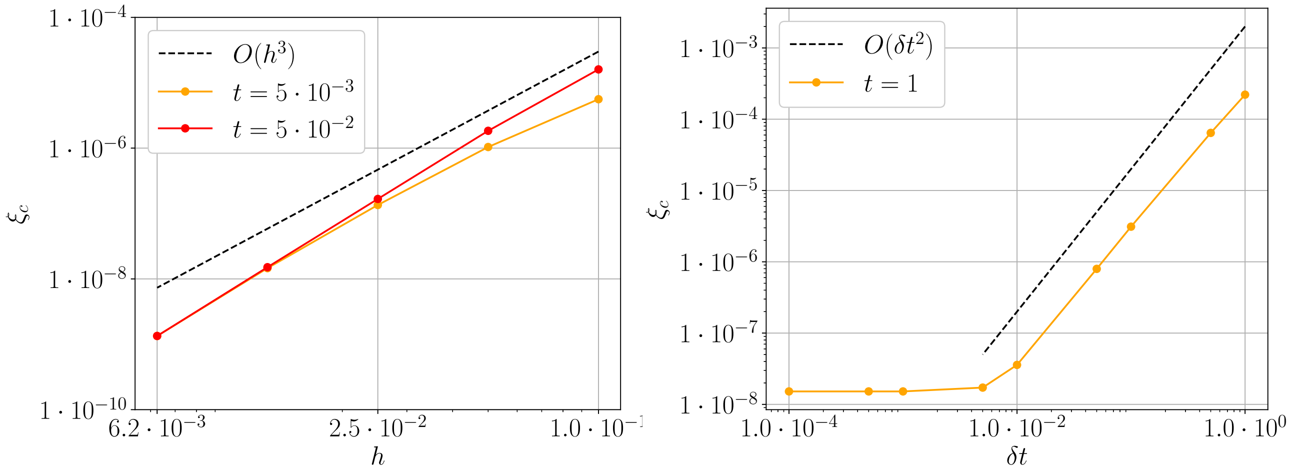

(a)

(b)

Figure 5.5 – (a) Order of convergence of ξ_c as a function of the mesh size h, at different times $t = 5 \cdot 10^{-3}$ and $t = 5 \cdot 10^{-2}$. The dashed line represents the theoretical order of convergence h^3. (b) Order of convergence of ξ_c as a function of the time step δt at $t = 1$. The dashed line represents the theoretical order of convergence t^2.

5.4 Investigation of the φ- and $\boldsymbol{H}$-solvers coupled with the c-solver in an LMB

In this section, we investigate the coherence of our numerical results with previous studies. We first compare the numerical results of the φ-solver coupled with the c-solver to the simulations of Weber et al. (2019), without flow. Then, we show that the $\boldsymbol{H}$-solver coupled with the c-solver give results very similar to those of the φ-solver. We only run axisymmetric simulations. The mesh is non-uniform, the mesh size h varies in the range $[0.00025, 0.0005]$ m.

The investigation is done in the same LMB setup that was used in section §4.5.3. This cell is a simplification of the setup studied by Weber et al. (2019), which is inspired from an experimental LMB setup, and shown on figure 5.6a. The setup that we have used is given in figure 5.6b. In the simplifications, we consider a cylindrical foam instead of a spherical foam, and we do not model the vessel made in tantalum (light grey). We only use copper current collectors. We will show that this simplified setup yields results similar to those of the original setup.

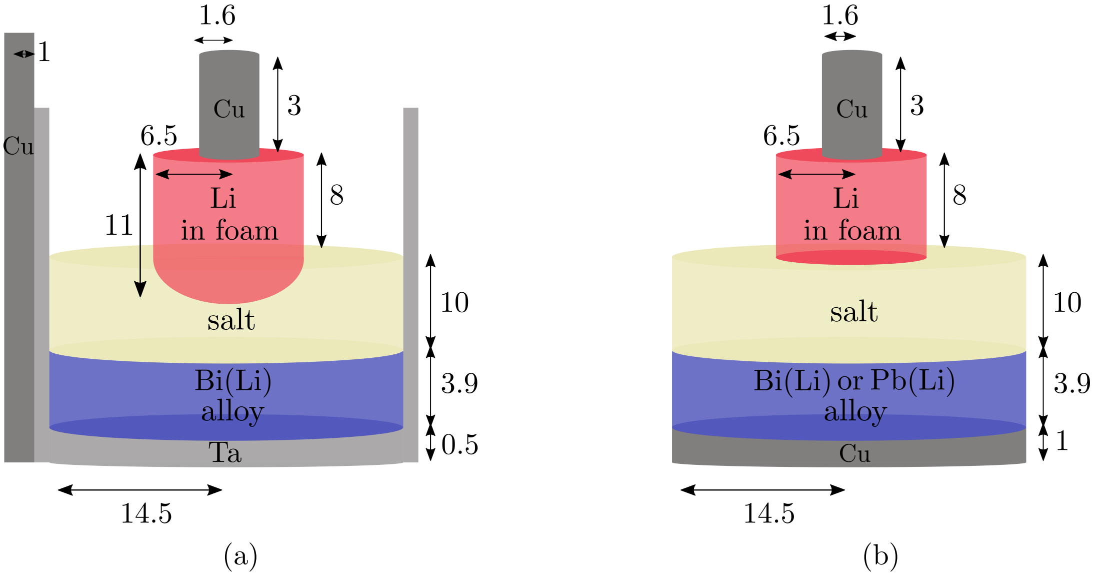

Figure 5.6 – (a) Scheme of the LMB setup used in Weber et al. (2019). (b) Scheme of the simplified LMB setup that we use in the simulations. The dimensions are in mm.

5.4.1 Comparison of the φ-solver coupled with the c-solver to the results of Weber et al. (2019)

In this section, we compare the numerical results of the φ-solver coupled with the c-solver to the study of Weber et al. (2019). We use the simplified setup of figure 5.6b. We consider a Li||Bi LMB as in Weber et al. (2019), where the material properties are modified with respect to Li||Pb properties. We take for the alloy the diffusion coefficient $D = 2 \cdot 10^{-8}\,\mathrm{m^2s^{-1}}$ and the electrical conductivity $\sigma = 7.2 \cdot 10^5\,\mathrm{Sm^{-1}}$. The electrical conductivity of the electrolyte is $\sigma_{\mathrm{el}} = 271\,\mathrm{Sm^{-1}}$ (Weber et al., 2019). The density of the alloy can be computed from the concentration of lithium c with the law (Wax et al., 2011):

$$\rho(c) = -1.3 \cdot 10^{-6}\, c^2 - 0.0382\, c + 9780.$$

Using this law, we can deduce the relation between the molar fraction of lithium x and the concentration c:

$$x(c) = \frac{c\mathcal{M}_{\mathrm{Bi}}}{-1.3 \cdot 10^{-6}\, c^2 + c\,(\mathcal{M}_{\mathrm{Bi}} - \mathcal{M}_{\mathrm{Li}} - 0.0382) + 9780},$$

where $\mathcal{M}_{\mathrm{Bi}} = 209.0\,\mathrm{kg\,mol^{-1}}$.
The equilibrium potential, required to compute the jump in potential, can be computed such as (Gasior et al., 1994)

$$\Phi(x) = \frac{0.19}{x + 0.41} + 0.5.$$

We run a simulation during the discharge phase using the φ-solver described in section §5.2.1, the c-solver, and without flow. The simulation starts with an homogeneous molar fraction of Li $x(t = 0) = 0.236$.

In figure 5.7a, we show snapshots of the molar fraction of Li x at different times (1, 5 and 10 min). The molar fraction is inhomogeneous at the alloy-electrolyte interface. This is explained by the fact that the foam has a smaller radius than the alloy, which is different from the results of section §2.2. Figure 5.7b shows the electrical potential φ as a function of z on the axis. The jump at the alloy-electrolyte interface is clearly visible and is around −0.8 V. The potential is almost constant in the current collectors, in the foam and in the alloy, and only varies significantly in the electrolyte. This can be also seen on figure 5.7c, where the electrical potential field is represented at $t = 10$ min. This confirms that the ohmic losses in the electrolyte dominate the losses in the other phases. The potential gradients are also the most significant in the electrolyte.

Even with the simplified setup, our results are substantially similar to the results of Weber et al. (2019).

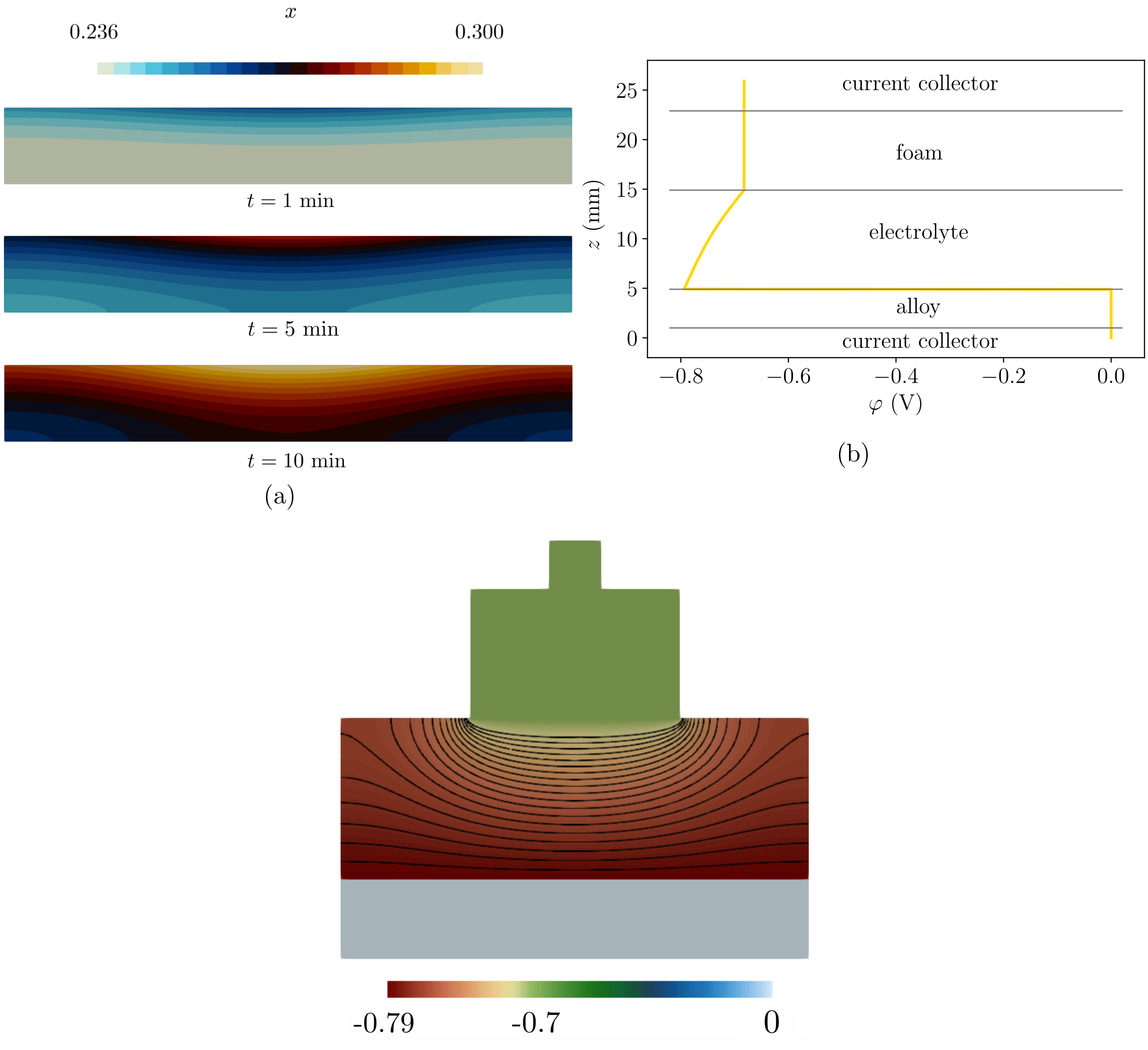

(a)

(b)

(c)

Figure 5.7 – Investigation of the φ-solver in axisymmetric computation. (a) Snapshots of the molar fraction of Li in the alloy, x, at different times: 1 min, 5 min, 10 min. (b) Potential on the axis vs z at $t = 1$ s. (c) Electrical potential field at $t = 1$ s in the total domain. Black lines are contours of the field.

5.4.2 Validation of the $\boldsymbol{H}$-solver coupled with the c-solver

In this section, we show that the $\boldsymbol{H}$-solver and the φ-solver coupled with the c-solver give very similar results, which allows us to validate the $\boldsymbol{H}$-solver. We compare numerical solutions of the $\boldsymbol{H}$-solver with the φ-solver that we use in the last section. We use the same LMB setup, but consider this time a Li||Pb battery. This is the LMB that we will use for some of the next studies in this chapter. We solve the electrical potential and magnetic field formulations described in section §5.2, without flow, in a discharge regime.

In figure 5.8a are represented snapshots of the molar fraction of Li x in the alloy computed with the two solvers at $t = 500$ s, in a meridian plane. The molar fraction fields obtained with both formulations are identical. Notice that the diffusion process is really similar in this Li||Pb battery to the diffusion in the Li||Bi battery of the previous section. Figure 5.8b shows the streamlines of the electrical current $\boldsymbol{j}$, colored by the amplitude of j_z, at the same time, $t = 500$ s. The current density $\boldsymbol{j}$ is computed using $\boldsymbol{j} = -\sigma\nabla\varphi$ in the φ-solver and using $\boldsymbol{j} = \nabla \times \boldsymbol{H}$ in the $\boldsymbol{H}$-solver. The streamlines are also very similar in both cases.

We then compare the computation of the electrical potential of the cell. In the φ-solver, we simply compute the difference between the potentials at the top and at the bottom of the cell. In the $\boldsymbol{H}$-solver, we use the formula (5.2.16). We plot in figure 5.8c E_{cell} as a function of time using both solvers. The cell potential decreases with time, as expected during a discharge phase. Both solvers yields identical results.

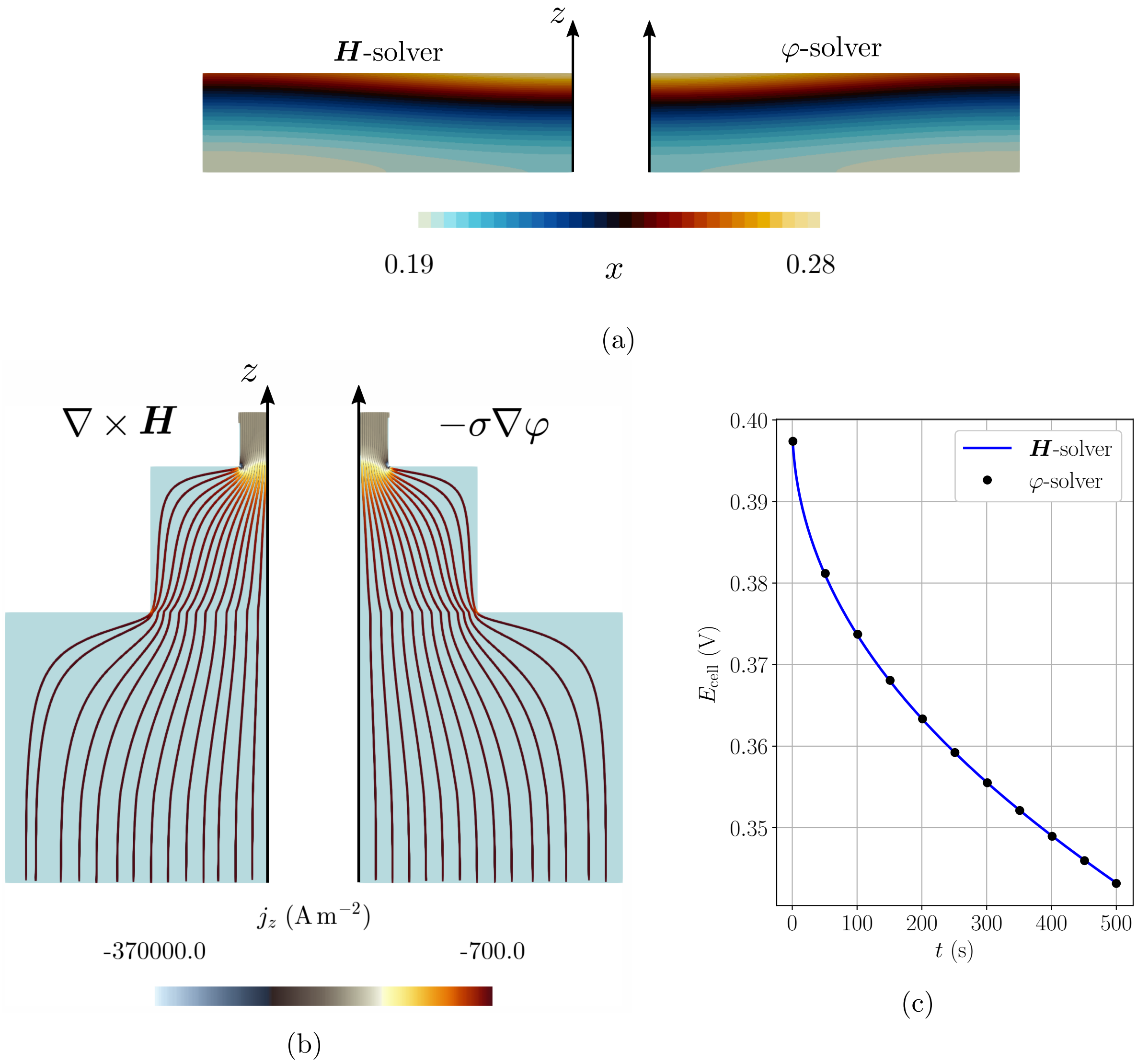

(a)

(b)

(c)

Figure 5.8 – Validation of the $\boldsymbol{H}$-solver in axisymmetric computation.(a) Snapshots of the molar fraction x at $t = 500$ s in a meridian plane with both solvers: (left) $\boldsymbol{H}$-solver, (right) φ-solver. (b) Streamlines of the current density colored by the amplitude of j_z in a meridian plane with both solvers: (left) $\boldsymbol{H}$-solver, (right) φ-solver. (c) Potential E_{cell} vs time using both solvers.

5.4.3 Conclusion

This study allowed us to show that the φ-solver is in good agreement with the study of Weber et al. (2019). We have seen that the ohmic losses and the potential gradients are dominant in the electrolyte. We have then validated the $\boldsymbol{H}$-solver, by comparing the numerical results with those of the φ-solver. In the following, we will use the $\boldsymbol{H}$-solver to conduct the numerical studies.

5.5 Numerical investigation of the effect of the jump in potential on the alloy composition

We investigate the effect of the jump coupling on the alloy composition in a Li||Pb battery, using the $\boldsymbol{H}$-solver. In a first part, we study this effect in the small LMB setup that we have used in the previous section. Then, we conduct the study in a larger setup so that the effects are more visible. In this work, we compare simulations with and without jump in order to analyze more precisely the influence of the jump coupling in different configurations.

5.5.1 Simulations in a small setup

We conduct the first study in the setup represented in figure 5.6b. The mesh is non-uniform, the mesh size h varies in the range $[0.00025, 0.0005]$ m.
We first run two simulations without flow in a discharging cell. We study a pure diffusive case without jump and a case with the jump coupling. We fix $I = 3.3$ A. The molar fraction distribution at $t = 500$ s is represented in figure 5.9 for both cases. In the pure diffusive case, the molar fraction decreases gradually from the axis to the borders, due to the shape of the foam, the molar fraction at the alloy-electrolyte interface is inhomogeneous. When the jump coupling is added, the molar fraction at the alloy-electrolyte interface is slightly homogenized and the maximal molar fraction is reduced. The jump coupling homogenizes the alloy in the radial direction, as expected. This can be also seen in figure 5.11 looking at the red and green curves, where we plot the surface molar fraction in the alloy as a function of the radius r. In the study of section §5.4.1, the electrical potential distribution in the battery has shown that the electrical potential is almost constant in the alloy, and the potential gradients are dominant in the electrolyte. Therefore, a current redistribution due to the jump coupling, which spatially depends on the molar fraction, occurs in the electrolyte, and the radial current increases at the alloy-electrolyte interface. The vertical current then decreases, and the material flux is more evenly distributed at this interface. The alloy is then more homogeneous in the radial direction.

We run a second simulation where we consider all the effects, i.e. the flow and the solutal buoyancy, as well as the jump coupling. Figure 5.10 shows a snapshot of the molar fraction field in the alloy at $t = 500$ s. We do not observe EVF effects as expected, since the flow is crushed by the solutal buoyancy. The alloy is almost homogeneous in the radial direction due to buoyancy, and the maximal molar fraction is also reduced compared to the cases with no buoyancy. This can be also seen on figure 5.11 (blue curve).

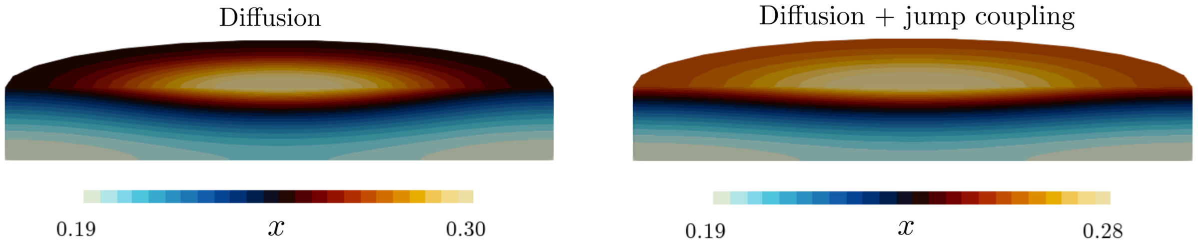

Figure 5.9 – $I = 3.3$ A. Snapshots of the molar fraction field in the alloy at $t = 500$ s in the pure diffusive case and in the case with the jump coupling.

This study shows that the jump coupling homogenizes the molar fraction field in the alloy. When the solutal buoyancy is added, the alloy is almost homogeneous in the radial direction.

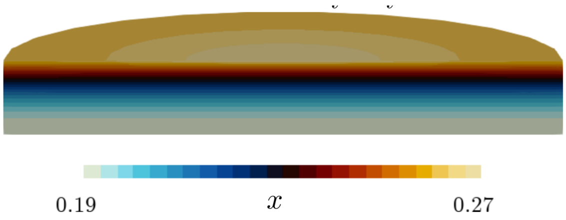

Figure 5.10 – $I = 3.3$ A. Snapshots of the molar fraction field in the alloy at $t = 500$ s with all the effects (jump, flow and buoyancy).

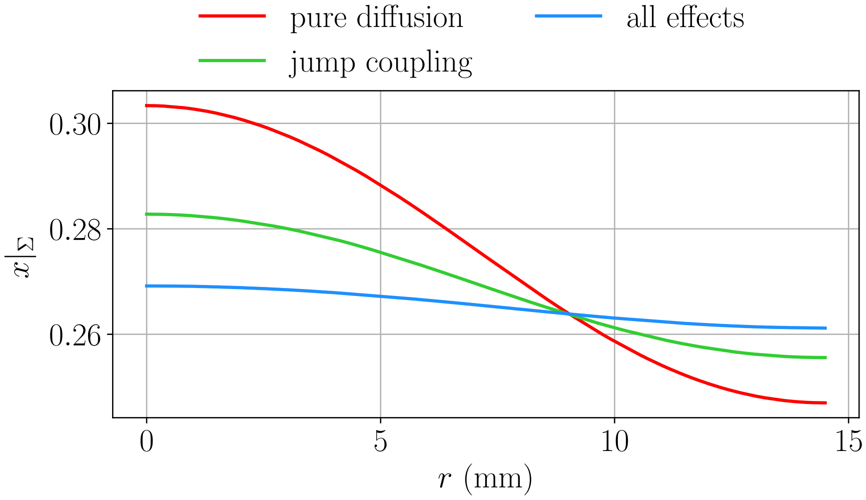

Figure 5.11 – Surface molar fraction $x|_\Sigma$ as a function of the radius at $t = 500$ s.

However, these effects are quite limited. The differences between the studied cases are not significant. This is why we have chosen to conduct another study in a larger setup, where the effects are more visible.

5.5.2 Simulations in a larger setup: with or without jump

We run the second study in a larger setup, with dimensions given in figure 5.12. This setup has been chosen so that the dimensions of the alloy and the electrolyte are equal to the ones in Herreman et al. (2020). The goal of this work is to analyze more precisely the impact of the jump coupling on the alloy composition. For this purpose, we compare simulations with and without jump coupling. We focus on four cases:

- a pure diffusive case (no flow)
- a case with EVF (no buoyancy)
- a case with buoyancy and EVF
- a case with a swirling EVF and buoyancy.

We fix $I = 10$ A. We focus on discharging cells. The mesh is non-uniform, the mesh size h varies in the range $[0.0005, 0.001]$ m.

In the first case, the flow is set to zero, $\boldsymbol{u} = \mathbf{0}$. Thus, only diffusion transports the lithium in the alloy. Figure 5.13 shows a comparison of the alloy composition and current density at $t = 500$s, with or without jump coupling. We can see in figure 5.13a that the molar fraction distribution in the alloy is quite similar without (top) and with (bottom) the jump coupling. Due to a slow diffusion, lithium accumulates near the alloy-electrolyte interface. The jump coupling slightly

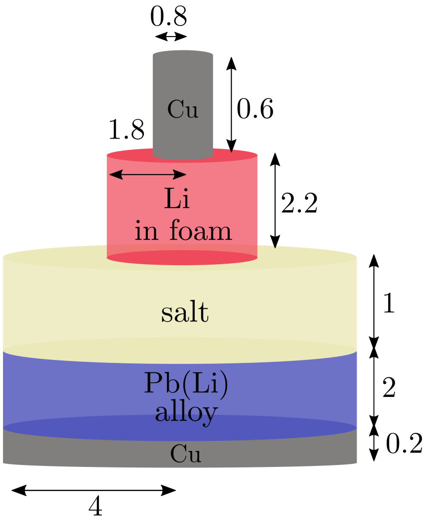

Figure 5.12 – Scheme of the larger setup. The dimensions are in cm.

homogenizes the surface of the alloy, compared to the case without jump coupling, and reduces the maximal molar fraction x. This can be also seen in figure 5.13c, where we plot the molar fraction at the alloy-electrolyte interface $x|_\Sigma$ as a function of the radius r. Figure 5.13b shows that the potential jump locally deflects the current density lines near the interface. This can be more clearly seen in figure 5.13d where we plot j_r and j_z as a function of the radius at the alloy-electrolyte interface. We can notice that the current distribution is slightly modified, and that j_z is more homogeneous with the jump coupling, which is in concordance with the homogenization of the Li-flux observed in figure 5.13a.

In the second case, we add the flow in the alloy, i.e. we set $\boldsymbol{u} \neq \boldsymbol{0}$, but solutal buoyancy is neglected, i.e. $\rho(c) = \rho_*$. The flow driven is a non-swirling electrovortex flow, $u_\theta = 0$. Figure 5.14 shows a comparison of the alloy composition and current density at $t = 500$s, with or without jump coupling. We can see in figure 5.14a that the molar fraction distribution in the alloy is clearly impacted by the flow (streamlines in black). At the top of the alloy, the flow transports the lithium from the lateral sides to the axis. Then, lithium is conducted to the bottom of the cell and then back to the sides. In this case, the jump coupling has a significant impact: we can notice that the surface is much more homogeneous with the jump coupling and that the maximal molar fraction is reduced from 0.46 to 0.37. The flow intensity is also impacted: the EVF is slightly less intense with jump coupling ($||\boldsymbol{u}||_{\max} = 2.7\times10^{-4}$ m s^{-1}) than without jump coupling ($||\boldsymbol{u}||_{\max} = 3.2\times10^{-4}$ m s^{-1}). Figure 5.14c shows that the jump coupling affects mostly the zone around the axis. Off-axis, the alloy composition remains quite similar in both cases. The same is observable for the currents. The current lines (figure 5.14b) are deflected close to the axis in the case with jump coupling, and the current densities j_r and j_z differ significantly close to the axis.

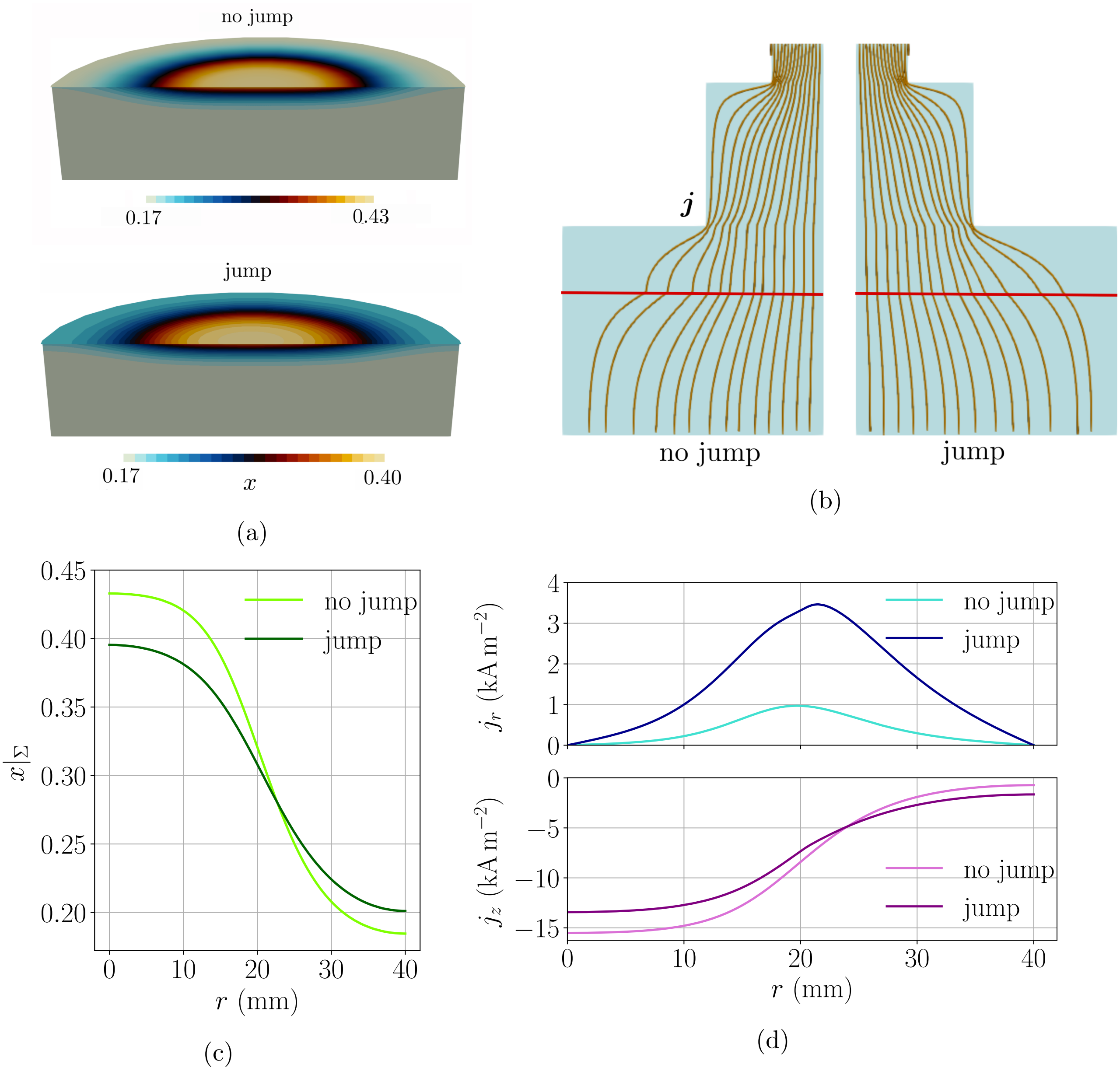

Figure 5.13 – I= 10 A. Molar fraction in the alloy and current density in pure diffusive case, at t = 500 s, with or without jump coupling. (a) Snapshots of the molar fraction of lithium in the alloy x. (b) Streamlines of the current density in the cell. (c) Molar fraction $x|_\Sigma$ at the alloy-electrolyte interface as a function of radius r.(d) Current density j_r (top) and j_z (bottom) at the alloy-electrolyte interface as a function of radius r.

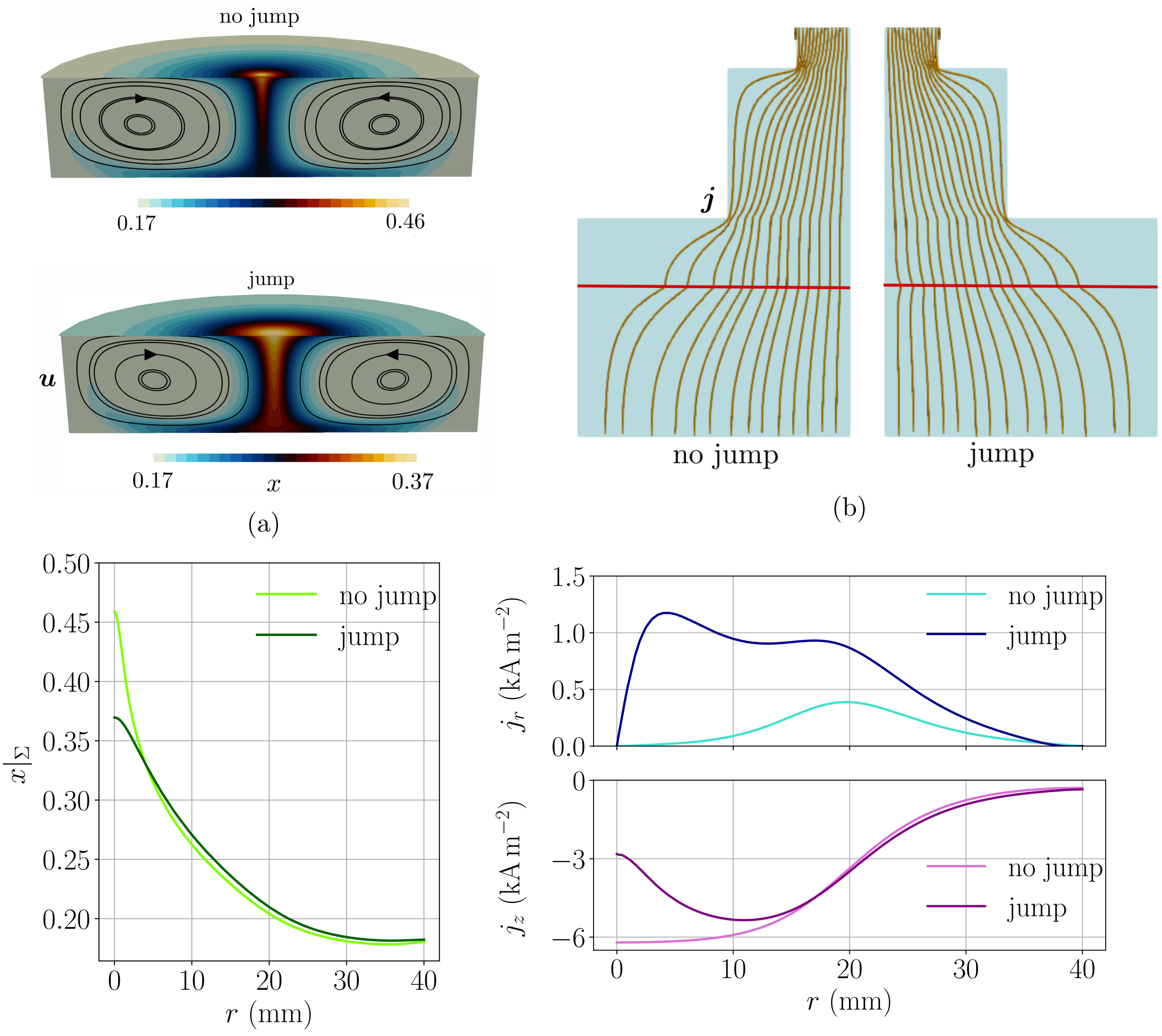

(a)

(b)

(c)

(d)

Figure 5.14 – I= 10 A. Molar fraction in the alloy and current density in the case with EVF and no buoyancy, at t = 500 s, with or without jump coupling. (a) Snapshots of the molar fraction of lithium in the alloy x. (b) Streamlines of the current density in the cell. (c) Molar fraction $x|_\Sigma$ at the alloy-electrolyte interface as a function of radius r. (d) Current density j_r (top) and j_z (bottom) at the alloy-electrolyte interface as a function of radius r.

In the third case, we consider the EVF and solutal buoyancy. We retrieve the same results as Herreman et al. (2020): the light stably stratified layer which forms at the top of the alloy cannot be pierced by EVF (see figure 5.15a, at $t = 500$ s). EVF is still present but it is compressed at the bottom of the alloy and becomes really weak ($||\boldsymbol{u}||_{\text{max}} = 2.3 \times 10^{-5}\ \text{m}\,\text{s}^{-1}$). Solutal buoyancy prevents enhanced mixing in this case. At the alloy-electrolyte interface, the alloy is quite homogeneous, $x|_\Sigma$ is quasi uniform. Thus, the potential jump coupling has very little effect. Since concentration gradients are low, we have $\boldsymbol{\nabla}\Phi(x|_\Sigma) \approx \boldsymbol{0}$, so the gradient of the potential jump in the interface condition (5.2.10) is almost zero. Therefore, it is normal that simulations with or without jump yield similar results. This is effectively what we obtain, current distribution (figures 5.15b and 5.15d) and molar fraction distribution (figures 5.15a and 5.15c) are almost identical in both cases.

In the fourth case, we consider a swirling EVF coupled with solutal buoyancy. This swirling EVF is driven by an external magnetic field fixed at $\boldsymbol{B} = 2 \cdot 10^{-3}$ T. We retrieve the same results as those of Herreman et al. (2021): this quite weak magnetic field induces a sufficiently intense flow to pierce the stably stratified layer (see figure 5.16a, at $t = 260$ s). The velocity field can be seen in figure 5.17a. At the alloy-electrolyte interface, the alloy is quite homogeneous, and the jump has then no real impact on the molar fraction distribution (figure 5.16c). Current lines (figure 5.16b) and interfacial current densities (figure 5.16d) remain quite similar in both cases. The azimuthal velocity u_θ, which is the dominant component of the velocity, is slightly reduced at the alloy-electrolyte interface in the case with the jump, but its effect is limited (figure 5.17b).

To conclude, the influence of the jump coupling on the alloy composition is quite moderate, since the surface of the alloy is much homogenized by solutal buoyancy effects which are dominant. The flow driven by the swirling EVF, which can counteract the solutal buoyancy, is also little affected by the jump coupling.

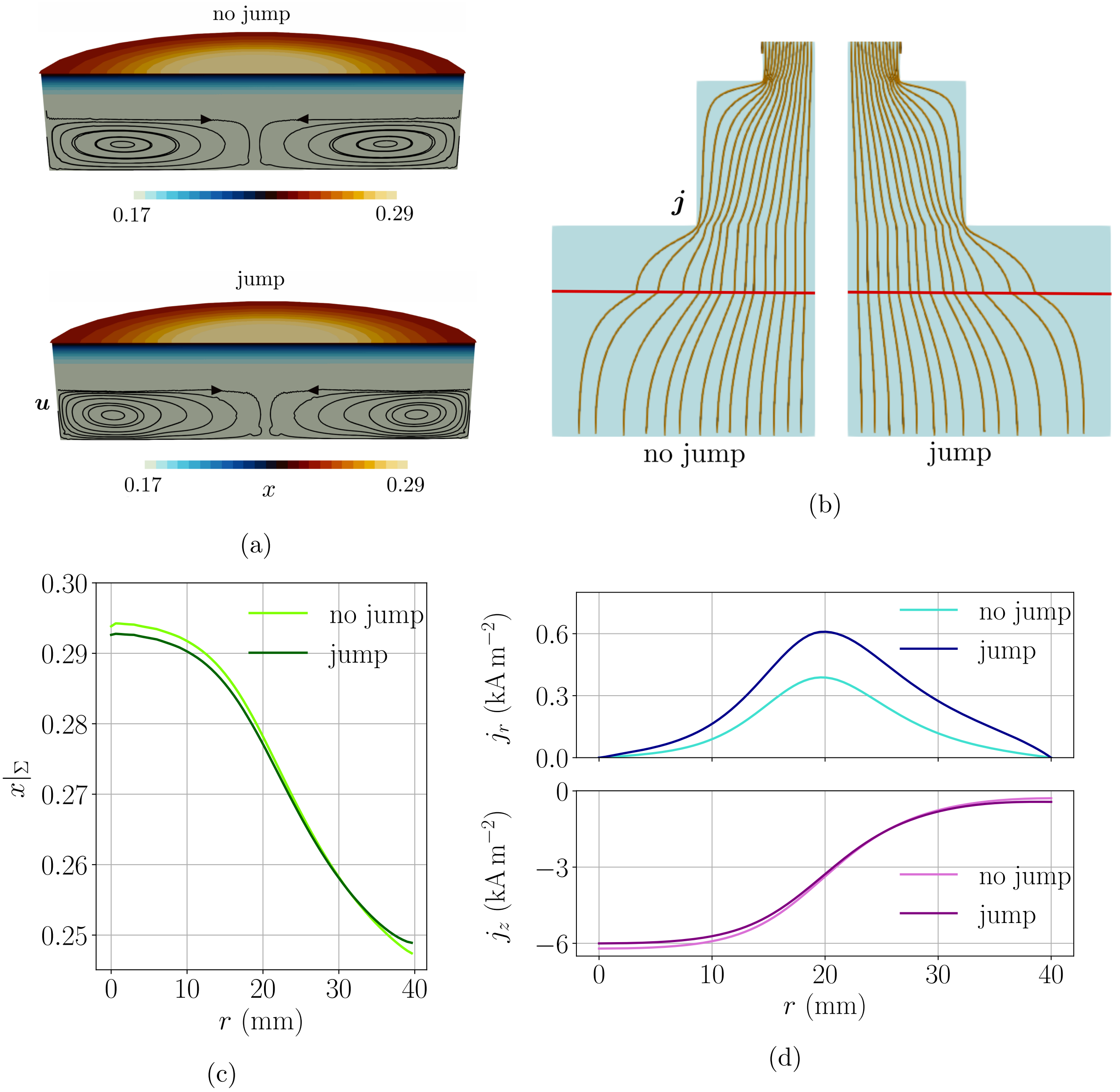

Figure 5.15 – $\boldsymbol{I}$= 10 A. Molar fraction in the alloy and current density in the case with EVF and buoyancy, at t = 500 s, with or without jump coupling. (a) Snapshots of the molar fraction of lithium in the alloy x. (b) Streamlines of the current density in the cell. (c) Molar fraction $x|_\Sigma$ at the alloy-electrolyte interface as a function of radius r. (d) Current density j_r (top) and j_z (bottom) at the alloy-electrolyte interface as a function of radius r.

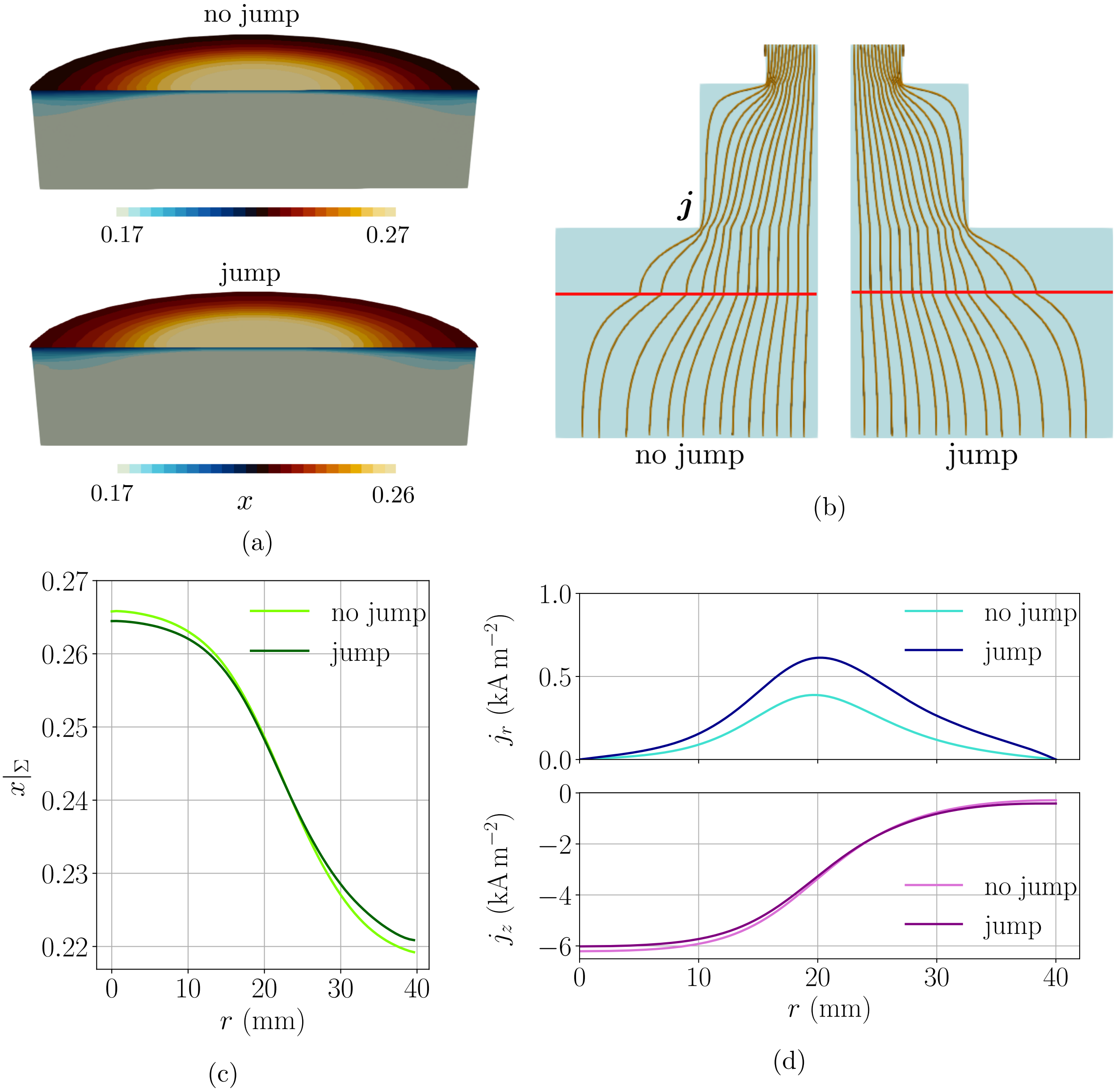

(a) (b) (c) (d)

Figure 5.16 – I= 10 A. Molar fraction in the alloy, current density in the case with swirling EVF and buoyancy, at t = 260 s, with or without jump coupling. (a) Snapshots of the molar fraction of lithium in the alloy x. (b) Streamlines of the current density in the cell. (c) Molar fraction $x|_\Sigma$ at the alloy-electrolyte interface as a function of radius r. (d) Current density j_r (top) and j_z (bottom) at the alloy-electrolyte interface as a function of radius r.

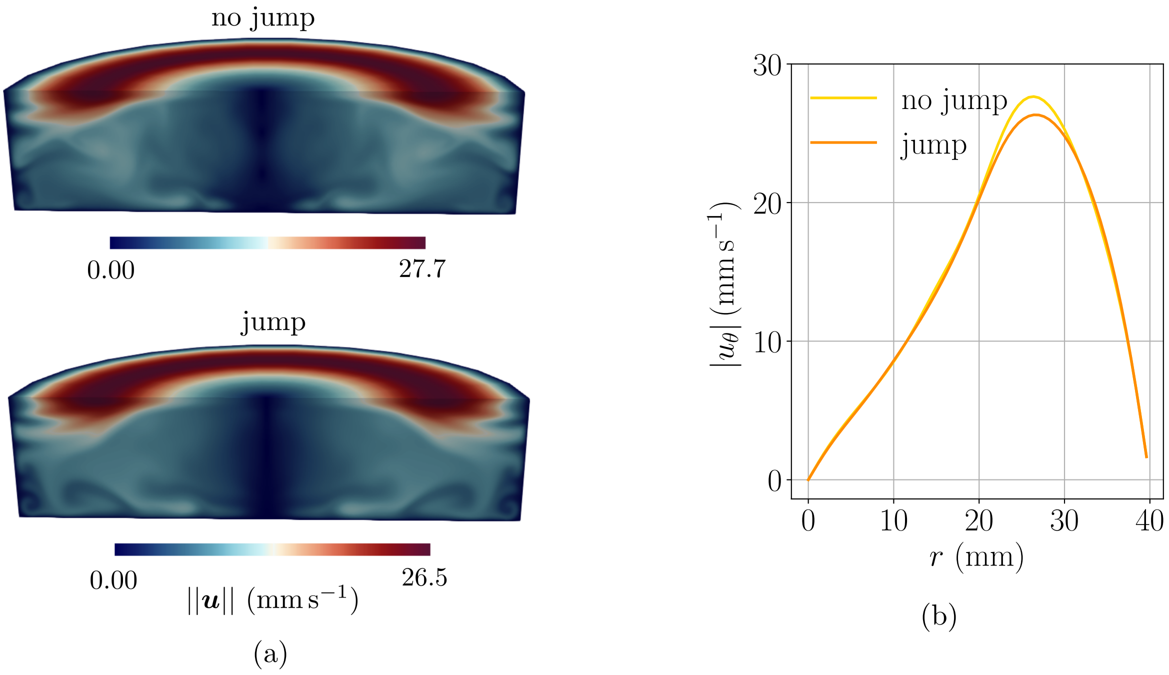

(a)

(b)

Figure 5.17 – Velocity in the alloy in the case with swirling EVF and buoyancy, at $t = 260$ s, with or without jump coupling. (a) Snapshots of the velocity magnitude in the alloy. (b) Azimuthal velocity u_θ at the alloy-electrolyte interface as a function of radius r.

5.6 A self-consistent potential computation

In this section, we are interested in the computation of the cell potential E_{cell}. In section §2.2 in chapter 2, we have computed the cell potential from the surface averaged molar fraction. We investigate how much this computation differs from a more consistent computation. We examine also how the ohmic losses and the mass transfer overpotentials are influenced by the jump coupling. We focus on the simulations of the previous section in the large LMB setup with non-swirling EVF and solutal buoyancy effects present.

We define E_{cell}, η_{mt} and η_Ω the cell potential, the mass transfer overpotential and the ohmic losses, respectively, computed with the formulas given by equations (5.2.16) and (5.2.17), in the simulation with the jump coupling. We recall the formulas here:

$$E_{\text{cell}} \simeq \varphi_{\text{jump}}|_{r=0} - \eta_\Omega, \quad \eta_\Omega = \int_{\text{electrolyte}} -\frac{\boldsymbol{j}}{\sigma_i} \cdot \boldsymbol{e}_z dz,$$

$$\eta_{\text{mt}} = |E_{\text{cell}} - E_{\text{cell,eq}} + \eta_\Omega|.$$

This potential computation is the most self-consistent.
We define $\widetilde{\eta}_\Omega$ and $\widetilde{E}_{\text{cell}}$ the ohmic losses and the cell potential, respectively, computed from simulations without jump coupling, i.e.:

$$\widetilde{E}_{\text{cell}} \simeq \Phi(x|_{\Sigma,r=0}) - \widetilde{\eta}_\Omega, \quad \widetilde{\eta}_\Omega = \int_{\text{electrolyte}} -\frac{\boldsymbol{j}}{\sigma_i} \cdot \boldsymbol{e}_z dz,$$

$$\widetilde{\eta}_{\text{mt}} = |\overline{E}_{\text{cell}} - E_{\text{cell,eq}} + \widetilde{\eta}_\Omega|. \tag{5.6.2a}$$

In section §2.2, the cell potential was computed from the surface averaged molar fraction. We define $\overline{E}_{\text{cell}}$ and $\overline{\eta}_{\text{mt}}$ such as

$$\overline{E}_{\text{cell}} = \Phi(\langle x \rangle_\Sigma) - \int_{\text{electrolyte}} -\frac{\boldsymbol{j}}{\sigma_i} \cdot \boldsymbol{e}_z dz, \qquad \overline{\eta}_{\text{mt}} = |\overline{E}_{\text{cell}} - E_{\text{cell,eq}} + \widetilde{\eta}_\Omega| \tag{5.6.3}$$

that we apply to the simulations without jump coupling (the ohmic losses are then also equal to $\widetilde{\eta}_\Omega$, they are not modified by operations on the molar fraction).

We present in figure 5.18 the three mass transfer overpotentials and cell potentials previously defined. We notice that the jump coupling modifies very little the mass transfer overpotential - $\widetilde{\eta}_{\mathrm{mt}}$ and η_{mt} are almost superposed, which is expected since the alloy composition is barely affected by this jump. However, the computation from the surface averaged molar fraction $\overline{\eta}_{\mathrm{mt}}$ is around 20% lower than the direct computation η_{mt}, which is a significant difference. When regarding the cell potential, the results are a bit different. $\overline{E}_{\mathrm{cell}}$ and E_{cell} differ only by around 3%. But we notice that E_{cell} and $\widetilde{E}_{\mathrm{cell}}$ are not superposed and differ by around 4%. Since the mass transfer overpotential is not modified by the jump coupling, this means that the ohmic losses in the electrolyte are impacted by the jump coupling.
Figure 5.19 shows the ohmic losses in the electrolyte η_Ω and $\widetilde{\eta}_\Omega$ as a function of time. We notice that $\widetilde{\eta}_\Omega$ remains constant with time, unlike η_Ω which decreases with time until reaching a constant. Without jump coupling, the current in the electrolyte is constant with time, and the ohmic losses do not vary. But the current distribution in the electrolyte is modified during time by the jump coupling, which explains the time variation observed. Moreover, at large times, η_Ω is 3% lower than $\widetilde{\eta}_\Omega$. Then the jump coupling reduces the ohmic losses. This can be easily explained: the jump coupling increases the radial current in the electrolyte, and decreases the vertical current j_z. The integral on the axis used to compute the ohmic losses is then reduced.

Therefore, the computation from a surface averaged molar fraction under-estimates the mass transfer overpotential. Even if the difference is quite weak on the cell potential, this approximation should be avoided. Moreover, the ohmic losses are slightly over-estimated when the jump coupling is neglected in the simulations. Hence, a self-consistent computation is the most accurate.

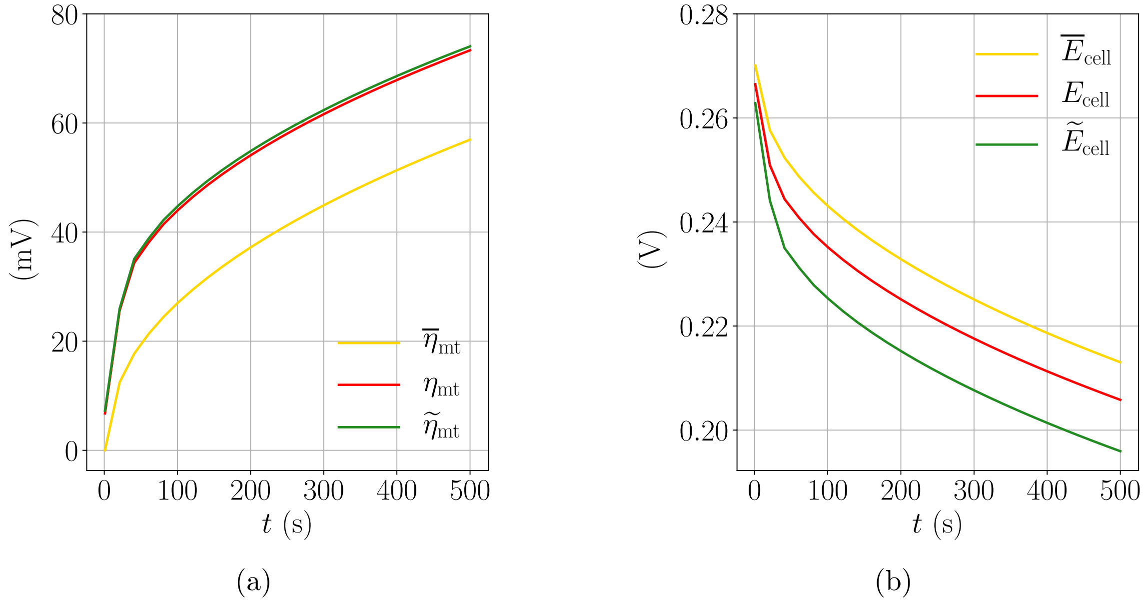

(a)

(b)

Figure 5.18 – (a) Overpotentials $\overline{\eta}_{\mathrm{mt}}$, $\widetilde{\eta}_{\mathrm{mt}}$ and η_{mt} vs time. (b) Potentials $\overline{E}_{\mathrm{cell}}$, $\widetilde{E}_{\mathrm{cell}}$ and E_{cell} vs time.

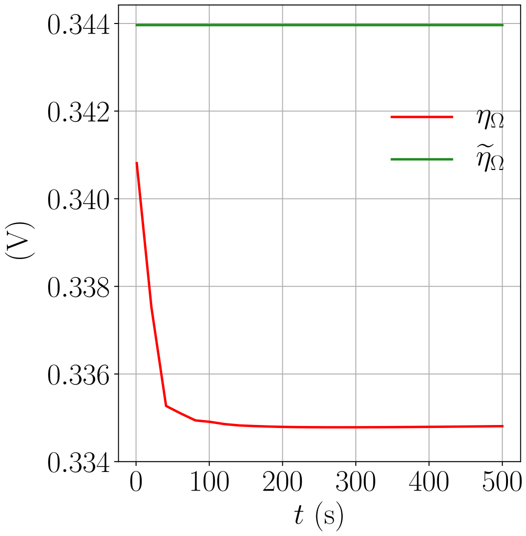

Figure 5.19 – Ohmic losses η_{Ω} and $\widetilde{\eta}_{\Omega}$ vs time.

5.7 Conclusion

In this chapter, we have studied the influence of a jump in potential on the alloy composition in a discharging LMB.
We have first implemented in SFEMaNS a c-solver for the concentration, which was not present, and validated this development. This has allowed us to extend our φ-solver and $\boldsymbol{H}$-solver by adding the concentration variable. Our numerical results are substantially similar to those of Weber et al. (2019).

Using the $\boldsymbol{H}$-solver, we have conducted a study in a small LMB setup. We have shown that the jump coupling homogenizes the alloy in the radial direction, compared to the case with pure diffusion only. Solutal buoyancy homogenizes even more the alloy in the radial direction. In this setup, all of these effects have a a quite limited impact on the alloy composition.

In the larger LMB setup, we have shown that, in realistic situations which consider the solutal buoyancy, the influence of the jump coupling is quite moderate, since the alloy surface is already much homogenized by the solutal buoyancy. Only slight differences are observed between simulations with and without jump coupling. Hence, the results from previous studies of chapter 2 and Herreman et al. (2020, 2021) which have ignored the jump coupling, remain more or less valid. However, our simulations have confirmed that flow motion and alloy composition are significantly impacted by buoyancy. This phenomenon cannot be ignored in LMBs models.
Furthermore, we have compared two ways of computing the cell potential: a computation from the averaged molar fraction, used in chapter 2, and a direct computation from its definition - difference of the potentials at the top and at the bottom of the cell. The post-processed computation yields major errors for the mass transfer overpotential, even though the total cell potential remains quite accurate. Thus, this post-processed computation should be avoided. In addition, the jump coupling impacts very moderately the mass transfer overpotential since its effect on the alloy composition is limited. However, we observe differences in the ohmic losses, since the jump influences the current distribution in the electrolyte. Therefore, it is more accurate to consider the potential jump in order to not over-estimate the ohmic overpotential.

Chapter 6

Electrocapillary flows

6.1 Introduction

Surface tension represents the force at a surface of a liquid created by molecular interactions. A variation of surface tension along a surface drives a Marangoni flow, directed from the zones of lower surface tension to the zones of higher surface tension (see figure 6.1 for a scheme of the situation). The surface tension can change with temperature, concentration, potential, and other parameters. In LMBs we can expect such changes, therefore Marangoni flows are likely in LMBs.

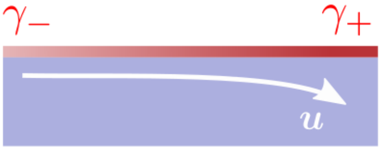

Figure 6.1 – Scheme representing a Marangoni flow due to spatial gradients of surface tension at a surface.

Thermal Marangoni flows (or thermocapillary flows) have already been investigated in LMBs. Köllner et al. (2017) have numerically considered thermal convection and thermocapillary flow in a Li||Pb-Bi LMB. Joule heating during operation causes local changes in temperature. At the interfaces, thermocapillary flow has been observed in these simulations.
Solutal Marangoni flows are also likely in LMBs, because the concentration of the alloy varies along the interface with the electrolyte. Numerical and experimental studies on solutal Marangoni flow have been realized in two-layer setups (Köllner et al. (2013, 2015)), but never in LMBs. Kelley and Weier (2018) attempted to estimate an order of magnitude of the variation of the surface tension with the alloy composition, but most often this dependency is unknown in LMBs.
Electrocapillary flows are also possible in LMBs. The surface tension varies with the jump in potential φ_{jump} at an interface between two conductive phases, a phenomenon that has been discovered by Lippmann (1873). This phenomenon is well-known in the context of the electrowetting of droplets. A liquid and conductive droplet is placed on an insulating layer, which separates the droplet from a solid conductor. When an electrical tension is applied between the droplet and the solid, the surface tension of the droplet is modified and so its shape. If the potential jump φ_{jump} varies spatially along an interface, so will the surface tension, and a so-called electrocapillary flow will be driven. Dreyer et al. (2018) have proposed a thermodynamic model for the variation of surface tension with a potential jump at the interface between a

liquid metal and an aqueous electrolyte. Their model includes the effect of the electrochemical double layer. In LMBs, we have seen that the jump in potential at the alloy-electrolyte interface depends on the molar fraction of the alloy and varies along this interface. Therefore, it is not excluded that variations in potential jump drive electrocapillary flows. This type of flow has never been investigated in LMBs.

In this chapter, we are interested in studying these flows structure and their intensity. Are electrocapillary flows able to mix the alloy? How are they affected by solutal buoyancy? A difficulty here is that the dependency of the alloy-electrolyte surface tension on the potential jump is not known. Dreyer et al. (2018) model chemical reactions and the thermodynamic state of the double layer, but this model requires a deep understanding of the electrochemical reactions and the knowledge of many material properties. We will use a simplified heuristic model for the dependency of the surface tension on the potential jump.
In this exploratory chapter, we focus on flows driven by electrocapillarity near the alloy-electrolyte interface. We present first our estimation of the surface tension variation with the jump in potential. Then, we present the model used, and finally some first results. This study is not finalized yet and will be continued in the future.

6.2 Surface tension law

Experimental studies have been conducted to analyze how the surface tension of the Li-Pb alloy varies with the temperature and the molar fraction of lithium in the alloy (Alchagirov et al. (2016)). However, up to our knowledge, no work has been realized to determine the variation of the surface tension of a Li-Pb alloy with the potential jump. We attempt to estimate this here.
The variation of surface tension γ with the difference in potential φ_{jump} at an interface Σ is given by the Lippmann equation (Bard and Faulkner, 2001):

$$\frac{\partial \gamma}{\partial \varphi_{\text{jump}}} = Q_s. \tag{6.2.1}$$

Here Q_s is the surface charge of the interface.
Our first idea was to try to determine Q_s. The Maxwell-Gauss equation gives $\nabla \cdot \boldsymbol{D} = Q$ where $\boldsymbol{D} = \epsilon_0 \sigma^{-1} \boldsymbol{j}$ is the displacement vector and Q the volume charge. We denote $\boldsymbol{D}_1$ and $\boldsymbol{D}_2$ the displacement vectors at each side of the interface. On Σ, the Maxwell-Gauss equation becomes $\boldsymbol{D}_1 \cdot \boldsymbol{n}_1 + \boldsymbol{D}_2 \cdot \boldsymbol{n}_2 = Q_s$, i.e. $D_{1,z} - D_{2,z} = Q_s$.
This means that

$$Q_s = \epsilon_0 \left(\frac{j_{1,z}}{\sigma_1} - \frac{j_{2,z}}{\sigma_2} \right)$$

However, j_z is continuous at the interface Σ, thus $j_{1,z} = j_{2,z}$. We denote j_s the value of the vertical current at the interface. This yields

$$Q_s = \epsilon_0 j_s \left(\frac{1}{\sigma_1} - \frac{1}{\sigma_2} \right) \tag{6.2.2}$$

Let us estimate numerically Q_s. In the LMB setup of figure 5.12 we have $\epsilon_0 = 8.8 \cdot 10^{-12}\,\mathrm{F\,m^{-1}}$, $\sigma_1 = 187\,\mathrm{S\,m^{-1}}$, $\sigma_2 = 7.39 \cdot 10^5\,\mathrm{S\,m^{-1}}$. If we take the current $\boldsymbol{I} = 10$ A, this yields the equivalent current density $\boldsymbol{J} = 2000\,\mathrm{A\,m^{-2}}$ - with $\boldsymbol{R} = 4$ cm - and this leads to $\boldsymbol{Q}_s \simeq 10^{-10}\ \mathrm{C\,m^{-2}}$. This value is really low, and would mean that the variation of the surface tension with the potential is negligible. However, this model is wrong, as it ignores the presence of the electrochemical double layer.

The work of Dreyer et al. (2018) contains a much more elaborate description of this electrocapillarity phenomena. They provide laws for the variation of γ with φ_{jump} for several parameters and several electrolyte types. All the proposed laws follow a similar parabolic trend. We suppose here that this trend also applies to our case of a Li-Pb alloy-electrolyte interface. This parabolic law depends on the double layer capacity C which is a function of the potential, $C = \dfrac{dQ_s}{d\varphi_{\text{jump}}}$:

$$\gamma = \gamma_0 - C(\varphi_{\text{jump}} - \varphi_{\text{jump},0})^2. \tag{6.2.3}$$

Here we will suppose C, γ_0 and $\varphi_{\text{jump},0}$ constant. Exact numerical values are unknown, so we choose to vary these parameters in acceptable intervals.

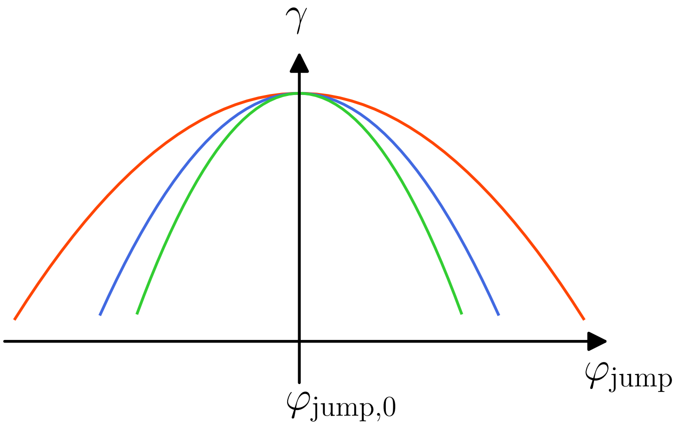

Figure 6.2 – Representations of the variation of the surface tension γ with the difference of potential φ_{jump}.

6.3 Model and numerics

6.3.1 Equations and boundary conditions

We consider the same large LMB setup as in figure 5.12. In our model, the potential jump appears at the alloy-electrolyte interface. We can use the same magnetic field formulation as in section §5.2 of chapter 5 to solve this jump. The main novelty will be that we add a hydrodynamical boundary condition that captures the electrocapillarity effect.
Let us recall the model. The magnetic field $\boldsymbol{H}$ verifies in all domains the equations

$$\nabla \times \left(\frac{\nabla \times \boldsymbol{H}}{\sigma_i}\right) = \mathbf{0}, \tag{6.3.1a}$$

$$\nabla \cdot \boldsymbol{H} = 0 \tag{6.3.1b}$$

where σ_i are the electrical conductivities of the different domains. The magnetic field boundary conditions are:

$$H_\theta|_{z=\mathcal{H}_{\text{cell}}} = \frac{I}{2\pi R_w^2} r, \tag{6.3.2a}$$

$$H_\theta|_{r>R_w} = \frac{I}{2\pi r}, \tag{6.3.2b}$$

$$(\nabla \times \boldsymbol{H}) \times \boldsymbol{n}|_{z=0} = \mathbf{0} \tag{6.3.2c}$$

and $\boldsymbol{H}_r = \boldsymbol{H}_z = 0$ on all borders. The potential jump at the interface is computed as:

$$\left(\frac{\boldsymbol{\nabla}\times\boldsymbol{H}}{\sigma}\right)_{\text{jump}} \times \boldsymbol{n} = -\boldsymbol{\nabla}_T(\varphi_{\text{jump}}) \times \boldsymbol{n} = -\boldsymbol{\nabla}(\Phi(x|_\Sigma)) \times \boldsymbol{n}. \tag{6.3.3}$$

In the alloy, the concentration c is solution of the advection-diffusion equation

$$\partial_t c \ + \ \boldsymbol{u}\cdot\boldsymbol{\nabla} c \ = \ D\nabla^2 c. \tag{6.3.4}$$

The material flux is equal to

$$D\partial_z c|_\Sigma \ = \ -\frac{j_z}{n_e F} \tag{6.3.5}$$

at the alloy-electrolyte interface and is zero at the other boundaries of the alloy.
As before, we do not solve the flow in the electrolyte. The velocity $\boldsymbol{u}$ in the alloy verifies

$$\rho_*(\partial_t \boldsymbol{u} \ + \ (\boldsymbol{u}\cdot\boldsymbol{\nabla})\boldsymbol{u}) \ = \ -\boldsymbol{\nabla} p \ - \rho(c) g \boldsymbol{e}_z + \boldsymbol{\nabla}\cdot(\rho_*\nu(\boldsymbol{\nabla} u \ + \ (\boldsymbol{\nabla} u)^T) \ + \ \boldsymbol{j}\times\boldsymbol{b} \tag{6.3.6a}$$

$$\nabla\cdot\boldsymbol{u} \ = \ 0 \tag{6.3.6b}$$

with p the pressure, g the gravity, μ_0 the magnetic permeability of vacuum, $\boldsymbol{b}$ the magnetic field such as $\boldsymbol{b} = \mu_0 \boldsymbol{H}$ and

$$\rho(c) \ = \ \rho_* \ - \ \chi\mathcal{M}_{\text{Li}}(c - c_*). \tag{6.3.7}$$

On the solid boundaries, we use a no-slip boundary condition. At the alloy-electrolyte interface, we still use a free boundary condition but this time, this condition needs to include Marangoni effects:

$$\rho_*\nu\,\partial_z \boldsymbol{u}_T = \boldsymbol{\nabla}_T\gamma. \tag{6.3.8}$$

Here $\boldsymbol{u}_T$ is the tangential velocity at the interface and

$$\gamma = \gamma_0 - C(\varphi_{\text{jump}} - \varphi_{\text{jump},0})^2 \tag{6.3.9}$$

is used to model te influence of surface tension on the flow. Considering equation (6.3.8), we do not need to know γ_0, because only the tangential gradient of γ influences the velocity. We estimate C between 0.1 and 1 $\mathrm{F\,m^{-2}}$ taking inspiration from the typical values calculated by Dreyer et al. (2018). This parameter is however unsure and will be varied in our study. We do not know $\varphi_{\text{jump},0}$ either, so we take $\varphi_{\text{jump},0} = \varphi_{\text{jump}}(t = 0)$. Notice that, with this choice, the surface tension γ can only decrease.
The simulations start with the eutectic alloy, $c = c_*$ everywhere and $\boldsymbol{u} = \boldsymbol{0}$.

The surface tension must remain positive, i.e. $C(\varphi_{\text{jump}} - \varphi_{\text{jump},0})^2$ should remain lower than γ_0. Typically, $\gamma_0 = O(0.1)\,\mathrm{Nm^{-1}}$. The maximal molar fraction x that we usually reach in our simulations is around 0.3. With $C = 1\,\mathrm{F\,m^{-2}}$, we estimate $C(\varphi_{\text{jump}} - \varphi_{\text{jump},0})^2 \sim 0.006\,\mathrm{Nm^{-1}}$, which is much lower than γ_0.

Normally, $\boldsymbol{\nabla}_T\gamma$ drives a flow in the electrolyte too. Modeling this flow requires to use a multiphase solver, or a hydrodynamical model with layers that can transfer tangential stress. This is not present in SFEMaNS and it is complex to develop. We then ignore the flow in the electrolyte.

In the numerical development, we have implemented the condition (6.3.8) in SFEMaNS.

6.3.2 Expected Marangoni flow

When the battery is in discharge, the incoming mass flux of lithium is higher near the center than on the sides, due to the thinner width of the foam. Gradients of molar fraction at the alloy-electrolyte interface create gradients of surface tension. Considering the law that we have chosen for the variation of γ (equation 6.3.9), the surface tension can only decrease. Therefore, γ decreases at the center of the interface. Gradients of surface tension are directed radially from the axis to the sides, and an electrocapillary flow is driven radially outwards. Figure 6.3 shows a sketch of the process.

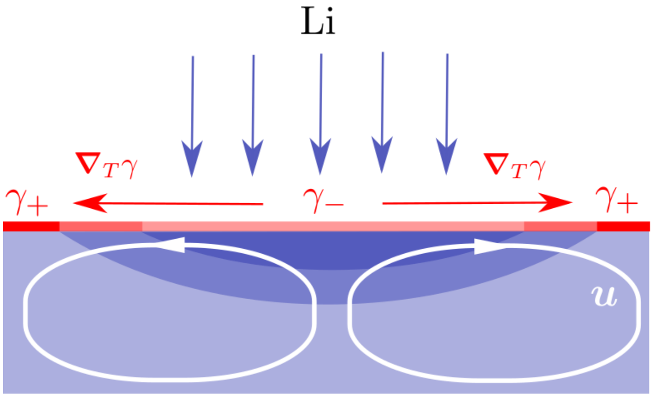

Figure 6.3 – Scheme showing how a Marangoni flow is driven by electrocapillarity effects in the alloy of our LMB setup.

6.4 Effect of electrocapillary flows on the alloy composition

We fix I= 10 A. We vary C in our simulations in the range [0.1,1] F m^{-2}, and analyze its influence on the flow and on the alloy composition. We study two cases: with and without solutal buoyancy. All simulations are axisymmetric.

6.4.1 Without buoyancy

We first ignore the solutal buoyancy, i.e. we set $\rho(c) = \rho_*$. In order to focus on electrocapillary flows, we deactivate the Lorentz force $\boldsymbol{j} \times \boldsymbol{b}$, and hence the EVF.
The mesh is non-uniform, the mesh size h varies in the range $[0.000125, 0.001]$ m.

Figure 6.4 shows the space-averaged velocity $\boldsymbol{u}$ as a function of time for different C. We observe that, for each capacity C, the velocity increases with time until reaching a maximum at $t = t_c$, and suddenly decreases to reach an almost constant value slightly above zero. The time t_c is shorter as C increases. We also notice that the maximal velocity mostly increases with C up to $C = 0.8$.

In order to understand better what happens, we plot on figure 6.5(a-c) snapshots of the molar fraction x and of the velocity magnitude in the alloy at t = 100, 600, 1100 s, for C = 1 F m^{-2} - these instants correspond to the black dots of figure 6.4. In figure 6.5d, we also show the molar fraction $x|_\Sigma$ at the surface of the alloy as a function of the radius at the same instants. At t = 100 s, which corresponds to the part where the velocity increases with time, we observe

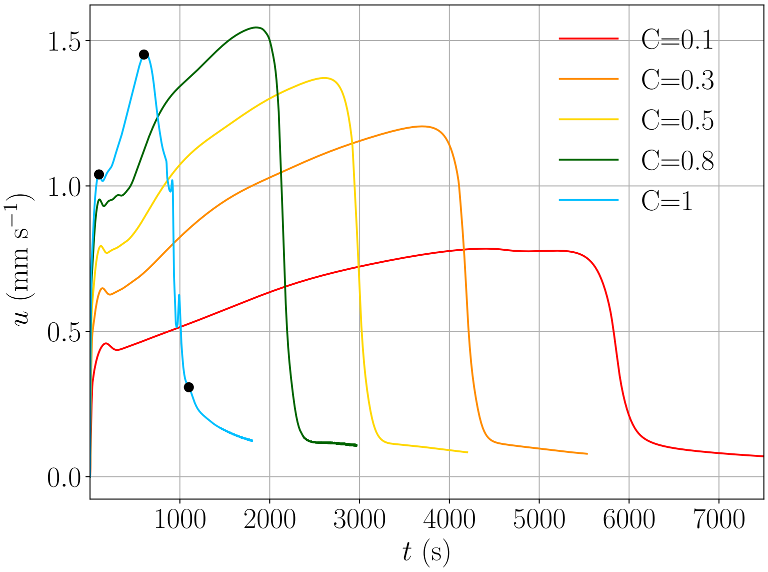

Figure 6.4 – Space-averaged velocity $\boldsymbol{u}$ as a function of time for different $\boldsymbol{C}$. The black dots represent the times for the snapshots of figure 6.5.

that the flow is driven radially outwards at the alloy-electrolyte interface. At the edges, it is driven downwards and loops back towards the axis at the bottom. This is consistent with our expectations (figure 6.3). A small recirculation zone can be observed at the bottom of the alloy. The flow velocity is the largest close to the interface. At $t = 600$ s, the velocity is maximal. The recirculation zone is larger than at t=100 s, and influences the molar fraction. At $t = 1100$ s, which corresponds to the part where the velocity is really low, the maximal velocity is drastically reduced and the recirculation zone has disappeared. We can notice that the molar fraction at the surface of the alloy $x|_\Sigma$ is really homogeneous, which was not the case for the instants before. This can be clearly seen in figure 6.5d. The quantity $x|_\Sigma$ homogenizes with time. These observations suggest that the electrocapillary flow driven by the local differences in surface tension homogenizes the surface of the alloy. As this surface becomes more homogeneous, the surface tension becomes almost constant along the surface, i.e. $\boldsymbol{\nabla}_T\gamma \simeq 0$. Since this gradient drives the flow, the velocity decreases. Electrocapillary flow has therefore a natural tendency to cancel itself.

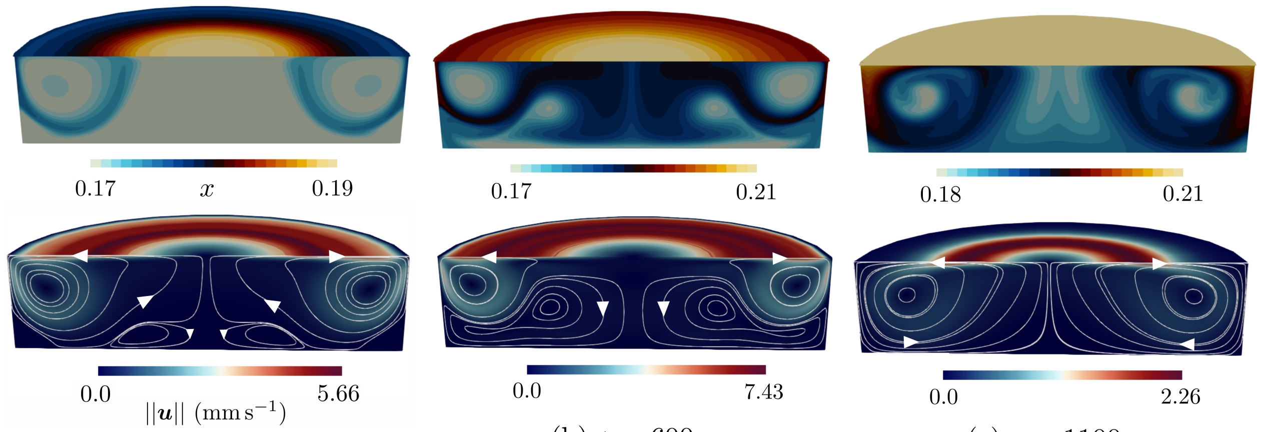

(a) t = 100 s (b) t = 600 s (c) t = 1100 s

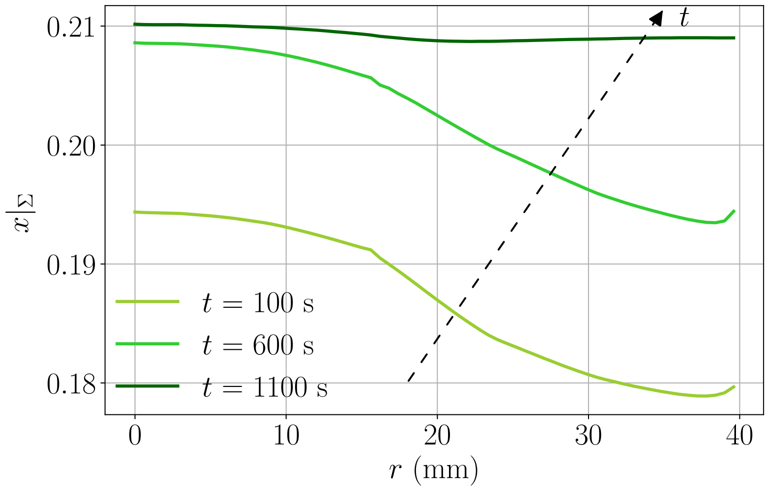

(d)

Figure 6.5 – (a,b,c) Snapshots of the molar fraction x (top) and of the velocity magnitude $||\boldsymbol{u}||$ (bottom) at different times. (d) Molar fraction at the alloy-electrolyte interface $x|_\Sigma$ as a function of the radius r, at different times.

6.4.2 With buoyancy

We run the same simulations but with the solutal buoyancy included. We still deactivate the EVF. Therefore, we do not consider the EVF in these series of simulation, i.e. we ignore the Lorentz force $\boldsymbol{j} \times \boldsymbol{b}$.
The mesh is non-uniform, the mesh size h varies in the range $[0.000075, 0.001]$ m.

Figure 6.6 shows the space-averaged velocity u as a function of time for different C. We observe for each C a peak in the velocity at short times, and then a few oscillations until the flow reaches a constant value. The higher C, the higher the velocity. However, in the late regime, the velocity values have the same order of magnitude, between 0.08 and 0.17 mm s^{-1}, to be compared with figure 6.4. The flow's intensity is much lower here than in the simulations without buoyancy. Solutal buoyancy significantly reduces the flow.

We plot on figure 6.7 snapshots of the molar fraction x and of the velocity magnitude in the alloy at t = 10, 100, 600 s, for C = 1 F m^{-2} - these instants correspond to the black dots of figure 6.6. We show also the molar fraction $x|_\Sigma$ at the surface of the alloy as a function of the radius at the same instants. At t = 10 s, which corresponds to the first peak in velocity, the

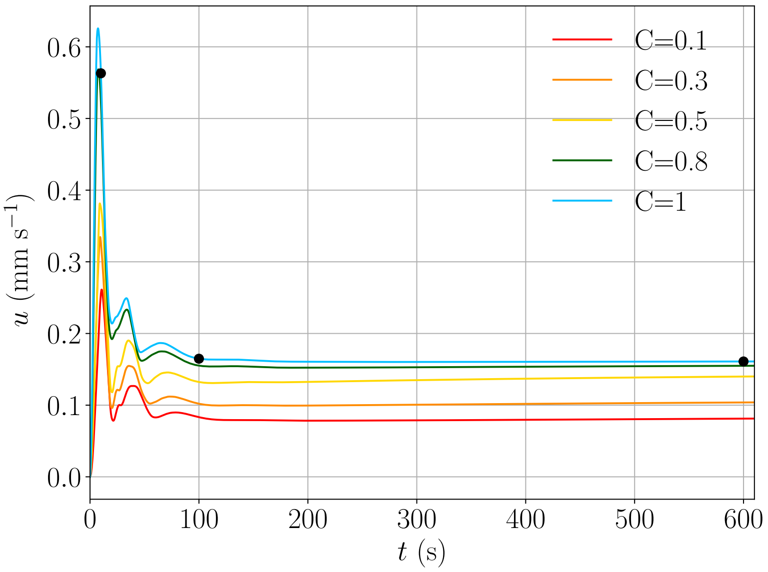

Figure 6.6 – Space-averaged velocity u as a function of time for different C. The black points represent the times for the snapshots of figure 6.7.

electrocapillary flow extends into the alloy and the maximal velocity is equal to 6.49 $\mathrm{mm\,s^{-1}}$. At t = 100 s, i.e. just after the last oscillation in figure 6.6, the flow structure is drastically modified: it is localized in a thin layer just below the alloy-electrolyte interface. The maximal velocity is also much reduced. At t = 600 s, the flow is in a stationary state quite similar to that of t = 100 s. The surface molar fraction $x|_\Sigma$ is significantly more homogeneous.
The localization of the flow in a thin layer can be explained as follows. The flow driven at the alloy-electrolyte interface is directed radially from the center to the edges, and is then driven downwards at the edges, like in the case with no buoyancy. However, as the fluid also becomes lighter at the top, the flow then needs to transport light fluid parcels into the heavier bulk. In these simulations, the flow is not intense enough anymore to drive the lighter fluid far down into the bulk. Instead, the lighter fluid goes back radially towards the center. The zone where the flow can mix the alloy is then restricted to a thin layer. The size of this zone depends on the flow intensity. Unlike the EVF, the electrocapillary flow is localized near the interface, and not in the bulk.

We now investigate the impact of electrocapillary flows on the mixing of the alloy phase. For this purpose, we plot on figure 6.8 the cell potential and the mass transfer overpotential as a function of time. We compare the case without flow, i.e. with the pure diffusion (dashed lines) to two cases with electrocapillary flows, with the two extreme values of C used for the studies, $C = 0.1\,\mathrm{F\,m^{-2}}$ and $C = 1\,\mathrm{F\,m^{-2}}$. With the lowest C, the drop in the cell potential is limited and the mass transfer overpotential is slightly reduced. With the highest C, the mixing seems more effective.

We have conducted three-dimensional simulations for the studied cases. The velocity magnitudes are quite low in these cases and the flow remains axisymmetric (data not shown).

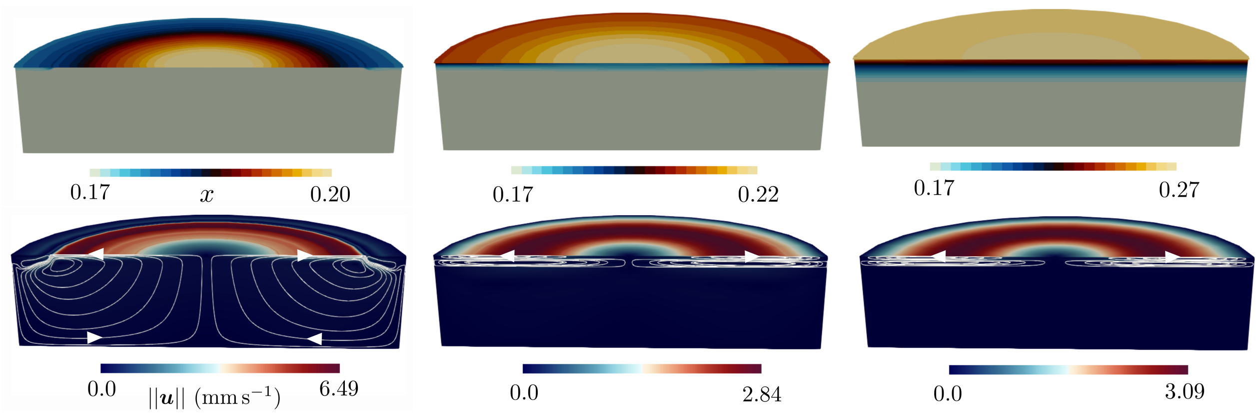

(a) t = 10 s (b) t = 100 s (c) t = 600 s

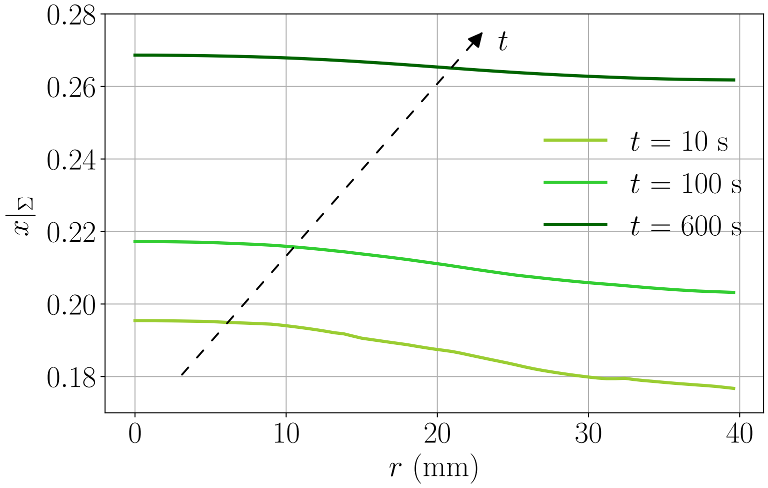

(d)

Figure 6.7 – (a,b,c) Snapshots of the molar fraction x (top) and of the velocity magnitude $||\boldsymbol{u}||$ (bottom) at different times. (d) Molar fraction at the alloy-electrolyte interface $x|_\Sigma$ as a function of the radius r, at different times.

With buoyancy and with EVF

We have seen in the previous chapters that solutal buoyancy has a very significant impact on the EVF. We have run a simulation taking into account the EVF and the electrocapillarity. No visible differences are observed compared to a case without EVF. This result is expected since solutal buoyancy significantly reduces the EVF intensity, which is compressed at the bottom of the alloy. The conclusions of the previous sections are not modified if the Lorentz force is activated.

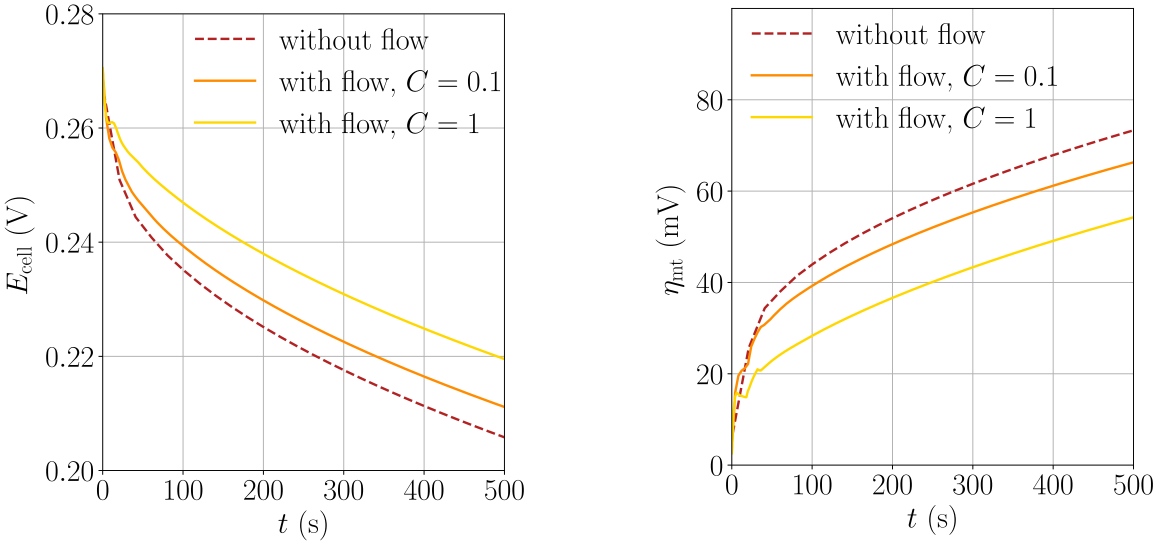

(a)

(b)

Figure 6.8 – Comparison between simulations with and without electrocapillary flow, with $C = 1\,\mathrm{F\,m^{-2}}$ and $C = 0.1\,\mathrm{F\,m^{-2}}$. (a) Cell potential E_{cell} vs time. (b) Overpotential η_{mt} vs time.

6.5 Conclusion

The jump in potential at the alloy-electrolyte interface modifies locally the surface tension at this interface giving rise to a Marangoni effect that drives electrocapillary flows. We have investigated how these flows may look like and how they impact the alloy composition using axisymmetric simulations.

We have estimated the dependency of the surface tension γ on the jump in potential as

$$\gamma = \gamma_0 - C(\varphi_{\mathrm{jump}} - \varphi_{\mathrm{jump,0}})^2 \tag{6.5.1}$$

and implemented this law in our numerical model. We have studied how the flow varies with changing C. Overall, the intensity of the flow increases with C. If we ignore solutal buoyancy, the electrocapillary flow is significantly contributing to the homogenization of the alloy. With solutal buoyancy, the flow is restricted to a thin layer and is less effective in the mixing process. In the future, it would be interesting to try to determine more precisely the law which connects the surface tension with the jump in potential, and also to theoretically estimate the flow's velocity and the height of the mixing layer in the case with buoyancy as a function of relevant parameters. In our model, we have neglected the flow in the electrolyte, which could significantly influence the flow in the alloy. It would be important to consider this flow in the future.

Chapter 7

Conclusion and Perspectives

Liquid metal batteries (LMBs) are a promising solution for large-scale and cheap energy storage and we need models to estimate the cell potential during operation. This potential depends on the alloy composition that is changing in time and space and is affected by diffusion and flows. Numerical simulations are essential to better understand battery interiors during operation, but they require accurate models and knowledge of material parameters.

During this PhD-thesis, we have numerically modeled magnetohydrodynamical flows and mass transport that occur inside liquid metal batteries. Our understanding of this complex, multiphysical system is still strongly evolving and so are the numerical models that can describe them. We have had to implement new algorithms in the SFEMaNS code and this allowed us to do several physically orientated studies. The work done during this PhD has lead to five research articles.

7.1 Achievements

In a first generation of studies, LMBs were not modeled as electrochemical cells. The variation of the alloy composition during operation was totally ignored and the focus was on flows inside LMBs. Around 2018, the mixing of the alloy by means of electrovortex flows (EVF) started to be investigated (for example by Ashour et al. (2018); Herreman et al. (2019b); Weber et al. (2018b)) and these studies concluded that electrovortex flow could be efficient to mix the alloy. Personnettaz et al. (2019) were first to show that mass transport in LMBs comes along with high variations of density in the alloy. We have therefore, during my M2 internship and the beginning of this PhD, investigated the effect of these solutal buoyancy effects, and studied how they affect electrovortex flows (chapter 2, section §2.2). We have found that, during charge, solutal convection is driven and dominates EVF. This convective flow mixes efficiently the alloy. During discharge, the solutal buoyancy is stabilizing and the electrovortex flow is not intense enough to prevent a light stratified layer from forming at the top of the alloy. A theoretical estimation of the flow intensity needed to mix the alloy suggests that the electrovortex flow cannot mix efficiently the alloy in realistic LMBs. This study highlighted that solutal buoyancy is really important in LMB alloys and should never be neglected in the models. This work has been published in Physical Review Fluids (Herreman et al., 2020).

The year later, I continued my research on LMBs in HZDR, Germany. During experiments in unsealed LMB prototypes done in this research center, it was observed that droplets could form near the top electrode. Experimental data also suggested possible detachment of these droplets during operation. We have attempted to understand this droplet detachment process (chapter

2, section §2.3). Starting from a droplet that is already formed, we have shown that, when the applied current is high enough, the droplet is cut by the Lorentz force and transported down towards the bottom electrode. When the droplet is initially large enough, it is not excluded that this can create short circuits. This work has been published in Journal of Power Sources (Bénard et al., 2021).

During this year abroad, the team in LISN continued the investigation of mixing of the alloy, by means of swirling electrovortex flow. This type of rotating electrovortex flow is driven when adding a small vertical external magnetic field. In Herreman et al. (2021), it was shown that such swirling electrovortex flow can counteract solutal buoyancy and mix the alloy efficiently. This study also suggested the existence of a particular flow regime governed by a rather unknown scaling law and we wanted to better understand this flow. Therefore, we have conducted a parametric study on swirling electrovortex flows in a liquid metal (chapter 3). We have chosen to carry out this study in a symmetrically connected setup with symmetrically opposed wire electrodes. In this setup we expect a counter-rotating von Kármán-like flow (without impellers). Our numerical investigation shows that axisymmetric simulations can lead to a very different flow structure than those observed in three-dimensional simulations. The velocity magnitude remains however of the same order as in three-dimensional simulations. We have found four different flow regimes, an inductive regime and three-induction less regimes: inertial, boundary layer and viscous. We retrieved scaling laws for each of these regimes from the literature. The particular intermediate boundary layer regime that motivated this study in the first place was not clearly visible in this symmetrical setup, even though it was very present in the simulations of Herreman et al. (2021). The existence of this regime likely depends on the degree of turbulence in the flow, since it is controlled by a laminar boundary layer. In our symmetrical setup, the flow destabilizes much more easily than in the setup of Herreman et al. (2021), therefore canceling this boundary layer regime. This work has been published in Journal of Fluid Mechanics (Bénard et al., 2022).

After this study, we focused back on LMBs. In most previous studies, the cell potential was computed in post-processing (as in Herreman et al. (2020)). However, the electrical potential distribution is complex in LMBs and locally connected to the composition of the alloy at the alloy-electrolyte interface. In the models we can capture this by allowing the potential to jump discontinuously at this interface. This jump depends on the local composition of the alloy and directly affects the current distribution in the cell, and hence the cell potential. The existence of this potential jump has only been considered in a few previous studies (Duczek et al., 2023; Weber et al., 2019, 2020). We wanted to improve our LMB simulations by including this jump in SFEMaNS. We also wanted to better understand the impact of this jump on the alloy composition and on the cell potential. This motivated the studies of chapters 4, 5 and 6.

The code SFEMaNS is a full MHD code which uses a magnetic field formulation that never solves the electrical potential. In order to be able to model the potential jump in our solver, we have had to find a magnetic field interface condition, that captures the effect of the discontinuous electrical potential (chapter 4). We have shown that a jump in electrical potential is actually equivalent to a jump in the tangential components of the electrical field. To test this, we have developed two new solvers, one using an electrical potential formulation and another one using a magnetic field formulation. We have validated both solvers by comparing numerical solutions with analytical solutions. We have then compared these solvers in different setups and showed that they are equivalent. This work has been published in Comptes Rendus. Mécanique (Bénard et al., 2023).

With this new solver, we could study the effect of the jump in potential on the alloy composition and on the cell potential (chapter 5). In this work we also consider the mass transport and capture how the local potential jump is connected to the alloy composition near the alloy-electrolyte interface. We have conducted several numerical studies in different LMB setups. We have observed that the jump in potential creates a current redistribution in the electrolyte that also homogenizes the material flux at the alloy-electrolyte interface. By comparing simulations with and without a jump, we have found that this jump has a slight impact on the alloy composition. Solutal buoyancy remains the dominant actor. Furthermore, we have succeeded to compute the cell potential in a self-consistent way. This is preferable to post-processed computations of the cell potential. We find that this jump in potential weakly affects the mass transfer overpotential and the ohmic losses, due to the current redistribution in the electrolyte. This work has been submitted to Journal of Power Sources in august 2023.

The spatial variations of the potential jump at the alloy-electrolyte interface can create surface tension gradients that may drive electrocapillary Marangoni flows in the alloy. We have started an exploratory study on these flows (chapter 6). We have first estimated the dependency of the surface tension with the jump in potential. We have then shown that, without solutal buoyancy, the electrocapillary flow cancels itself after a certain time: the flow is homogenizing the composition of the alloy and hence it reduces the surface gradients that power the Marangoni flow. When included, solutal buoyancy has a major effect on the electrocapillary flow structure: this flow becomes localized in a thin layer close to the alloy-electrolyte interface.

7.2 Perspectives

The existing models can already quite accurately describe the main phenomena in LMBs. Flows and mass transport have been well investigated. The cell potential computation, as well as the electrical potential description, have been improved. However, further work is necessary to describe more realistic LMBs.

Multiphase model

In all of our work, the flow in the electrolyte has been ignored. The velocity boundary conditions at the alloy-electrolyte interface have been modeled as no-slip or free-slip boundary conditions, but neither really applies. The flow in the electrolyte could affect the flow in the alloy through the stress conditions at the interface. Therefore, a logical next step in the numerical development would be to implement a multiphase model where the flow in the electrolyte is considered. We would model the stress conditions at the alloy-electrolyte interface but keep the interface flat and non-deformable. We could then still use our magnetic field-based interface condition for the potential jump. This multiphase model will modify some of our preliminary results on electrocapillary flows.

Improving the setup model

In our simulations, we could also consider different setups, maybe more realistic. In existing prototypes, the current leaves the cell at the lateral edges as in the setup used by Weber et al. (2019), and not at the bottom of the cell. The current distribution in the alloy is significantly modified by this difference in design. We should analyze how the flow and the concentration distributions are impacted.

In our models, we have considered the foam as solid and made of pure lithium. We have also considered a smooth interface between the foam and the electrolyte, even though the foam is a porous solid. The upper metal-electrolyte interface is therefore likely not smooth and depends on the porosity of the foam. This may have an impact on the study of section §2.3 of chapter 2. We should investigate the droplet formation at the rough bottom of the foam. The shape of the foam-electrolyte interface is complex, and the current at this interface is probably locally not homogeneous. It would be interesting to model more precisely the foam and to examine how the current and the battery are affected by its porosity.

Electrochemical properties

The electrochemical properties of materials in LMBs are actually really intricate and deserve more investigation. We have considered mass transport and density variations in the alloy, but we have neglected a lot of other phenomena. For instance, intermetallic phases can form when the concentration of light metal in the alloy reaches a critical value. In our simulations, we stayed below this critical concentration but, in real cells, solid intermetallic phases may form. It would be interesting to model phase changes in the alloy.

Furthermore, ions are transported in the electrolyte, whose composition and volume changes during operation. We have fully neglected interface displacements. In addition, we have modeled only one jump, but there are actually two potential jumps in an LMB, one at each interface. It would be interesting to determine the value of each jump and to implement them both in our model, in order to see if our conclusions are modified.

Manufacturing

Theoretical modeling of LMBs is interesting but we also think that more investments should be done in the real manufacturing of LMBs. Which materials are the most relevant, what is the ideal thickness of the electrolyte, which cheap materials can we use for the vessel, and should we modify the general shape of the setup (foam, wire loop, three-layer...), for instance, are important questions that deserved to be investigated.

Appendix A

Résumé en français

A.1 Introduction

Dans le contexte actuel du réchauffement climatique, les moyens de production d'énergie doivent évoluer, en privilégiant des énergies respectueuses de l'environnement comme les énergies renouvelables. Celles-ci doivent être développées à grande échelle, pour répondre au besoin croissant en énergie. Cependant, les énergies renouvelables sont produites de manière intermittente et ne peuvent répondre aux pics de demande en énergie. C'est pourquoi des solutions pour le stockage massif d'énergie doivent être mises en place. Il existe différents types de systèmes de stockage qui peuvent répondre à cette demande. Parmi ceux-ci, le stockage électrochimique, en particulier au sein de batteries, est une solution viable. Parmi ces batteries, les batteries à métaux liquides (BMLs) représentent un candidat prometteur car elles peuvent être moins chères et ont une durée de vie plus longue que d'autres types de batteries.

Les BMLs sont composées de trois couches : une couche supérieure en métal liquide dénommée électrode négative, une couche intermédiaire constituée d'un électrolyte en sel fondu et une couche inférieure qui est un alliage formé entre un métal liquide et le métal liquide supérieur, dénommée électrode positive.

Les BMLs doivent cependant répondre à certaines contraintes : elles doivent rester peu chères et garder une grande efficacité. Cela influence les configurations possibles : une des configurations les plus utilisées dans les expériences est composée d'une electrode négative où le métal liquide est contenu dans une mousse (solide poreux) et est maintenu par capillarité. Cela permet de faciliter l'isolation des métaux par rapport au contenant. De plus, les matériaux utilisés doivent rester abordables.

Pour améliorer l'efficacité, le potentiel de la batterie, qui est déjà naturellement assez faible et décroit lors du fonctionnement, doit être optimisé. Ce potentiel peut être décomposé en une somme de surpotentiels et d'un potentiel d'équilibre :

$$E_{\text{cell}} = E_{\text{cell,eq}} \pm (\eta_{\Omega} + \eta_{\text{mt}} + \eta_{\text{ct}}). \tag{A.1.1}$$

Le potentiel d'équilibre $E_{\text{cell,eq}}$ est le potentiel de la batterrie lorsqu'aucun courant n'est appliqué, η_{Ω} est le surpotentiel dû aux chutes ohmiques, η_{mt} celui dû au transport de masse et η_{ct} celui dû au transport de charges. Ces surpotentiels doivent rester aussi faibles que possible. η_{mt} est dû à l'accumulation de métal supérieur en haut de la couche d'alliage, à cause de la faible diffusion des ions du métal supérieur dans l'alliage. Cette inhomogénéité de l'alliage augmente η_{mt}. Pour réduire ce surpotentiel, on peut mélanger l'alliage grâce à des écoulements. Cependant, ces écoulements peuvent être néfastes car ils peuvent déformer les interfaces jusqu'à induire un court-circuit.

Les simulations numériques sont nécessaires pour étudier les phénomènes apparaissant dans les BMLs car les expériences ne permettent pas l'accès à toutes les quantités d'intérêt. Cependant, les simulations numériques nécessitent des modèles précis. Il est donc important d'étudier les approximations et simplifications qui peuvent être faites ou pas. Nous résumons maintenant différentes générations d'études numériques présentes dans la littérature.

Dans une première génération d'études, le transport de matière a été ignoré. Des instabilités magnétohydrodynamiques, telles que l'instabilité de Tayler et l'instabilité de Metal Pad Roll, ont été étudiées, ainsi que la convection thermique et l'écoulement electrovortex (EVF). Ce dernier apparaît quand les collecteurs de courant ont un rayon plus petit que le système qui contient le fluide. Ces études ont conclu que l'instabilité de Tayler ne pouvait pas apparaître dans des batteries de taille réalistes, que l'instabilité de Metal Pad Roll apparaît principalement au niveau de l'interface supérieure, que la convection thermique ne peut pas mélanger l'alliage et que l'écoulement electrovortex semble efficace pour mélanger l'alliage.

Dans une deuxième génération d'études, le transport de matière a été pris en compte, ce qui a modifié de manière significative certains résultats. Pendant la charge, le phénomène de convection solutale se met en place et mélange efficacement l'alliage. Pendant la décharge, une couche légère stratifiée apparaît en haut de l'alliage. Cette couche ne peut être percée par l'écoulement electrovortex qui n'est pas assez intense pour mélanger l'alliage. Cependant, l'écoulement electrovortex tournant, qui est généré lorsqu'un champ magnétique extérieur est appliqué, est lui efficace pour le mélange, même pour de faibles champs magnétiques.

Dans une troisième génération d'études, le saut de potentiel, qui apparaît à l'interface alliage-electrolyte, a été pris en compte. Ce saut est en fait une modélisation macroscopique de la double couche électrochimique. Il modifie les courants et donc la composition de l'alliage. Les modèles qui ont été utilisés montrent de bons résultats comparés aux expériences mais ne montrent pas l'effet du saut sur la composition de l'alliage, ni comment les distributions de courant et de concentration sont modifiées.

Dans cette thèse, nous nous intéressons au problème du mélange, en particulier avec l'écoulement electrovortex (EVF), et à l'amélioration de notre modèle numérique.

A.2 Contributions pré-doctorales

Avant ce doctorat, j'ai contribué à certains travaux portant sur les batteries à métaux liquides. Nous présentons d'abord le travail réalisé pendant mon stage de M2, effectué au LISN en 2019, où l'effet de la flottabilité solutale sur l'EVF dans les batteries à métaux liquides a été étudié. Nous avons vu que le mélange de l'alliage est essentiel pour limiter la chute du potentiel de la batterie. Plusieurs études ont conclu que l'EVF est efficace pour mélanger l'alliage, mais ces études n'ont pas modélisé le transport de matière. Nous étudions alors numériquement l'EVF couplé avec le transport de matière.

Pendant la décharge, nous montrons que l'EVF n'est pas assez intense pour percer la couche stratifiée légère au sommet de l'alliage et n'a pas d'effet sur le mélange. Le processus de diffusion domine l'EVF en raison de la flottabilité solutale. Nous avons trouvé trois régimes d'écoulement et estimé l'intensité minimale de l'écoulement nécessaire pour mélanger efficacement l'alliage. Cela a montré que l'EVF peut mélanger efficacement l'alliage dans une petite cellule pour des densités de courant non réalistes. Pour des densités de courant réalistes, l'EVF ne peut mélanger l'alliage que dans une très grande cellule. Nous en déduisons donc que l'EVF ne peut pas être utilisé pour le processus de mélange dans les BMLs réalistes, qui sont plutôt petites. Pendant la charge, la convection solutale entre en jeu et mélange efficacement l'alliage. Ce phénomène domine l'EVF, qui n'est plus visible après un court laps de temps, et est clairement tridimensionnel. Nous avons pu estimer théoriquement une loi d'échelle pour l'intensité de l'écoulement créé.

Ensuite, nous présentons le travail réalisé durant mon année de recherche à HZDR à Dresde, en Allemagne, en 2019-2020. Des détachements de gouttes et des courts-circuits locaux ont été observés dans des expériences. Nous souhaitons comprendre le détachement de ces gouttes et leur transfert dans l'alliage, car cela peut conduire à des courts-circuits qui peuvent être néfastes aux BMLs.
Nous étudions deux configurations : une configuration où les trois couches de la BML sont liquides et une configuration où l'electrode négative est une mousse. Nous imposons une perturbation initiale qui est une déformation de l'interface supérieure dans le cas de la configuration trois couches et une goutte attachée à la mousse dans le cas de la configuration mousse. Nous montrons que le processus de détachement des gouttes est dû à la force de Lorentz qui, pour une densité de courant suffisamment élevée, domine les forces de gravité et de tension superficielle et pince la goutte. Dans la configuration à trois couches, il existe toujours un courant critique dépendant de la taille de la déformation, au-delà duquel une goutte se détache. En dessous de ce courant, l'interface se restabilise. Mais ce courant n'est pas réaliste pour des déformations de taille raisonnable. Par conséquent, aucun détachement de gouttes n'est attendu dans ce cas, et aucun court-circuit n'est observé. Dans le cas de la mousse, il existe également un courant critique pour chaque taille de perturbation, mais ce courant critique est réaliste et atteignable dans les vraies BMLs. Nous observons de plus que des court-circuits peuvent se produire.

A.3 Étude numérique de l'écoulement electrovortex tournant dans un cylindre

Afin de mieux comprendre les différents régimes d'écoulement, nous étudions et caractérisons numériquement l'écoulement électrovortex tournant dans un cylindre rempli de métal liquide GaInSn. Ce cylindre est connecté de manière symétrique à deux collecteurs de courant en cuivre, l'un sur et l'autre sous le cylindre. Nous résolvons avec le code SFEMaNS les équations de la magnétohydrodynamique pour mener cette étude. Nous notons J la densité de courant imposée dans le cylindre, B le champ magnétique extérieur et ν la viscosité. La hauteur du cylindre est $\mathcal{H}$, son rayon est R et le rayon des collecteurs de courant est R_w.

Nous menons d'abord une étude paramétrique en faisant varier les paramètres J, B et ν et en nous concentrant sur des simulations axisymétriques. En faisant varier J, nous constatons que, pour de faibles densités de courant, l'écoulement est stationnaire et se fait principalement à proximité des contacts électriques. Lorsque J est supérieur à une valeur critique que nous avons pu déterminer, l'écoulement devient instationnaire et remplit tout le cylindre. L'intensité de l'écoulement U augmente avec J, suivant différents régimes : $U \sim J$ pour les faibles densités de courant, $U \sim J^{2/3}$ pour les densités de courant intermédiaires et $U \sim J^{1/2}$ pour les fortes densités de courant. Lorsque B varie, si B est inférieur à une valeur critique, l'écoulement est turbulent et l'intensité de l'écoulement augmente avec le champ magnétique suivant les lois $U \sim B^{2/3}$ puis $U \sim B^{1/2}$ pour des B plus élevés. Mais, lorsque B est supérieur à une valeur critique, l'intensité de l'écoulement diminue avec B et devient stable jusqu'à ce qu'il soit concentré dans une région cylindrique fine joignant les bords des collecteurs de courant supérieur et inférieur. Dans ce régime, $U \sim B^{-1}$. En faisant varier ν, nous pouvons trouver les régimes suivants, de ν faible à ν élevé : $\nu^{-1/9}$ ou ν^0 puis ν^{-1}.
L'étude paramétrique nous permet de mettre en évidence l'existence de différents régimes d'écoulement, que nous pouvons expliquer théoriquement. Nous pouvons distinguer quatre

régimes d'écoulements:

- un régime inductif pour les grands B, où la vitesse varie comme

$$U \sim \frac{J}{\sigma B}, \tag{A.3.1}$$

- un régime visqueux et sans induction, pour des vitesses faibles :

$$U \sim \frac{JBR^2}{\rho \nu}, \tag{A.3.2}$$

- un régime inertiel et sans induction, pour des vitesses élevées :

$$U \sim \left(\frac{JBR}{\rho}\right)^{1/2} \quad \text{ou} \quad U \sim \left(\frac{JBR}{\rho}\right)^{5/9} \left(\frac{R}{\nu}\right)^{1/9}. \tag{A.3.3}$$

  Notons qu'il existe deux lois d'échelle possibles dans ce régime et qu'il est difficile de distinguer celle qui est la plus adaptée dans les simulations.

- un régime de couche limite et sans induction, pour des vitesses intermédiaires :

$$\left(\frac{JB}{\rho}\right)^{2/3} \frac{R}{\nu^{1/3}}. \tag{A.3.4}$$

Nous étudions ensuite l'influence de la géométrie sur l'intensité de l'écoulement. En faisant varier le rayon des fils R_w, nous remarquons que la vitesse augmente lorsque R_w/R diminue. Il est assez difficile de modéliser théoriquement la variation de la vitesse U avec R_w/R, mais nous avons trouvé deux lois d'échelle possibles :

$$U \approx U_0 \begin{cases} 1 - (4R_w^2/3R^2), & \text{(Millere)} \\ 1 - R_w^2/R^2, & \text{(uniforme)} \end{cases} \tag{A.3.5}$$

qui dépendent des conditions d'interface utilisées pour modéliser le profil de densité de courant entre le cylindre et le collecteur de courant (profil de Millere ou profil uniforme).

La loi observée dans les simulations pour de fortes densités de courant semble se situer entre les deux lois trouvées théoriquement. Ces lois théoriques sont donc assez précises, mais pas pour les faibles densités de courant où une variation linéaire avec le rayon r semble plus exacte. En faisant varier les rapports de forme $\mathcal{H}/R$ du cylindre, nous constatons que plus le rapport de forme est petit, plus l'écoulement est concentré dans une petite région proche de l'axe. Pour un faible rapport de forme, l'écoulement se situe plutôt dans le régime de la couche limite et, pour des rapports de forme élevés, c'est le régime inertiel qui est le plus précis. En comparant une cellule asymétrique (où il y a seulement un collecteur de courant situé en bas du cylindre) et une cellule symétrique, celle que l'on a utilisée pour les études précédentes, nous montrons que l'écoulement est beaucoup moins turbulent lorsque la cellule est asymétrique et que le régime de la couche limite est clairement visible dans ce cas, contrairement à la cellule symétrique où l'on observe plutôt un régime inertiel.

Nous effectuons des simulations tridimensionnelles dans le cadre de l'étude du paramètre J. Il existe plusieurs bifurcations entre différents régimes, du plus faible au plus grand courant : l'écoulement est d'abord axisymétrique, puis devient tridimensionnel avec un mode azimutal 2 prédominant mais reste stationnaire, puis reste tridimensionnel avec un mode 2 prédominant mais devient instationnaire, et enfin devient turbulent, où tous les modes azimutaux sont nourris. Dans le régime où l'écoulement est tridimensionnel et stationnaire, nous retrouvons un écoulement qui a une structure similaire à l'écoulement de von Kármán avec des disques lisses tournant en sens inverse. En comparant les simulations axisymétriques et tridimensionnelles, nous remarquons que la distribution spatiale de l'écoulement peut être significativement différente. Pourtant, la vitesse moyenne reste dans les deux cas du même ordre de grandeur. Ainsi, lorsque l'on ne s'intéresse qu'à l'intensité de la vitesse de l'écoulement, les simulations axisymétriques peuvent constituer une bonne approximation. De plus, nous retrouvons le régime inertiel dans les simulations tridimensionnelles, mais le régime de la couche limite n'est pas du tout visible.

Le régime de la couche limite ne semble exister que lorsque l'écoulement n'est pas trop turbulent, ce qui est le cas dans la cellule asymétrique ou à faible rapport de forme par exemple. Cela pourrait expliquer pourquoi ce régime n'est pas visible dans les simulations tridimensionnelles et peu visible dans le cylindre symétrique où l'écoulement est plus turbulent. Nous supposons que le régime de la couche limite nécessite une couche limite laminaire, et ne peut être observé lorsque la turbulence est trop intense.

A.4 Modélisation des distributions discontinues de potentiel électrique avec une formulation en champ magnétique

Nous avons pour but d'étudier l'impact du saut en potentiel électrique sur la composition de l'alliage, en utilisant le modèle de Weber et al. (2019), avec notre code SFEMaNS. Ce code utilise une décomposition spectrale dans la direction azimutale et en éléments finis dans le plan méridional. Cependant, SFEMaNS est basé sur le champ magnétique $\boldsymbol{H}$ et ne résout pas la variable potentiel φ. Pour remédier à ce problème, nous introduisons donc une condition d'interface basée sur le champ magnétique pour modéliser des distributions discontinues de potentiel électrique. Ainsi, un saut en potentiel électrique φ_{saut} est équivalent à un saut sur le terme $\left(\frac{\boldsymbol{\nabla}\times\boldsymbol{H}}{\sigma}\right)$ tel que :

$$\boldsymbol{n}\times\left(\frac{\boldsymbol{\nabla}\times\boldsymbol{H}}{\sigma}\right)_{\text{saut}} = -\boldsymbol{n}\times\boldsymbol{\nabla}_T(\varphi_{\text{saut}}). \tag{A.4.1}$$

Nous proposons donc une formulation en champ magnétique pour décrire des distributions discontinues de potentiel électrique utilisant cette condition.

Pour valider cette formulation, nous nous plaçons dans un cylindre $\boldsymbol{\Omega}$ présentant une interface Σ, ce qui divise le domaine en deux sous-domaines $\boldsymbol{\Omega}_1$ et $\boldsymbol{\Omega}_2$, de conductivités électriques σ_1 et σ_2. Les bords où des conditions de Neumann sont imposées sont notés Γ_N et ceux où des conditions de Dirichlet sont imposées sont notés Γ_D.

Tout d'abord, nous développons un code utilisant une formulation en potentiel électrique et résolvant le problème :

$$-\boldsymbol{\nabla}\cdot(\sigma\boldsymbol{\nabla}\varphi) = 0 \qquad \text{dans } \boldsymbol{\Omega}_1 \text{ et } \boldsymbol{\Omega}_2, \tag{A.4.2a}$$

$$\varphi_1 - \varphi_2 = \varphi_{\text{saut}} \qquad \text{sur } \Sigma, \tag{A.4.2b}$$

$$(\sigma_1\boldsymbol{\nabla}\varphi_1 - \sigma_2\boldsymbol{\nabla}\varphi_2)\cdot\boldsymbol{n} = 0 \qquad \text{sur } \Sigma. \tag{A.4.2c}$$

$$\varphi = g_D \quad \text{sur } \Gamma_D \qquad \text{et} \qquad \boldsymbol{\nabla}\varphi\cdot\boldsymbol{n} = 0 \quad \text{sur } \Gamma_N. \tag{A.4.2d}$$

Nous déterminons ensuite des solutions analytiques de ce système, afin de pouvoir valider le solveur. Nous réalisons des tests de convergence en comparant l'erreur entre des solutions analytiques du problème et les solutions numériques corespondantes. Cela nous permet de valider le code.

Ensuite nous développons un code utilisant une formulation en champ magnétique et résolvant le problème suivant :

$$\begin{aligned}
\nabla \times \left(\frac{\nabla \times \boldsymbol{H}}{\sigma} \right) &= \boldsymbol{0} \qquad \text{dans } \boldsymbol{\Omega}_1 \text{ et } \boldsymbol{\Omega}_2, && \text{(A.4.3a)}\\
\nabla \cdot (\mu \boldsymbol{H}) &= \boldsymbol{0} \qquad \text{dans } \boldsymbol{\Omega}_1 \text{ et } \boldsymbol{\Omega}_2, && \text{(A.4.3b)}\\
\left(\frac{\nabla \times \boldsymbol{H}_1}{\sigma_1} - \frac{\nabla \times \boldsymbol{H}_2}{\sigma_2} \right) \times \boldsymbol{n} = \left(\frac{\nabla \times \boldsymbol{H}}{\sigma} \right)_{\text{saut}} &\times \boldsymbol{n} \qquad \text{sur } \Sigma, && \text{(A.4.3c)}\\
(\boldsymbol{H}_1 - \boldsymbol{H}_2) \times \boldsymbol{n} = \boldsymbol{0}& \qquad \text{sur } \Sigma, && \text{(A.4.3d)}\\
\mu(\boldsymbol{H}_1 - \boldsymbol{H}_2) \cdot \boldsymbol{n} = 0& \qquad \text{sur } \Sigma. && \text{(A.4.3e)}\\
\boldsymbol{H} = \boldsymbol{H}_D& \qquad \text{sur } \Gamma_D. && \text{(A.4.3f)}
\end{aligned}$$

Comme avec le solveur en potentiel électrique, nous validons ce code grâce à des tests de convergence construits avec des solutions analytiques.

Nous montrons enfin que les deux formulations sont bien équivalentes en comparant la densité de courant obtenue dans les deux cas avec des solutions analytiques, dans le cylindre et dans une configuration de batterie à métaux liquides.

A.5 Influence du potentiel électrique sur la composition de l'alliage

Nous nous sommes ensuite intéressés à l'influence du saut de potentiel à l'interface alliage-électrolyte sur la composition de l'alliage dans une BML Li||Pb, où l'électrode négative est une mousse.

Nous implémentons d'abord dans SFEMaNS la variable de concentration, qui n'était pas présente, et validons ce développement. Cela nous permet d'étendre notre solveur en champ magnétique en ajoutant les variables de concentration et de vitesse. Ce solveur a été validé en utilisant le solveur en potentiel électrique couplé avec la concentration et les résultats de Weber et al. (2019).

En utilisant le solveur en champ magnétique, nous menons une première étude dans une configuration similaire à celle de Weber et al. (2019) et de mêmes dimensions. Nous avons analysé l'effet du saut de potentiel sur la composition de l'alliage. Le saut de potentiel homogénéise la composition en surface de l'alliage, par rapport au cas de la diffusion pure. Cela induit une réduction du surpotentiel de transport de masse η_{mt}. En ajoutant la flottabilité solutale et l'EVF, on remarque que la composition à la surface de l'alliage est très homogène. Dans cette configuration, les effets du saut et de la flottabilité ont un impact assez limité sur la composition de l'alliage. Nous menons ensuite une autre étude dans une configuration de plus grandes dimensions.

Dans cette nouvelle configuration, nous comparons des simulations avec et sans saut de potentiel. Dans un premier cas, nous ne prenons en compte que la diffusion et ignorons l'écoulement. On observe que le saut homogénéise la composition en surface et modifie les lignes de courant. Dans un deuxième cas, nous ajoutons l'écoulement electrovortex mais ignorons la flottabilité. Dans cette situation, l'écoulement electrovortex fait apparaître de forts gradients de concentration à la surface près de l'axe central, qui sont significativement lissés par le saut. En ajoutant la flottabilité, nous remarquons que la composition en surface est déjà très homogène.

Ainsi, l'influence du saut est assez faible. Nous pouvons aussi faire cette remarque dans le cas d'un écoulement electrovortex tournant, qui rend également la composition en surface assez homogène. Seulement de faibles différences sont observées entre les simulations avec et sans saut. Par conséquent, les résultats des études précédentes qui ont ignoré le saut restent valables. Cependant, nos simulations ont montré une nouvelle fois que l'écoulement et la composition de l'alliage sont fortement influencés par la flottabilité. Ce phénomène ne peut être ignoré dans les modèles pour les BMLs. En outre, nous avons comparé deux façons de calculer le potentiel de la cellule : une ancienne méthode de calcul à partir de la fraction molaire moyenne à la surface de l'alliage et un calcul direct à partir de sa définition - la différence des potentiels en haut et en bas de la cellule. Le calcul post-traité produit des erreurs majeures pour le surpotentiel de transport de masse, même si le potentiel total de la cellule demeure assez proche de la valeur directement calculée. Par conséquent, ce calcul utilisant la moyenne de la fraction molaire devrait être évité. De plus, le saut en potentiel n'a qu'un impact très modéré sur le surpotentiel de transport de masse car son effet sur la composition de l'alliage est limité. Cependant, nous observons que le surpotentiel ohmique est réduit par ce saut, car il modifie la distribution du courant dans l'électrolyte. Par conséquent, il est plus précis de modéliser le saut de potentiel afin de ne pas surestimer le surpotentiel ohmique.

A.6 Écoulements électrocapillaires

Nous étudions enfin l'impact des écoulements électrocapillaires sur la composition de l'alliage. Le saut en potentiel électrique modifie localement la tension de surface entre l'alliage et l'électrolyte. Des gradients de tension de surface apparaissent donc à l'interface alliage-électrolyte, ce qui entraîne un écoulement dirigé des zones à faible tension de surface aux zones à forte tension de surface.

Tout d'abord, nous estimons la dépendance de la tension de surface γ avec le saut en potentiel avec la loi

$$\gamma = \gamma_0 - C(\varphi_{\text{saut}} - \varphi_{\text{saut},0})^2 \tag{A.6.1}$$

où C est une constante et $\varphi_{\text{saut},0}$ est le saut à $t = 0$. Comme nous ne connaissons pas C, nous estimons sa valeur d'après Dreyer et al. (2018) et la faisons varier dans l'intervalle $[0,1;1]\,\mathrm{F\,m^{-2}}$. La tension de surface influence la vitesse à l'interface alliage-électrolyte par la condition :

$$\rho_* \nu\, \partial_z \boldsymbol{u}_T = \boldsymbol{\nabla}_T \gamma. \tag{A.6.2}$$

où $\boldsymbol{\nabla}_T \gamma$ est le gradient tangentiel de la tension de surface.

Dans un premier cas, nous avons ignoré la flottabilité. Nous remarquons que la vitesse augmente avec C. De grandes différences de tension superficielle à l'interface alliage-électrolyte induisent un écoulement qui s'intensifie avec le temps et homogénéise la composition en surface. Lorsque la composition en surface devient plus homogène, les gradients de tension superficielle sont moins importants et l'intensité de l'écoulement diminue jusqu'à devenir presque nulle.

L'ajout de la flottabilité solutale a un impact significatif sur l'écoulement. Nous observons des oscillations rapides qui s'amortissent jusqu'à ce que la vitesse de l'écoulement atteigne une valeur presque constante. La composition en surface de l'alliage devient très homogène et l'écoulement est localisé dans une couche fine près de l'interface alliage-électrolyte. Dans ce cas, l'écoulement électrocapillaire est suffisamment intense pour limiter la chute de potentiel et réduire le surpotentiel dû au transfert de masse, pour toutes les valeurs de C étudiées. Plus C est élevé, plus ce surpotentiel est réduit.

A.7 Conclusion

Au cours de cette thèse, nous avons modélisé numériquement les écoulements magnétohydrodynamiques et le transport de masse qui se produisent à l'intérieur des batteries à métaux liquides. Notre compréhension de ce système complexe et multiphysique est encore en pleine évolution, tout comme les modèles numériques qui peuvent les décrire. Nous avons dû implémenter de nouveaux algorithmes dans le code SFEMaNS, ce qui nous a permis de réaliser plusieurs études orientées vers la physique du système. Le travail effectué au cours de cette thèse a donné lieu à cinq articles de recherche.

Nous avons d'abord mené une première étude sur l'effet de la flottabilité solutale sur l'écoulement electrovortex. Nous avons montré que, pendant la décharge, cet écoulement ne peut pas contrer la flottabilité et n'est pas assez intense pour mélanger l'alliage. Pendant la charge, un mouvement de convection solutale se met naturellement en place et mélange efficacement l'alliage.
L'équipe au LISN a continué l'étude et montré qu'un écoulement electrovortex tournant est efficace poue le mélange de l'alliage. Cette étude a suggéré l'existence d'un régime d'écoulement particulier. Cela a motivé une étude paramétrique sur l'écoulement electrovortex tournant. Nous avons mené cette étude dans un cylindre connecté de manière symétrique à deux collecteurs de courant. Nous avons trouvé l'existence de quatre régimes d'écoulements. Le régime particulier de couche limite n'est pas vraiment visible dans cette configuration symétrique, et ne semble exister que lorsque la turbulence n'est pas trop forte et que la couche limite reste laminaire.
Ensuite nous sommes revenus sur les BMLs. Comme les études existantes sur le saut en potentiel ne fournissent pas de détails sur l'effet du saut sur la composition de l'alliage et la distribution de courant, nous avons voulu implémenter ce saut dans notre code. Cependant, dans le code SFEMaNS, la variable potentiel n'est pas présente, le code ne résout que le champ magnétique. Nous avons donc déterminé une condition d'interface pour modéliser un saut de potentiel avec la variable en champ magnétique. Nous avons développé un solveur implémentant cette condition et nous l'avons validé.
Ensuite, nous avons étudié l'effet du saut en potentiel sur la composition de l'alliage et le calcul du potentiel. Nous avons montré que le saut en potentiel redistribue les courants dans la batterie et homognénéise le flux de matériel. Cependant, ce saut affecte peu la composition de l'alliage qui est déjà homogénéisé par la flottabilité. Mais il réduit également modérément les chutes ohmiques et modifie donc le potentiel total de la cellule. Il est plus précis de le prendre en compte dans les modèles.
Le saut en potentiel varie spatialement à l'interface alliage-électrolyte et modifie la tension de surface. Les gradients de tension de surface qui apparaissent entraînent des écoulements électrocapillaires. Nous avons montré que ces écoulements sont très impactés par la flottabilité et sont concentrés dans une fine couche près de l'interface alliage-électrolyte.

Plusieurs perspectives peuvent être envisagées pour la poursuite de ces travaux. Dans toutes nos études, l'écoulement dans l'électrolyte a été ignoré. Les conditions limites de vitesse à l'interface alliage-électrolyte ont été modélisées avec des conditions limites de glissement ou de non glissement. Cependant, l'écoulement dans l'électrolyte pourrait affecter l'écoulement dans l'alliage à travers les contraintes à cette interface. Par conséquent, la prochaine étape consisterait à les implémenter dans le modèle et à examiner dans quelle mesure le mouvement du fluide et la concentration dans l'alliage sont affectés. En outre, nous avons dit qu'il y a en fait deux sauts de potentiel dans une BML, un à chaque interface. Il serait également intéressant de modéliser plus précisément la configuration de BML, avec des courants qui sortent par les côtés de la cellule et non par le bas. Ensuite, modéliser plus précisément la mousse, qui est poreuse et peut conduire à la formation de gouttes, pourrait améliorer notre modèle. Nous pourrions également améliorer notre prise en compte des propriétés électrochimiques des matériaux. Une autre perspective serait d'étudier la construction pratique de ces batteries, comme par exemple déterminer quels matériaux et quelle configuration sont les plus adaptés dans le contexte du stockage massif de l'énergie.

Bibliography

B. B. Alchagirov, F. F. Dyshekova, and R. Kh. Arkhestov. Surface tension of lead–lithium melts. *Russian Journal of Physical Chemistry A*, 90:2262–2269, 2016.

J. G. Andrews and R. E. Craine. Fluid flow in a hemisphere induced by a distributed source of current. *Journal of fluid mechanics*, 84(2):281–290, 1978.

R. F. Ashour, D. H. Kelley, A. Salas, M. Starace, N. Weber, and T. Weier. Competing forces in liquid metal electrodes and batteries. *Journal of Power Sources*, 378:301–310, 2018. ISSN 0378-7753.

D. R. Atthey. A mathematical model for fluid flow in a weld pool at high currents. *Journal of Fluid Mechanics*, 98(4):787–801, 1980.

A. J. Bard and L. R. Faulkner. Electrochemical Methods: Fundamental and Applications 2nd edition wiley & sons inc. *New York, capitulo*, 5, 2001.

S. A. Barriga. *An electrochemical investigation of the chemical diffusivity in liquid metal alloys.* PhD thesis, Massachusetts Institute of Technology, 2013.

A. Beltrán. MHD natural convection flow in a liquid metal electrode. *Applied Thermal Engineering*, 114:1203–1212, 2017.

S. Bénard, N. Weber, G. M. Horstmann, S. Landgraf, and T. Weier. Anode-metal drop formation and detachment mechanisms in liquid metal batteries. *Journal of Power Sources*, 510: 230339, 2021.

S. Bénard, W. Herreman, J.-L. Guermond, and C. Nore. Numerical simulations of swirling electrovortex flows in cylinders. *Journal of Fluid Mechanics*, 950:A28, 2022.

S. Bénard, L. Cappanera, W. Herreman, and C. Nore. Magnetic field based finite element method for magneto-static problems with discontinuous electric potential distributions. *Comptes Rendus. Mécanique*, 2023. Online first.

M. Berhanu, R. Monchaux, S. Fauve, N. Mordant, F. Pétrélis, A. Chiffaudel, F. Daviaud, B.e Dubrulle, L. Marié, F. Ravelet, M. Bourgoin, Ph. Odier, J.-F. Pinton, and R. Volk. Magnetic field reversals in an experimental turbulent dynamo. *Europhysics Letters*, 77(5):59001, 2007.

V. Bojarevics and M. V. Romerio. Long waves instability of liquid metal-electrolyte interface in aluminium electrolysis cells: a generalization of Sele's criterion. *European journal of mechanics series b fluids*, 13:33–33, 1994.

V. Bojarevičs and E. V. Shcherbinin. Azimuthal rotation in the axisymmetric meridional flow due to an electric-current source. *Journal of Fluid Mechanics*, 126:413–430, 1983.

V. Bojarevics, R. Millere, and A. I. Chaikovsky. Investigation of the azimuthal perturbation growth in the flow due to an electric current point source. 1:147–148, 1981.

V. Bojarevics, J. A. Freibergs, E. I. Shilova, and E. V. Shcherbinin. *Electrically Induced Vortical Flows*. Kluwer Academic Publishers, 1989.

D. J. Bradwell, H. Kim, A. H. C. Sirk, and D. R. Sadoway. Magnesium–antimony liquid metal battery for stationary energy storage. *Journal of the American Chemical Society*, 134(4): 1895–1897, 2012.

S. C. Brenner and L. R. Scott. *The mathematical theory of finite element methods*, volume 3. Springer, 2008.

E. J. Cairns and H. Shimotake. High-Temperature Batteries: Research in high-temperature electrochemistry reveals compact, powerful energy-storage cells. *Science*, 164(3886):1347–1355, 1969.

E. J. Cairns, C. E. Crouthamel, A. K. Fischer, M. S. Foster, J. C. Hesson, C. E. Johnson, H. Shimotake, and A. D. Tevebaugh. Galvanic cells with fused-salt electrolytes. Technical report, Argonne National Lab., Ill., 1967.

A. Y. Chudnovskii. Evaluating the intensity of a single class of electrovortex flows MHD. *Magnetohydrodynamics*, 25(3):406–408, 1989a.

A. Y. Chudnovskii. Modeling electrovortex flows. *Magnetohydrodynamics*, 25(3):337–342, 1989b.

P. A. Davidson. Swirling flow in an axisymmetric cavity of arbitrary profile, driven by a rotating magnetic field. *Journal of Fluid Mechanics*, 245:669–699, 1992.

P. A. Davidson. Cambridge texts in applied mathematics. *An Introduction to Magnetohydrodynamics; Cambridge University Press: Cambridge, NY, USA*, 2001.

P. A. Davidson and R. I. Lindsay. Stability of interfacial waves in aluminium reduction cells. *Journal of Fluid Mechanics*, 362:273–295, 1998.

P. A. Davidson, R. J. Kinnear, D .and Lingwood, D. J. Short, and X. He. The role of Ekman pumping and the dominance of swirl in confined flows driven by Lorentz forces. *European Journal of Mechanics-B/Fluids*, 18(4):693–711, 1999.

P. A. Davidson, O. Wong, J. W. Atkinson, and A. Ranjan. Magnetically driven flow in a liquid-metal battery. *Phys. Rev. Fluids*, 7:074701, Jul 2022.

E. M. De Les Valls, L. A. Sedano, L. Batet, I. Ricapito, A. Aiello, O. Gastaldi, and F. Gabriel. Lead–lithium eutectic material database for nuclear fusion technology. *Journal of nuclear materials*, 376(3):353–357, 2008.

W. Dreyer, C. Guhlke, M. Landstorfer, and R. Müller. New insights on the interfacial tension of electrochemical interfaces and the Lippmann equation. *European Journal of Applied Mathematics*, 29(4):708–753, 2018.

C. Duczek, N. Weber, O. E. Godinez-Brizuela, and T. Weier. Simulation of potential and species distribution in a Li||Bi liquid metal battery using coupled meshes. *Electrochimica Acta*, page 141413, 2023. ISSN 0013-4686.

EC. EU strategic dependencies and capacities: second stage of in-depth reviews. *European Commission*, 2022. URL `https://ec.europa.eu/docsroom/documents/48878/attachments/2/translations/en/renditions/native`.

EC. Energy Storage - Underpinning a decarbonised and secure EU energy system. *European Commission*, 2023. URL `https://energy.ec.europa.eu/system/files/2023-03/SWD_2023_57_1_EN_document_travail_service_part1_v6.pdf`.

A. Ern and J.-L. Guermond. *Theory and practice of finite elements*, volume 159. Springer, 2004.

A. Ern and J.-L. Guermond. *Finite Elements II.* Springer, 2021.

A. Ern, A. F. Stephansen, and P. Zunino. A discontinuous Galerkin method with weighted averages for advection–diffusion equations with locally small and anisotropic diffusivity. *IMA Journal of Numerical Analysis*, 29(2):235–256, 2009.

W. Gasior and Z. Moser. Thermodynamic study of liquid lithium–lead alloys using the EMF method. *Journal of nuclear materials*, 294(1-2):77–83, 2001.

W. Gasior, Z. Moser, and W. Zakulski. Bi-Li system thermodynamic properties and the phase diagram calculations. *Archives of metallurgy*, 39(4):355–369, 1994.

Jean-Frédéric Gerbeau, Claude Le Bris, and Tony Lelièvre. *Mathematical methods for the magnetohydrodynamics of liquid metals.* Clarendon Press, 2006.

J.-L. Guermond and J. Shen. On the error estimates for the rotational pressure-correction projection methods. *Mathematics of Computation*, 73(248):1719–1737, 2004.

J.-L. Guermond, R. Laguerre, J. Léorat, and C. Nore. An interior penalty Galerkin method for the MHD equations in heterogeneous domains. *J. Comput. Phys.*, 221(1):349–369, 2007.

J.-L. Guermond, R. Laguerre, J. Léorat, and C. Nore. Nonlinear magnetohydrodynamics in axisymmetric heterogeneous domains using a Fourier/finite element technique and an interior penalty method. *J. Comput. Phys.*, 228:2739–2757, 2009.

J.-L. Guermond, J. Léorat, F. Luddens, C. Nore, and A. Ribeiro. Effects of discontinuous magnetic permeability on magnetodynamic problems. *J. Comput. Phys.*, 230:6299–6319, 2011.

W. Herreman, C. Nore, L. Cappanera, and J.-L. Guermond. Tayler instability in liquid metal columns and liquid metal batteries. *Journal of Fluid Mechanics*, 771:79–114, 2015.

W. Herreman, C. Nore, J.-L. Guermond, L. Cappanera, N. Weber, and G. M. Horstmann. Perturbation theory for metal pad roll instability in cylindrical reduction cells. *Journal of Fluid Mechanics*, 878:598–646, 2019a.

W. Herreman, C. Nore, P. Ziebell Ramos, L. Cappanera, J.-L. Guermond, and N. Weber. Numerical simulation of electrovortex flows in cylindrical fluid layers and liquid metal batteries. *Phys. Rev. Fluids*, 4:113702, 2019b.

W. Herreman, S. Bénard, C. Nore, P. Personnettaz, L. Cappanera, and J.-L. Guermond. Solutal buoyancy and electrovortex flow in liquid metal batteries. *Phys. Rev. Fluids*, 5:074501, 2020.

W. Herreman, C. Nore, L. Cappanera, and J.-L. Guermond. Efficient mixing by swirling electrovortex flows in liquid metal batteries. *Journal of Fluid Mechanics*, 915:A17, 2021.

W. Herreman, L. Wierzchalek, G. M. Horstmann, L. Cappanera, and C. Nore. Stability theory for metal pad roll in cylindrical liquid metal batteries. *Journal of Fluid Mechanics*, 962:A6, 2023.

G. M. Horstmann, N. Weber, and T. Weier. Coupling and stability of interfacial waves in liquid metal batteries. *Journal of Fluid Mechanics*, 845:1–35, 2018.

J. C. R. Hunt and D. G. Malcolm. Some electrically driven flows in magnetohydrodynamics Part 2. Theory and experiment. *Journal of Fluid Mechanics*, 33(4):775–801, 1968.

J. C. R. Hunt and K. Stewartson. Magnetohydrodynamic flow in rectangular ducts. II. *Journal of Fluid Mechanics*, 23(3):563–581, 1965.

J. C. R. Hunt and K. Stewartson. Some electrically driven flows in magnetohydrodynamics Part 3. The asymptotic theory for flow between circular electrodes. *Journal of Fluid Mechanics*, 38(2):225–242, 1969.

IEA. World Energy Outlook 2022. 2022. URL `https://iea.blob.core.windows.net/assets/830fe099-5530-48f2-a7c1-11f35d510983/WorldEnergyOutlook2022.pdf`.

O. Kazak. Modeling of vortex flows in direct current (dc) electric arc furnace with different bottom electrode positions. *Metallurgical and Materials Transactions B*, 44:1243–1250, 2013.

O. V. Kazak and A. N. Semko. Electrovortex motion of a melt in dc furnaces with a bottom electrode. *Journal of engineering physics and thermophysics*, 84:223–231, 2011.

O. V. Kazak and A. N. Semko. Numerical modeling of electro-vortical flows in a confined volume. *Journal of Engineering Physics and Thermophysics*, 85:1167–1178, 2012.

D. H. Kelley and D. R. Sadoway. Mixing in a liquid metal electrode. *Physics of Fluids*, 26(5): 057102, 2014.

D. H. Kelley and T. Weier. Fluid mechanics of liquid metal batteries. *Applied Mechanics Reviews*, 70(2), 2018.

R. A. Khairulin, R. N. Abdullaev, S. V. Stankus, A. S. Agazhanov, and I. V. Savchenko. Volumetric properties of lithium–lead melts. *International Journal of Thermophysics*, 38: 1–10, 2017a.

R. A. Khairulin, S. V. Stankus, and R. N. Abdullaev. Interdiffusion in lithium–lead melts. *Thermophysics and Aeromechanics*, 24(5):773–778, 2017b.

A. Kharicha, I. Teplyakov, Yu. Ivochkin, M. Wu, A. Ludwig, and A. Guseva. Experimental and numerical analysis of free surface deformation in an electrically driven flow. *Experimental Thermal and Fluid Science*, 62:192–201, 2015.

H. Kim, D. A. Boysen, J. M. Newhouse, B. L. Spatocco, B. Chung, P. J. Burke, D. J. Bradwell, K. Jiang, A. A. Tomaszowska, K. Wang, W. Wei, L. A. Ortiz, S. A. Barriga, S. M. Poizeau, and D. R. Sadoway. Liquid metal batteries: Past, present, and future. *Chemical Reviews*, 113(3):2075–2099, 2013a.

Hojong Kim, Dane A Boysen, Takanari Ouchi, and Donald R Sadoway. Calcium–bismuth electrodes for large-scale energy storage (liquid metal batteries). *Journal of Power Sources*, 241:239–248, 2013b.

I. Kolesnichenko, P. Frick, V. Eltishchev, S. Mandrykin, and F. Stefani. Evolution of a strong electrovortex flow in a cylindrical cell. *Physical Review Fluids*, 5(12):123703, 2020.

T. Köllner, K. Schwarzenberger, K. Eckert, and T. Boeck. Multiscale structures in solutal Marangoni convection: Three-dimensional simulations and supporting experiments. *Physics of Fluids*, 25(9):092109, 2013.

T. Köllner, K. Schwarzenberger, K. Eckert, and T. Boeck. Solutal Marangoni convection in a Hele–Shaw geometry: Impact of orientation and gap width. *The European Physical Journal Special Topics*, 224(2):261–276, 2015.

T. Köllner, T. Boeck, and J. Schumacher. Thermal Rayleigh-Marangoni convection in a three-layer liquid-metal-battery model. *Physical Review E*, 95(5):053114, 2017.

LC. Net-zero power – Long-duration energy storage for a renewable grid. *LDES Council, McKinsey & Company*, 2021. URL https://www.ldescouncil.com/assets/pdf/LDES-brochure-F3-HighRes.pdf.

Gabriel Lippmann. *Beziehungen zwischen den capillaren und elekrischen Erscheinungen*. 1873.

K. Liu, F. Stefani, N. Weber, T. Weier, and B. W. Li. Numerical and experimental investigation of electro-vortex flow in a cylindrical container. *Magnetohydrodynamics*, 56(1):27–41, 2020.

J. Lück and A. Latz. Theory of reactions at electrified interfaces. *Physical Chemistry Chemical Physics*, 18(27):17799–17804, 2016.

S. Lundquist. On the hydrodynamic viscous flow generated by a diverging electric current. 1969.

D. Martelli, A. Venturini, and M. Utili. Literature review of lead-lithium thermophysical properties. *Fusion Engineering and Design*, 138:183–195, 2019.

R. P. Millere, V. I. Sharamkin, and E. V. Shcherbinin. Effect of a longitudinal magnetic field on electrically driven rotational flow in a cylindrical vessel. *Magnetohydrodynamics*, 16(1): 66–69, 1980.

R. Monchaux, M. Berhanu, M. Bourgoin, M. Moulin, Ph. Odier, J.-F. Pinton, R. Volk, S. Fauve, N. Mordant, F. Pétrélis, A. Chiffaudel, F. Daviaud, B. Dubrulle, C. Gasquet, L. Marié, and F. Ravelet. Generation of a magnetic field by dynamo action in a turbulent flow of liquid sodium. *Physical Review Letters*, 98(4):044502, 2007.

P. Moresco and T. Alboussiere. Experimental study of the instability of the Hartmann layer. *Journal of Fluid Mechanics*, 504:167–181, 2004.

J. M. Newhouse and D. R. Sadoway. Charge-transfer kinetics of alloying in Mg-Sb and Li-Bi liquid metal electrodes. *Journal of The Electrochemical Society*, 164(12):A2665, 2017.

X. Ning, S. Phadke, B. Chung, H. Yin, P. Burke, and D. R. Sadoway. Self-healing Li–Bi liquid metal battery for grid-scale energy storage. *Journal of Power Sources*, 275:370–376, 2015.

C. Nore, L. S. Tuckerman, O. Daube, and S. Xin. The 1 [ratio] 2 mode interaction in exactly counter-rotating von Kármán swirling flow. *Journal of Fluid Mechanics*, 477:51–88, 2003.

C. Nore, M. Tartar, O. Daube, and L. S. Tuckerman. Survey of instability thresholds of flow between exactly counter-rotating disks. *Journal of Fluid Mechanics*, 511:45–65, 2004.

T. Ouchi, H. Kim, X. Ning, and D. R. Sadoway. Calcium-antimony alloys as electrodes for liquid metal batteries. *Journal of The Electrochemical Society*, 161(12):A1898, 2014.

P. Personnettaz. *Simulations of mass transport in liquid metal electrodes.* PhD thesis, 2022.

P. Personnettaz, P. Beckstein, S. Landgraf, T. Köllner, M. Nimtz, N. Weber, and T. Weier. Thermally driven convection in Li|| Bi liquid metal batteries. *Journal of Power Sources*, 401: 362–374, 2018.

P. Personnettaz, S. Landgraf, M. Nimtz, N. Weber, and T. Weier. Mass transport induced asymmetry in charge/discharge behavior of liquid metal batteries. *Electrochemistry Communications*, 105:106496, 2019. ISSN 1388-2481.

P. Personnettaz, S. Landgraf, M. Nimtz, N. Weber, and T. Weier. Effects of current distribution on mass transport in the positive electrode of a liquid metal battery. *arXiv preprint arXiv:2104.00144*, 56(2/3):247–255, 2020.

P. Personnettaz, T. S. Klopper, N. Weber, and T. Weier. Layer coupling between solutal and thermal convection in liquid metal batteries. *International Journal of Heat and Mass Transfer*, 188:122555, 2022.

Y. Plevachuk, V. Sklyarchuk, S. Eckert, G. Gerbeth, and R. Novakovic. Thermophysical properties of the liquid Ga–In–Sn eutectic alloy. *Journal of Chemical & Engineering Data*, 59(3): 757–763, 2014.

A. Poyé, O. Agullo, N. Plihon, W. J. T. Bos, V. Desangles, and G. Bousselin. Scaling laws in axisymmetric magnetohydrodynamic duct flows. *Phys. Rev. Fluids*, 5:043701, Apr 2020.

B. Schulz. Thermophysical properties of the Li (17) Pb (83) alloy. *Fusion Engineering and Design*, 14(3-4):199–205, 1991.

T. Sele. Instabilities of the metal surface in electrolytic cells. *Paper from" Light Metals 1977".*, 1, 1977.

Y. Shen and O. Zikanov. Thermal convection in a liquid metal battery. *Theoretical and Computational Fluid Dynamics*, 30(4):275–294, 2015.

J. A. Shercliff. Fluid motions due to an electric current source. *Journal of Fluid Mechanics*, 40 (2):241–250, 1970.

C. Sozou. On fluid motions induced by an electric current source. *Journal of Fluid Mechanics*, 46(1):25–32, 1971.

C. Sozou and W. M. Pickering. Magnetohydrodynamic flow due to the discharge of an electric current in a hemispherical container. *Journal of fluid mechanics*, 73(4):641–650, 1976.

B. L. Spatocco and D. R. Sadoway. Cost-Based Discovery for Engineering Solutions. *Advances in Electrochemical Science and Engineering: Electrochemical Engineering Across Scales: From Molecules to Processes*, pages 227–262, 2015.

F. Stefani, T. Weier, T. Gundrum, and G. Gerbeth. How to circumvent the size limitation of liquid metal batteries due to the Tayler instability. *Energy conversion and management*, 52 (8-9):2982–2986, 2011.

R. J. Tayler. The adiabatic stability of stars containing magnetic fields–I: Toroidal fields. *Monthly Notices of the Royal Astronomical Society*, 161(4):365–380, 1973.

L. J. P. Timmermans, P. D. Minev, and F. N. Van De Vosse. An approximate projection scheme for incompressible flow using spectral elements. *International journal for numerical methods in fluids*, 22(7):673–688, 1996.

Yu V Vandakurov. Theory for the stability of a star with a toroidal magnetic field. *Soviet Astronomy, Vol. 16, p. 265*, 16:265, 1972.

K. J. Vetter. *Electrochemical kinetics*. Academic Press, 1967.

D. A. Vinogradov, Yu. P. Ivochkin, and I. O. Teplyakov. Effect of the earth's magnetic field on the electric-vortex-flow structure, 2018.

V. K. Vlasyuk. Effects of fusible-electrode radius on the electrovortex flow in a cylindrical vessel. *Magnetohydrodynamics*, 4:101–106, 1987.

W. J. Walsh, E. C. Gay, J. D. A., J. E. Kincinas, E. J. Cairns, and D. S. Webster. Lithium/chalcogen secondary cells for components in electric vehicular-propulsion generating systems. *ANL-7999*, 1971.

K. Wang, K. Jiang, B. Chung, T. Ouchi, P. J. Burke, D. A. Boysen, D. J. Bradwell, H. Kim, U. Muecke, and D. R. Sadoway. Lithium–antimony–lead liquid metal battery for grid-level energy storage. *Nature*, 514(7522):348–350, 2014.

J.-F. Wax, M. R. Johnson, L. E. Bove, and M. Mihalkovic. Multi-Scale Study of the Static Structure of Liquid Li70-Bi30 Alloy. 15:01002, 2011.

N. Weber, V. Galindo, F. Stefani, T. Weier, and T. Wondrak. Numerical simulation of the Tayler instability in liquid metals. *New Journal of Physics*, 15(4):043034, 2013.

N. Weber, V. Galindo, F. Stefani, and T. Weier. Current-driven flow instabilities in large-scale liquid metal batteries, and how to tame them. *Journal of Power Sources*, 265:166–173, 2014.

N. Weber, V. Galindo, J. Priede, F. Stefani, and T. Weier. The influence of current collectors on Tayler instability and electro-vortex flows in liquid metal batteries. *Physics of Fluids*, 27 (1):014103, 2015.

N. Weber, P. Beckstein, V. Galindo, W. Herreman, C. Nore, F. Stefani, and T. Weier. Metal pad roll instability in liquid metal batteries. *Magnetohydrodynamics*, 53(1):129–140, 2017a.

N. Weber, P. Beckstein, W. Herreman, G. M. Horstmann, C. Nore, F. Stefani, and T. Weier. Sloshing instability and electrolyte layer rupture in liquid metal batteries. *Physics of fluids*, 29(5):054101, 2017b.

N. Weber, P. Beckstein, V. Galindo, M. Starace, and T. Weier. Electro-vortex flow simulation using coupled meshes. *Comput. Fluids*, 168:101–109, 2018a.

N. Weber, M. Nimtz, P. Personnettaz, A. Salas, and T. Weier. Electromagnetically driven convection suitable for mass transfer enhancement in liquid metal batteries. *Applied Thermal Engineering*, 143:293–301, 2018b.

N. Weber, S. Landgraf, K. Mushtaq, M. Nimtz, P. Personnettaz, T. Weier, J. Zhao, and D. Sadoway. Modeling discontinuous potential distributions using the finite volume method, and application to liquid metal batteries. *Electrochimica Acta*, 318:857–864, 2019.

N. Weber, M Nimtz, P. Personnettaz, T. Weier, and D. Sadoway. Numerical simulation of mass transfer enhancement in liquid metal batteries by means of electro-vortex flow. *Journal of Power Sources Advances*, 1:100004, 2020. ISSN 2666-2485.

T. Weier, A. Bund, W. El-Mofid, G. M. Horstmann, C. C. Lalau, S. Landgraf, M. Nimtz, M. Starace, F. Stefani, and N. Weber. Liquid metal batteries-materials selection and fluid dynamics. 228(1):012013, 2017.

T. Weier, I. Grants, G. M. Horstmann, S. Landgraf, M. Nimtz, P. Personnettaz, F. Stefani, and N. Weber. Conductivity influence on interfacial waves in liquid metal batteries and related two-layer systems. *arXiv preprint arXiv:2104.04211*, 2021.

J. Xu, O. S. Kjos, K. S Osen, A. M. Martinez, O. E. Kongstein, and G. M. Haarberg. Na-Zn liquid metal battery. *Journal of Power Sources*, 332:274–280, 2016. ISSN 0378-7753.

F. Zhang, J. Jin, J. Xu, and Z. Shi. Anode reaction mechanisms of na— nacl-cacl2— zn liquid metal battery. *Journal of Energy Chemistry*, 72:81–87, 2022.

V. G. Zhilin, Y. P. Ivochkin, A. A. Oksman, G. R. Lurin'sh, A. I. Chaikovskii, A. Y. Chudnovskii, and E. V. Shcherbinin. An experimental investigation of the velocity field in an axisymmetric electrovortical flow in a cylindrical container. *Magnetohydrodynamics*, 3:110–116, 1986.

O. Zikanov. Metal pad instabilities in liquid metal batteries. *Physical Review E*, 92(6):063021, 2015.

O. Zikanov. Shallow water modeling of rolling pad instability in liquid metal batteries. *Theoretical and Computational Fluid Dynamics*, 32(3):325–347, 2018.